

**Investigation and Optimization of Electrochemical Systems via Simulation and Theory**

by

Vishwas Goel

A dissertation submitted in partial fulfillment  
of the requirements for the degree of  
Doctor of Philosophy  
(Materials Science and Engineering and Scientific Computing)  
in the University of Michigan  
2023

Doctoral Committee:

Professor Katsuyo Thornton, Chair  
Professor Neil P. Dasgupta  
Professor Jeff Sakamoto  
Professor Donald Siegel, University of Texas, Austin

Vishwas Goel

vishwasg@umich.edu

ORCID iD: 0000-0002-5513-6584

© Vishwas Goel 2023

## **DEDICATION**

*In memory of my late father, Shri Kapoor Chand Goel,  
who taught me the true meaning of hard work.*

## ACKNOWLEDGEMENTS

There are so many wonderful people without whom this dissertation would not have been possible. First and foremost is my advisor, Prof. Katsuyo Thornton, who took a chance with me by openly welcoming me into her group despite my nonexistent background in computational research. I cannot thank her enough for all the time she invested in me and my work. Her guidance and constructive feedback shaped me into the researcher that I am today, and her dedication and work ethic will keep inspiring me forever. I am also grateful to Prof. Neil Dasgupta and Prof. Jeff Sakamoto, who served on my dissertation committee and offered excellent opportunities to collaborate. Their feedback brought additional insight to my research, thereby elevating its quality. I would also like to thank Prof. Donald Siegel for serving on my committee and for his valuable input.

In addition to my committee, I would also like to thank the members of the Thornton group, both past and present, for all the support and help they provided over the years. I could not have found my footing in the group without the help of Dr. David Montiel, Dr. Beck Andrews, Dr. Saeed Kazemiabnavi, and Prof. Hui-Chia Yu. Additionally, I am grateful to my fellow scholars and collaborators, Dr. Kuan-Hung (Michael) Chen, Dr. Yuxin Chen, Ms. Min Ji Namkoong at the University of Michigan, and Mr. Dalton Cox at Northwestern University, who made research fun and exciting.

My grad-school experience would have been lackluster without the friends I made here, including Kunal, Anshul, Mohit, Aaditya, Kaushik, Akarsh, Thomas, Max, Aaron, Prashant,

Sumit, and many others. They stood by me, uplifted my spirits during tough times, spent time with me, and created fun memories for me. In addition, I also want to thank my best friend, Lokap, who always believed in me and is a constant source of motivation in my life. Furthermore, I also want to acknowledge the role of every teacher in my life, without whom I would not have reached this stage. Last but not least, on the list of people to thank is my loving and caring family. They have always encouraged me to pursue my dreams and passions. I cannot thank them enough for the sacrifices they made for my education, especially after my father's passing. Instead of burdening me with familial responsibilities, they pushed me to achieve my potential.

I also acknowledge the funding agencies and computational facilities that provided resources for this work. The research on Li-ion batteries was supported by the Office of Energy Efficiency and Renewable Energy (EERE) of the U.S. Department of Energy under Award Number DE-EE0008362. The funding for the corrosion work was provided by the U.S. Department of Energy, Office of Basic Energy Sciences, Division of Materials Sciences and Engineering, under Award No. DE-SC0008637 as part of the Center for Predictive Integrated Structural Materials Science (PRISMS Center) at the University of Michigan. Furthermore, the research on fuel cells was supported by the U.S. National Science Foundation, Division of Material Research under the grant numbers DMR-1912151 and DMR-1912530. Additionally, the funding from the Rackham Predoctoral Fellowship and the MICDE Fellowship also played a tremendous role in supporting this work. The computational resources were provided by the Extreme Science and Engineering Discovery Environment (XSEDE) (allocation No. TG-DMR110007), which is supported by the U.S. National Science Foundation under grant number ACI-1053575 and by the National Energy Research Scientific Computing Center (NERSC), a DOE Office of Science User Facility supported by the Office of Science of the U.S. Department of Energy under Contract No.

DE-AC02–05CH11231. Additional access to computational resources and simulation tools was provided by the Advanced Research Computing (ARC) and CAEN at the University of Michigan.

## Table of Contents

Dedication .....	ii
Acknowledgements .....	iii
List of Tables .....	x
List of Figures .....	xii
List of Acronyms .....	xvii
Abstract .....	xix
Chapter 1 Introduction and Motivation.....	1
1.1 Motivation .....	1
1.2 Dissertation overview .....	5
1.3 Author contributions .....	7
Chapter 2 Background .....	9
2.1 Li-ion batteries .....	9
2.2 Microgalvanic corrosion in Mg alloys .....	14
2.3 Solid oxide fuel cells .....	17
2.4 Governing equations .....	20
2.4.1 Electronic transport .....	20
2.4.2 Ionic transport in a binary electrolyte.....	21
2.4.3 Solid-state transport of neutral species.....	26
2.4.4 Electrochemical reaction .....	26

2.4.5 Electrochemical impedance spectroscopy (EIS) .....	28
Chapter 3 Methods .....	30
3.1 Finite difference method .....	30
3.1.1 Introduction .....	30
3.1.2 Discretization methods and associated error .....	31
3.1.3 FDM solution to 1D diffusion equation .....	34
3.2 Finite element method.....	39
3.2.1 Introduction .....	39
3.2.2 Derivation of the weak form.....	41
3.2.3 Discretization and assembly.....	43
3.2.4 PRISMS-PF and deal.II.....	50
3.3 Smoothed boundary method.....	51
3.3.1 Introduction .....	51
3.3.2 Derivation of the SBM form.....	52
Chapter 4 Effect of Laser Patterning on the Fast-Charging Performance of Energy-Dense Li-ion Batteries .....	55
4.1 Introduction: Fast charging of energy-dense Li-ion batteries .....	55
4.2 Summary of experimental results for laser-patterned electrodes .....	58
4.3 Governing equations to model the fast-charging performance of Li-ion battery electrodes.....	61
4.4 Model parameterization for Li-ion battery electrodes.....	66
4.4.1 Electrode parameters .....	67
4.4.2 Separator parameters .....	72
4.4.3 Automated parameterization procedure .....	73
4.5 Simulation results for the effect of laser patterning on the fast-charging performance of graphite electrodes.....	83
4.6 Chapter 4 Summary.....	86



4.7 Chapter 4 Appendix .....	87
Chapter 5 Optimization of the Highly Ordered Laser-Patterned Electrode Architecture Using Continuum-Level Simulations .....	91
5.1 Introduction: Optimal design of the laser-patterned electrode for fast charging .....	91
5.2 Optimization of the HOLE architecture .....	92
5.2.1 Quantification of the current homogeneity and $Da_{II}$ .....	100
5.2.2 Semi-analytical estimation of the time-averaged $f_{\xi}$ and $Da_{II}$ .....	112
5.2.3 Optimal HOLE configuration for 6C charging .....	116
5.2.4 Effect of materials properties and electrode design on $Da_{II}$ and the optimal configuration .....	118
5.3 Chapter 5 Summary .....	121
5.4 Chapter 5 Appendix .....	122
Chapter 6 Effect of Material Properties and Microstructure on the Microgalvanic Corrosion Behavior of Mg Alloys .....	126
6.1 Introduction: Microgalvanic corrosion of Mg alloys .....	126
6.2 Governing equations for microgalvanic corrosion .....	129
6.3 Simulation results for the effect of the material properties of the $\beta$ phase, the electrolyte, and the alloy microstructure on corrosion behavior .....	136
6.3.1 Sensitivity analyses .....	136
6.3.2 Effect of microstructure on corrosion behavior .....	149
6.4 Chapter 6 Summary .....	164
6.5 Chapter 6 Appendix .....	165
Chapter 7 Effect of Material Properties on the Impedance Behavior and Tortuosity of SOFC Cathodes .....	171
7.1 Introduction: Application of electrochemical impedance spectroscopy to characterize SOFC cathodes .....	171
7.2 Model equations for impedance calculation .....	175
7.3 Numerical implementation of the impedance model .....	181

7.4 Derivation for impedance expressions and transcendental equation for tortuosity .....	182
7.5 Extension to the ALS model .....	186
7.6 Simulated impedance and tortuosity calculation.....	191
7.7 Chapter 7 Summary.....	198
7.8 Chapter 7 Appendix .....	199
Chapter 8 Summary and Future Work .....	210
8.1 Summary .....	210
8.2 Future work .....	213
8.2.1 Fast charging of energy-dense Li-ion batteries .....	213
8.2.2 Microgalvanic corrosion in Mg alloys .....	214
8.2.3 Impedance modeling of SOFC cathodes .....	215
8.3 Conclusion.....	216

## LIST OF TABLES

Table 3.1. A list of the value of $\Theta$ for common time-stepping schemes, along with their accuracy and stability. ....	37
Table 4.1. The list of symbols and description for the variables in the model equations. ....	65
Table 4.2. PSO hyperparameters and their values. ....	75
Table 4.3. The minimum and maximum values set for each parameter obtained using the PSO algorithm. ....	76
Table 4.4. Anode parameter values identified and used in this work, along with their sources and comparison with the ranges of values surveyed from the literature. ....	80
Table 4.5. Cathode parameter values identified and used in this work, along with their sources and comparison with the ranges of values surveyed from the literature. ....	81
Table 4.6. Values of the remaining model parameters identified and used in this work, along with their sources and comparison with the ranges of values surveyed from the literature. ....	82
Table 5.1. List of values of $d_h$ used in the 4C optimization study along with corresponding values of $\mu_h$ and $\delta_h$ . ....	95
Table 5.2. The list of symbols used in Section 5.2 along with their description. ....	102
Table 5.3. List of Li-site fraction ranges corresponding to graphite OCV plateaus. ....	106
Table 6.1 List and description of the variables and symbols used in the model equations. ....	134
Table 6.2. Parameter values used in the simulations presented here, unless specified otherwise, along with their sources. ....	136
Table 6.3. A comparison of the four microstructures used for the 2D system. In all cases, the area fraction of the $\beta$ phase is set to 21%. ....	151
Table 6.4. A comparison of the four microstructures used for the 3D system. Note that the red and green regions in the figures represent the $\alpha$ and $\beta$ domains, respectively. ....	159
Table 6.5. Numerical parameters used in the sensitivity analyses. ....	166

Table 6.6. Numerical parameters used in the simulations performed to study the effect of the microstructure. ....	167
Table 7.1. Sets of boundary conditions applied to the system of equations, Eqs. 7.14 and. 7.15. ....	179
Table 7.2. List and description of the variables and symbols used in this chapter. ....	180
Table 7.3. List of the errors in the real and imaginary components of impedance calculated for three different grids.....	202

## LIST OF FIGURES

Figure 1.1. A schematic representation of various applications of electrochemistry in the modern world. ....	2
Figure 1.2. A schematic showing the overview of the Materials Genome Initiative approach, which involves the integration of experiments, computation, and data-driven methods. ....	3
Figure 1.3. Examples of the three electrochemical systems, namely, Li-ion batteries (LIBs), Mg alloys undergoing microgalvanic corrosion, and solid oxide fuel cells (SOFCs), investigated in this dissertation. ....	5
Figure 2.1. A schematic showing the following formats of Li-ion batteries: (a) cylindrical cell, (b) prismatic cell, (c) coin cell, and (d) pouch cell. ....	10
Figure 2.2. A schematic showing the basic structure of a Li-ion battery, along with the motion of Li ions and electrons during (a) charging and (b) discharging. ....	11
Figure 2.3. (a) Volumetric energy density of a $\text{LiNi}_{0.6}\text{Mn}_{0.2}\text{Co}_{0.2}\text{O}_2$ (NMC622)/graphite cell calculated as a function of cathode thickness and cathode porosity. (b) C/3 Discharge capacity of cells with different cathode loadings at various charging rates. (c) Optical images of the graphite electrode extracted out of the cells with three different cathode loadings after cycling. The silver deposit on the electrodes is the plated Li. ....	13
Figure 2.4. Schematic of the Highly Ordered Laser-patterned Electrode (HOLE) architecture formed by ablating vertical channels in the electrode using laser. ....	14
Figure 2.5. (a) A schematic representation of the galvanic corrosion of Zn due to its coupling with Fe in an aqueous environment. Zn ions dissolve from the anodic region, creating electrons that travel to the cathodic region and reduce oxygen to form water at the cathode/electrolyte interface. (b) An example of the galvanic corrosion, where the nut corrodes due to its galvanic coupling with the screw. ....	15
Figure 2.6. The SEM image of an AZ91 alloy sample after (a) 1 hr and (b) 18 hrs of immersion in 1N (or 1M) NaCl solution (at different locations in the same sample). ....	16
Figure 2.7. A schematic of a solid oxide fuel cell (SOFC) operating in (a) the fuel cell mode and (b) the electrolysis mode. ....	19
Figure 3.1. A schematic showing the finite-difference discretization of a function $f(x)$ . The black dots on the x-axis represent the finite number of points used to discretize the domain. ....	32

Figure 3.2. A schematic of the discretization of the 1D domain considered in the example here. The filled nodes represent the extents of the first, $e^{th}$ , and the last elements in the domain, while the empty nodes represent the intermediate elements.....	44
Figure 4.1. Schematic illustration of the Highly Order Laser-Patterned Electrode (HOLE) architecture. The black outline in the HOLE pattern represents the hexagonal symmetry of the channels (highlighted in blue) in the electrode.....	56
Figure 4.2. Summary of 4C and 6C experimental results (normalized discharge capacity and columbic efficiency as functions of cycle number) for the pouch cells based on control (unmodified) and HOLE (laser-modified) anodes.....	59
Figure 4.3. A schematic of a Li-ion cell. The thickness of the cell is oriented along the Z axis..	61
Figure 4.4. Categorization of the model parameters. The superscript next to each parameter, †, ‡, or §, indicates the sources of the parameter values, which corresponds to experiments, automated parameterization procedure, and literature, respectively.....	67
Figure 4.5. Flow chart showing the PSO algorithm.....	74
Figure 4.6. Comparison between the experimental and simulated voltage traces for the anode in the (a) control cell and (b) HOLE cell (with the HOLE patterned anode). The experimental data are shown in solid curves, while the simulation data are shown with dashed curves. The data show six rates from 0.1C (black) to 6C (cyan).....	78
Figure 4.7. The evolution of the objective function obtained for the anode and the cathode in the control cell (with unmodified electrodes). The error for the anode is on the left y-axis, and that for the cathode is on the right y-axis. ....	78
Figure 4.8. Comparison between the experimental and simulated voltage traces for the cathode in the (a) control cell and (b) HOLE cell (with the HOLE patterned anode). The experimental data are shown in solid curves, while the simulation data are shown with dashed curves. The data show six rates from 0.1C (black) to 6C (cyan).....	79
Figure 4.9. Evolution of Li-ion concentration in the electrolyte phase of the (a) control graphite anode at $t = 20, 40, 80,$ and $125$ s, (b) HOLE graphite anode at time $t = 20, 40, 80, 125, 245,$ and $364$ s during 4C charging.....	84
Figure 4.10. Evolution of the magnitude of reaction rate in the (a) control graphite anode at $t = 20, 40, 80,$ and $125$ s, (b) HOLE graphite anode at time $t = 20, 40, 80, 125, 245,$ and $364$ s during 4C charging. The color indicates the magnitude of the reaction rate in $A/cm^3$ according to the color bar on the right.....	86
Figure 4.11. The experimentally obtained open-circuit voltage as a function of the lithium site fraction for (a) graphite and (b) $LiN_{0.5}M_{0.3}C_{0.2}O_2$ (NMC-532). ....	88
Figure 4.12. Diffusion coefficient of lithium in graphite as a function of the lithium site fraction. ....	88

Figure 4.13. The intrinsic properties of the electrolyte as a function of Li-ion concentration. ....	89
Figure 4.14. (a) Comparison of the voltage vs. SOC plot for the control anode and the control anode with no mass transport limitations during 4C charging. (b) The evolution of RCD along the anode thickness for the two control anodes. ....	90
Figure 5.1. Schematic of a triangle formed by three adjacent channels, simulated voltage vs. SOC plots and the accessible capacity as a function of $d_h$ at 4C for all HOLE configurations considered here. ....	95
Figure 5.2. Time series of the simulated reaction current density distribution (RCD) for the control and HOLE anode ( $d_h = 85 \mu m$ ) during 4C charging. The times for the images were selected when the anode voltage is 0.3V, 0.2V, 0.1V, 0.05V, and 0V, as noted at the bottom of the figure. ....	98
Figure 5.3. Time series of the simulated RCD distribution in three HOLE anodes with $d_h = 55, 145, \text{ and } 235 \mu m$ during 4C charging. The times for the images were selected when the anode voltage is 0.3V, 0.2V, 0.1V, 0.05V, and 0V, as noted at the bottom of the figure. ....	100
Figure 5.4. The OCV vs. Li-site fraction plot (black, left y-axis) and its derivative (blue, right y-axis). The red, purple, and blue shaded areas represent the regions corresponding to the first, second, and third plateau, respectively. ....	106
Figure 5.5. Simulated reaction current density (RCD), fractional contribution to current from the peak and the corresponding volume, and the Damköhler number. ....	108
Figure 5.6. Comparison of the simulated and semi-analytically obtained time-averaged active volume fraction ( $f_\xi$ ) and Damköhler number. ....	113
Figure 5.7. 6C results for semi-analytically obtained time-averaged Damköhler number, simulated voltage vs. SOC plot for six HOLE anodes, and the simulated accessible capacity. ....	117
Figure 5.8. The half-cell configuration used in the 3D simulations for the optimization study. The view in (a) shows Li electrode on the top, and (b) shows the graphite electrode on top. The channels are highlighted in blue. ....	123
Figure 5.9. Comparison of the 4C results (voltage vs. SOC and the accessible capacity) for the loading-adjusted anode with other anodes considered here. ....	124
Figure 5.10. The custom mesh used in the 3D simulations for the optimization study. The view in (a) shows Li electrode on the top, and (b) shows the graphite electrode on top. ....	125
Figure 6.1. Results for the corrosion current, morphology of the corroded surface, and the Wagner length from the sensitivity analysis with respect to the exchange current density of the $\beta$ phase. ....	138

Figure 6.2. The plot of the electrolyte potential,  $\Phi_e$ , along the metal/electrolyte interface at  $t = 0$  s for different values of  $i_{\text{corr},\beta}$  considered in the sensitivity analysis. The grey dashed line represents the  $\alpha/\beta$  interface; the  $\beta$  domain lies on the right side of the line. .... 140

Figure 6.3. The simulated morphology of the metal/electrolyte interface for (a)  $i_{\text{corr},\beta} = 1 \text{ A/m}^2$  and  $i_{\text{max}} = 1 \times 10^3 \text{ m}^2$  at  $t = 72\text{s}$  and (b)  $i_{\text{corr},\beta} = 5 \times 10^{-3} \text{ A/m}^2$  and  $i_{\text{max}} = 1 \times 10^2 \text{ A/m}^2$  at  $t = 4000 \text{ s}$ . The red, green, and blue regions correspond to the  $\alpha$ ,  $\beta$ , and electrolyte phases, respectively. .... 140

Figure 6.4. The plot of  $W_\alpha$  along the  $\alpha$ /electrolyte interface for  $i_{\text{corr},\beta} = 1.7 \times 10^{-2} \text{ A/m}^2$  at  $t = 1110 \text{ s}$ . The color indicates the value of  $W_\alpha$  according to the color bar on the right. .... 142

Figure 6.5. Results for the corrosion current, morphology of the corroded surface, and the Wagner length from the sensitivity analysis with respect to the corrosion potential of the  $\beta$  phase. .... 144

Figure 6.6. Results for the corrosion current, morphology of the corroded surface, and the Wagner length from the sensitivity analysis with respect to the electrolyte conductivity. .... 147

Figure 6.7. Corrosion current as a function of time and cathode surface area per unit length for the 2D microstructures. .... 152

Figure 6.8. The plot of  $S_\beta$  (the cathode surface area per unit length perpendicular to the simulation plane) vs. time for the 2D microstructures studied in this work. .... 154

Figure 6.9. Time series of the corrosion evolution in the four 2D microstructures investigated here, which are presented in different rows. Times selected are 200s (the first column), 400s (the second column), and 600s (the third column). .... 157

Figure 6.10. Corrosion current as a function of time and cathode surface for the 3D microstructures. .... 161

Figure 6.11. Time series of the corrosion evolution in the four 3D microstructures investigated, which are presented in different rows. Times selected are 250 s (the first column), 500 s (the second column), and 750 s (the third column). .... 163

Figure 6.12. The plot of the electrolyte potential,  $\Phi_e$ , along the metal/electrolyte interface at  $t = 0$  s for different values of  $E_{\text{corr},\beta}$  considered in the sensitivity analysis. The grey dashed line represents the  $\alpha/\beta$  interface; the  $\beta$  domain lies on the right side of the line. .... 168

Figure 6.13. The relation between the corrosion current and  $S_\beta$  (the cathode surface area per unit length perpendicular to the simulation plane) for Case 4 with different values of  $\kappa_e$  and  $i_{\text{max}}$ . 169

Figure 6.14. The plot of (a) the corrosion current vs. time and (b) the cathode area vs. time for the 3D microstructures studied here. .... 169

Figure 7.1. A schematic of oxygen transport withing the solid phase (grey region) of a MIEC SOFC cathode. .... 175



Figure 7.2. Simulated results for the spatial variation in $C_R$ and $C_I$ in a model cylindrical microstructure for two values of $\hat{\kappa}^{3D}$ .....	187
Figure 7.3. Calculated $\langle\alpha\rangle$ vs. $\hat{\omega}$ (BCC BC) at (a) $\hat{\kappa}^{3D} = 0.0231$ , (b) 0.05, and (c) 0.1.....	190
Figure 7.4. DC value of $\langle\alpha\rangle$ , $\langle\alpha_0\rangle$ , as a function of $\hat{\kappa}^{3D}$ .....	190
Figure 7.5. Nyquist plots obtained from 3D calculations for the BCC BC (black curve) and 1D FLG model (blue curve) for (a) $\hat{\kappa}^{3D} = 0.0231$ , (b) 0.05, and (c) 0.1.....	192
Figure 7.6. Calculated $\tau$ vs. $\hat{\omega}$ relations (BCC BC) for $\hat{\kappa}^{3D} = 0.0231$ (blue circles), 0.05 (magenta squares), and 0.1 (green diamonds). .....	193
Figure 7.7. The distribution of the real and imaginary components of the concentration amplitude calculated for the BCC BC, $\hat{\omega} = 0.018$ and (a) $\hat{\kappa}^{3D} = 0.0231$ , (b) 0.05, and (c) 0.1.....	196
Figure 7.8. The distribution of the real and imaginary components of the concentration amplitude calculated for the BCC BC, $\hat{\omega} = 1.038$ and (a) $\hat{\kappa}^{3D} = 0.0231$ , (b) 0.05, and (c) 0.1.....	197
Figure 7.9. Comparisons of the calculated $\tau$ vs. $\hat{\omega}$ relations (BCC BC) by using $\langle\alpha_0\rangle$ (blue curve) and $\langle\alpha\rangle$ (black curve) for (a) $\hat{\kappa}^{3D} = 0.0231$ , (b) 0.05, and (c) 0.1. ....	198
Figure 7.10. Plot of $C_R$ and $C_I$ as a function of cylinder radius for the three grid configurations at $x = 0.1$ and (a) $\hat{\omega} = 1.038$ , (b) $\hat{\omega} = 42$ , and (c) $\hat{\omega} = 95$ .....	203
Figure 7.11. Nyquist plots obtained from 3D calculations for the TCC BC (black circles) and 1D FLG-TCC model (blue squares) for (a) $\hat{\kappa}^{3D} = 0.0231$ , (b) 0.05, and (c) 0.1. ....	205
Figure 7.12. Calculated $\tau$ vs. $\hat{\omega}$ relations (TCC BC) for $\hat{\kappa}^{3D} = 0.0231$ (blue circles), 0.05 (magenta squares), and 0.1 (green diamonds). .....	206
Figure 7.13. The distribution of the real and imaginary components of the concentration amplitude calculated for the TCC BC, $\hat{\omega} = 0.018$ and (a) $\hat{\kappa}^{3D} = 0.0231$ , (b) 0.05, and (c) 0.1. ....	207
Figure 7.14. The distribution of the real and imaginary components of the concentration amplitude calculated for the TCC BC, $\hat{\omega} = 1.038$ and (a) $\hat{\kappa}^{3D} = 0.0231$ , (b) 0.05, and (c) 0.1. ....	208
Figure 7.15. Comparison of calculated $\tau$ vs. $\hat{\omega}$ relations (TCC BC) by using $\langle\alpha_0\rangle$ (blue curve) and $\langle\alpha\rangle$ (black curve) for (a) $\hat{\kappa}^{3D} = 0.0231$ , (b) 0.05, and (c) 0.1.....	209

## LIST OF ACRONYMS

<b>ADLR</b>	Alternating Direction Line Relaxation
<b>ALS</b>	Adler-Lane-Steele
<b>BC</b>	Boundary Condition
<b>BCC</b>	Blocking Current Collector
<b>CE</b>	Coulombic Efficiency
<b>CFL</b>	Courant Friedrichs Lewy
<b>DOF</b>	Degrees of Freedom
<b>EIS</b>	Electrochemical Impedance Spectroscopy
<b>EVs</b>	Electric Vehicles
<b>FDM</b>	Finite Difference Method
<b>FEM</b>	Finite Element Method
<b>FIB</b>	Focused Ion Beam
<b>FLG</b>	Finite Length Gerischer
<b>GITT</b>	Galvanostatic Intermittent Titration Technique
<b>HER</b>	Hydrogen Evolution Reaction
<b>HOLE</b>	Highly Ordered Laser-Patterned Electrode
<b>LIBs</b>	Li-Ion Batteries
<b>MGI</b>	Materials Genome Initiative
<b>MIEC</b>	Mixed Ion Electron Conductor
<b>N/P ratio</b>	Negative-to-Positive-capacity ratio
<b>NCA</b>	Lithium Nickel Cobalt Aluminum Oxide
<b>NMC</b>	Lithium Nickel Manganese Cobalt Oxide
<b>OCV</b>	Open Circuit Voltage
<b>OER</b>	Oxygen Evolution Reaction
<b>ORR</b>	Oxygen Reduction Reaction

<b>PDEs</b>	Partial Differential Equations
<b>PSO</b>	Particle Swarm Optimization
<b>R&amp;D</b>	Research and Development
<b>RCD</b>	Reaction Current Density
<b>RHS</b>	Right Hand Side
<b>SBM</b>	Smoothed Boundary Method
<b>SCE</b>	Standard Calomel Electrode
<b>SEI</b>	Solid Electrolyte Interface
<b>SOFCs</b>	Solid Oxide Fuel Cells
<b>TCC</b>	Transmissive Current Collector

## ABSTRACT

Electrochemical systems are ubiquitous in our modern lives in many forms, including energy storage and conversion devices like batteries and fuel cells, which enable our modern consumer electronics and underpin our shift away from fossil fuels, and corrosion, which affects many metallic structures. However, the physical phenomena that underlie the working of such systems often involve several mechanisms spanning multiple length scales. Due to this complexity, the research and development (R&D) of electrochemical systems has been challenging. The goal of this Ph.D. dissertation is to accelerate the R&D of electrochemical systems by adopting a Materials Genome Initiative (MGI)-based approach, which integrates modern computational tools and data-driven methods with experiments. The approach is employed to achieve four goals. The first is to implement modeling and simulation techniques that incorporate the relevant physics and solve the resulting mathematical model in complex geometries. This aspect also includes a machine-learning-based automated parameterization algorithm developed to determine unknown model parameters. The second is to generate insights into the behavior of the system, especially into the characteristics like the reaction current density distribution that cannot be easily obtained via experiments. The third is to optimize the system design for superior performance by exploiting these insights. The last goal is to reduce the computational cost associated with the approach by developing analytical and semi-analytical frameworks. These goals are achieved to varying extents for Li-ion batteries, Mg alloys undergoing microgalvanic corrosion, and solid oxide fuel cells.

For Li-ion batteries, the tradeoff between the energy density and fast-charging capability in conventional electrodes is overcome by employing a novel-electrode architecture and studying

its effect on the fast-charging performance using electrode-level simulations parameterized by machine learning. The novel architecture is formed by ablating vertical channels along the thickness of the electrodes with laser, and it is referred to as the Highly Ordered Laser-Patterned Electrode architecture. Simulations and theoretical analyses resulted in scientific understanding and an approach to optimizing such an architecture. For Mg alloys, an open-source software application in PRISMS-PF has been developed to simulate the microgalvanic corrosion behavior. Using the application, the effect of the electrochemical properties and the spatial distribution of second phases on the corrosion behavior is elucidated, and design strategies are devised for the alloy microstructure to minimize the corrosion rate. Finally, for solid-oxide fuel cells, the impedance behavior of a mixed ion-electron conducting cathode with an experimentally determined microstructure is simulated, and the effect of material properties on the impedance behavior is studied. Furthermore, the Adler-Lane-Steele model, a widely used analytical model for determining the impedance response, is extended to account for the spatial variation of the vacancy-concentration amplitude due to the reaction at the pore/solid interface.

# CHAPTER 1

## Introduction and Motivation

### 1.1 Motivation

Electrochemical systems involve conversion of electrical energy into chemical energy or vice versa. They play a major role in our modern lives due to their application in critical technologies, including energy storage and conversion devices like batteries and fuel cells,<sup>1-7</sup> industrial processes like electrorefining,<sup>8</sup> electroplating,<sup>9,10</sup> and seawater desalination,<sup>11</sup> and technological devices such as sensors,<sup>12</sup> as schematically shown in Figure 1.1. In addition to these applications, the understanding of electrochemistry also enables strategies to protect against the corrosion of structural components.<sup>13</sup> The importance of electrochemical systems can also be judged based on their economic impact on the modern world. For instance, the global market sizes for rechargeable batteries and fuel cells in 2020 were around \$120 billion and \$7 billion, respectively,<sup>14,15</sup> and are expected to grow at a compound annual growth rate of  $> 5\%$ .<sup>15,16</sup> Furthermore, the annual loss due to corrosion is estimated to be about 3.4% of the global GDP, or \$ 3.5 trillion.<sup>13</sup> In addition to their economic impact, electrochemical systems have a major role to play in the adoption of renewable energy resources because they enable the generation and storage of electricity from renewable energy, thereby overcoming the intermittency issues associated with such resources.

## Applications of Electrochemistry

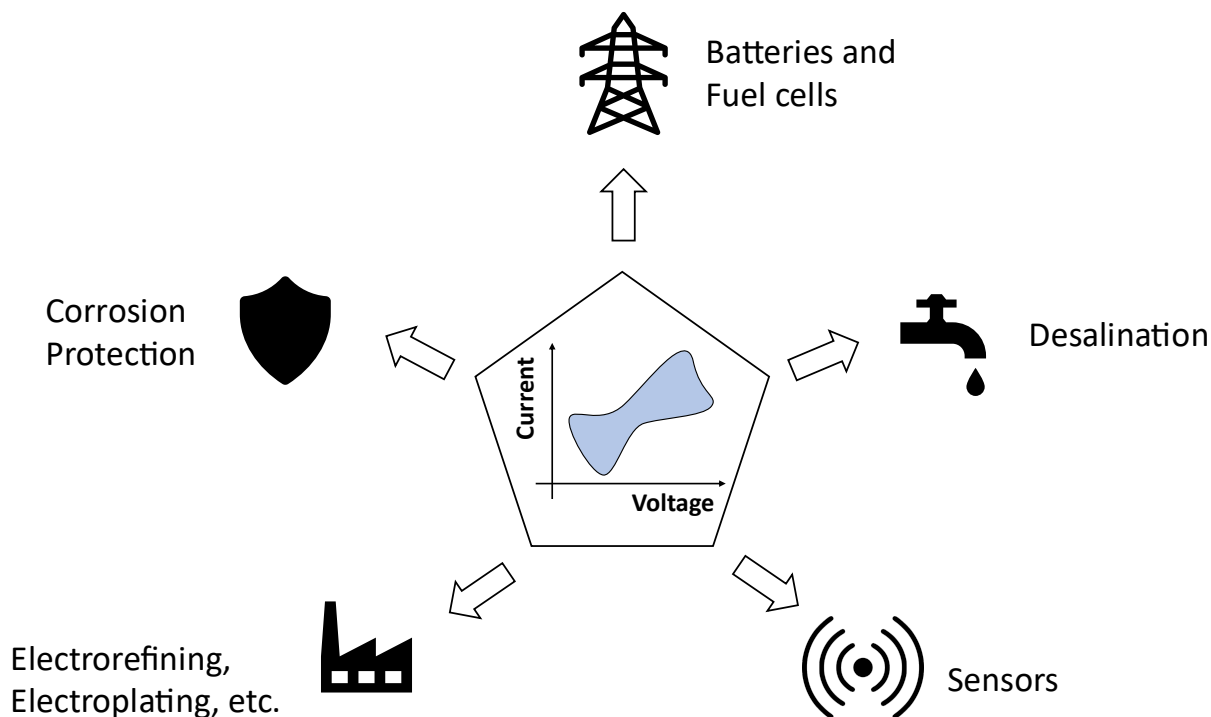


Figure 1.1. A schematic representation of various applications of electrochemistry in the modern world.

Despite the significant impact of electrochemical systems on our modern lives, their research and development have been challenging due to a complex interplay among the underlying mechanisms that span multiple length scales. For instance, in the last 3 decades, the specific energy density of Li-ion batteries (LIBs) has only increased fourfold (300 Wh/Kg vs. 75 Wh/Kg),<sup>17,18</sup> while the transistor count on central processing units increased by a factor of  $10^5$  in the same duration.<sup>19</sup> A key reason limiting the progress is the strong coupling between the three fundamental aspects, namely, thermodynamics, reaction kinetics, and transport kinetics, on the performance of the system. For instance, changing the active material in a LIB electrode alters all three aspects, which makes it challenging to predict the subsequent effect on the battery performance without

exhaustive experiments, which are both time and resource consuming. Thus, to accelerate the research and development of electrochemical systems, a Materials Genome Initiative (MGI)<sup>20</sup>-based approach is needed, which involves the integration of computational tools and data-driven methods with experiments and the open sharing of data. Figure 1.2 shows the key aspects of MGI schematically.<sup>20</sup>

Such an approach not only enables a high-throughput exploration of the vast design space, but also facilitates the determination of quantities that are difficult to measure. For instance, experimental monitoring of the evolution of the Li concentration distribution in a LIB electrode requires sophisticated measurements involving operando X-ray diffraction computed tomography.<sup>21</sup> Despite the sophistication of these measurements, the spatial and temporal resolutions are often limited, especially in 3D. On the other hand, the same information can be obtained with much higher resolution via electrode-level modeling,<sup>22-24</sup> provided that the underlying model is representative of the electrode under consideration.

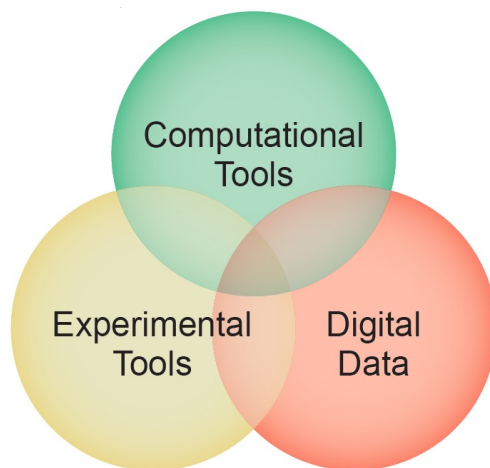


Figure 1.2. A schematic showing the overview of the Materials Genome Initiative approach, which involves the integration of experiments, computation, and data-driven methods. Reproduced with permission from Ref. 20. Public domain.



In this dissertation, an MGI-based approach is implemented for three electrochemical systems: LIBs, Mg alloys undergoing microgalvanic corrosion, and solid oxide fuel cells (SOFCs), as shown in Figure 1.3. It details the computational tools and data-driven methods employed to study these systems, along with a comprehensive discussion of the results. The data generated here is also shared publicly on Materials Commons, an online repository for collaboration and open sharing of data.<sup>25</sup> The corresponding experiments, wherever required, are carried out by our collaborators, and only their summary is provided here. For LIBs, the intrinsic tradeoff between the energy density and fast-charging capability in conventional electrodes is overcome by employing a novel electrode architecture, called Highly Ordered Laser-Patterned Electrode (HOLE),<sup>22,24</sup> formed by ablating channels into the electrode. Electrode-level simulations parameterized by machine learning are carried out to understand the effect of the HOLE architecture on the 15- and 10-minute (4C and 6C) fast-charging performance of energy-dense LIBs. Subsequently, the architecture is optimized for the best fast-charging performance, and a theoretical framework is developed to reduce the cost of associated computation.

For Mg alloys, microgalvanic corrosion (a form of localized corrosion) is studied by phase-field modeling, wherein simulations are conducted to isolate the effect of the corrosion parameters and the spatial distribution of second phases in the alloy, as well as the environment, on the microgalvanic-corrosion behavior. Based on the simulation results, strategies for corrosion mitigation are proposed. Furthermore, an open-source software application<sup>26</sup> is developed within the PRISMS-PF framework<sup>27</sup> to simulate the microgalvanic corrosion, which is shared with the materials-science community. Finally, for SOFCs, a continuum-scale model is developed to determine the effect of the material properties on the impedance behavior of mixed ion-electron conducting SOFC cathodes with an experimentally determined microstructure. In addition, the

Adler-Lane-Steele model, a widely used analytical model for determining the impedance response, is extended to account for the spatial variation of the vacancy-concentration amplitude caused by the reaction at the pore/solid interface.

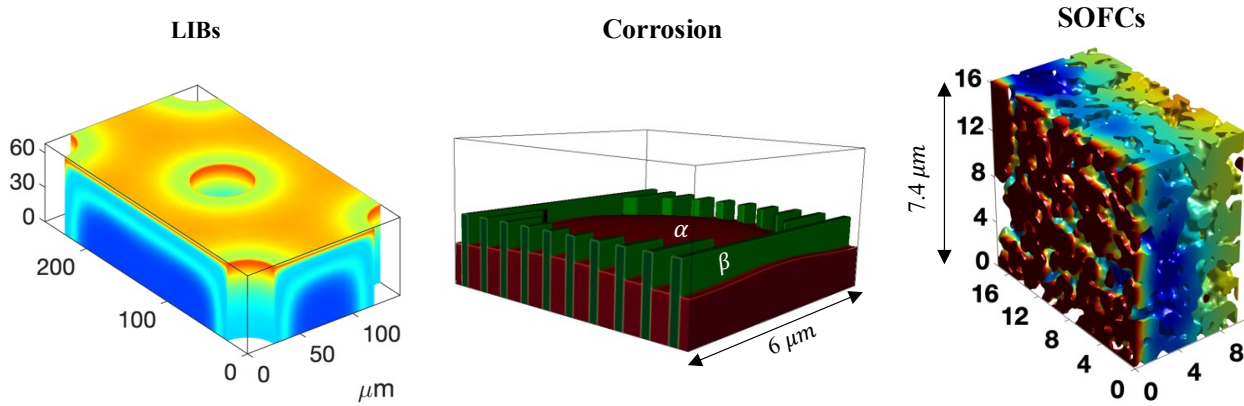


Figure 1.3. Examples of the three electrochemical systems, namely, Li-ion batteries (LIBs), Mg alloys undergoing microgalvanic corrosion, and solid oxide fuel cells (SOFCs), investigated in this dissertation.

## 1.2 Dissertation overview

This dissertation consists of eight chapters, and a brief description of each chapter is provided in the following text. In Chapter 2, we provide the background on each electrochemical system examined here and the mechanisms that underlie its operation. We also describe the mathematical equations used to model the basic physical processes, including the ionic transport in a binary electrolyte, the electrochemical reaction kinetics, and electronic transport in the electrode. Note that these equations are tailored to the physical system under consideration in the following chapters.

In Chapter 3, we describe the numerical methods used to solve the model equations, which include the finite difference method, the finite element method, and the smoothed boundary method. For each method, we provide an example to illustrate the application of the method.

In Chapter 4, we elucidate the effect of laser patterning of the graphite anode on the 4C and 6C fast-charging performance of energy-dense LIBs via electrode-level modeling. We present the model equations used to simulate the effect of the HOLE architecture formed by laser patterning and describe the parameterization process, including machine learning-based automation. Using the simulation results, we show the effect of the HOLE architecture on the electrolyte concentration and the reaction current density. In addition, we provide a summary of the corresponding experimental result to complement the discussion.

In Chapter 5, we use the parameterized model obtained in Chapter 4 to identify the optimal inter-channel spacing for the architecture at a fixed volume retention and explain its characteristics using the second Damköhler number. We also develop a semi-analytical framework to reduce the computational cost associated with identifying the optimal configuration and demonstrate its utility in determining the optimal HOLE design for 6C charging.

In Chapter 6, we investigate the microgalvanic corrosion behavior observed in Mg alloys by phase-field modeling. We provide details on the model equations and parameters and then present the results for sensitivity analyses that investigate the effect of the exchange current density and the corrosion potential of second phases on the corrosion behavior. In addition, the effect of the electrolyte conductivity is also discussed. Finally, we elucidate the influence of the spatial distribution of second phases in the microstructure on the corrosion behavior.

In Chapter 7, we study the impedance behavior of a SOFC cathode using microstructure-level modeling. Details such as governing equations, nondimensionalization, and numerical implementation are presented, along with the simulation results. The simulations elucidate the effect of the surface reaction on the spatial variation of the vacancy-concentration amplitude. Furthermore, the results elucidate the effect of the material properties and the frequency of the

applied load on the effective tortuosity of the cathode. In addition, we extend the well-known Adler-Lane-Steele (ALS) model<sup>28,29</sup> to account for the spatial variation of the concentration amplitude. Finally, in Chapter 8, we summarize the dissertation and discuss the future work that can be built upon this dissertation.

### **1.3 Author contributions**

Chapters 4 and 5 are based on three manuscripts, Chen et al. (Journal of Power Sources 471 (2020) 228475),<sup>22</sup> Goel et al. (Energy Storage Materials 57 (2023) 44),<sup>24</sup> and Goel et al. (MethodsX 8 (2021) 101425).<sup>30</sup> The experimental portion of the work presented in these manuscripts were conceived by N. P. Dasgupta and J. Sakamoto, while K. Thornton envisioned the computational studies. K.-H. Chen and M. J. Namkoong performed experiments for electrochemical characterization under the supervision of N. P. Dasgupta and J. Sakamoto. C. Yang carried out the laser ablation under the guidance of J. Mazumder. S. Kazemiabnavi and S.M. Mortuza initially implemented the modeling approach. V. Goel further developed the modeling approach by introducing the automated parameterization capability and by implementing anisotropic ionic transport in the electrolyte and then used the model to conduct simulations and analysis under the guidance of K. Thornton. All the respective authors of the manuscripts reviewed and edited them.

Chapter 6 is based on two manuscripts, Goel et al. (MRS Communications (2022) 12:1050),<sup>31</sup> and Goel et al. (submitted to Journal of Electrochemical Society, in revision).<sup>26</sup> K. Thornton and D. Montiel conceived the study presented in this chapter. V. Goel developed the open-source software application<sup>26</sup> in PRISMS-PF,<sup>27</sup> performed the simulations, and conducted the analysis under the supervision of K. Thornton. D. Montiel contributed to the development the

application through regular discussions and software troubleshooting. The development effort also involved Y. Lyu during the early stage of the project. All the respective authors of the manuscripts reviewed and edited them.

Chapter 7 is based on Goel et al. (*Frontiers in Chemistry* (2021) 9:627699).<sup>32</sup> K. Thornton and S.A. Barnett conceived the study. V. Goel performed the simulations and conducted the analysis under the supervision of K. Thornton. All the authors reviewed and edited the manuscript.

## CHAPTER 2

### Background

#### 2.1 Li-ion batteries

Li-ion batteries (LIBs) are the key rechargeable-battery technology that has ushered in the age of consumer electronics, electric vehicles (EVs), and grid-storage systems that enable the utilization of renewable energy sources like solar and wind into our energy mix.<sup>1-4</sup> LIBs enabled these technologies because of their high energy density, high voltage, low self-discharge, moderate fast-charging capabilities, and moderate cycle life.<sup>1-4</sup> Commercial LIBs are in three main form factors, namely, cylindrical, prismatic, and pouch formats, as shown in Figure 2.1,<sup>33</sup> and range from 1 Ah to 100 Ah in charge capacity. On the other hand, LIBs used in research and development are typically limited to the coin-cell (also shown in Figure 2.1) and pouch-cell formats with a charge capacity up to 1 Ah. Irrespective of the form factor of a LIB, its building block remains the same. A LIB building block typically consists of three components, namely, a cathode, an anode, and a separator,<sup>1-4</sup> as shown in Figure 2.2.<sup>34</sup> By convention, the cathode and anode in rechargeable batteries are defined as the electrodes where reduction and oxidation take place during discharging, respectively, and the same nomenclature is followed for charging.<sup>35</sup> All three components typically have porous structures in state-of-the-art LIBs.<sup>36</sup> These pores are filled with a liquid electrolyte that enables the Li-ion transport. The solid region in the electrode comprises of three constituents: an active material, which stores Li; a carbon additive, which enhances the electronic conductivity of the electrode; and a polymer binder, which binds the solid constituents together.<sup>36</sup> The binder

also ensures adhesion of the solid region to the current collector, a metallic foil that collects the current produced by electrochemical reactions.<sup>36</sup> The solid region in the separator consists of only a polymer material, which ensure electronic isolation of the two electrodes and provides the required mechanical integrity.

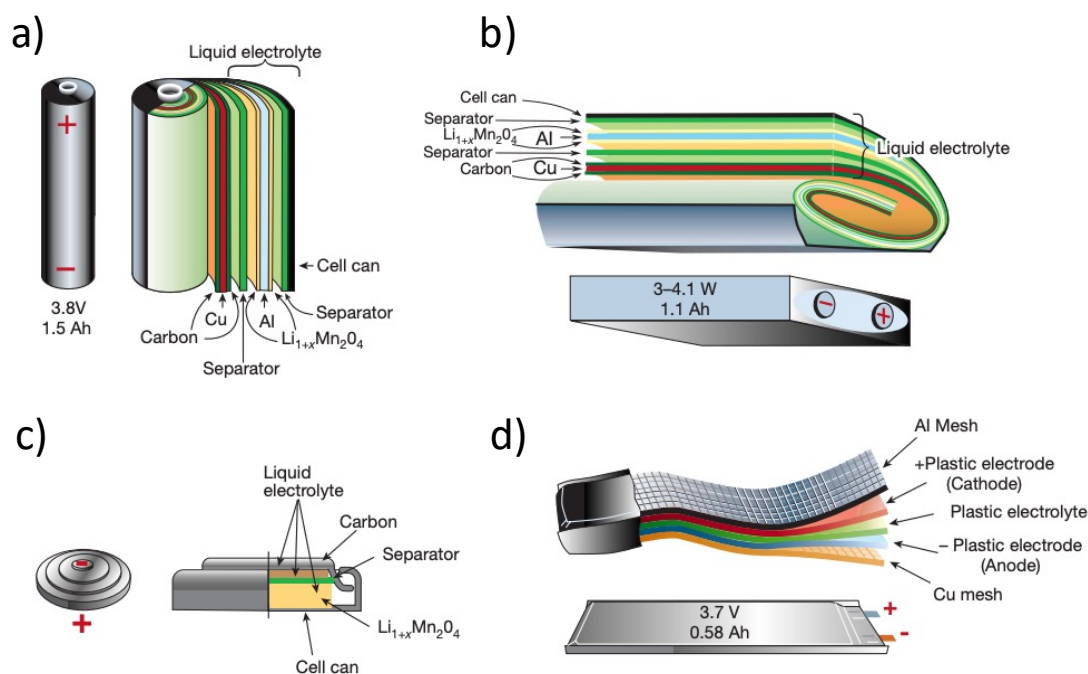


Figure 2.1. A schematic showing the following formats of Li-ion batteries: (a) cylindrical cell, (b) prismatic cell, (c) coin cell, and (d) pouch cell. Reproduced with permission from Ref. 33. Copyright 2001, Springer Nature Limited.

Figure 2.2a shows the operation of a LIB during charging. The application of an external power source to the LIB causes an electrochemical reaction at the active material/electrolyte interface in the cathode that leads to the generation of Li ions and electrons.<sup>1,4</sup> The Li ions and electrons travel inside the cell through the electrolyte and externally through the circuit, respectively, to reach the anode.<sup>1,4</sup> At the anode, another electrochemical reaction occurs at the

active material/electrolyte interface that consumes the incoming Li ions and electrons.<sup>1,4</sup> The exact opposite process takes place during discharging of a LIB,<sup>1,4</sup> as shown in Figure 2.2b.

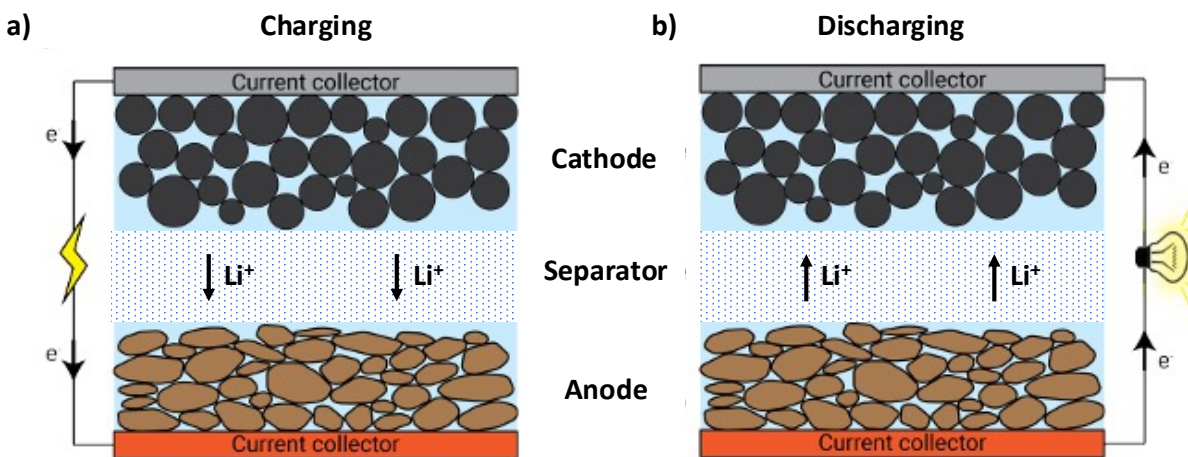
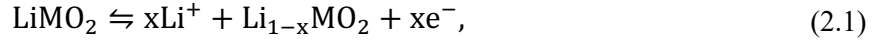


Figure 2.2. A schematic showing the basic structure of a Li-ion battery, along with the motion of Li ions and electrons during (a) charging and (b) discharging. This schematic is adapted from Chen et al.<sup>34</sup>

The active material is typically an *intercalation material* that has a relatively open lattice, in which Li ions can be reversibly inserted and removed without any significant change in the crystal structure of the material.<sup>37</sup> The insertion and extraction of Li ions into and from the host material is called lithiation and delithiation of the active material (or the electrode), respectively. The intercalation materials for the cathode typically include metal chalcogenides like  $\text{LiTiS}_2$ , transition metal oxides, like  $\text{LiCoO}_2$  and  $\text{LiNi}_{1/3}\text{Mn}_{1/3}\text{Co}_{1/3}\text{O}_2$ , and polyanion compounds like  $\text{LiFePO}_4$ .<sup>37</sup> The candidates for the anode active materials are typically carbon based like graphite and hard carbon, along with some transition metal oxides like  $\text{Li}_4\text{Ti}_5\text{O}_{12}$ .<sup>37</sup> Note that there exist other types of active materials known as the *conversion materials*, where the crystal structure changes significantly upon lithiation or delithiation.<sup>37</sup> However, the work carried out in this dissertation focuses on intercalation materials for both electrodes.



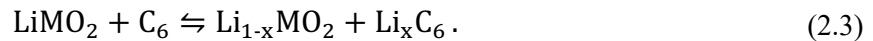
A typical reversible electrochemical reaction that takes place at the active material/electrolyte interface in the cathode is as follows:<sup>36</sup>



where M is a transition metal like Co. The reaction at the active material/electrolyte in the anode is as follows:<sup>36</sup>



Thus, the full cell reaction can be written as<sup>36</sup>



The work carried out in this dissertation focuses on the intrinsic tradeoff between the energy density and fast-charging capability of LIBs. To build compact and light batteries, i.e., batteries with high energy density, thick electrodes with low porosities are needed. Gallagher et al.<sup>38</sup> showed this effect of the cathode thickness and porosity on the volumetric energy density of a  $\text{LiNi}_{0.6}\text{Mn}_{0.2}\text{Co}_{0.2}\text{O}_2$  (NMC622)/graphite cell with a fixed anode porosity, as reproduced in Figure 2.3a.<sup>38</sup> However, designing such electrodes severely limits the charging rate, measured in terms of C-rate (a rate of  $x\text{C}$  means that the charging/discharging time is  $x^{-1}$  hrs). As shown in Figure 2.3b (from Gallagher et al.<sup>38</sup>), the C/3 discharge capacity sharply decreases when the galvanostatic charge rate is increased from C/3 to 1C for cells with the cathode loading greater than 3.3 mAh/cm<sup>2</sup>.<sup>38</sup> In these cells, the anode loading is also increased concomitantly to maintain the negative-to-positive capacity (N/P) ratio to be greater than 1, which is commonly done in commercial cells. Furthermore, on continued 1C charging, the discharge capacity of the cells continues to degrade. The same phenomenon is observed for the cell with the cathode loading of 3.3 mAh/cm<sup>2</sup> at the charge rate of 1.5C, as shown in Figure 2.3b.<sup>38</sup> Thus, not only the full design

capacity is not accessed, but the observed discharge capacity also decreases with continued cycling. The reason behind this degradation in the discharge capacity (commonly referred to as the capacity fade) is reported to be severe Li plating on the graphite electrode, as shown in Figure 2.3c,<sup>38</sup> whereby Li ions, instead of intercalating in graphite particles, deposit on the particle surface in the form of metallic Li.<sup>39</sup>

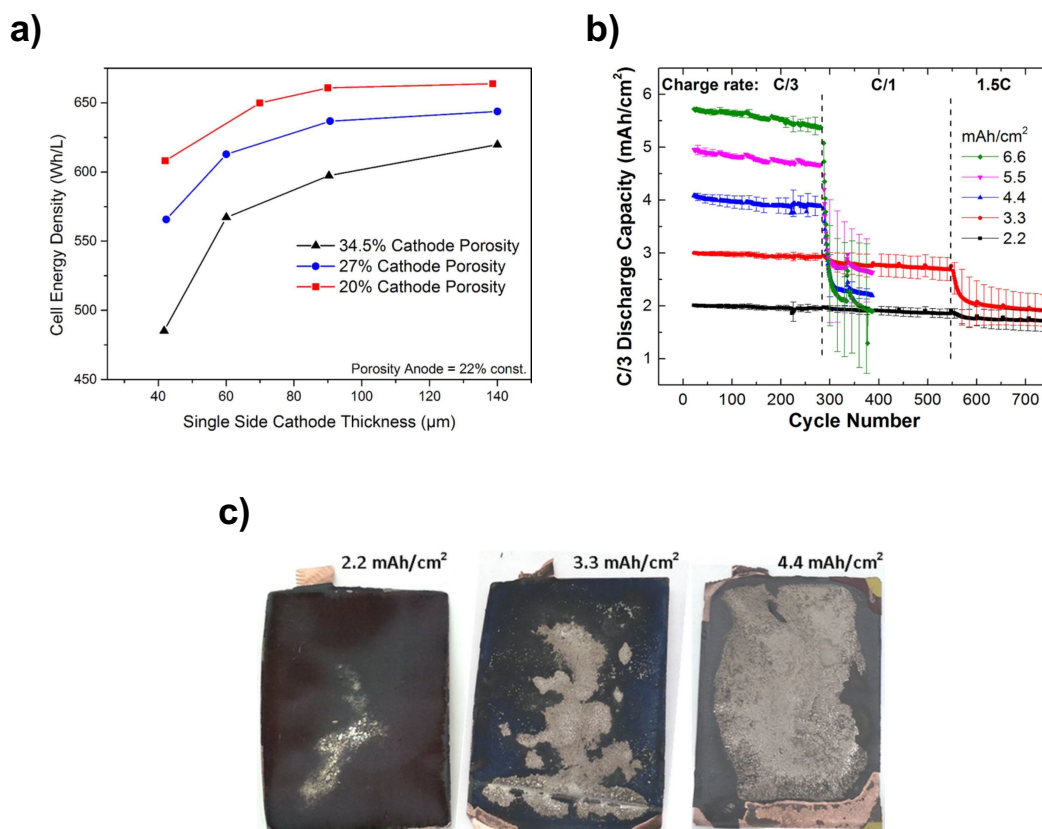


Figure 2.3. (a) Volumetric energy density of a  $\text{LiNi}_{0.6}\text{Mn}_{0.2}\text{Co}_{0.2}\text{O}_2$  (NMC622)/graphite cell calculated as a function of cathode thickness and cathode porosity. (b) C/3 Discharge capacity of cells with different cathode loadings at various charging rates. (c) Optical images of the graphite electrode extracted out of the cells with three different cathode loadings after cycling. The silver deposit on the electrodes is the plated Li. Reproduced with permission from Ref. 38. Copyright 2015, the authors. Published by ECS.

To overcome this tradeoff between the energy density and fast charging capability, we investigate the effect of employing the HOLE architecture<sup>22,24</sup> on the fast-charging performance

of the graphite anode by employing electrode-level modeling in Chapters 4 and 5. Figure 2.4 shows a schematic of the HOLE architecture.

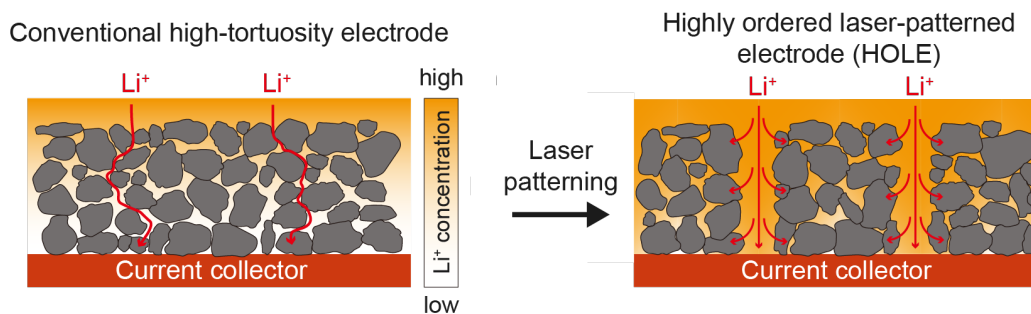


Figure 2.4. Schematic of the Highly Ordered Laser-patterned Electrode (HOLE) architecture formed by ablating vertical channels in the electrode using laser. Reproduced with permission from Ref. 22. Copyright 2020, Elsevier B.V.

## 2.2 Microgalvanic corrosion in Mg alloys

Corrosion is a natural process that converts metals and alloys into more chemically stable species. Galvanic corrosion is a special type of corrosion that occurs when metals or alloys with different electrochemical potentials are joined together and placed in contact with an electrolyte.<sup>40</sup> In such a system, a galvanic cell forms, where the metal undergoing corrosion acts as the anode due to its lower electrochemical potential, and the other metal acts as the cathode because of its higher electrochemical potential.<sup>40</sup> The contact between the two metals provides an electronic pathway, while the electrolyte provides an ionic pathway to complete the cell, as shown schematically in Figure 2.5a. Figure 2.5b shows an example of galvanic corrosion in a screw-nut pair, where the nut corrodes due to its galvanic coupling with the screw.<sup>41</sup> When this phenomenon is observed in the microstructure of an alloy due to the difference in the electrochemical potentials of constituent phases, it is called *microgalvanic corrosion*.

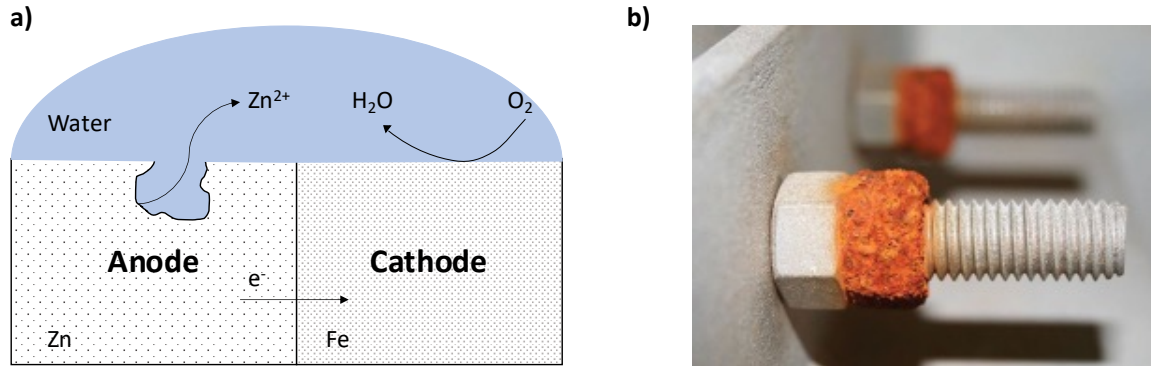


Figure 2.5. (a) A schematic representation of the galvanic corrosion of Zn due to its coupling with Fe in an aqueous environment. Zn ions dissolve from the anodic region, creating electrons that travel to the cathodic region and reduce oxygen to form water at the cathode/electrolyte interface. (b) An example of the galvanic corrosion, where the nut corrodes due to its galvanic coupling with the screw. The figure (b) is reproduced with permission from Ref. 41. Copyright 2016, National Council of Structural Engineers Associations.

Microgalvanic corrosion is observed in many alloys, including steels,<sup>42–44</sup> Al alloys,<sup>45</sup> Mg alloys,<sup>46–50</sup> high-entropy alloys.<sup>51,52</sup> It is one of the most common forms of localized corrosion in Mg alloys that severely limits their widespread adoption.<sup>46</sup> Barring poor corrosion resistance, Mg alloys are a leading candidate for the lightweighting of automobiles because they exhibit the highest strength-to-weight ratio.<sup>46</sup> Figure 2.6 shows the progression of the microgalvanic corrosion in the AZ91 alloy.<sup>53</sup> Note how the Mg-rich matrix (or the  $\alpha$  phase) undergoes corrosion, while the second phase, also called the  $\beta$  phase, remains uncorroded. Thus, the  $\alpha$  and  $\beta$  phases act as the anode and the cathode, respectively, in the microgalvanic couple that formed in the microstructure. The roles of various phases are decided by their electrochemical potentials, which, in turn, are determined by the composition and the structure of the phase. For instance, in Mg-Ca alloys, the  $\beta$  (precipitate) phase acts as the anode and the  $\alpha$  (matrix) phase acts as the cathode.<sup>49</sup>

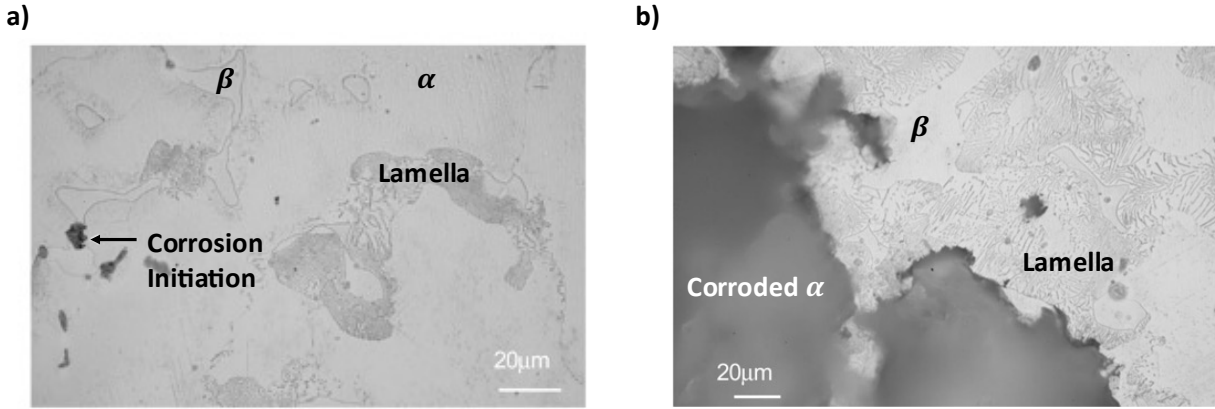


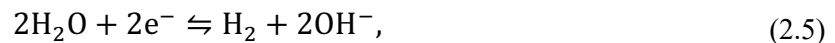
Figure 2.6. The SEM image of an AZ91 alloy sample after (a) 1 hr and (b) 18 hrs of immersion in 1N (or 1M) NaCl solution (at different locations in the same sample). Reproduced with permission from Ref. 53. Copyright 2008, WILEY-VCH Verlag GmbH & Co. KGaA, Weinheim. Distinct regions in the microstructures are noted in both (a) and (b). The location of corrosion initiation is highlighted in (a) with an arrow.

The typical anodic reaction during the microgalvanic corrosion is that of Mg oxidation.

Thus, at the  $\alpha$ /electrolyte interface, where  $\alpha$  is the anode, the following occurs.<sup>46</sup>



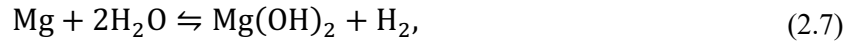
The cathodic reaction at the  $\beta$ /electrolyte interface in aqueous electrolytes can either be the hydrogen evolution reaction (HER) or the oxygen reduction reaction (ORR) depending on the pH of the electrolyte. In acidic electrolytes, the HER takes place, which can be expressed as<sup>46</sup>



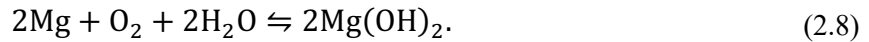
while in alkaline electrolytes, the ORR occurs<sup>46</sup>:



Consequently, the full-cell reaction in acidic electrolyte is<sup>46</sup>



while that in alkaline electrolytes is<sup>46</sup>



In the absence of any externally applied current, the net current of the microgalvanic couple is zero because the anodic and cathodic currents balance each other. Thus, the corrosion rate is determined by either of the currents. It is also common to convert current into mass loss per unit time or thickness loss per unit time for a fixed cross-sectional area.<sup>46</sup> The rate of microgalvanic corrosion (or the corrosion current) in Mg alloys is heavily dependent on the alloy microstructure, electrochemical properties of various phases in the microstructure, and the surrounding environment.<sup>27,30,31,34</sup> Due to this dependence, predicting and analyzing the corrosion behavior becomes challenging, especially with an experiments-only approach. For instance, heat treating an alloy not only alters its microstructure, but also changes the composition of the phases, which can affect their electrochemical properties. Thus, to decouple the effect of the above factors on the corrosion behavior of Mg alloys, we carry out phase-field simulations in Chapter 6. Specifically, we study the effect of the corrosion potential and the exchange current density of the  $\beta$  phase, the electrolyte conductivity, and the spatial distribution of the  $\beta$  phase in the microstructure on the corrosion dynamics.

### 2.3 Solid oxide fuel cells

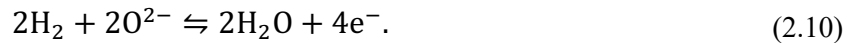
Solid oxide fuel cells (SOFCs) are electrochemical devices that convert chemical energy stored in  $\text{O}_2$  and a fuel (like  $\text{H}_2$  or  $\text{CH}_4$ ) into electrical energy with higher efficiency ( $> 55\%$ ) than

conventional heat engines (< 40%).<sup>5-7,54</sup> This mode of operation is known as the fuel cell mode. SOFCs can also be efficiently operated in the opposite direction to convert electrical energy into chemical energy, also known as the electrolysis mode.<sup>5-7</sup> Due to this reversible operation capability, SOFCs can play a major role in integrating renewable energy sources into our energy mix. For instance, they can be operated in the electrolysis mode during daytime, where the solar energy is used to produce a fuel like H<sub>2</sub>, and then in the fuel cell mode at night to generate electricity from the produced fuel.<sup>5</sup>

A SOFC consists of two porous solid electrodes (cathode and anode) placed on either sides of a solid electrolyte.<sup>5</sup> During the operation of a SOFC cell in the fuel cell mode, an oxidizing gas (e.g., oxygen) is reduced at the cathode by the electrons generated from the oxidation of fuel gas (e.g., hydrogen) at the anode and transported via an external circuit. The resultant oxygen ions then diffuse through the ion-conducting electrolyte and react with the hydrogen ions at the anode/electrolyte interface, thereby generating water and power, as shown in Figure 2.7a. At the cathode, the following reaction takes place in the fuel cell mode:<sup>6</sup>



while at the anode, fuel oxidation occurs as<sup>6</sup>



Therefore, the full cell reaction is as follows.<sup>6</sup> In addition, the electrolysis mode is shown in Figure 2.7b.



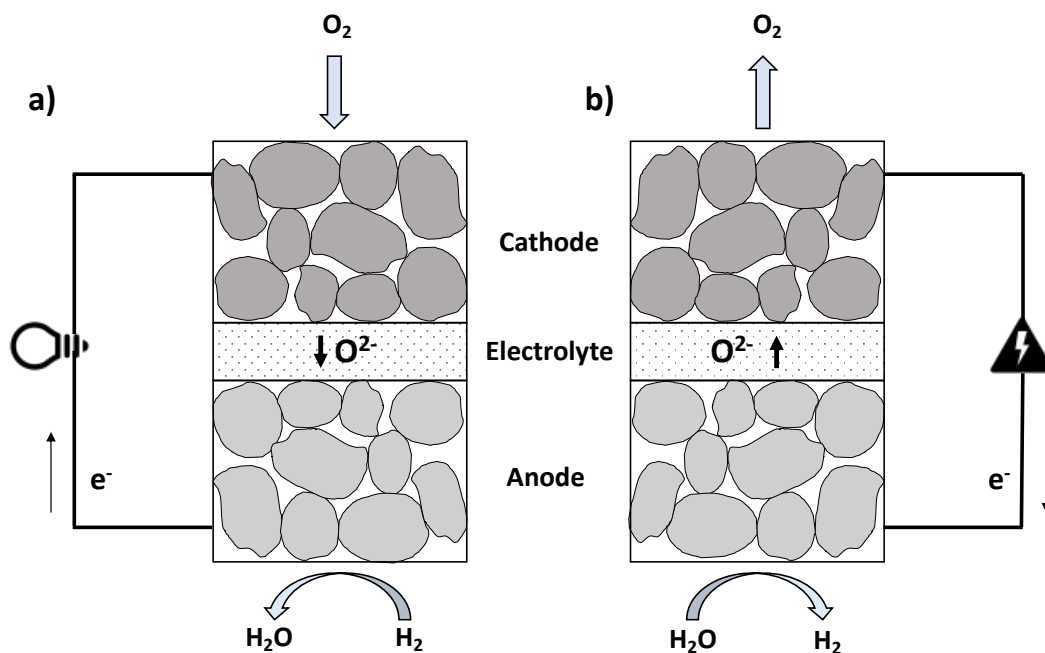


Figure 2.7. A schematic of a solid oxide fuel cell (SOFC) operating in (a) the fuel cell mode and (b) the electrolysis mode.

The conventional SOFC cathodes like  $(La,Sr)MnO_3$  (LSM) are purely electronic conductors.<sup>55</sup> Therefore, an ionically conducting material like yttria-stabilized zirconia (YSZ) is added to the cathode to facilitate ionic transport.<sup>55</sup> Thus, the oxygen reduction process is limited to the triple phase boundaries, where the three phases, namely, the gas phase, the electronically conducting phase, and the ionically conducting phase meet.<sup>55</sup> Due to this limitation, the operation of SOFCs requires temperatures between 800 and 1000°C, which delivers the required performance by increasing the reaction rate coefficient to compensate for the limited surface area. However, such high temperature requirement makes them cost-ineffective.<sup>55</sup> One way to mitigate this issue is to employ mixed ion and electron conductors (MIEC) as the cathode material. In such cathodes, the oxygen reduction reaction can take place anywhere on the cathode/gas interface, leading to faster reaction kinetics at a given temperature.<sup>55,56</sup> However, the performance of such mixed-



conducting cathodes is co-limited by the diffusion of oxygen ions in the bulk of the cathode and the rate of oxygen reduction at the cathode surface.<sup>57</sup> This co-limitation is studied here by simulating the electrochemical impedance response of an MIEC cathode with experimentally determined microstructure in response to various frequencies of the applied AC load and material properties, such as the bulk diffusivity of oxygen ions and the reaction rate constant of the reduction reaction. Subsequently, their effect on the effective tortuosity of the microstructure is also elucidated. The results are discussed in detail in Chapter 7.

## 2.4 Governing equations

In this section, mathematical equations that represent the general physical phenomena observed in electrochemical systems, such as the electronic transport in a solid, the ionic transport in a binary electrolyte, and the solid-state diffusion of neutral species are discussed. These equations are modified according to the system under consideration in the following chapters. Furthermore, the equations used to model the electrochemical impedance response of a general system are also provided.

### 2.4.1 Electronic transport

The electronic current density,  $\mathbf{i}_s$ , resulting from an electrostatic-potential gradient in the solid phase can be written as<sup>35</sup>

$$\mathbf{i}_s = -\sigma_s \nabla \Phi_s, \quad (2.12)$$

where  $\sigma_s$  and  $\Phi_s$  represent the electronic conductivity and the electrostatic potential of the solid phase, respectively. This equation is used with modifications in Chapters 4 and 5.

### 2.4.2 Ionic transport in a binary electrolyte

An electrolyte that contains only one solvent and one salt is called a binary electrolyte.<sup>35</sup> Thus, in such electrolytes, only one anionic and one cationic species are present. The motion of these ions results in ionic current in the electrolyte. There can be three driving forces for the ionic current, namely, migration, diffusion, and convection.<sup>35</sup> Migration refers to the motion of ions under the influence of an electrostatic-potential gradient. Diffusion refers to ionic transport due to the concentration gradients in the electrolyte. Convection refers to ionic motion due to the bulk movement of the electrolyte. The net current density in the electrolyte,  $\mathbf{i}_e$ , is a sum of the current densities due to these three forces, as shown in Eq. 2.13.<sup>35</sup>

$$\mathbf{i}_e = F \sum_j z_j \mathbf{N}_j^{Tot}, \quad (2.13)$$

where  $z_j$  and  $\mathbf{N}_j^{Tot}$  are the charge number and the total flux of the  $j^{th}$  species, and  $F$  represents the Faraday's constant. Since there are only two ionic species in the binary electrolytes, the subscript  $j$  has two values;  $j = +$  and  $-$  represent the cation and the anion, respectively. As stated above, the total flux for each ionic species is a sum of the migration ( $\mathbf{N}_j^{Mig}$ ), diffusive ( $\mathbf{N}_j^{Diff}$ ), and convective fluxes ( $\mathbf{N}_j^{Conv}$ ). Thus,<sup>35</sup>

$$\mathbf{N}_j^{Tot} = \mathbf{N}_j^{Mig} + \mathbf{N}_j^{Diff} + \mathbf{N}_j^{Conv}. \quad (2.14)$$

The three types of fluxes can be written as<sup>35</sup>

$$\mathbf{N}_j^{Mig} = -z_j u_j c_j F \nabla \Phi_e, \quad (2.15)$$

$$\mathbf{N}_j^{Diff} = -D_j \nabla c_j, \text{ and} \quad (2.16)$$

$$\mathbf{N}_j^{Conv} = c_j \mathbf{v}_e, \quad (2.17)$$

where  $u_j$ ,  $c_j$ , and  $D_j$  represent the mobility, concentration, and diffusivity of the  $j^{\text{th}}$  species, respectively. Furthermore,  $\Phi_e$  and  $\mathbf{v}_e$  represent the electrostatic potential and the bulk velocity of the electrolyte. Substituting Eqs. 2.14 to 2.17 into Eq. 2.13 results in the following expression for  $\mathbf{i}_e$ .<sup>35</sup>

$$\mathbf{i}_e = F \sum_j (-z_j^2 u_j c_j F \nabla \Phi_e - z_j D_j \nabla c_j + z_j c_j \mathbf{v}_e). \quad (2.18)$$

It should be noted that the condition of electroneutrality can be applied to such electrolytes, which necessitates that<sup>35</sup>

$$\sum_j z_j c_j = 0. \quad (2.19)$$

Thus, by the virtue of electroneutrality, the last term of Eq. 2.18 becomes zero. Therefore, in an electrically neutral electrolyte, the bulk motion does not cause a net current. Thus, Eq. 2.18 becomes<sup>35</sup>

$$\mathbf{i}_e = -\sum_j z_j^2 F^2 u_j c_j \nabla \Phi_e - \sum_j z_j F D_j \nabla c_j. \quad (2.20)$$

The coefficient of the first term on the right hand side (RHS) of Eq. 2.20 is defined as the electrolyte conductivity, as<sup>35</sup>

$$\kappa_e = \sum_j z_j^2 F^2 u_j c_j. \quad (2.21)$$

Next, we consider the mass transport of ions in the electrolyte. The condition of mass conservation for each ion necessitates that<sup>35</sup>

$$\frac{\partial c_j}{\partial t} = -\nabla \cdot \mathbf{N}_j^{\text{Tot}}, \quad (2.22)$$

in the absence of any source or sink of ions in the electrolyte, such as a reaction. Substituting the expression for  $\mathbf{N}_j^{\text{Tot}}$  into Eq. 2.22 gives<sup>35</sup>

$$\frac{\partial c_j}{\partial t} = -\nabla \cdot (-z_j u_j c_j F \nabla \Phi_e - D_j \nabla c_j + c_j \mathbf{v}_e). \quad (2.23)$$

It is common in text books to write the mass conservation equation in terms of  $i_e$ ,<sup>35</sup> which requires a relationship between  $\nabla\Phi_e$  and  $\nabla c_j$ . Such a relationship can be obtained by defining the electrolyte concentration,  $c_e$ , as<sup>35</sup>

$$c_e \equiv \frac{c_j}{\mu_j}, \quad (2.24)$$

where  $\mu_j$  is the total number of ions of the  $j^{\text{th}}$  species formed by the dissociation of 1 molecule of the salt. Substituting Eq. 2.24 into Eq. 2.23 and cancelling  $\mu_j$  on both sides give<sup>35</sup>

$$\frac{\partial c_e}{\partial t} = \nabla \cdot (z_j u_j c_e F \nabla \Phi_e + D_j \nabla c_e - c_e \mathbf{v}_e). \quad (2.25)$$

Now, Eq. 2.25 can be written entirely in terms of  $c_e$  and  $\mathbf{i}_e$ , i.e., without  $\Phi_e$ . However, we first need to modify Eq. 2.20 by substituting Eq. 2.24 into it<sup>35</sup>

$$\mathbf{i}_e = (-\sum_j z_j^2 u_j \mu_j) F^2 c_e \nabla \Phi_e - (\sum_j z_j D_j \mu_j) F \nabla c_e. \quad (2.26)$$

By dividing both sides of Eq. 2.26 by  $z_+ \mu_+ F$ , the following relation can be obtained

$$\begin{aligned} \frac{\mathbf{i}_e}{z_+ \mu_+ F} &= \frac{-\sum_j z_j^2 u_j \mu_j}{z_+ \mu_+} F c_e \nabla \Phi_e - \frac{\sum_j z_j D_j \mu_j}{z_+ \mu_+} \nabla c_e \\ &= -\frac{z_+^2 u_+ \mu_+ + z_-^2 u_- \mu_-}{z_+ \mu_+} F c_e \nabla \Phi_e - \frac{z_+ D_+ \mu_+ + z_- D_- \mu_-}{z_+ \mu_+} \nabla c_e \end{aligned} \quad (2.27)$$

Furthermore, due to the condition of electroneutrality, there exists a relation between  $z_j$  and  $\mu_j$  as follows

$$\sum_j z_j \mu_j = 0. \quad (2.28)$$

Using Eq. 2.28 to substitute  $z_- \mu_-$  into Eq. 2.27 and performing algebraic manipulations give

$$\frac{\mathbf{i}_e}{z_+ \mu_+ F} = (z_- u_- - z_+ u_+) F c_e \nabla \Phi_e + (D_- - D_+) \nabla c_e. \quad (2.29)$$

Moreover,  $u_j$  and  $D_j$  are related via the Einstein's relation,<sup>35</sup>

$$u_j = \frac{D_j}{k_B T}, \quad (2.30)$$

where  $k_B$  is the Boltzmann constant and  $T$  is the electrolyte temperature. Substituting Eq. 2.30 into Eq. 2.29 gives<sup>35</sup>

$$\frac{\mathbf{i}_e}{z_+ \mu_+ F} = \left( \frac{z_- D_- - z_+ D_+}{k_B T} \right) F c_e \nabla \Phi_e + (D_- - D_+) \nabla c_e. \quad (2.31)$$

Thus,  $F c_e \nabla \Phi_e$  can be written as<sup>35</sup>

$$F c_e \nabla \Phi_e = \frac{k_B T}{z_+ D_+ - z_- D_-} \left( (D_- - D_+) \nabla c_e - \frac{\mathbf{i}_e}{z_+ \mu_+ F} \right). \quad (2.32)$$

Substituting Eq. 2.32 and the Einstein's relation (Eq. 2.30) into the mass conservation equation (Eq. 2.25) with  $j = +$  and performing algebraic manipulations result in<sup>35</sup>

$$\frac{\partial c_e}{\partial t} = \nabla \cdot \left( \left( \frac{D_+ D_- (z_+ - z_-)}{z_+ D_+ - z_- D_-} \right) \nabla c_e - \left( \frac{z_+ D_+}{(z_+ D_+ - z_- D_-)} \right) \frac{\mathbf{i}_e}{z_+ \mu_+ F} - c_e \mathbf{v}_e \right). \quad (2.33)$$

The coefficients of the first and second terms inside the divergence on the RHS of Eq. 2.33 (the quantities in parentheses) are known as the *ambipolar diffusivity* (denoted by  $D_e$ ) and the *transference number* for the cationic species (denoted by  $t_+$ ), respectively.<sup>35</sup> Thus, Eq. 2.33 can be written more concisely as<sup>35</sup>

$$\begin{aligned} \frac{\partial c_e}{\partial t} &= \nabla \cdot \left( D_e \nabla c_e - \frac{t_+ \mathbf{i}_e}{z_+ \mu_+ F} - c_e \mathbf{v}_e \right) \\ &= \nabla \cdot (D_e \nabla c_e) - \frac{t_+ \nabla \cdot \mathbf{i}_e}{z_+ \mu_+ F} - \frac{\mathbf{i}_e \cdot \nabla t_+}{z_+ \mu_+ F} - c_e \nabla \cdot \mathbf{v}_e - \mathbf{v}_e \cdot \nabla c_e. \end{aligned} \quad (2.34)$$

Further simplifications can be made to Eq. 2.34 based on physical constraints and assumptions. The condition for charge conservation requires that<sup>35</sup>

$$\nabla \cdot \mathbf{i}_e = 0. \quad (2.35)$$

Furthermore, if the electrolyte is assumed to be incompressible, then<sup>35</sup>

$$\nabla \cdot \mathbf{v}_e = 0. \quad (2.36)$$

Thus, under the constraint of charge conservation and the assumption of incompressibility, the mass conservation equation (Eq. 2.34) for the electrolyte can be written as<sup>35</sup>

$$\frac{\partial c_e}{\partial t} = \nabla \cdot (D_e \nabla c_e) - \frac{\mathbf{i}_e \cdot \nabla t_+}{z_+ \mu_+ F} - \mathbf{v}_e \cdot \nabla c_e. \quad (2.37)$$

Moreover, if  $D_e$  and  $t_+$  are assumed to be constant, which is true for dilute electrolytes, then the mass conservation equation becomes<sup>35</sup>

$$\frac{\partial c_e}{\partial t} = D_e \nabla^2 c_e - \mathbf{v}_e \cdot \nabla c_e. \quad (2.38)$$

Therefore, for a binary electrolyte with the constant electrolyte properties ( $D_e$  and  $t_+$ ), the mass conservation equation can be expressed entirely in terms of the electrolyte concentration and velocity, even in the presence of an electric field. Finally, if  $\mathbf{v}_e = 0$ , which is often observed in the electrochemical systems investigated in this dissertation, the mass conservation equation reduces to a simple diffusion equation with constant diffusivity, i.e.,<sup>35</sup>

$$\frac{\partial c_e}{\partial t} = D_e \nabla^2 c_e. \quad (2.39)$$

Note that the current density equation (Eq. 2.20) is used with modifications in Chapters 4, 5 and 6, while modified forms of the mass conservation equation (Eq. 2.37) are used in Chapters 4, 5 and 7.

### 2.4.3 Solid-state transport of neutral species

The transport of neutral species inside a solid domain is governed by diffusion. Thus, the mass conservation equation can be written as<sup>35</sup>

$$\frac{\partial c_s}{\partial t} = \nabla \cdot (D_s \nabla c_s), \quad (2.40)$$

where  $c_s$  and  $D_s$  represent the concentration and diffusivity of the diffusing species in the solid phase. This equation is used in Chapters 4 and 5.

### 2.4.4 Electrochemical reaction

An electrochemical reaction involves a redox pair, where a species undergoes oxidation (loss of electron), and another species undergoes reduction (gain of electron). Equation 2.41 provides an example of such a reaction, where  $S_O$  and  $S_R$  represent the species undergoing oxidation and reduction, respectively.<sup>35</sup>



The forward reaction, i.e., the reduction reaction is called the cathodic reaction, while the backward reaction, i.e., the oxidation reaction is called the anodic reaction. At equilibrium, the rates of forward and backward reactions are the same. However, if such a system is perturbed by the application of an external potential or current, the reaction in one direction is favored.

The rate of an electrochemical reaction at an electrode/electrolyte interface is characterized by the current density,  $i_{rxn}$ , at the interface. The current density is typically calculated using the Butler-Volmer equation that relates  $i_{rxn}$  to the concentrations and electrostatic potentials of the species participating in the electrochemical reaction. A general form of the Butler-Volmer equation can be written as<sup>35</sup>

$$i_{rxn} = i_0 \left( \exp\left(\frac{\alpha_a n F}{RT} \eta\right) - \exp\left(-\frac{\alpha_c n F}{RT} \eta\right) \right), \quad (2.42)$$

where  $i_0$  is the exchange current density,  $n$  is the number of electrons involved in the reaction,  $\eta$  is the reaction overpotential, and  $\alpha_a$  and  $\alpha_c$  are the charge transfer coefficients for the reactions in the anodic and cathodic directions, respectively. Note that both  $\alpha_a$  and  $\alpha_c$  can only have values between 0 and 1 in this formulation. Furthermore, in general,  $i_0$  is dependent on the concentrations of both  $S_0$  and  $S_R$ .

The overpotential,  $\eta$ , is a difference between the electrode potential,  $\Phi$ , and the equilibrium potential of the electrode,  $\Phi_{Eq}$ , as shown below.<sup>35</sup>

$$\eta = \Phi - \Phi_{Eq}. \quad (2.43)$$

The electrode potential is defined as the difference between the electrostatic potentials of the solid ( $\Phi_s$ ) and the electrolyte ( $\Phi_e$ ), i.e.,  $\Phi = \Phi_s - \Phi_e$ . A large  $\eta$  for a given value of  $i_{rxn}$  implies that more energy is required to drive the reaction (if nonspontaneous) or less energy can be extracted from the reaction (if spontaneous) than the theoretical maximum based on the thermodynamics.<sup>35</sup> Based on the magnitude of  $\eta$ , the Butler-Volmer equation (Eq. 2.42) can be further simplified.<sup>35</sup>

Namely, if

$$\eta \gg \left(\frac{\alpha_a n F}{RT}\right)^{-1}, \quad (2.44)$$

then

$$i_{rxn} \approx i_0 \exp\left(\frac{\alpha_a n F}{RT} \eta\right), \quad (2.45)$$

and if

$$\eta \ll -\left(\frac{\alpha_c n F}{RT}\right)^{-1}, \quad (2.46)$$

then



$$i_{rxn} \approx i_0 \exp\left(-\frac{\alpha_c n F}{RT} \eta\right). \quad (2.47)$$

The relations provided in Eqs. 2.44 and 2.47 are known as the anodic and cathodic Tafel equations, respectively.<sup>35</sup> The Butler-Volmer equation and the Tafel equations are used with modifications in Chapters 4 and 5 and Chapter 6, respectively.

### 2.4.5 Electrochemical impedance spectroscopy (EIS)

The impedance,  $Z$ , of any electrochemical system is obtained by applying an AC voltage with a small amplitude,  $\Delta V$ , across the system, measuring the amplitude of the resultant current,  $\Delta I$ , and then dividing the two quantities as

$$Z = \frac{\Delta V}{\Delta I}. \quad (2.48)$$

Note that both  $\Delta V$  and  $\Delta I$  are functions of position within the system, and  $\Delta I$  also depends on the phase difference between the applied AC voltage and the resulting current. Furthermore,  $Z$  depends on the frequency of the AC voltage,  $\omega$ . The applied voltage causes a perturbation in the concentration of the electrochemically active species in the electrochemical system. Using Nernst's equation,<sup>58</sup>  $\Delta V$  can be related to the amplitude of the perturbation in the concentration,  $\Delta C$ , as

$$\Delta V = \frac{RT}{nF} \ln\left(\frac{\Delta C}{C_0}\right), \quad (2.49)$$

where  $R$  is the universal gas constant,  $T$  is the temperature,  $n$  is the number of electrons transferred in the electrochemical reaction,  $F$  is Faraday's constant, and  $C_0$  is the equilibrium concentration of the electrochemically active species.

Since  $\Delta V$  is small, it is reasonable to assume that  $\Delta C \ll C_0$ . Thus, Eq. 2.49 can be approximated as

$$\Delta V \approx \frac{RT}{nF} \frac{\Delta C}{C_0}. \quad (2.50)$$

The current amplitude is related to the flux of the electrochemically active species across the loading boundary, as described below:

$$\Delta I = nFA\langle J \rangle, \quad (2.51)$$

where  $\langle J \rangle$  is the area-averaged flux normal to the loading boundary and  $A$  is the cross-sectional area of the loading boundary. Therefore, using Eq. 2.48, the impedance of the system can be calculated as:

$$Z = \frac{RT\Delta C}{n^2F^2AC_0} \frac{1}{\langle J \rangle}. \quad (2.52)$$

Furthermore, the DC impedance for the system is defined as  $Z_0 = RTL/(n^2F^2ADC_0)$ ,<sup>59</sup> where  $L$  and  $D$  are the thickness of the system and the diffusivity of the electrochemically active species, respectively. Thus, the expression for the AC impedance can be simplified as:

$$\frac{Z}{Z_0} = \frac{D\Delta C/L}{\langle J \rangle}. \quad (2.53)$$

This equation is used to calculate the impedance response of the MIEC cathodes considered in Chapter 7.

## **CHAPTER 3**

### **Methods**

In this chapter, the methods used for solving the model equations considered in this dissertation are detailed. Three methods are discussed: the finite difference method (FDM), the finite element method (FEM), and the smoothed boundary method (SBM). The first two methods are numerical techniques for solving differential equations that approximate a continuous field problem with infinite degrees of freedom (DOF) by a discretized field with finite DOF and subsequently obtain the solutions by solving the resulting linear system. However, they differ in how discretization is achieved. The SBM, on the other hand, is a mathematical approach that uses a smoothed boundary instead of a sharp boundary where the boundary conditions are defined. It enables solutions to differential equations in complex geometries without the need to generate a conformal mesh. The SBM form of differential equations can be solved by a variety of numerical methods, including FDM and FEM.

### **3.1 Finite difference method**

#### ***3.1.1 Introduction***

The FDM is a numerical technique to solve differential equations. It converts the differential equations into a set of difference equations and solving the resulting linear system. It approximates derivatives of a function at discrete points, using the values of the function at

neighboring points. Its implementation is much simpler and more straightforward than other methods like the FEM, and thus, it is widely used in scientific computing. Although the origins of the FDM can be traced back to the works of Euler and Lagrange, the seminal paper by Courant, Friedrichs, and Lewy (CFL)<sup>60</sup> is often cited as the formal beginning.<sup>61</sup> In the paper,<sup>60</sup> the authors derived a five-point approximation of Laplace's equation and established the convergence of the FDM solution when a sufficiently small step size is used. They also formalized the FDM for the wave equation and discovered the CFL condition, which must be met to ensure the numerical stability of the approximated solution for the wave equation.<sup>60</sup> However, their work focused on proving the numerical solution's existence, and thus no error estimates were provided. Following Thomee,<sup>61</sup> the error bounds for the FDM were first provided by Gerschgorin<sup>62</sup> in the context of elliptic differential equations. Subsequently, Von Neumann,<sup>63</sup> Fritz John,<sup>64</sup> Crank and Nicolson,<sup>65</sup> Lax,<sup>66,67</sup> and Wendroff<sup>67</sup> further developed for the parabolic and hyperbolic partial differential equations.

### ***3.1.2 Discretization methods and associated error***

In the FDM, a first-order derivative can be discretized in multiple ways. Three common methods are discussed in the following text. Consider a 1D domain ranging from 0 to  $L$  along the  $x$ -axis and  $f(x)$  to be the function of interest. To numerically approximate  $\frac{df}{dx}$ , we first need to discretize the domain with a finite number of equally spaced points, as shown in Figure 3.1. The derivative at any point  $x_i$  within the domain (not the boundaries) can be evaluated by using any of the following schemes:<sup>68</sup>

Forward difference  $\frac{df}{dx}\Big|_i \approx \frac{f(x_i + h) - f(x_i)}{h},$  (3.1)

Backward difference  $\frac{df}{dx}\Big|_i \approx \frac{f(x_i) - f(x_i - h)}{h},$  (3.2)

Center difference  $\frac{df}{dx}\Big|_i \approx \frac{f(x_i + h) - f(x_i - h)}{2h}.$  (3.3)

Here,  $x_i$  is the position of the  $i^{th}$  point and  $h$  is the distance between two adjacent points. Note that  $\approx$  is used instead of  $=$  to highlight that the RHS approximates the derivative. Furthermore, note that the forward and backward schemes are also called the forward Euler method and the backward Euler method, respectively.<sup>68</sup>

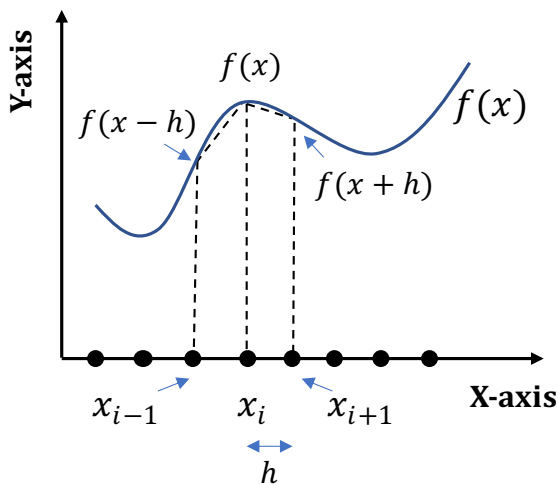


Figure 3.1. A schematic showing the finite-difference discretization of a function  $f(x)$ . The black dots on the x-axis represent the finite number of points used to discretize the domain.

The choice of the scheme determines the accuracy of the numerical approximation. For instance, both the forward-difference and backward-difference schemes exhibit first-order accuracy, i.e., the error due to the approximation of the derivative with the finite difference, also

called the *truncation error*, scales linearly with  $h$ .<sup>68</sup> On the other hand, the center-difference scheme exhibits second-order accuracy, i.e., the error scales linearly with  $h^2$ .<sup>68</sup> Therefore, for a given value of  $h$ , the center-difference scheme is more accurate than the other two schemes, as it exhibits a higher order of accuracy.<sup>68</sup> However, the center-difference scheme can lead to numerical instabilities for certain differential equations.<sup>68</sup> Thus, the choice of scheme is also dependent on the problem under consideration. Furthermore, the dependence of the error on the step size,  $h$ , suggests minimizing it, but doing so increases the computational cost. Furthermore, making the ratio between  $h$  and  $L$  smaller than the machine precision leads to a significant *round-off error*.<sup>68</sup> Thus, careful selection of  $h$  is needed to achieve sufficient accuracy at acceptable computational cost.

To obtain higher-order derivatives, the schemes listed above can be either used individually (in a recursive manner) or as a combination. For instance, it is common to approximate the second-order derivative,  $\frac{d^2f}{dx^2}$ , by first using the backward-difference scheme, followed by the forward-difference scheme, as shown below. This approximation exhibits second-order accuracy.<sup>68</sup>

$$\begin{aligned} \frac{d^2f}{dx^2}\Big|_i &\approx \frac{\frac{df}{dx}\Big|_i - \frac{df}{dx}\Big|_{i-1}}{h} = \frac{\frac{f(x_i+h) - f(x_i)}{h} - \frac{f(x_i) - f(x_i-h)}{h}}{h} \\ &= \frac{f(x_i+h) - 2f(x_i) + f(x_i-h)}{h^2}. \end{aligned} \tag{3.4}$$

The time derivatives can also be discretized using FDM in a similar manner as above. Since only the first-order time derivatives are encountered in this work, we discuss their discretization below. Consider the following ordinary differential equation (ODE)

$$\frac{dg(t)}{dt} = p(t), \quad (3.5)$$

where  $g(t)$  and  $p(t)$  are function of time,  $t$ . Let the time be distributed in equal parts of duration,  $\Delta t$ , and the superscript  $j$  represent the time index such that  $t^{j+1} = t^j + \Delta t$ . Then the ODE can be discretized using following schemes:

Forward Euler 
$$\frac{g(t^{j+1}) - g(t^j)}{\Delta t} \approx p(t^j), \quad (3.6)$$

Backward Euler 
$$\frac{g(t^{j+1}) - g(t^j)}{\Delta t} \approx p(t^{j+1}), \quad (3.7)$$

Mid-point or Crank

Nicolson (in the case 
$$\frac{g(t^{j+1}) - g(t^j)}{\Delta t} \approx \frac{1}{2} (p(t^{j+1}) + p(t^j)). \quad (3.8)$$

of parabolic PDEs)

The discussion on the accuracy of these schemes is carried out in the next section (Section 3.1.3)

### **3.1.3 FDM solution to 1D diffusion equation**

In this section, the process of solving partial differential equations (PDEs) using the FDM is demonstrated by considering the 1D diffusion equation as an example. The 1D diffusion equation can be written as

$$\frac{\partial C}{\partial t} = \frac{\partial}{\partial x} \left( D \frac{\partial C}{\partial x} \right), \quad (3.9)$$

where  $C$  and  $D$  are the concentration and diffusivity of the diffusing species, respectively. The domain has a length of  $L$  along the  $x$ -axis. The concentration at  $t = 0$  is uniform throughout the

domain and has a value of  $C_0$ . At  $x = 0$  boundary, we assume the Dirichlet boundary condition (BC) as follows:

$$C(x = 0) = C_*, \quad (3.10)$$

where  $C_*$  is the concentration value at  $x = 0$ . At  $x = L$  boundary, we assume the Neumann BC:

$$-\left(D \frac{\partial C}{\partial x}\right)\Big|_{x=L} = J, \quad (3.11)$$

where  $J$  is the flux at  $x = L$ .

Now, we consider the discretization of the spatial derivatives first. Let the 1D domain be discretized using  $N + 1$  equally spaced points. Thus, the grid resolution,  $h = L/N$ . Subsequently, the RHS of Eq. 3.9 at any position  $x_i$  in the domain, where  $i$  is the spatial discretization index, can be approximated as the following.

$$\begin{aligned} & \frac{\left(D \frac{\partial C}{\partial x}\right)\Big|_{i+\frac{1}{2}} - \left(D \frac{\partial C}{\partial x}\right)\Big|_{i-\frac{1}{2}}}{h} \\ &= \frac{\frac{(D_{i+1} + D_i)(\tilde{C}_{i+1} - \tilde{C}_i)}{2} - \frac{(D_i + D_{i-1})(\tilde{C}_i - \tilde{C}_{i-1})}{2}}{h} \\ &= \frac{(D_{i+1} + D_i)(\tilde{C}_{i+1} - \tilde{C}_i) - (D_i + D_{i-1})(\tilde{C}_i - \tilde{C}_{i-1})}{2h^2}, \end{aligned} \quad (3.12)$$

where  $\tilde{C}$  represents the numerical approximation of  $C$ . Note that if the diffusivity is constant, which is assumed from hereon for this section, the RHS becomes

$$D \frac{\tilde{C}_{i+1} - 2\tilde{C}_i + \tilde{C}_{i-1}}{h^2}, \quad (3.13)$$



which is equivalent to the form provided in Eq. 3.4 except for the presence of  $D$ . Equation 3.13 provides a pointwise expression for the RHS of Eq. 3.9. It can also be written in a matrix-vector form for the entire domain (except the boundaries) as<sup>68</sup>

$$\frac{D}{h^2} \begin{bmatrix} -2 & 1 & 0 & \cdots & 0 \\ 1 & -2 & 1 & 0 & \vdots \\ 0 & \ddots & \ddots & \ddots & \vdots \\ \vdots & \ddots & 1 & -2 & 1 \\ 0 & \cdots & 0 & 1 & -2 \end{bmatrix}_{(N-1) \times (N-1)} [\tilde{C}_2 \ \tilde{C}_3 \ \cdots \ \tilde{C}_{N-1} \ \tilde{C}_N]^T. \quad (3.14)$$

Equation 3.14 can be written more succinctly by defining the global matrix and the vector on its RHS as  $\vec{G}$  and  $\vec{C}$ , respectively. Then, the RHS becomes<sup>68</sup>

$$\frac{D}{h^2} \vec{G} \vec{C}. \quad (3.15)$$

The concentration value at the boundaries,  $\tilde{C}_1$  and  $\tilde{C}_{N+1}$  are known from the boundary conditions; specifically, according to Eqs. 3.10 and 3.11, we have  $\tilde{C}_1 = C_*$ , and  $\tilde{C}_{N+1} = -\frac{Jh}{D} + \tilde{C}_N$ .<sup>68</sup>

Next, the time derivative is discretized. Since different time-stepping schemes can be selected, a parameterized form is used to express them generally. Combining the discretized form of the right-hand side of the PDE above with this parameterized form of the time derivative, we obtain

$$\frac{\tilde{C}^{j+1} - \tilde{C}^j}{\Delta t} = \frac{D}{h^2} \vec{G} (\Theta \tilde{C}^j + (1 - \Theta) \tilde{C}^{j+1}), \quad (3.16)$$

where the superscript  $j$  represents the time index and  $\Delta t$  is the time-step size. The parameter  $\Theta$  is used to compactly express the time-stepping schemes corresponding to Eqs. 3.6 to 3.8.<sup>68</sup> Table 3.1 lists the  $\Theta$  values of  $\Theta$  that correspond to common schemes.

Table 3.1. A list of the value of  $\Theta$  for common time-stepping schemes, along with their accuracy and stability.<sup>68</sup>

$\Theta$	Scheme name	Accuracy of scheme	Stability
1	Forward Euler	First order	Conditionally stable
1/2	Crank-Nicolson	Second order	Unconditionally stable
0	Backward Euler	First order	Unconditionally stable

Collecting terms corresponding to the same time index on each side in Eq. 3.16 gives<sup>68</sup>

$$\tilde{\mathbf{C}}^{j+1} - (1 - \Theta) \frac{D\Delta t}{h^2} \vec{G} \tilde{\mathbf{C}}^{j+1} = \tilde{\mathbf{C}}^j + \Theta \frac{D\Delta t}{h^2} \vec{G} \tilde{\mathbf{C}}^j. \quad (3.17)$$

As listed in Table 3.1,  $\Theta = 1$  represents the forward Euler time-stepping scheme, where the concentration at time index  $j + 1$  is known explicitly in terms of that at the time index  $j$ . Thus, there is no need to solve a linear system at every time step. Due to this property, such discretization is also called an *explicit method*.<sup>68</sup> Some of the benefits of this method include ease of implementation and reduced computational cost of each time step due to its explicit nature. However, its numerical stability is dependent on the values of  $\Delta t$ ,  $h$ , and  $D$ . For the method to remain numerically stable, the following condition is required:

$$\Delta t \leq \frac{h^2}{pD}. \quad (3.18)$$

Here,  $p = 2, 4, \text{ or } 6$  for 1D, 2D, or 3D, respectively. Thus, if  $h$  is decreased to half its value to improve the accuracy of the spatial discretization, as explained above, the time step must be

reduced by a factor of 4 to maintain the numerical stability. This requirement limits the size of the time step that can be used for the computation, and therefore, it increases the overall computational cost. The accuracy of the Forward Euler time-stepping scheme is first order in time, i.e., the error in the time discretization is proportional to  $\Delta t$ .<sup>68</sup>

The other two schemes listed in Table 3.1 are known as *implicit methods* because they involve a solution of the linear system at every time step, which increases the associated computational cost for each step.<sup>68</sup> However, their benefit arises from their unconditional stability, i.e., no dependence of  $\Delta t$  on  $h$  for numerical stability. Therefore,  $\Delta t$  can be set independently of  $h$  if the temporal discretization is accurate enough. The Backward Euler scheme ( $\Theta = 0$ ) exhibits first-order accuracy in time, while the Crank-Nicolson scheme ( $\Theta = 0.5$ ) exhibits second-order accuracy in time. Thus, out of the three methods, the Crank-Nicolson scheme is the most accurate for a given value of  $\Delta t$ .<sup>68</sup>

To ensure that obtained numerical solution is accurate enough, a convergence test needs to be carried out. In the test, both  $h$  and  $\Delta t$  are reduced (either simultaneously or individually, depending on the numerical scheme and its stability), and a corresponding change in the solution is observed. The solution is deemed converged if the change becomes insignificant compared to the solution. Though many metrics can be used to quantify the change in the solution, one of the most common metrics used is the ratio between the  $L_2$  norms of the change vector and the solution vector.

## 3.2 Finite element method

### 3.2.1 Introduction

FEM is a numerical technique used to approximate solutions to PDEs, which discretizes the computational domain into several finite-sized subdomains called *finite elements*. Each element has a simple geometry, e.g., triangular, quadrilateral, and hexahedral. The PDE solution is determined at the *nodes* of each element that exist at the element's vertices, edge centers, face centers, body center, etc., by solving a system of linear equations formed by discretizing the *weak form* of the PDE. The solution in the rest of the space is obtained by interpolating the nodal values using polynomial functions.

The system of linear equations is obtained by applying the weak form of the PDE to each element and integrating over the element. The integrals are then approximated using numerical quadrature that replaces the integrals with sums over the quadrature points within the element and results in the linear system. One of the biggest advantages of the FEM is its ability to handle complex geometries and irregular domains. By dividing the domain into smaller elements, the FEM can approximate the solution to a high degree of accuracy, even in domains with irregular shapes or boundaries. Despite its advantages, the FEM has some limitations. For instance, it can be more difficult to implement even for simple problems than other methods like the FDM. Furthermore, it requires the use of a conformal mesh to obtain sufficiently accurate results, which is challenging to generate in the 3D microstructures observed in some materials science problems.

#### 3.2.1.1 Weak form

The weak form of a PDE is a mathematical formulation that allows the use of functional analysis techniques for solving the PDE.<sup>69,70</sup> In the weak form, the PDE is expressed as an integral

equation involving a *test or weighting function* and its derivatives. It is called the weak form because it imposes weaker requirements on the smoothness of the solution than the original form of the equation. In the standard form of the PDE, also called the *strong form*, the PDE must hold pointwise throughout the equation's domain, which requires that the solution be sufficiently smooth to satisfy the equation at every point. This requirement can be restrictive, especially for nonlinear or high-order PDEs, and can make finding solutions difficult. In contrast, the weak form only requires the solution to satisfy when integrated over individual elements within the domain of the equation. This approach allows for a broader class of functions to be considered as solutions, including functions that may not be smooth or even continuous.

### ***3.2.1.2 Element types***

The accuracy of the solution obtained using the FEM is dependent on the element type used to discretize the domain, as well as the size of the element and the nature of the solution. The elements can be divided into multiple categories based on the spatial dimension, type, and order. For instance, elements may be segments in 1D, triangles and quadrilaterals in 2D, and tetrahedra, hexahedra, and triangular prisms in 3D. For each element (like segments), the location of the nodes and quadrature points of the element can vary, which results in different types of elements. For instance, in standard Lagrangian elements, the nodes and quadrature points are different, while those for the Gauss-Lobatto elements are collocated. Finally, for each element with a fixed type, the element order can vary, which corresponds to the degree of the polynomial basis functions that the element uses to approximate the solution.

The element is selected based on the dimensionality of the problem and, if a conformal mesh is required, the geometry of the problem. For selecting other characteristics, the

computational cost vs. accuracy tradeoff needs to be considered. Although both the type and order can be tuned together to obtain the best performance in terms of cost and accuracy, it is common to fix the type of elements and then tune the element order. For instance, COMSOL Multiphysics® uses Lagrangian elements by default, while PRISMS-PF<sup>27</sup> uses Gauss-Lobatto elements, and both software allow users to vary the element order according to their needs. Using higher-order elements results in more accurate solutions because higher-degree polynomials can approximate complex functions (like the hyperbolic tangent function used in the smoothed boundary method) more closely for a given element size. However, increasing the order not only increases the computational overhead but can also make the method prone to Runge’s phenomenon, in which oscillations at the edges of an interval are observed when interpolation is carried out using high-degree polynomials over a set of equally spaced points.<sup>71</sup> In our experience, quadratic elements provide the best performance in terms of cost and accuracy for the systems considered in this dissertation.

### ***3.2.2 Derivation of the weak form***

The FEM uses the weak form of a PDE. In this subsection, the process of deriving the weak form of an evolution equation used in Chapter 6 is discussed. The strong form of the evolution equation is as follows:

$$\frac{\partial \psi}{\partial t} = \nabla \cdot (M_\psi \nabla \mu_\psi) - v |\nabla \psi|, \quad (3.19)$$

where  $\psi$  is an order parameter,  $M_\psi$  and  $\mu_\psi$  are the mobility and the chemical potential for the phase represented by  $\psi$ , respectively, and  $v$  is the normal component of the velocity of the interface between the phase represented by  $\psi$  and another phase. To derive the weak form, one needs to

multiply the strong form with a test or weighting function,  $w$ , and integrate over the entire domain, as shown in Eq. 3.20. The weighting function can be any arbitrary function, but for mathematical convenience, it is designed to have a value of zero at the domain boundary in this subsection.

$$\int_{\Omega} w \left( \frac{\partial \psi}{\partial t} \right) d\Omega = \int_{\Omega} w \left( \nabla \cdot (M_{\psi} \nabla \mu_{\psi}) \right) d\Omega - \int_{\Omega} w (v |\nabla \psi|) d\Omega, \quad (3.20)$$

where  $\Omega$  represents the domain. The key idea in deriving the weak form for the FEM is to transfer gradients from the variable of interest,  $\psi$  in this case, to  $w$ . To achieve this, the first term on the right-hand side (RHS) needs to be simplified first using an identity of the product rule for differentiation, as shown below.

$$\int_{\Omega} w \left( \frac{\partial \psi}{\partial t} \right) d\Omega = \int_{\Omega} \left( \nabla \cdot (w M_{\psi} \nabla \mu_{\psi}) \right) d\Omega - \int_{\Omega} \nabla w \cdot M_{\psi} \nabla \mu_{\psi} d\Omega - \int_{\Omega} w (v |\nabla \psi|) d\Omega. \quad (3.21)$$

Applying the divergence theorem to the first term on the RHS in Eq. 3.21 gives

$$\int_{\Omega} w \left( \frac{\partial \psi}{\partial t} \right) d\Omega = \int_{\Gamma} w M_{\psi} \nabla \mu_{\psi} \cdot \hat{n} d\Gamma - \int_{\Omega} \nabla w \cdot M_{\psi} \nabla \mu_{\psi} d\Omega - \int_{\Omega} w (v |\nabla \psi|) d\Omega, \quad (3.22)$$

where  $\Gamma$  represents the boundary of the domain and  $\hat{n}$  represents the unit normal to that boundary.

Since  $w|_{\Gamma} = 0$ , by design, the first term of the RHS in Eq. 3.22 becomes zero. Thus,

$$\int_{\Omega} w \left( \frac{\partial \psi}{\partial t} \right) d\Omega = - \int_{\Omega} \nabla w \cdot M_{\psi} \nabla \mu_{\psi} d\Omega - \int_{\Omega} w (v |\nabla \psi|) d\Omega, \quad (3.23)$$

which is the weak form of Eq. 3.19.

The implementation in PRISMS-PF<sup>27</sup> needs the time derivative to be discretized as well, along with a separate collection of the terms containing the weighting function and the terms

containing the gradient of the weighting function. The time derivative is discretized using the Forward Euler scheme, as described in Section 3.1. Thus, Eq. 3.23 becomes

$$\int_{\Omega} w \left( \frac{\psi^{j+1} - \psi^j}{\Delta t} \right) d\Omega = - \int_{\Omega} \nabla w \cdot M_{\psi}^j \nabla \mu_{\psi}^j d\Omega - \int_{\Omega} w (v^j |\nabla \psi^j|) d\Omega, \quad (3.24)$$

where the superscript is the index of the time step and  $\Delta t$  is the time-step size. By bringing the term containing  $\psi^j$  on the RHS of Eq. 3.24, multiplying the equation with  $\Delta t$ , and collecting terms as described above, we obtain

$$\int_{\Omega} w(\psi^{j+1}) d\Omega = - \int_{\Omega} \nabla w \cdot (\Delta t M_{\psi}^j \nabla \mu_{\psi}^j) d\Omega + \int_{\Omega} w(\psi^j - \Delta t v^j |\nabla \psi^j|) d\Omega, \quad (3.25)$$

which is identical to Eq. 36 in the documentation of the microgalvanic application of PRISMS-PF.<sup>26,72</sup>

### 3.2.3 Discretization and assembly

In this section, the discretization and assembly process involved in the application of the FEM is illustrated by using the 1D diffusion equation as an example. The diffusion equation (described in Section 3.1) is selected to show the similarities in the linear systems of equations derived using the FEM and FDM. The weak form for the 1D diffusion equation is derived following the steps discussed above. Let  $w$  be the weighting function such that  $w(x = 0) = 0$ . By multiplying the 1D diffusion equation with  $w$  and integrating over the entire domain, we obtain

$$\int_L w \frac{\partial C}{\partial t} dx = \int_L w \frac{\partial}{\partial x} \left( D \frac{\partial C}{\partial x} \right) dx. \quad (3.26)$$

Applying the identity from the product rule gives



$$\int_L w \frac{\partial C}{\partial t} dx = \int_L \frac{\partial}{\partial x} \left( wD \frac{\partial C}{\partial x} \right) dx - \int_L \frac{\partial w}{\partial x} D \frac{\partial C}{\partial x} dx. \quad (3.27)$$

Using the divergence theorem results in the following equation.

$$\int_L w \frac{\partial C}{\partial t} dx = -wD \frac{\partial C}{\partial x} \Big|_{x=0} + wD \frac{\partial C}{\partial x} \Big|_{x=L} - \int_L \frac{\partial w}{\partial x} D \frac{\partial C}{\partial x} dx. \quad (3.28)$$

Inputting the BC at  $x = L$  and noting that  $w(x = 0) = 0$  by design simplifies Eq. 3.28, as shown below.

$$\int_L w \frac{\partial C}{\partial t} dx = -Jw|_{x=L} - \int_L \frac{\partial w}{\partial x} D \frac{\partial C}{\partial x} dx. \quad (3.29)$$

So far,  $w$  is considered as any arbitrary function with only one constraint, i.e.,  $w(x = 0) = 0$ . Thus, Eq. 3.29 is equivalent of Eq. 3.9 (and the associated BCs) without any approximation. To obtain a numerical solution, the domain is divided into multiple elements with the same size. Figure 3.2 shows the 1D domain discretized into  $N$  elements of equal size,  $h_e$ . Thus, the weak form can be written as the sum of the weak form for each element as shown below.<sup>70</sup>

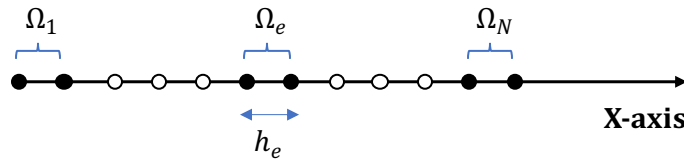


Figure 3.2. A schematic of the discretization of the 1D domain considered in the example here. The filled nodes represent the extents of the first,  $e^{th}$ , and the last elements in the domain, while the empty nodes represent the intermediate elements.

$$\sum_{e=1}^N \left( \int_{\Omega_e} w \frac{\partial C}{\partial t} dx \right) = -Jw|_{x=L} - \sum_{e=1}^N \left( \int_{\Omega_e} \frac{\partial w}{\partial x} D \frac{\partial C}{\partial x} dx \right), \quad (3.30)$$

where  $\Omega_e$  represents the  $e^{th}$  element. The second approximation is that both  $w$  and  $C$  for each element can be written as a sum of specified basis functions and arbitrary parameters as<sup>70</sup>

$$w \approx w^h = \sum_{A=1}^n a^A \phi^A(x), \quad (3.31)$$

$$C \approx C^h = \sum_{B=1}^n b^B \psi^B(x), \quad (3.32)$$

where  $w^h$  and  $C^h$  are approximations to  $w$  and  $C$ , respectively. The functions  $\phi^A(x)$  and  $\psi^B(x)$  are the basis functions, and  $a$  and  $b$  represent the arbitrary parameters. The superscripts  $A$  and  $B$  are dummy indices that represent the nodes in an element, and  $n$  represents the number of nodes in the element. Note that when the  $\phi^i(x) = \psi^i(x)$  for all  $i \in [1, n]$ , the resulting weak form is known as the *Galerkin form*,<sup>70</sup> which is shown below.

$$\sum_{e=1}^N \left( \int_{\Omega_e} w^h \frac{\partial C^h}{\partial t} dx \right) \approx -JW^h|_{x=L} - \sum_{e=1}^N \left( \int_{\Omega_e} \frac{\partial w^h}{\partial x} D \frac{\partial C^h}{\partial x} dx \right), \quad (3.33)$$

Note the use of  $\approx$  instead of  $=$  in Eq. 3.33 signifies that the Galerkin form approximates the original weak form (Eq. 3.29) in a similar manner as the finite difference form (discussed in Section 3.1) approximates the strong form.

Next, we use linear polynomials as the basis functions for the weighting function and the solution. Thus,  $w^h$  and  $C^h$  in the  $e^{th}$  element can be written as<sup>70</sup>

$$w^h = \sum_{A=1}^n \Gamma^A(x) a_e^A = \Gamma^1(x) a_e^1 + \Gamma^2(x) a_e^2, \quad (3.34)$$

$$C^h = \sum_{B=1}^n \Gamma^B(x) b_e^B = \Gamma^1(x) b_e^1 + \Gamma^2(x) b_e^2, \quad (3.35)$$

where  $\Gamma^1$  and  $\Gamma^2$  are the linear basis functions, and  $a_e^A$  and  $b_e^B$  are the values of  $w^h$  and  $C^h$  at the element nodes. The superscripts  $A$  and  $B$  are dummy indices used to represent the nodes in an element. Since linear basis functions (or linear elements) are used here, both  $A$  and  $B$  take values of 1 and 2. The functions  $\Gamma^1$  and  $\Gamma^2$  are obtained using the mapping between the physical element and a bi-unit domain, parameterized by a variable  $\xi$  that spans between -1 and 1. The basis functions are written as<sup>70</sup>

$$\Gamma^1(x(\xi)) = \frac{1 - \xi}{2}, \quad (3.36)$$

$$\Gamma^2(x(\xi)) = \frac{1 + \xi}{2}, \quad (3.37)$$

Furthermore, the spatial derivatives of  $\Gamma^1$  and  $\Gamma^2$  can be written as the following.<sup>70</sup> Note that the parentheses with the basis functions are dropped from hereon for brevity.

$$\frac{\partial \Gamma^1}{\partial x} = \frac{\partial \Gamma^1}{\partial \xi} \frac{\partial \xi}{\partial x} = -\frac{1}{2} \frac{\partial \xi}{\partial x}, \quad (3.38)$$

$$\frac{\partial \Gamma^2}{\partial x} = \frac{\partial \Gamma^2}{\partial \xi} \frac{\partial \xi}{\partial x} = \frac{1}{2} \frac{\partial \xi}{\partial x}. \quad (3.39)$$

To determine  $\frac{\partial \xi}{\partial x}$ , the isoparametric form is used, where the same basis functions are used to map the physical element from a bi-unit domain as those for the solution. Thus,<sup>70</sup>

$$x = \Gamma^1 x_e^1 + \Gamma^2 x_e^2 = \frac{x_e^1 + x_e^2}{2} + \frac{\xi(x_e^2 - x_e^1)}{2}, \quad (3.40)$$

where  $x_e^1$  and  $x_e^2$  are the node locations of the  $e^{th}$  element. Therefore,<sup>70</sup>

$$\frac{\partial x}{\partial \xi} = \frac{(x_e^2 - x_e^1)}{2} = \frac{h_e}{2}. \quad (3.41)$$

Since the isoparametric form is invertible<sup>70</sup>

$$\frac{\partial \xi}{\partial x} = \left(\frac{\partial x}{\partial \xi}\right)^{-1} = \frac{2}{h_e}. \quad (3.42)$$

Substituting Eq. 3.34 and Eq. 3.35 into Eq. 3.33 and assuming the diffusivity to be a constant result in the following equation.

$$\begin{aligned} & \sum_{e=1}^N \left( \int_{\Omega_e} \Sigma_{A=1}^2 \Gamma^A a_e^A \frac{\partial \Sigma_{B=1}^2 \Gamma^B b_e^B}{\partial t} dx \right) \\ &= -J\Gamma^2 a_N^2 - D \sum_{e=1}^N \left( \int_{\Omega_e} \frac{\partial \Sigma_{A=1}^2 \Gamma^A a_e^A}{\partial x} \frac{\partial \Sigma_{B=1}^2 \Gamma^B b_e^B}{\partial x} dx \right). \end{aligned} \quad (3.43)$$

To make the notation more compact, the time derivative is denoted using  $(\dot{\phantom{x}})$  only for this section. Furthermore, since only the nodal values are assumed to change with time (elements do not change with time in this illustration), the  $(\dot{\phantom{x}})$  symbol is used only for the nodal values corresponding to the solution on the LHS ( $b_e^B$ ). Since  $a_e^A$ ,  $b_e^B$ , and  $b_e^B$  do not depend on  $x$  within an element, they can be taken out of the integrals. Thus, by incorporating these changes and insights and substituting Eqs. 3.36 to 3.42 into Eq. 3.43, the following equation is obtained.<sup>73,74</sup>

$$\begin{aligned} & \sum_{e=1}^N a_e^A \left( \int_{-1}^1 \Sigma_{A=1}^2 \Gamma^A \Sigma_{B=1}^2 \Gamma^B \frac{h_e}{2} d\xi \right) \dot{b}_e^B \\ &= -J\Gamma^2 a_N^2 \\ & - D \sum_{e=1}^N a_e^A \left( \int_{-1}^1 \sum_{A=1}^2 \left( \frac{\partial \Gamma^A}{\partial x} \right) \sum_{B=1}^2 \left( \frac{\partial \Gamma^B}{\partial x} \right) \frac{h_e}{2} d\xi \right) \dot{b}_e^B. \end{aligned} \quad (3.44)$$

Now, using the matrix-product notation to write the product of sums that exists on both sides of Eq. 3.44, the equation can be expressed as<sup>73,74</sup>

$$\begin{aligned}
& \sum_{e=1}^N [a_e^1 \ a_e^2] \left( \int_{-1}^1 \begin{bmatrix} \Gamma^1 \Gamma^1 & \Gamma^1 \Gamma^2 \\ \Gamma^2 \Gamma^1 & \Gamma^2 \Gamma^2 \end{bmatrix} d\xi \right) \frac{h_e}{2} [b_e^1 \ b_e^2]^T \\
& = -J\Gamma^2 a_N^2 \\
& - D \sum_{e=1}^N [a_e^1 \ a_e^2] \left( \int_{-1}^1 \begin{bmatrix} \frac{\partial \Gamma^1}{\partial \xi} \frac{\partial \Gamma^1}{\partial \xi} & \frac{\partial \Gamma^1}{\partial \xi} \frac{\partial \Gamma^2}{\partial \xi} \\ \frac{\partial \Gamma^2}{\partial \xi} \frac{\partial \Gamma^1}{\partial \xi} & \frac{\partial \Gamma^2}{\partial \xi} \frac{\partial \Gamma^2}{\partial \xi} \end{bmatrix} d\xi \right) \frac{4}{h_e^2} \frac{h_e}{2} [b_e^1 \ b_e^2]^T.
\end{aligned} \tag{3.45}$$

The components of matrices in Eq. 3.45 are obtained by using the relations for the basis functions and their derivatives with respect to  $\xi$ , which is followed by the analytical solution of the integrals to obtain the following equation.<sup>73,74</sup>

$$\begin{aligned}
& \sum_{e=1}^N [a_e^1 \ a_e^2] \begin{bmatrix} 2 & 1 \\ 1 & 2 \end{bmatrix} \frac{h_e}{6} [b_e^1 \ b_e^2]^T \\
& = -J\Gamma^2 a_N^2 - D \sum_{e=1}^N [a_e^1 \ a_e^2] \left( \begin{bmatrix} 1 & -1 \\ -1 & 1 \end{bmatrix} \right) \frac{1}{h_e} [b_e^1 \ b_e^2]^T.
\end{aligned} \tag{3.46}$$

By performing the global assembly, i.e., writing the sum over all the elements into a matrix-vector product form, the final linear system can be obtained, as shown below. Note that the following mapping is used to convert the local nodal indices to the global index:  $a_e^A = a_{e+A-1}$ .<sup>73,74</sup>

$$\begin{aligned}
& [a_1 \ a_2 \ \dots \ a_N \ a_{N+1}] \begin{bmatrix} 2 & 1 & 0 & \dots & \dots & 0 \\ 1 & 4 & 1 & 0 & \dots & \vdots \\ 0 & 1 & 4 & 1 & 0 & \vdots \\ \vdots & 0 & \ddots & \ddots & \ddots & \vdots \\ \vdots & \vdots & 0 & 1 & 4 & 1 \\ 0 & \dots & \dots & 0 & 1 & 2 \end{bmatrix}_{(N+1) \times (N+1)} \frac{h_e}{6} [b_1 \ b_2 \ \dots \ b_N \ b_{N+1}]^T \\
& = [a_1 \ a_2 \ \dots \ a_N \ a_{N+1}] \begin{bmatrix} -1 & 1 & 0 & \dots & \dots & 0 \\ 1 & -2 & 1 & 0 & \dots & \vdots \\ 0 & 1 & -2 & 1 & 0 & \vdots \\ \vdots & 0 & \ddots & \ddots & \ddots & \vdots \\ \vdots & \vdots & 0 & 1 & -2 & 1 \\ 0 & \dots & \dots & 0 & 1 & -1 \end{bmatrix}_{(N+1) \times (N+1)} \frac{D}{h_e} [b_1 \ b_2 \ \dots \ b_N \ b_{N+1}]^T \\
& \quad - [a_1 \ a_2 \ \dots \ a_N \ a_{N+1}] [0 \ 0 \ \dots \ 0 \ J]^T.
\end{aligned} \tag{3.47}$$

Note that the value of  $b_1 = C_*$  according to the BC. By defining the vector containing  $a_i$ ,  $b_i$ , and  $J$  as  $\mathbf{A}$ ,  $\mathbf{B}$  and  $\mathbf{F}$ , respectively, and the matrices on the LHS and RHS as  $\vec{M}$  and  $\vec{K}$ , respectively, Eq. 3.47 can be written as<sup>73,74</sup>

$$\mathbf{A} \vec{M} \dot{\mathbf{B}} \frac{h_e}{6} = \mathbf{A} \left( \vec{K} \mathbf{B} \frac{D}{h_e} - \mathbf{F} \right). \tag{3.48}$$

Note that the matrix  $\vec{K}$  also has the tridiagonal structure as the global matrix,  $\vec{G}$ , assembled in Section 3.1 for the FDM. In fact, the internal matrix within  $\vec{K}$  that ranges from the row numbers 2 to  $N$  the column numbers 2 to  $N$  is the same as  $\vec{G}$ . Since Eq. 3.48 needs to hold for any  $\mathbf{A}$ ,<sup>73,74</sup>

$$\vec{M} \dot{\mathbf{B}} = 6 \vec{K} \mathbf{B} \frac{D}{h_e^2} - \frac{6}{h_e} \mathbf{F}. \tag{3.49}$$

Next, the time derivative is discretized using the Forward Euler scheme, as discussed in Section 3.1 (see Table 3.1 and the associated text). Thus,<sup>73,74</sup>

$$\vec{M} \frac{(\mathbf{B}^{j+1} - \mathbf{B}^j)}{\Delta t} = 6\vec{K} \mathbf{B}^j \frac{D}{h_e^2} - \frac{6}{h_e} \mathbf{F}^j, \quad (3.50)$$

where the subscript  $j$  represent the time index. By collecting all the terms containing  $j$  on the RHS, we can get the final expression for the FEM solution at  $j + 1$ <sup>73,74</sup>

$$\mathbf{B}^{j+1} = \vec{M}^{-1} \left( 6\vec{K} \frac{D\Delta t}{h_e^2} + \vec{M} \right) \mathbf{B}^j - \vec{M}^{-1} \frac{6\Delta t}{h_e} \mathbf{F}^j. \quad (3.51)$$

Note that the stability condition and accuracy implications remain the same as those discussed in Section 3.1.

### 3.2.4 PRISMS-PF and deal.II

The FEM library, deal.II, is a general-purpose collection of codes written in C++ that enables the development of custom tools for solving PDEs.<sup>71</sup> It is actively developed and supported by a large international group of researchers. It is used for both commercial and academic projects as it provides access to prebuilt and extensively tested codes that can manage grid refinement, DOF handling, mesh inputs, result outputs, parallel computing, etc. The development of such codes is a highly time-consuming and nontrivial task. In addition to these general capabilities, the PRISMS-PF framework is based on the deal.II library for the following reasons.<sup>27</sup> First, the library offers inbuilt capabilities like adaptive meshing with quadtrees and octrees; templated classes and functions to enable dimension and element-order independent programming; multi-level parallelization (vectorization, threading, and MPI); advanced solvers like Krylov solvers; and matrix-free approach with partial assembly that enables efficient explicit time stepping.<sup>27</sup> In addition, deal.II also offers capabilities to input meshes from other software like Dream3D.

Finally, the presence of a large and supportive user community enables a quick resolution of queries.

However, the use of deal.II has some disadvantages as well. In addition to the limitations of the FEM itself, such as the more complex implementation and steeper learning curve than the FDM, deal.II also suffers from the following issues. First, due to the vast size of the library, expanding it to generate a new capability is challenging, as one needs to be aware of the subcomponents of the library that are involved in the capability building. Second, its implementation for GPU-based computation is different from that of CPU-based computation. Thus, the modification of legacy codes to benefit from GPU acceleration is not trivial. Finally, at time of this dissertation writing, the library does not provide support for GPUs from leading vendors like Intel and AMD; it only supports NVIDIA's GPUs.

### **3.3 Smoothed boundary method**

#### ***3.3.1 Introduction***

Smoothed boundary method (SBM)<sup>75</sup> is an approach for solving PDEs with general boundary conditions imposed on arbitrarily shaped boundaries. It employs a smooth function called the *domain parameter* that has a value of 1 within the region of interest and 0 outside it, and at the interface, the domain parameter varies smoothly over a finite length. Thus, in the SBM, the interface has a finite thickness, as opposed to the sharp-interface approach, where the boundaries have zero thickness. The domain parameter is used to modify the PDE under consideration, as illustrated below, using the diffusion equation as an example. The SBM offers a variety of benefits over the sharp-interface approach. First, it enables us to solve PDEs in complex geometries without the need to build a conformal mesh, which is both time consuming and challenging to obtain in



the complex microstructures observed in materials science problems.<sup>75</sup> Thus, with the application of the SBM, complex geometries can be discretized using regular grids.<sup>75</sup> Second, it allows for easy handling of the boundary conditions, especially at arbitrarily shaped or evolving boundaries, both internal and external.<sup>75</sup>

### 3.3.2 Derivation of the SBM form

Let  $\psi$  be the domain parameter corresponding to a solid region where diffusion is occurring, and at the boundary of the region, there is a flux of the diffusing species. Thus, in the solid region<sup>75</sup>

$$\frac{\partial C}{\partial t} = \nabla \cdot (D\nabla C), \quad (3.52)$$

where  $C$  and  $D$  are the concentration and diffusivity of the diffusing species in the solid region. At the boundary,<sup>75</sup>

$$J = -D\nabla C \cdot \hat{n}, \quad (3.53)$$

where  $\hat{n}$  is the unit normal to the boundary. To obtain the SBM form, Eq. 3.52 is multiplied by  $\psi$ . Thus,<sup>75</sup>

$$\psi \frac{\partial C}{\partial t} = \psi \nabla \cdot (D\nabla C). \quad (3.54)$$

Using the identity of the product rule for differentiation, we obtain<sup>75</sup>

$$\psi \frac{\partial C}{\partial t} = \nabla \cdot (\psi D \nabla C) - \nabla \psi \cdot (D \nabla C). \quad (3.55)$$

Note that  $\nabla \psi$  represents the boundary of the solid region and, it is related to the unit normal as  $\nabla \psi = |\nabla \psi| \hat{n}$ . Thus, substituting this relation for  $\nabla \psi$  into Eq. 3.55 gives<sup>75</sup>

$$\begin{aligned} \psi \frac{\partial C}{\partial t} &= \nabla \cdot (\psi D \nabla C) - |\nabla \psi| \hat{n} \cdot (D \nabla C) \\ &= \nabla \cdot (\psi D \nabla C) + |\nabla \psi| J. \end{aligned} \quad (3.56)$$

Finally, the SBM form is obtained by dividing Eq. 3.56 by  $\psi$ <sup>75</sup>

$$\frac{\partial C}{\partial t} = \frac{1}{\psi} \nabla \cdot (\psi D \nabla C) + \frac{|\nabla \psi|}{\psi} J. \quad (3.57)$$

The same process as above can be repeated in the case of Dirichlet boundary conditions with a small modification: the PDE is multiplied by  $\psi^2$  instead of  $\psi$ , as shown by Yu et al.<sup>75</sup>

The SBM form of the PDE can be discretized, by either FDM or FEM, to obtain a numerical solution, as discussed above. The error implications discussed above for these methods are also applicable to the SBM form. However, the use of a smoothed interface instead of a sharp interface introduces an additional error. This error is dependent on the ratio between the interfacial thickness and the smallest feature size of interest in the domain, and the number of grid points within the interface.<sup>75</sup> A thinner interface with more grid points result in a lower error but at an increased computational cost. As a rule of thumb, a ratio between the interfacial thickness and the smallest feature size of less than 0.1 and four grid points within the interface ( $0.1 \leq \psi \leq 0.9$ ) is a good setup to obtain a preliminary numerical solution. However, further analysis is needed to ensure that the error is not significant. This can be done by first increasing the number of grid points in the interface and then by decreasing the interfacial thickness and analyzing the change in the

obtained value of the field of interest (like the concentration in the example provided here).<sup>75</sup> The thickness and the resolution are deemed sufficient in terms of numerical accuracy when the solution does not change significantly upon further refinement.<sup>75</sup> We refer the readers to Section 7.8 (see Figure 7.10, Table 7.3, and the associated text) for an example of this error analysis.

## CHAPTER 4

### Effect of Laser Patterning on the Fast-Charging Performance of Energy-Dense Li-ion Batteries\*

#### 4.1 Introduction: Fast charging of energy-dense Li-ion batteries

In this chapter, we employ the Materials Genome Initiative-based approach to enable high-energy-density lithium-ion batteries (LIBs) that can be charged in less than 10 minutes. Such batteries are necessary to accelerate the public acceptance of electric vehicles. Conventionally, LIBs utilize porous electrodes consisting of a solid phase containing the Li-storage active material and a pore phase filled with an electrolyte that conducts Li ions. This conventional design can be tailored to achieve high energy density by increasing the volume fraction of the active material and the electrode thickness. However, the transport of Li ions becomes severely limited in such electrodes, especially during high C-rate operations.<sup>76,77</sup> Consequently, significant concentration gradients develop through the electrode thickness, which results in large cell polarization and significantly reduces the accessible capacity of the electrodes under fast-charging conditions.<sup>38,78–81</sup> Moreover, due to concentration polarization during fast charging, regions of the anode can reach electrochemical potential values lower than the potential of Li metal (0 V vs. Li/Li<sup>+</sup>). Consequently, Li plating on the anodes becomes thermodynamically favorable. The formation of metallic Li dendrites on the anode surface is highly irreversible because the exposure of fresh Li

---

\* This chapter is adapted from V. Goel et al., *Energy Storage Materials*, 57 (2023), 44<sup>24</sup>; K.-H. Chen et al., *Journal of Power Sources*, 471 (2020), 228475<sup>22</sup>; and V. Goel et al., *MethodsX*, 8 (2021), 101425.<sup>30</sup>

to the electrolyte results in solid electrolyte interface (SEI) growth and electrolyte decomposition.<sup>82</sup> In addition, during charging/discharging, the plated Li dendrites can become electrically or electrochemically disconnected from the anode surface, resulting in the formation of inactive or “dead Li.”<sup>82</sup> Therefore, the irreversible dead Li formation and SEI growth on plated Li cause permanent loss of Li inventory and low Coulombic efficiency, leading to significant capacity fade and the eventual cell failure.<sup>39,83–85</sup> On the other hand, thin electrodes with high porosities have been shown to exhibit high power density.<sup>76,77</sup> Unfortunately, the energy density of a battery decreases as the mass fraction of electrochemically inactive components (separators, current collectors, binders, etc.) increases. To overcome this tradeoff, laser-patterning is employed to create the highly ordered laser-patterned electrode (HOLE) architecture, as shown in Figure 4.1, for graphite anodes with  $>3$  mAh/cm<sup>2</sup> loading.

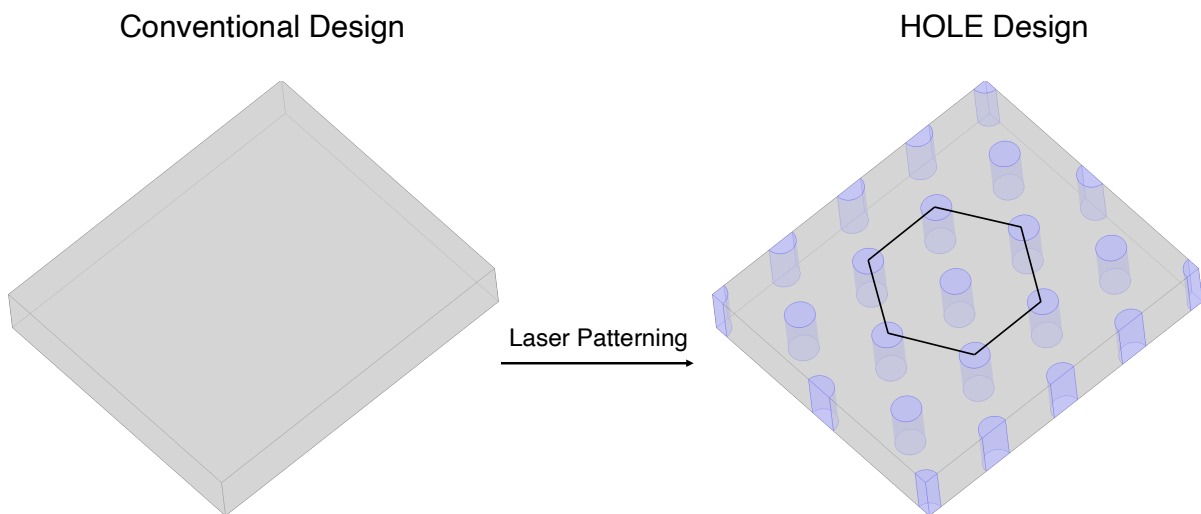


Figure 4.1. Schematic illustration of the Highly Order Laser-Patterned Electrode (HOLE) architecture. The black outline in the HOLE pattern represents the hexagonal symmetry of the channels (highlighted in blue) in the electrode. Reproduced with permission from Ref. 24. Copyright 2023, the authors. Published by Elsevier B.V.

Recently, several experimental and modeling-based studies have shown that the generation of vertical channels in thick electrodes via laser patterning is an effective way of overcoming these

tradeoffs.<sup>22,86-98</sup> For instance, our experimental results (conducted by Kuan-Hung Chen and Min Ji Namkoong under the guidance of Prof. Neil Dasgupta and Prof. Jeff Sakamoto, respectively) demonstrate that industrially relevant pouch cells ( $> 2$  Ah) based on the HOLE architecture retained  $> 97\%$  and  $> 93\%$  capacity after 100 cycles of 4C and 6C fast-charge cycling, respectively. While the corresponding retention in cells with the unpatterned electrodes was only 69% and 59%. After 600 fast-charge cycles, the capacity retention of the HOLE cells was 91% at 4C and 86% at 6C charge rates. However, despite the growing volume of work on the effects of electrode architectures on the fast-charging performance of LIBs, there is a lack of mechanistic understanding of the effect of the HOLE architecture on the fast-charging performance. Without such an understanding, it is challenging to modify the HOLE architecture per the fast-charging performance requirements.

In this chapter, we overcome this challenge by developing an understanding of the effect of the HOLE architecture on the fast-charging performance of thick graphite electrodes with electrode-level simulations. We begin by summarizing our experimental results. Subsequently, we describe the model formulation, along with a workflow for model parameterization to ensure that the identified parameter set is representative of the electrodes under investigation. The workflow also includes an automated parameterization procedure based on the particle swarm optimization algorithm.<sup>99,100</sup> We then use the parameterized model to simulate the fast-charging performance of the graphite electrodes. Our results show that the HOLE architecture improves the Li-ion transport in the anode volume and the homogeneity of the reaction current density distribution and thus enables fast charging.

## 4.2 Summary of experimental results for laser-patterned electrodes

In this section, a summary of the experimental results is provided, which are obtained by Kuan-Hung Chen and Min Ji Namkoong under the guidance of Prof. Neil Dasgupta and Prof. Jeff Sakamoto, respectively. Pouch cells (with  $\sim 2.2$  Ah capacity) based on the control and HOLE graphite anodes were assembled and cycled at 4C and 6C separately. Further details on the construction of the pouch cells and the design specifications of the HOLE architecture can be found elsewhere.<sup>22</sup> The protocol used for cycling the cells is shown in Figure 4.2e for 6C. In short, each cell was charged using a CCCV protocol, where the constant current charging was maintained until the cell voltage of 4.15 V was achieved, which was followed by a constant voltage hold until the total charging time (including the CC portion) of 10 minutes was reached. For 4C, this time was set at 15 minutes. The discharge was carried out at 0.5C with a standard CCCV protocol, where the CC portion was maintained until a voltage of 3.0 V was achieved, followed by a CV hold until the current dropped below 0.1C.

Figure 4.2a shows the discharge capacity of the control (black curve) and HOLE cells (red curve) that were charged at 4C. The cells were first charged/discharged at a 0.5C rate for 3 cycles to measure the total cell capacity ( $\approx 2.2$  Ah), followed by 100 cycles of 4C charge/0.5C discharge. In addition, 3 cycles of 0.5C charge/discharge were repeated after every 50 fast-charge cycles to quantify the capacity fade of the cells. The y-axis shows the cell capacity (normalized to the initial cell capacity) to facilitate a direct comparison. Both the control and HOLE cells exhibit stable cycling at a 0.5C charge rate. However, upon fast charging at 4C, the control cell exhibits a significant capacity fade within the first 40 cycles with a concomitant decrease in the Coulombic efficiency (CE) to 95.9%, as shown in Figure 4.2b. This sharp drop in the capacity is attributed to severe Li plating at the anode/separator interface, as discussed elsewhere.<sup>22</sup> From cycle 40 to 100,

the capacity reaches a plateau; correspondingly, the CE increases back to >99.5%. By comparing the charge/discharge capacities at 0.5C, it is shown that the capacity retention is 69.1% after 100 fast-charge cycles (capacity fade of 30.9%).

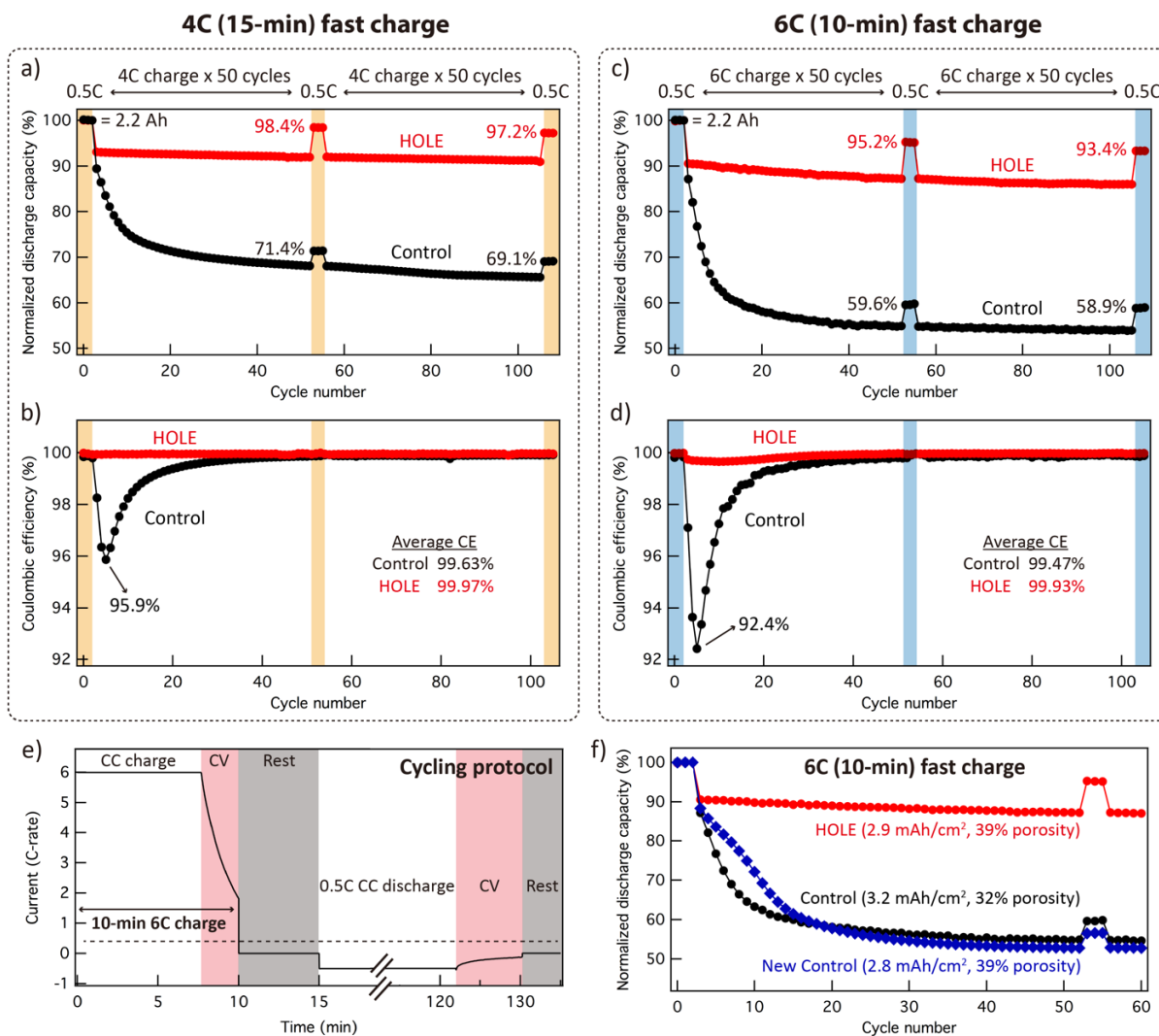


Figure 4.2. Summary of 4C and 6C experimental results (normalized discharge capacity and coulombic efficiency as functions of cycle number) for the pouch cells based on control (unmodified) and HOLE (laser-modified) anodes. Normalized discharge capacity and (b) Coulombic efficiency vs. cycle number under 4C conditions. (c) Normalized discharge capacity and (d) Coulombic efficiency vs. cycle number under 6C conditions. (e) Cycling protocol for evaluating fast-charge capability at 6C charge rate. (f) Comparison of the normalized discharge capacity vs. cycle number of the control, HOLE, and new control cells showing the capacity fade during 6C charging. Reproduced with permission from Ref. 22. Copyright 2020, Elsevier B.V.



The HOLE cell, on the other hand, shows a significantly improved capacity retention and CE during 4C charging, as shown in Figure 4.2a and Figure 4.2b. More specifically, the HOLE cell retained 97.2% of its initial cell capacity with no rapid decrease in its CE throughout cycling. Correspondingly, no visible Li plating is observed on the patterned anode post cycling, as described elsewhere.<sup>22</sup> Similar improvements are observed at 6C, where the HOLE cell retained >93% of its initial capacity after 100 fast-charge cycles, while the control cell only retained 59% of its initial capacity, as shown in Figure 4.2c. The behavior of the CE for both cells for 6C cycling is analogous to that for 4C cycling, as shown in Figure 4.2d. Furthermore, to show that the improvement observed due to the HOLE architecture cannot be simply replicated by increasing the porosity and decreasing the loading of the anode (to match the specifications of the patterned anode) in the control cell, a separate control cell was assembled. This separate control cell had an anode with lower loading and higher porosity than the original anode in the control cell, and it is referred to as the new control anode hereafter. Figure 4.2f shows the capacity fade of the three cell configurations (control, HOLE, new control) during 6C charging. As shown in the figure, a similar trend in capacity fade is observed between the control and new control cells despite the lower electrode loading and higher porosity. Thus, the improvement enabled by the HOLE architecture cannot be simply attributed to its higher overall porosity and lower loading.

To develop a mechanistic understanding of the improved performance enabled by the HOLE architecture, 3D continuum scale modeling is employed. The model details, such as the underlying equations, parameterization, and the generated simulation results, are presented in the following sections.

### 4.3 Governing equations to model the fast-charging performance of Li-ion battery electrodes

As described in Chapter 2 (Section 2.1), a Li-ion cell contains three primary domains: the cathode, the anode, and the separator. A schematic of a cell composed of these domains is shown in Figure 4.3. The porous electrode theory treats each of these domains as an effective medium with averaged properties.<sup>101,102</sup> It also describes the mass and the charge transport inside each of these domains along with the electrochemical reaction that occurs within the electrochemically active regions of the cell (the cathode and the anode). We apply the model described by Newman and coworkers,<sup>103–106</sup> which is summarized below. A list of the symbols used in the model equations is provided in Table 4.1 along with their description.

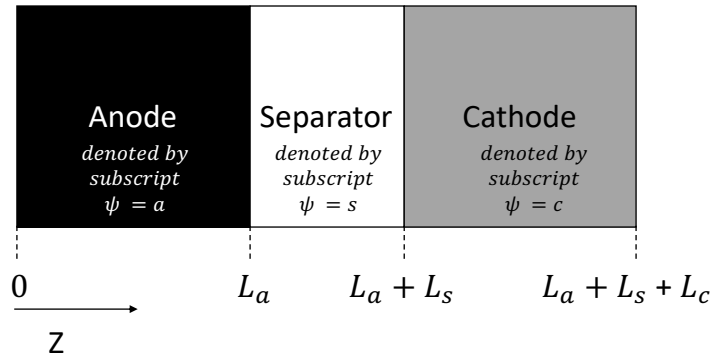


Figure 4.3. A schematic of a Li-ion cell. The thickness of the cell is oriented along the Z axis. Reproduced with permission from Ref. 22. Copyright 2020, Elsevier B.V.

Let subscript  $\psi = c, s,$  and  $a$  denote the domains of cathode, separator, the anode, respectively. Then, the mass transport of Li-ions in the electrolyte within each domain is governed by diffusion and electrochemical reaction as<sup>103–106</sup>:

$$\varepsilon_{\psi} \frac{\partial c_{e,\psi}}{\partial t} = \nabla \cdot (D_{eff,\psi} \nabla c_{e,\psi}) + (1 - t_{+,\psi}^0) \frac{\xi_{\psi}}{F} - \frac{\mathbf{i}_{e,\psi}}{F} \cdot \nabla t_{+,\psi}^0, \quad (4.1)$$

where  $\varepsilon_{\psi}$  is the volume fraction of the electrolyte,  $c_{e,\psi}$  is the Li-ion concentration in the electrolyte,  $D_{eff,\psi}$  is the effective diffusion coefficient of the electrolyte in the porous medium. The

electrochemical reaction current density (RCD), the ionic current density in the electrolyte, and the transference number of Li-ions in the electrolyte are denoted by  $\xi_\psi$ ,  $i_{e,\psi}$ , and  $t_{+,\psi}^0$ , respectively, and  $F$  is Faraday's constant. Note that when anisotropy is present,  $D_{eff,\psi}$  is a tensor, but we use the scalar notation for simplicity. Also note that the RCD is zero inside the separator since it is electrochemically inactive. The following boundary conditions are imposed on the mass transport equation:

$$-D_{eff,a}\nabla c_{e,a}\big|_{z=0} = 0, \quad (4.2)$$

$$-D_{eff,c}\nabla c_{e,c}\big|_{z=L_a+L_s+L_c} = 0, \quad (4.3)$$

$$-D_{eff,a}\nabla c_{e,a}\big|_{z=L_a^-} = -D_{eff,s}\nabla c_{e,s}\big|_{z=L_a^+}, \quad (4.4)$$

$$-D_{eff,s}\nabla c_{e,s}\big|_{z=(L_a+L_s)^-} = -D_{eff,c}\nabla c_{e,c}\big|_{z=(L_a+L_s)^+}, \quad (4.5)$$

where  $L_a$ ,  $L_s$ , and  $L_c$  are the thicknesses of the anode, the separator, and the cathode, respectively (see Figure 4.3). The no-flux boundary conditions (Eqs. 4.2 and 4.3) represent the current collectors that do not allow Li-ion penetration, while the boundary conditions described by Eqs. 4.4 and 4.5 represent absence of accumulation of ions at each electrode/separator interface.

Within each electrode ( $\psi = a$  or  $c$ ) the mass transport of lithium inside the active material particles is controlled by diffusion. The assumption that these particles are spheres of radius  $R_{p,\psi}$  enables the diffusion equation to be written in spherical coordinates as<sup>103–106</sup>:

$$\frac{\partial c_{p,\psi}}{\partial t} = \frac{1}{r^2} \frac{\partial}{\partial r} \left( D_{p,\psi} r^2 \frac{\partial c_{p,\psi}}{\partial r} \right), \quad (4.6)$$

where  $c_{p,\psi}$  represents the lithium concentration in the active material,  $D_{p,\psi}$  is diffusion coefficient of lithium inside the active material, and  $r$  is the radial coordinate defined within a spherical particle. The boundary conditions for the mass transport of lithium inside the active material are:

$$-D_{p,\psi} \frac{\partial c_{p,\psi}}{\partial r} \Big|_{r=0} = 0, \quad (4.7)$$

$$-D_{p,\psi} \frac{\partial c_{p,\psi}}{\partial r} \Big|_{r=R_{p,\psi}} = -\xi_{\psi} / (a_{\psi}^p F). \quad (4.8)$$

The current density in the electrolyte phase within each domain ( $\psi = a, s, \text{ or } c$ ) due to the electrostatic potential and chemical gradients is calculated by<sup>103–106</sup>

$$i_{e,\psi} = -\kappa_{eff,\psi} \nabla \phi_{e,\psi} + \frac{2RT}{F} \kappa_{eff,\psi} \left( 1 + \frac{\partial \ln(f_{\pm,\psi})}{\partial \ln(c_{e,\psi})} \right) (1 - t_{+,\psi}^0) \nabla \ln(c_{e,\psi}), \quad (4.9)$$

where  $\kappa_{eff,\psi}$  is the effective ionic conductivity of the electrolyte in the domain,  $\frac{\partial \ln(f_{\pm,\psi})}{\partial \ln(c_{e,\psi})}$  accounts for the salt activity coefficient dependence on the electrolyte concentration,  $R$  is the universal gas constant, and  $T$  is the cell temperature. Note that when anisotropy is present,  $\kappa_{eff,\psi}$  is a tensor, but we use the scalar notation for simplicity. Since the ionic current density is zero at the electrode/current collector interfaces,

$$\mathbf{i}_{e,a} \Big|_{z=0} = 0 \quad (4.10)$$

$$\mathbf{i}_{e,c} \Big|_{z=L_a+L_s+L_c} = 0 \quad (4.11)$$

Furthermore, the condition for charge conservation and charge neutrality in the electrolyte phase necessitates that<sup>103–106</sup>

$$\nabla \cdot \mathbf{i}_{e,\psi} = \xi_{\psi}. \quad (4.12)$$

The electrostatic potential of the solid phase inside each electrode ( $\phi_{sp,\psi}$ ,  $\psi = a \text{ or } c$ ) is determined from charge conservation, along with the (generalized) Ohm's law, as<sup>103–106</sup>:

$$\nabla \cdot (\sigma_{eff,\psi} \nabla \phi_{sp,\psi}) = \xi_{\psi}, \quad (4.13)$$

Where  $\sigma_{eff,\psi}$  is the effective electrical conductivity of the electrode. Note that, although  $\sigma_{eff,\psi}$  is a tensor when anisotropy is present, we use the scalar notation for simplicity. The electronic charge flux at the cathode/current collector interface is set by the applied current density  $\mathbf{i}_{app}$  as

$$-\sigma_{eff,c} \nabla \phi_{sp,c} \Big|_{z=L_a+L_s+L_c} = \mathbf{i}_{app} . \quad (4.14)$$

The electronic charge flux at the electrode/seperator interfaces is zero, which results in the following boundary conditions:

$$-\sigma_{eff,a} \nabla \phi_{sp,a} \Big|_{z=L_a} = 0 \quad (4.15)$$

$$-\sigma_{eff,c} \nabla \phi_{sp,c} \Big|_{z=L_a+L_s} = 0. \quad (4.16)$$

Furthermore, the electrostatic potential at the anode/current collector interface is set to zero,  $\phi_{sp,a} \Big|_{z=0} = 0$ . The electrochemical reaction at the active material/electrolyte interface is modeled using the Butler-Volmer equation<sup>103–106</sup>

$$\xi_\psi = \alpha_\psi^p i_{0,\psi} \left( \exp\left(\frac{0.5F}{RT} \eta_\psi\right) - \exp\left(\frac{-0.5F}{RT} \eta_\psi\right) \right), \quad (4.17)$$

where  $\eta_\psi$  is the overpotential,  $\alpha_\psi^p$  is the active surface area per unit electrode volume, and  $i_{0,\psi}$  is the exchange current density, which is assumed to have the following dependence on the Li-ion concentration in the electrolyte and Li concentration in the active material<sup>103–106</sup>:

$$i_{0,\psi} = F k_\psi \left( c_{p,\psi}^{max} - c_{p,\psi}^{surf} \right)^{1/2} \left( c_{p,\psi}^{surf} \right)^{1/2} \left( \frac{c_{e,\psi}}{c_{e,ref}} \right)^{1/2}, \quad (4.18)$$

where  $c_{p,\psi}^{surf}$  and  $c_{p,\psi}^{max}$  represent the surface and the maximum lithium concentration inside the active material particles, respectively, and  $k_\psi$  denotes the reaction rate constant. The quantity  $c_{e,ref}$  has a value of 1 mol/m<sup>3</sup>. Finally the overpotential, in the presence of a resistive film (SEI), is calculated by<sup>103–106</sup>

$$\eta_{\psi} = \phi_{sp,\psi} - \phi_{e,\psi} - U_{\psi} - \xi_{\psi} \rho_{\psi} / a_{\psi}^p, \quad (4.19)$$

where  $U_{\psi}$  is the open circuit voltage of the active material and  $\rho_{\psi}$  is the area specific resistance of the SEI layer.

Table 4.1. The list of symbols and description for the variables in the model equations. Reproduced with permission from Ref. 24. Copyright 2023, the authors. Published by Elsevier B.V.

Symbol	Description
$\psi$	Subscript indicating the domain ( $a$ for anode, $s$ for separator, and $c$ for cathode)
$p$	Subscript indicating the active material
$z$	Coordinate for the cell thickness, m
$c_{e,\psi}$	Electrolyte concentration, mol/m <sup>3</sup>
$\varepsilon_{\psi}$	Electrolyte volume fraction (porosity)
$D_L$	Intrinsic diffusivity of the electrolyte, m <sup>2</sup> /s
$D_{eff,\psi}$	Effective electrolyte diffusivity, m <sup>2</sup> /s; $D_{eff,\psi} = \chi_{\psi} D_L$
$\chi_{\psi}$	Ratio between the effective and intrinsic values of the electrolyte diffusivity and conductivity; $\chi_{\psi} = \frac{D_{eff,\psi}}{D_L} = \frac{\kappa_{eff,\psi}}{\kappa_L}$ .
$t_{+,\psi}^0$	Transference number for the Li ions in the electrolyte
$a_{p,\psi}$	Surface area of the active material per unit volume of the electrode. For spherical particles, it is equal to $3 \frac{\varepsilon_{p,\psi}}{R_{p,\psi}}$ , m <sup>2</sup> /m <sup>3</sup>
$i_{e,\psi}$	Electrolyte current density, A/m <sup>2</sup>
$F$	Faraday's constant, C/mol
$\xi$	Reaction current per unit electrode volume, or reaction current density, A/m <sup>3</sup>
$R_{p,\psi}$	Radius of the active material particles, m
$\varepsilon_{p,\psi}$	Volume fraction of the active material particles in the electrode
$L_{\psi}$	Thickness of the domain, m
$c_{p,\psi}$	Li concentration in the active material, mol/m <sup>3</sup>
$r$	Radial coordinate defined within the spherical active material particles, m
$D_{p,\psi}$	Diffusion coefficient of Li inside the active material particles, m <sup>2</sup> /s
$\kappa_{eff,\psi}$	Effective electrolyte conductivity in the domain, S/m; $\kappa_{eff,\psi} = \chi_{\psi} \kappa_L$
$\kappa_L$	Intrinsic conductivity of the electrolyte, S/m

$\phi_{e,\psi}$	Electrostatic potential of the electrolyte, V
$R$	Universal gas constant, J/(mol K)
$T$	Cell temperature, K
$\left(1 + \frac{\partial \ln(f_{\pm,\psi})}{\partial \ln(c_{e,\psi})}\right)$	Thermodynamic factor, which represents the dependence of the electrolyte activity coefficient on the electrolyte concentration
$\sigma_{eff,\psi}$	Effective electronic conductivity of the electrode, S/m; $\sigma_{eff,\psi} = \frac{\varepsilon_{p,\psi}}{\tau_{\psi}^2} \sigma_{\psi}$ . We assume that the tortuosity for the electronic transport is same as the ionic transport
$\sigma_{\psi}$	Electronic conductivity of the active material mixed with carbon additive, S/m
$sp$	Subscript indicating the solid phase, which includes the active material, the carbon additive, and the binder, inside an electrode
$\phi_{sp,\psi}$	Electrostatic potential of the solid phase, V
$i_{app}$	Applied current density on the cathode, A/m <sup>2</sup>
$i_{0,\psi}$	Exchange current density used in the Butler-Volmer equation, A/m <sup>2</sup>
$k_{\psi}$	Reaction rate constant, m/s
$\eta_{\psi}$	Local overpotential in the electrode that drives the electrochemical reaction, V
$U_{\psi}$	Open circuit voltage (OCV), V
$\rho_{\psi}$	Area specific resistance of the SEI layer on the active material particles, $\Omega\text{m}^2$
$c_{p,\psi}^{surf}$	Local Li concentration on the surface of the active material particles, mol/m <sup>3</sup>
$c_{p,\psi}^{max}$	Maximum Li concentration inside the active material particles, mol/m <sup>3</sup>

#### 4.4 Model parameterization for Li-ion battery electrodes

As can be observed from the model equations described in Section 4.3, the model has many input parameters, which can be divided into two categories, those associated with the electrodes and others associated with the separator, as shown in Figure 4.4. Ideally, each parameter value would be determined by performing relevant experiments to fully reflect the battery system under consideration. However, the experimental measurements of many parameters, including but not limited to effective and intrinsic ionic diffusivity and conductivity in the electrolyte, Li diffusivity in the active material, transference number, and reaction rate constant, are both time- and resource-

consuming. Therefore, values of the parameters that cannot be easily determined experimentally are instead obtained by a combination of literature data and by matching the model prediction and experimental data. In this section, we first describe each parameter for the electrodes and the separator and discuss its effect on fast-charging performance of the battery. We then explain our approaches for determining the values of parameters, which include an automated ML-based parameterization procedure for matching the model prediction with experimental results. The details of this procedure are provided in Section 4.4.3.

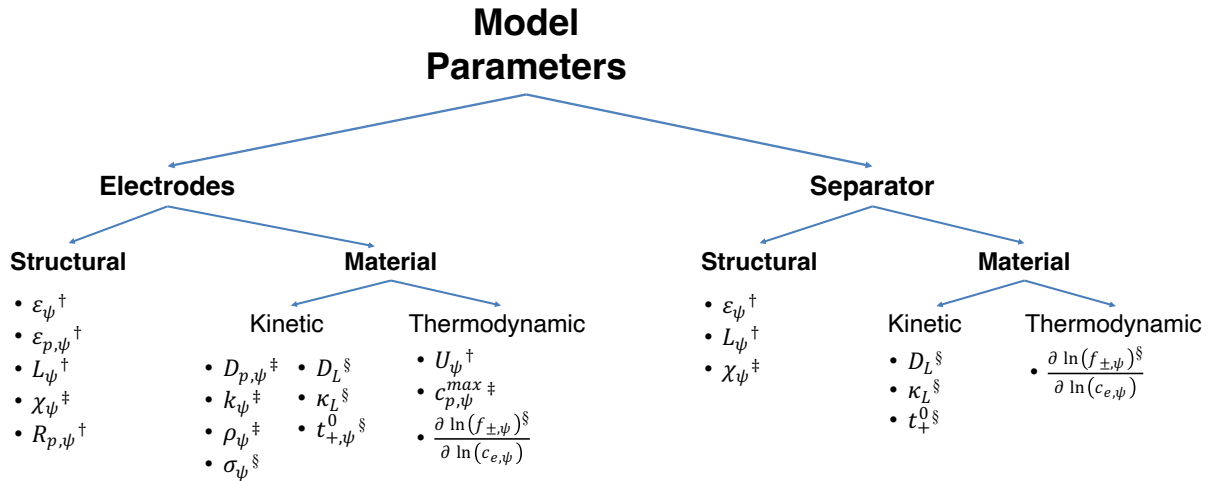


Figure 4.4. Categorization of the model parameters. The superscript next to each parameter, †, ‡, or §, indicates the sources of the parameter values, which corresponds to experiments, automated parameterization procedure, and literature, respectively. Reproduced with permission from Ref. 24. Copyright 2023, the authors. Published by Elsevier B.V.

#### 4.4.1 Electrode parameters

The electrode parameters can be further subdivided into two subcategories: structural and material, which are discussed in detail below.



#### 4.4.1.1 Structural

The structural parameters constitute the quantities that account for the cell structure and the electrode microstructure, such as the electrode thickness,  $L_\psi$ ; the radius of the active material particles,  $R_{p,\psi}$ ; the volume fraction of the electrolyte,  $\varepsilon_\psi$ ; and the volume fraction of the active material,  $\varepsilon_{p,\psi}$ . We note that  $\varepsilon_\psi$  and  $\varepsilon_{p,\psi}$  are related as  $\varepsilon_\psi + \varepsilon_{p,\psi} = 1 - \varepsilon_{f,\psi}$ , where  $\varepsilon_{f,\psi}$  is the volume fraction of the filler phases, including carbon additives and binder in the electrode. Thus, if  $\varepsilon_{f,\psi}$  is fixed,  $\varepsilon_\psi$  and  $\varepsilon_{p,\psi}$  become linearly dependent on each other. The structural parameters also include  $\chi_\psi$ , which represents the ratio between the effective and intrinsic values of the diffusivity and conductivity for the electrolyte phase, i.e.,  $\chi_\psi = \frac{D_{eff,\psi}}{D_L} = \frac{\kappa_{eff,\psi}}{\kappa_L}$ . The value of  $\chi_\psi$  can be related to  $\varepsilon_\psi$  and the electrode tortuosity,  $\tau_\psi$ , which signifies the length of the microscopic path of the ions within the electrode via  $\chi_\psi = \frac{\varepsilon_\psi}{\tau_\psi^2}$ .<sup>107</sup>

These structural parameters affect the battery characteristics in a variety of manners. For instance,  $\varepsilon_\psi$ ,  $\varepsilon_{p,\psi}$ , and  $L_\psi$  determine the loading of the active material in the electrode and thus the maximum capacity. Increasing  $\varepsilon_{p,\psi}$  and/or  $L_\psi$  (with other parameters fixed) raises the maximum capacity of the electrode. In addition, the structural parameters also influence fast-charging performance; for example,  $\chi_\psi$  and  $L_\psi$  affect the ionic diffusion and migration dynamics in the electrode. To enhance Li-ion transport, it is necessary to increase  $\chi_\psi$  and/or reduce  $L_\psi$ . However, these changes decrease the maximum capacity due to the reduced loading of the active material. Similarly,  $R_{p,\psi}$  affects the solid-state diffusion dynamics, and it is desirable to decrease  $R_{p,\psi}$  to enhance Li transport within active material particles.<sup>108–110</sup> Furthermore,  $R_{p,\psi}$ , along with  $\varepsilon_{p,\psi}$ , also influence the value of the specific surface area of the active material,  $a_{p,\psi}$ . Since  $a_{p,\psi}$  is directly proportional to  $\varepsilon_{p,\psi}$  and inversely proportional to  $R_{p,\psi}$ , increasing  $\varepsilon_{p,\psi}$  and/or reducing

$R_{p,\psi}$ <sup>108–110</sup> generally leads to more electrochemically active area, which consequently improves fast-charging performance of the electrode. However, such a design strategy often leads to high first-cycle losses, because the increased SEI formation.<sup>108,111</sup> Thus, one needs to consider the tradeoff between enhanced fast-charging performance and increased first-cycle losses when choosing the values of  $R_{p,\psi}$  and  $\varepsilon_{p,\psi}$ .

All structural parameters are set during the design and construction of the electrode except for  $\chi_\psi$ , which depends on the microstructure after the calendaring process. The R50 value (i.e., half of the particles are smaller in radius than this value) of the active-material powder is used for  $R_{p,\psi}$ . An automated parameterization process (described later in Section 4.4.3) was chosen to determine  $\chi_\psi$  for the following reasons. First, the experimental techniques such as electrochemical impedance spectroscopy (EIS)<sup>112–117</sup> and X-ray tomography imaging,<sup>114,118–122</sup> combined with calculations,<sup>32,59,119,121,123–125</sup> that are used for determining  $\tau_\psi$  (and hence  $\chi_\psi$  using the relation  $\chi_\psi = \frac{\varepsilon_\psi}{\tau_\psi}$ ) are resource intensive, and the results obtained from different techniques may not agree with each other,<sup>114,115</sup> Second, the literature values for  $\tau_\psi$  (and hence  $\chi_\psi$ ) cannot necessarily be used for a particular battery system, because they are highly sensitive to the electrode composition and processing. Third, through this method, we account for any discrepancy between the input value and the actual value of the intrinsic transport properties of the electrolyte that arises from experimental uncertainties. It should be noted that  $\chi_\psi$  is treated as a second-rank tensor in 3D space for the HOLE anode to account for the anisotropy of the Li-ion transport, as discussed in previous publications.<sup>22,30</sup>

#### 4.4.1.2 Material

The model parameters that are determined by material properties fall under this second category. Such parameters can be further divided into three subcategories, as shown in Figure 4.4. The first subcategory is that of the kinetic parameters, which include the transport parameters and reaction-rate parameters. For the active material, the kinetic parameters are the solid-state diffusivity,  $D_{p,\psi}$ ; the electronic conductivity,  $\sigma_\psi$ ; the area specific resistance of the SEI layer,  $\rho_\psi$ ; and the reaction rate constant,  $k_\psi$ . For the electrolyte, the parameters are the ionic diffusivity,  $D_L$ ; the ionic conductivity,  $\kappa_L$ ; and the transference number,  $t_{+,\psi}^0$ . For achieving high-rate performance, a high  $D_{p,\psi}$  is desired to ensure fast diffusion of Li within the active material particles, as well as a large  $k_\psi$ , which results in low activation overpotential. Additionally, a small  $\rho_\psi$  and high  $\sigma_\psi$  are desired as they result in low overpotential at particle-electrolyte interface and small Ohmic overpotential, respectively. Similarly, large values of  $D_L$ ,  $\kappa_L$ , and  $t_{+,\psi}^0$  would result in fast Li-ion transport in the electrolyte, and thereby reduce the large concentration gradient that typically develops in the electrode during a high C-rate operation.

The kinetic parameters for the active material can potentially be determined using the galvanostatic intermittent titration technique (GITT) and the EIS techniques. However, these measurements tend to have significant uncertainties due to the difficulty in determining the active surface area.<sup>126</sup> Moreover, the measurements obtained using GITT and EIS often do not agree with each other.<sup>127,128</sup> Owing to these challenges, the values reported in the literature can span multiple orders of magnitude; for instance, the range of the solid-state diffusivity of Li within graphite particles has been reported to be as wide as seven orders of magnitude.<sup>129</sup> Thus, we chose to obtain these parameters using the automated parameterization procedure (explained later in Section 4.4.3). We assumed each of  $k_\psi$ ,  $\rho_\psi$ , and  $D_{p,c}$  to be a constant value (independent of concentration,

etc.); however, since the Li diffusivity in the graphite anode,  $D_{p,a}$ , is known to have a strong dependence on the Li concentration in graphite, we obtained a functional form of  $D_{p,a}$  vs. Li concentration from the literature<sup>130</sup> and scaled that function by a pre-factor, which is determined by the automated parameterization procedure. On the other hand, the kinetic parameters for the electrolyte are well studied and documented, and therefore we adopted their values directly from the literature.<sup>131</sup>

The next subcategory is of thermodynamic parameters, which includes parameters such as the equilibrium potential or the OCV,  $U_\psi$ , and the maximum concentration,  $c_{p,\psi}^{max}$ , for the active material, as well as the thermodynamic factor,  $\left(1 + \frac{\partial \ln(f_{\pm,\psi})}{\partial \ln(c_{e,\psi})}\right)$ , for the electrolyte. Although the thermodynamic parameters do not directly determine the fast-charging performance of the electrode, they can exacerbate the existing kinetic limitations in the system. For instance, if  $U_\psi$  has one or more plateaus where it is nearly constant with respect to the state of charge (SOC), it can lead to highly inhomogeneous distribution of the reaction current density, which can severely reduce the accessible capacity under high C-rate conditions.<sup>23,104,132,133</sup> However, this effect is only observed when transport limitations are present in the electrolyte and active material. In their absence, the plateaus in  $U_\psi$  do not affect the accessible capacity (see Figure 4.14 and the associated text in the Section 4.7).

We experimentally obtained  $U_\psi$  for both electrodes by performing slow (C/33) charging of a three-electrode cell. Furthermore, we obtained  $c_{p,\psi}^{max}$  through the automated parameterization procedure (explained later in Section 4.4.3) because of two reasons. First, the density of the active materials used in this study were not accurately known (only the tap density of the powder was provided by the supplier). Second, a wide range of values for  $c_{p,\psi}^{max}$  is reported in the literature. For

instance, the reported maximum Li concentration in a carbon electrode ranges from 16,100 mol/m<sup>3</sup><sup>134,135</sup> to ~31,000 mol/m<sup>3</sup><sup>136,137</sup> in the literature. The discrepancy originates from the fact that two different specific capacities (theoretical and practical) are used to convert the voltage vs. capacity data for  $U_\psi$  to the voltage vs. Li-site fraction data, which is required for the Newman model. However, the information regarding which specific capacity was used in the analysis is often not provided. This shows the importance of reporting all the information about the materials, processing, and testing conditions used in such studies. Finally, the thermodynamic factor for the electrolyte was obtained from the literature.<sup>131</sup>

#### ***4.4.2 Separator parameters***

The parameter categorization for the separator is the same as that for the electrodes, except for the fact that the separator is electronically insulating and has no active material. For high fast-charging-performance, a separator with high  $\epsilon_s$ , low  $\tau_s$  (and therefore, high  $D_{eff,s}$  and  $\kappa_{eff,s}$ ), and low  $L_s$  is required while ensuring the mechanical strength against Li dendrite penetration and high electronic insulation.<sup>138</sup> Such a design would also enhance the energy density of the battery because it reduces the weight of the electrochemically inactive components. The structural parameters were measured experimentally, except for  $\chi_s$ , which was obtained using the automated parameterization procedure (described in Section 4.4.3) due to the reasons discussed above for the electrodes. Since the material parameters for the separator are only related to the electrolyte, they are obtained from the literature.<sup>131</sup> Note that the electrolyte parameters are individually defined in different domains to ensure the model's applicability to a wide variety of Li-ion battery designs, including, for example, solid-state batteries, in which the separator and electrodes could have different electrolytes.

#### 4.4.3 Automated parameterization procedure

To determine the remaining model parameters, we employed an ML algorithm based on particle swarm optimization (PSO).<sup>99,100</sup> We selected PSO because of two reasons. First, the runtime of PSO is independent of the number of unknown parameters, and there are many in this case. Second, since PSO tracks both local and global optimum at every iteration, the probability of its convergence to a local optimum can be reduced if a sufficiently large swarm size is used. We note that other optimization algorithms such as genetic algorithms<sup>139–141</sup> or the algorithm proposed by Huang et al.<sup>142</sup> can also be used to implement the automated parameterization procedure. However, a comparative analysis of these algorithms is beyond the scope of this study. We also note that our implementation of the algorithm is similar to the work of Arunachalam et al.<sup>143</sup> As in that work, we implemented PSO in MATLAB and used COMSOL to solve the Newman model. The interface between the two software was managed using COMSOL LiveLink for MATLAB. For an individual C-rate, the error used in the objective function for PSO is defined as the integral of the square of voltage difference between the experimental result,  $V_m^{exp.}$ , and the simulated result,  $V_m^{sim.}$ , with respect to the normalized accessible capacity,  $\hat{Q}_m$ . The objective function,  $\hat{e}_T$ , is then obtained as the sum of errors for all C-rates, which are indexed using  $m$ :

$$\hat{e}_T = \sum_m \int_0^1 (V_m^{exp.} - V_m^{sim.})^2 d\hat{Q}_m. \quad (4.20)$$

Next, we discuss our implementation of PSO. Figure 4.5 shows the flowchart for the PSO algorithm used in this work. Our implementation is based on the work of Clerc et al.,<sup>99</sup> which is a modified version of the original algorithm developed by Kennedy et al.<sup>100</sup> Clerc et al.<sup>99</sup> suggested the use of a constriction coefficient,  $\kappa$ , for calculating the personal ( $c_1$ ) and social ( $c_2$ ) acceleration

coefficients instead of the choice of  $c_1 = c_2 = 2$  in Ref. 100. The relations between the acceleration and constriction coefficients are listed in Table 4.2, along with their values.

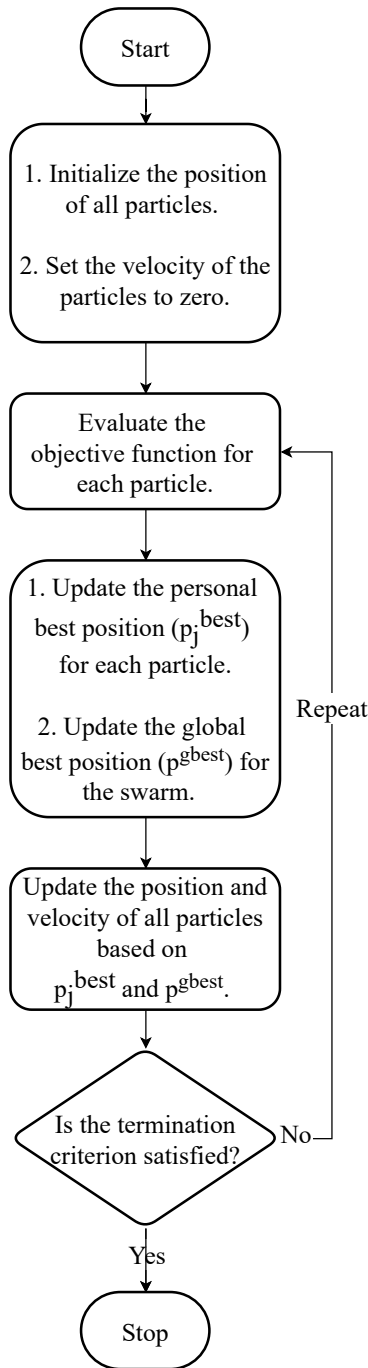


Figure 4.5. Flow chart showing the PSO algorithm. Reproduced with permission from Ref. 24. Copyright 2023, the authors. Published by Elsevier B.V.

Table 4.2. PSO hyperparameters and their values.<sup>99</sup> Reproduced with permission from Ref. 24. Copyright 2023, the authors. Published by Elsevier B.V.

Parameter	Value
$\kappa$	1
$\varphi_1$	2.05
$\varphi_2$	2.05
$\varphi$	$\varphi_1 + \varphi_2 = 4.1$
$\aleph$	$\frac{2\kappa}{ 2 - \varphi - \sqrt{(\varphi^2 - 4\kappa)} } = 0.7298$
$w$	$\aleph = 0.7298$
$c_1$	$\aleph\varphi_1 = 1.4962$
$c_2$	$\aleph\varphi_2 = 1.4962$

The position coordinates for each particle are initialized using random numbers obtained from a uniform distribution between minimum and maximum values of the model parameters (using the function *unifrnd* in MATLAB<sup>®</sup>), while the velocity is set to zero. These values are provided for each parameter in Table 4.3. Subsequently, in every iteration, the velocity and position of each particle is updated as follows.

$$v_j^{i+1} = wv_j^i + c_1 \times Y \circ (p_j^{best} - p_j^i) + c_2 \times Y \circ (p^{gbest} - p_j^i), \quad (4.21)$$

$$p_j^{i+1} = p_j^i + v_j^{i+1}, \quad (4.22)$$

where  $Y$  is a vector of random numbers between 0 and 1 with size equal to the number of unknown parameters,  $v$  and  $p$  are vectors (having a length equal to the number of unknown parameters) that represent the particle velocity and position, respectively. The symbol  $\circ$  represents the Hadamard product (elements wise multiplication) between the vectors. The subscript  $j$  represents the particle number and the superscript  $i$  represents the iteration number; and the variables  $p_j^{best}$  and  $p^{gbest}$



represent the personal best position for the  $j^{th}$  particle and global best position for the swarm (i.e., with minimum value of the objective function), respectively. Note that these positions may not change in every iteration. We also note that both the velocity and position for each particle are restricted to a predetermined range, which is individually set for each parameter. This is done to avoid unphysical values for the parameters like negative reaction rate constants or diffusion coefficients (for Fickian diffusion). The lower and upper bounds for each parameter, denoted by  $X_l$  and  $X_u$ , respectively, are listed in Table 4.3. Note that the range for each parameter is set such that it encompasses the literature-reported values, as listed in Table 4.3. Note that  $D_{p,a}^{coeff}$  is a prefactor, which is used to scale the literature reported function of Li diffusivity in graphite shown in Figure 4.12 in Section 4.7, i.e.,  $D_{p,a} = D_{p,a}^{coeff} \times D_s$ . The minimum and maximum velocity are set equal to  $-0.5(X_u - X_l)$  and  $0.5(X_u - X_l)$ , respectively.

Table 4.3. The minimum and maximum values set for each parameter obtained using the PSO algorithm. Reproduced with permission from Ref. 24. Copyright 2023, the authors. Published by Elsevier B.V.

Parameter	Lower Bound ( $X_l$ )	Upper Bound ( $X_u$ )
$D_{p,a}^{coeff}$	$1 \times 10^{-3}$	1
$c_{p,a}^{max}$	$2 \times 10^4$	$3.5 \times 10^4$
$\chi_a$	$1 \times 10^{-3}$	$3 \times 10^{-1}$
$k_a$ (m/s)	$1 \times 10^{-13}$	$1 \times 10^{-9}$
$\rho_a$ ( $\Omega\text{m}^2$ )	$1 \times 10^{-8}$	$1 \times 10^{-4}$
$D_{p,c}$ ( $\text{m}^2/\text{s}$ )	$1 \times 10^{-16}$	$1 \times 10^{-12}$
$c_{p,c}^{max}$	$4 \times 10^4$	$6 \times 10^4$
$\chi_c$	$1 \times 10^{-3}$	$3 \times 10^{-1}$
$k_c$ (m/s)	$1 \times 10^{-14}$	$1 \times 10^{-10}$
$\rho_c$ ( $\Omega\text{m}^2$ )	$1 \times 10^{-3}$	1
$\chi_s$	$1 \times 10^{-3}$	$6 \times 10^{-1}$

To train the ML model, we needed experimental data. Dr. Kuan-Hung Chen and Prof. Neil Dasgupta provided this data in the form of voltage vs. capacity curves for galvanostatic charging of the control anode (the unmodified anode design) at six C-rates (0.1C, 0.5C, 1C, 2C, 4C, and 6C). Thus, this data for the control anode was used as the *training* dataset. The simulated results obtained using the automatically identified parameters are compared with the experimental results for the anode in the control cell in Figure 4.6a. As can be seen, the two datasets match closely with each other. The corresponding evolution of the objective function is provided in Figure 4.7 (blue curve with the left y-axis). Next, we performed simulations for galvanostatic charging of the HOLE anode to validate the identified parameters. Therefore, the data for the HOLE anode served as the *test* dataset. We note that the ratios between the in-plane and through-plane values of  $D_{eff,a}$  and  $\kappa_{eff,a}$  were obtained manually for the HOLE anode because the performance of the control cell is insensitive to the anisotropy in the electrode tortuosity. The simulated and experimental results are compared in Figure 4.6b for the HOLE anode. The close match between the two datasets validates the trained ML model and highlights the prediction accuracy of the trained model when accounting for a change in the electrode design. Moreover, it shows that only the 1D form of the Newman model is sufficient for the parameterization purpose (except for the in-plane value of the effective transport properties), which is much faster to solve than the 3D form.

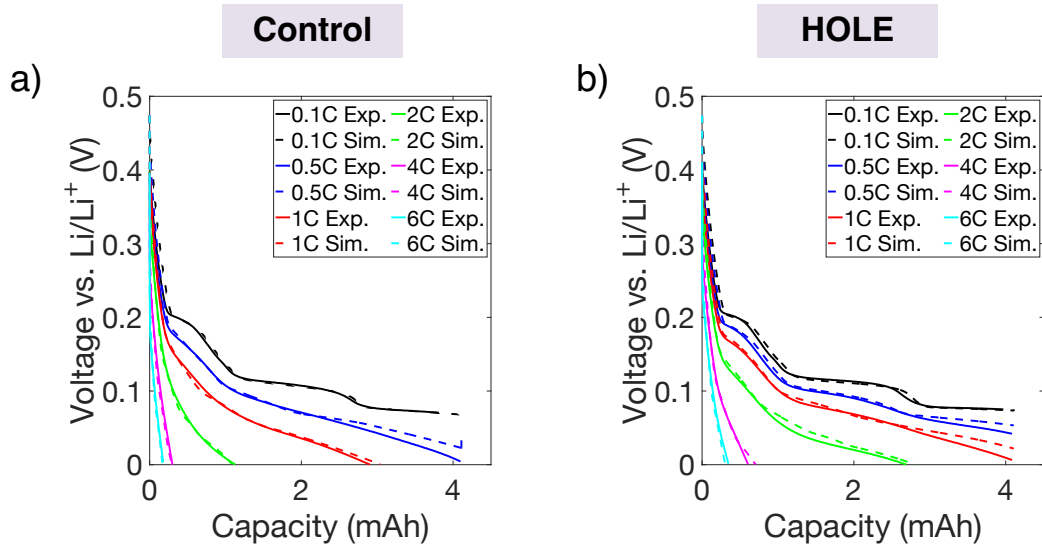


Figure 4.6. Comparison between the experimental and simulated voltage traces for the anode in the (a) control cell and (b) HOLE cell (with the HOLE patterned anode). The experimental data are shown in solid curves, while the simulation data are shown with dashed curves. The data show six rates from 0.1C (black) to 6C (cyan). Reproduced with permission from Ref. 24. Copyright 2023, the authors. Published by Elsevier B.V.

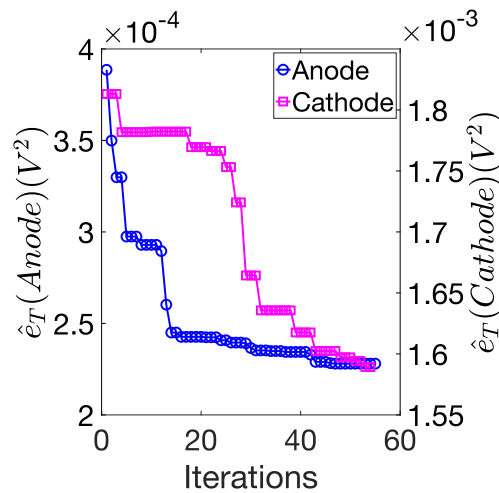


Figure 4.7. The evolution of the objective function obtained for the anode and the cathode in the control cell (with unmodified electrodes). The error for the anode is on the left y-axis, and that for the cathode is on the right y-axis. Reproduced with permission from Ref. 24. Copyright 2023, the authors. Published by Elsevier B.V.

To further demonstrate the efficacy of the ML algorithm, we applied it to the cathodes in the control and HOLE cells and provided the results in Figure 4.8. The evolution of the objective

function for the cathode in the control cell is provided in Figure 4.7 (magenta plot with the right y-axis). Following the same approach as the anodes, the measurements for the cathode in the control and HOLE cells were used as the training and test datasets, respectively. As can be seen, the simulated curves match well with the experimental measurements for both the cells. The final set of parameters identified for both the anode and the cathode in this section are listed in Table 4.4 and Table 4.5, respectively, along with their sources and a comparison with the literature reported values (where available). The values of the remaining model parameters are listed in Table 4.6. In Section 4.5, we use the model to investigate the effect of the HOLE architecture on the fast-charging performance of the graphite. Subsequently, we discuss the simulations-based optimization of HOLE design for fast-charging performance in the next chapter.

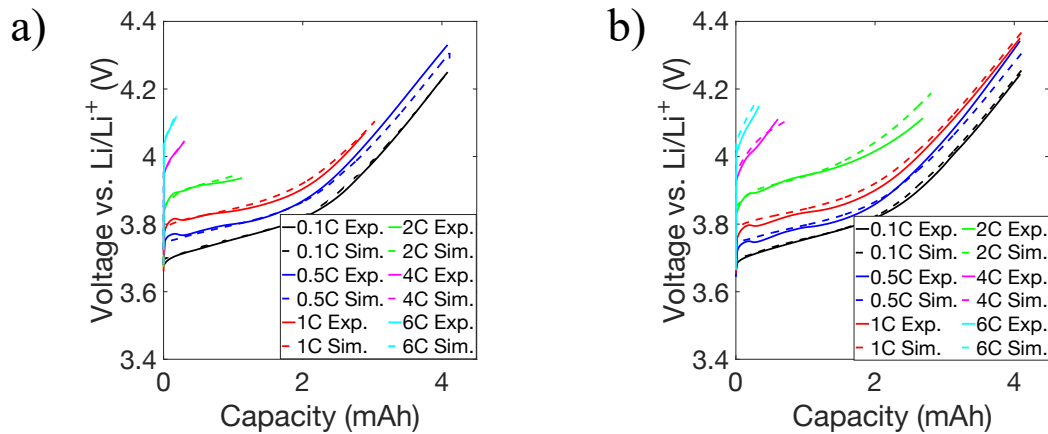


Figure 4.8. Comparison between the experimental and simulated voltage traces for the cathode in the (a) control cell and (b) HOLE cell (with the HOLE patterned anode). The experimental data are shown in solid curves, while the simulation data are shown with dashed curves. The data show six rates from 0.1C (black) to 6C (cyan). Reproduced with permission from Ref. 24. Copyright 2023, the authors. Published by Elsevier B.V.

Table 4.4. Anode parameter values identified and used in this work, along with their sources and comparison with the ranges of values surveyed from the literature. Reproduced with permission from Ref. 24. Copyright 2023, the authors. Published by Elsevier B.V.

Parameters	Values	Units	Sources	Range of values in literature (if available)
Thickness ( $L_a$ )	$6.8 \times 10^{-5}$	m	Experiment	--
Particle radius ( $R_{p,a}$ )	$4.06 \times 10^{-6}$	m	Experiment	--
Electrolyte volume fraction ( $\varepsilon_a$ )	$3.132 \times 10^{-1}$	--	Experiment	--
Active material volume fraction ( $\varepsilon_{p,a}$ )	$6.456 \times 10^{-1}$	--	Experiment	--
Reaction rate constant ( $k_a$ )	$1.824 \times 10^{-10}$	m/s	Automated parameterization	$1.7 \times 10^{-11}$ – $1.5 \times 10^{-10}$ m/s <sup>137,144–147</sup>
Max Li concentration in graphite ( $c_{p,a}^{max}$ )	$2.95 \times 10^4$	mol/m <sup>3</sup>	Automated parameterization	$3.054 \times 10^4$ – $3.192 \times 10^4$ mol/m <sup>3</sup> <sup>137,144–146</sup>
Initial Li concentration in graphite ( $c_{p,a} _{t=0}$ )	$1.77 \times 10^1$	mol/m <sup>3</sup>	Assumed	--
Li diffusion coefficient in graphite ( $D_{p,a}$ )	$0.4252 \times D_s$	m <sup>2</sup> /s	Automated parameterization	--
Effective Li-ion diffusion coefficient ( $D_{eff,a}$ )	$2.15 \times 10^{-2} \times \begin{bmatrix} 1.2D_L & 0 & 0 \\ 0 & 1.2D_L & 0 \\ 0 & 0 & D_L \end{bmatrix}$	m <sup>2</sup> /s	Automated parameterization (except for the ratio between the in-plane and through-plane values)	--
Effective electrical conductivity ( $\sigma_{eff,a}$ )	$4.43 \times 10^{-2} \times \sigma_{s,Carbon}$	S/m	Automated parameterization	$1 \times 10^1$ – $2.2 \times 10^2$ S/m <sup>134,137,144</sup>
Effective Li-ion conductivity ( $\kappa_{eff,a}$ )	$2.15 \times 10^{-2} \times \begin{bmatrix} 1.2\kappa_L & 0 & 0 \\ 0 & 1.2\kappa_L & 0 \\ 0 & 0 & \kappa_L \end{bmatrix}$	S/m	Automated parameterization (except for the in-plane to through-plane ratio)	--
Initial Li-ion concentration in the electrolyte ( $c_{e,a} _{t=0}$ )	$1 \times 10^3$	mol/m <sup>3</sup>	Experiment	--
Area specific resistance of the SEI layer, ( $\rho_a$ )	$3.3 \times 10^{-7}$	$\Omega\text{m}^2$	Automated parameterization	--

Table 4.5. Cathode parameter values identified and used in this work, along with their sources and comparison with the ranges of values surveyed from the literature. Reproduced with permission from Ref. 24. Copyright 2023, the authors. Published by Elsevier B.V.

Parameters	Values	Units	Sources	Range of values in literature (if available)
Thickness ( $L_c$ )	$6 \times 10^{-5}$	m	Experiment	--
Particle radius ( $R_{p,c}$ )	$4.65 \times 10^{-6}$	m	Experiment	--
Electrolyte volume fraction ( $\varepsilon_c$ )	$3.411 \times 10^{-1}$	--	Experiment	--
Active material volume fraction ( $\varepsilon_{p,c}$ )	$6.062 \times 10^{-1}$	--	Experiment	--
Reaction rate constant ( $k_c$ )	$1.545 \times 10^{-11}$	m/s	Automated parameterization	$1 \times 10^{-11} - 9.2 \times 10^{-11}$ m/s <sup>137,144,145</sup>
Max Li concentration in NMC-532 ( $c_{p,c}^{max}$ )	$5.018 \times 10^4$	mol/m <sup>3</sup>	Automated parameterization	$4.7408 \times 10^4 - 4.858 \times 10^4$ mol/m <sup>3</sup> <sup>137,144,145</sup>
Initial Li concentration in NMC-532 ( $c_{p,c} _{t=0}$ )	$4.9176 \times 10^4$	mol/m <sup>3</sup>	Assumed	--
Li diffusion coefficient in NMC-532 ( $D_{p,c}$ )	$1.0825 \times 10^{-14}$	m <sup>2</sup> /s	Automated parameterization	$2 \times 10^{-16} - 3 \times 10^{-14}$ m <sup>2</sup> /s <sup>137,144,148-150</sup>
Effective Li-ion diffusion coefficient ( $D_{eff,c}$ )	$3.47 \times 10^{-2} \times D_L$	m <sup>2</sup> /s	Automated parameterization	--
Effective electrical conductivity ( $\sigma_{eff,c}$ )	$6.17 \times 10^{-2} \times \sigma_{s,NMC}$	S/m	Automated parameterization	$1 \times 10^1 - 7 \times 10^1$ S/m <sup>137,144,145</sup>
Effective Li-ion conductivity ( $\kappa_{eff,c}$ )	$3.47 \times 10^{-2} \times \kappa_L$	S/m	Automated parameterization	--
Initial Li-ion concentration in the electrolyte ( $c_{e,c} _{t=0}$ )	$1 \times 10^3$	mol/m <sup>3</sup>	Experiment	--
Area specific resistance of the SEI layer, ( $\rho_c$ )	$1.65 \times 10^{-2}$	$\Omega m^2$	Automated parameterization	--

Table 4.6. Values of the remaining model parameters identified and used in this work, along with their sources and comparison with the ranges of values surveyed from the literature. Reproduced with permission from Ref. 24. Copyright 2023, the authors. Published by Elsevier B.V.

Parameters	Values	Units	Sources	Range of values in literature (if available)
<b>Intrinsic material properties</b>				
Diffusion coefficient of the electrolyte, $D_L$	$(2.2 \times 10^{-10} - 4.24 \times 10^{-10})$ (Figure 4.13a)	m <sup>2</sup> /s	Literature <sup>151</sup>	--
Ionic conductivity of the electrolyte, $\kappa_L$	$(1 \times 10^{-6} - 9.5 \times 10^{-1})$ (Figure 4.13b)	S/m	Literature <sup>151</sup>	--
Transference number in the electrolyte, $t_+^0$	$1.1 \times 10^{-1} - 3.7 \times 10^{-1}$ (Figure 4.13c)	--	Literature <sup>151</sup>	--
Activity coefficient of the electrolyte, $\frac{\partial \ln(f_{\pm})}{\partial \ln(c_L)}$	0 – 2.5 (Figure 4.13d)	--	Literature <sup>151</sup>	--
Li-ion diffusion coefficient in graphite, $D_s$	$(6.6 \times 10^{-16} - 4.2 \times 10^{-13})$ (Figure 4.12)	m <sup>2</sup> /s	Literature <sup>130</sup>	$1 \times 10^{-15} - 1 \times 10^{-9}$ m <sup>2</sup> /s <sup>129</sup>
Electronic conductivity of NMC, $\sigma_{s,NMC}$	$6.8 \times 10^1$	S/m	Literature <sup>136</sup>	--
Electronic conductivity of graphite, $\sigma_{s,Carbon}$	$1 \times 10^2$	S/m	Literature <sup>147</sup>	--
<b>Separator</b>				
Thickness ( $L_s$ ) – three-electrode cell	$2.2 \times 10^{-4}$	m	Experiment	--
Thickness ( $L_s$ ) – pouch cell	$1.2 \times 10^{-5}$	m	Experiment	--
Volume fraction of electrolyte ( $\varepsilon_s$ )	$7.1 \times 10^{-1}$	--	Experiment	--
Effective Li-ion diffusion coefficient ( $D_{eff,s}$ )	$5.5 \times 10^{-1} \times D_L$	m <sup>2</sup> /s	Automated parameterization	--
Effective Li-ion conductivity ( $\kappa_{eff,s}$ )	$5.5 \times 10^{-1} \times \kappa_L$	S/m	Automated parameterization	--
Initial Li-ion concentration in the electrolyte ( $c_{e,s} _{t=0}$ )	$1 \times 10^3$	mol/m <sup>3</sup>	Experiment	--
<b>Other</b>				
Temperature	$2.98 \times 10^2$	K	Experiment	--
IC current density (determined based on the cathode loading)	$2.326 \times 10^1$	A/m <sup>2</sup>	Experiment	--
Volume retention after laser patterning ( $\Omega_R$ )	0.895	--	Experiment	--

Inter-channel spacing ( $d_h$ )	$8.5 \times 10^{-5}$	m	Experiment	--
Top radius of the channel (at the anode/separator interface)	$2.15 \times 10^{-5}$	m	Experiment	--
Bottom radius of the channel (at the anode/separator interface)	$6 \times 10^{-6}$	m	Experiment	--

#### 4.5 Simulation results for the effect of laser patterning on the fast-charging performance of graphite electrodes

Figure 4.9c compares the simulated voltage (vs. a Li reference) vs. time curves for the control and HOLE anodes during 4C charging. The simulation for each cell was terminated when the anode voltage reached 0 V. As expected, the HOLE anode was able to maintain a voltage above 0 V for a longer period of charging time than the control anode (364 s vs. 125 s), which shows that the polarization at the HOLE anode is lower than that in the control anode. This decrease in the polarization is facilitated by improved access of Li-ions to graphite particles in the bulk of the HOLE anode through the channel design. Figure 4.9a and Figure 4.9b compare the Li-ion concentration evolution in the electrolyte phase of the control and HOLE anodes. As shown in the figures, Li-ion concentration far from the anode/separator interface in the HOLE anode (Figure 4.9b) is higher than that in the control anode (Figure 4.9a) at all times. Due to the improved Li-ion transport, a reduction in the local Li-ion concentration near the anode/separator interface can be seen in the HOLE anode compared to the control anode.



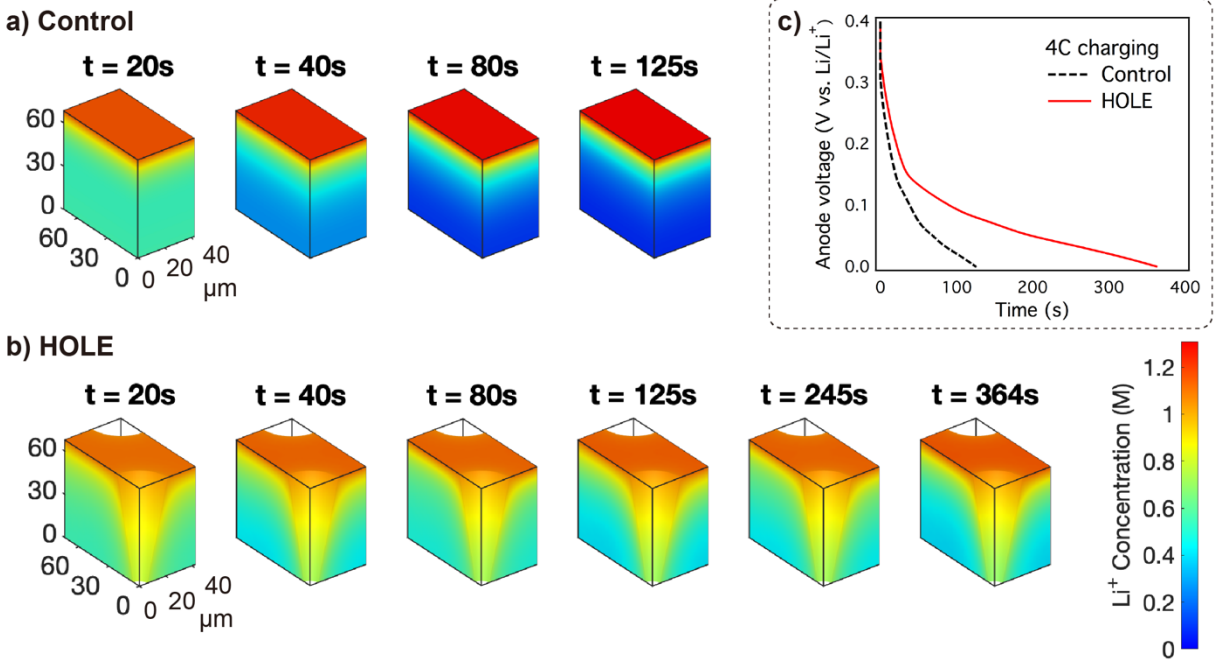


Figure 4.9. Evolution of Li-ion concentration in the electrolyte phase of the (a) control graphite anode at  $t = 20, 40, 80,$  and  $125\text{ s}$ , (b) HOLE graphite anode at time  $t = 20, 40, 80, 125, 245,$  and  $364\text{ s}$  during 4C charging. The color indicates the Li-ion concentration according to the color bar on the right. The anode/separator interface is at the top of the anodes shown in (a) and (b). (c) Simulated voltage response of the anode in the control cell (dashed, black line), and in the HOLE cell (solid, red line). Reproduced with permission from Ref. 22. Copyright 2020, Elsevier B.V.

Due to the ionic transport limitation in the control anode, electrochemical reaction is concentrated near the anode/separator interface, as shown in Figure 4.10a. This intensification of the reaction near the anode/separator interface causes the corresponding anode volume to lithiate faster than the entire bulk. Since the diffusion of Li-ions into the control anode is limiting, and the surface of the graphite particles near the anode/separator interface is fully lithiated, if the charging is continued, the incoming Li-ions will be highly likely to plate on the anode/separator interface. Therefore, the control anode has a high propensity for Li plating. The HOLE anode, on the other hand, experiences a much more homogenous distribution of the reaction in its bulk, as shown in Figure 4.10b. Thus, lithiation occurs more uniformly in the HOLE anode instead of being limited

to the volume near the anode/separator interface. If the charging is continued below 0 V, the incoming Li-ions will have direct pathways through the channels to penetrate deeper into the thickness of the anode and react with the unreacted active material even when the surface of the graphite particles near the anode/separator is fully lithiated. Thus, the introduction of channels facilitates a reduction in the propensity for Li plating in the HOLE anode as compared to the control anode during fast charging, as well as maintaining the anode voltage above 0 V for a longer period.

The ripples in the reaction rate in the anode bulk arise due to the form of the open circuit potential of graphite (specifically, plateaus and the transitions between the plateaus; see Figure 4.11 and the associated text in Section 4.7), along with the electrostatic potential and the concentration gradients in the electrolyte phase. The small noise in the reaction rate magnitude at the anode/separator interface for the HOLE anode is a numerical artifact that disappears when an extremely fine mesh is used and does not alter the evolution of the physical quantities presented here (as confirmed by direct testing). We note that results provided in Figure 4.9 and Figure 4.10 correspond to the parameter values set before the automated parameterization was implemented.<sup>22</sup> Nonetheless, the inference made here is still valid even for the latest parameter set, as noted in the next chapter.

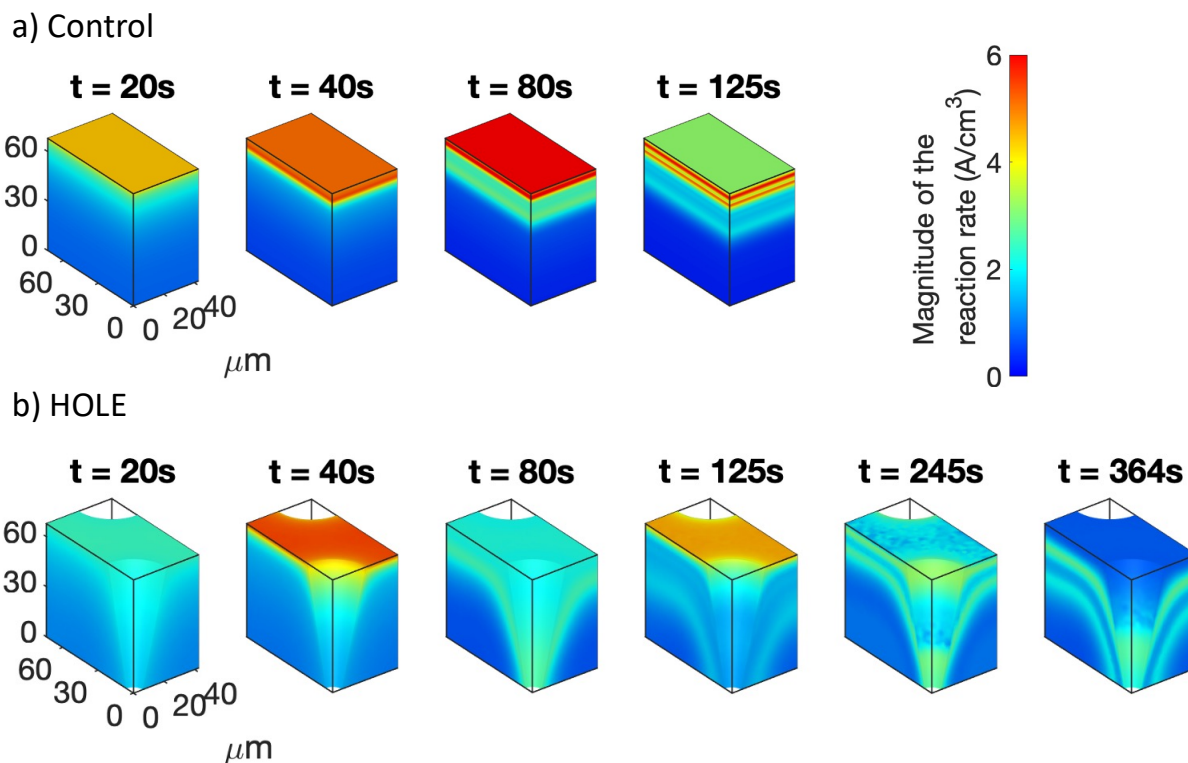


Figure 4.10. Evolution of the magnitude of reaction rate in the (a) control graphite anode at  $t = 20, 40, 80,$  and  $125\text{ s}$ , (b) HOLE graphite anode at time  $t = 20, 40, 80, 125, 245,$  and  $364\text{ s}$  during  $4\text{C}$  charging. The color indicates the magnitude of the reaction rate in  $\text{A}/\text{cm}^3$  according to the color bar on the right. The anode/separator interface is at the top of the anodes shown in (a) and (b). Reproduced with permission from Ref. 22. Copyright 2020, Elsevier B.V.

#### 4.6 Chapter 4 Summary

In this chapter, we employed continuum-scale modeling to develop mechanistic understanding of the effect of the HOLE architecture on the fast-charging performance of thick graphite anodes. First, we summarized the experimental results (obtained by Kuan-Hung Chen (Dasgupta Group) and Min Ji Namkoong (Sakamoto Group)), which showed that industrially relevant pouch cells ( $> 2\text{ Ah}$ ) based on the HOLE architecture retained  $> 97\%$  and  $> 93\%$  capacity after 100 cycles of  $4\text{C}$  and  $6\text{C}$  fast-charge cycling, respectively. While the corresponding retention in cells with the unpatterned electrodes was only  $69\%$  and  $59\%$ . We then described model

equations and the associated parameters in detail, along with a workflow to identify those parameters. The workflow includes a categorization of the model parameters, identification of the source(s) for each parameter, and development of an automated parameterization procedure based on the particle swarm optimization (PSO) algorithm. We used the three-electrode voltage vs. capacity measurements obtained at six different C-rates for the control and HOLE cells to calibrate and validate the parameter set, respectively. Subsequently, based on the simulation results, we established that the HOLE architecture enables fast charging in thick graphite anode by enhancing the Li-ion transport and the homogeneity of the reaction distribution within the anode volume. Consequently, it reduces the intensification of the electrochemical reaction near the anode/separator interface, which mitigates Li plating. In the next chapter, we extend this work by examining the effect of the HOLE design parameters using the parameterized model and identify the optimal HOLE geometry for superior fast-charging performance. Furthermore, we reduce the computational cost associated with the optimization by developing a semi-analytical framework based on the second Damköhler number.

## **4.7 Chapter 4 Appendix**

### ***Composition-dependent material properties***

All the composition-dependent material properties used in the model are shown in Figure 4.11 to Figure 4.14. Kuan-Hung Chen provided the open circuit voltage (OCV) measurements for the graphite and NMC electrodes by galvanostatically lithiating them at C/33.

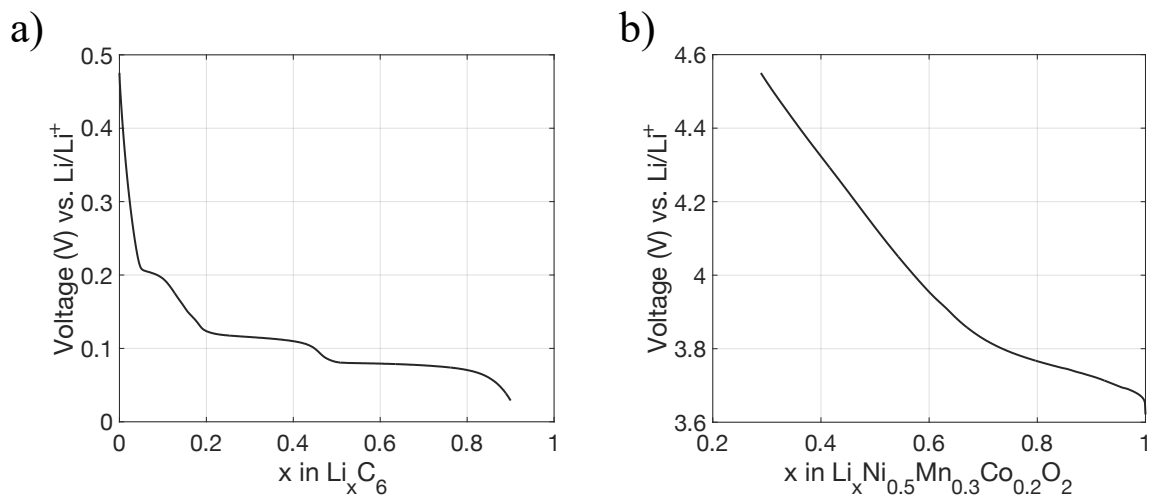


Figure 4.11. The experimentally obtained open-circuit voltage as a function of the lithium site fraction for (a) graphite and (b)  $\text{LiNi}_{0.5}\text{Mn}_{0.3}\text{Co}_{0.2}\text{O}_2$  (NMC-532). Reproduced with permission from Ref. 24. Copyright 2023, the authors. Published by Elsevier B.V.

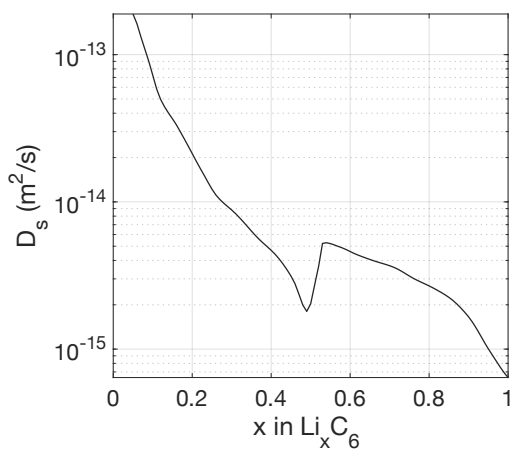


Figure 4.12. Diffusion coefficient of lithium in graphite as a function of the lithium site fraction.<sup>130</sup> Reproduced with permission from Ref. 24. Copyright 2023, the authors. Published by Elsevier B.V.

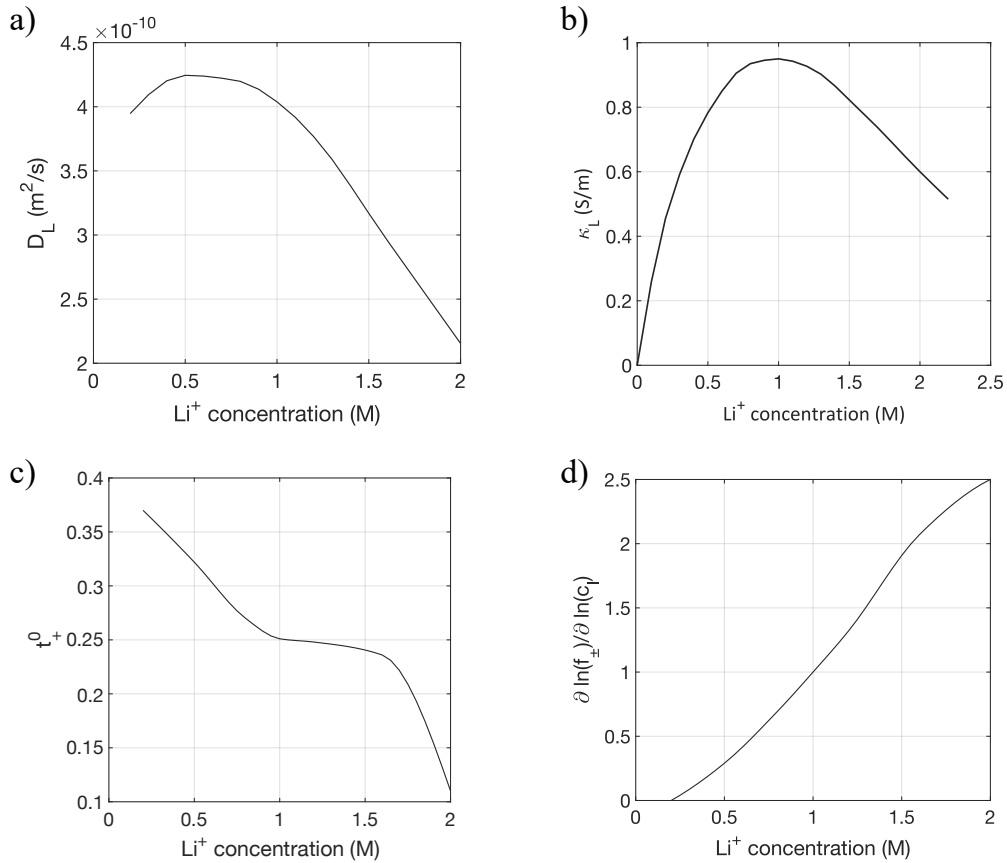


Figure 4.13. The intrinsic properties of the electrolyte as a function of Li-ion concentration. Diffusion coefficient, (b) ionic conductivity, (c) transference number of Li-ion, and (d) the dependence of the salt activity coefficient on the electrolyte concentration.<sup>151</sup> Reproduced with permission from Ref. 24. Copyright 2023, the authors. Published by Elsevier B.V.

### ***Results with no mass-transport limitation***

To show that the presence of peaks in the reaction current density (RCD) distribution do not affect the accessible capacity during fast charging in the absence of any mass transport limitation, we performed a 4C simulation for the control anode without such limitations. We artificially set high values of the effective electrolyte diffusivity (and conductivity) and the Li diffusion in graphite in the control anode; the electrolyte properties were set 14.5 times higher, and the solid diffusivity was set 1000 times higher than the values used in Section 4.5. The simulated results are compared with those for the control anode (same as Section 4.5) in Figure 4.14a. Two

insights are obtained from the comparison. First, despite the presence of inhomogeneity in RCD, the control anode with no mass transport limitations achieves the fully charged state (an SOC value of 1) at 4C, with the final voltage of  $\approx 0.091$  V, which is well above the point where Li plating is possible. As a reference, the baseline control anode reached an SOC of 0.167. Second, having mass transport limitations make the peaks in RCD taller (as noted by the increased value) and narrower (as noted by the decrease in penetration depth of the peak).

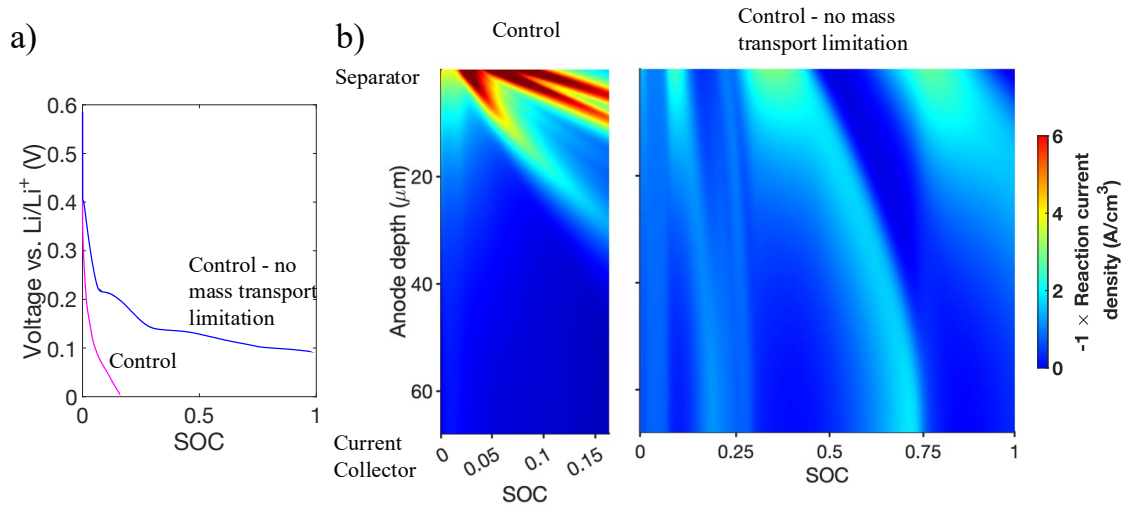


Figure 4.14. (a) Comparison of the voltage vs. SOC plot for the control anode and the control anode with no mass transport limitations during 4C charging. (b) The evolution of RCD along the anode thickness for the two control anodes. The values of RCD can be found on the color bar on the right. Note that the max value on the color bar is set to 6  $\text{A/cm}^3$  for the same reason provided in the main text. Reproduced with permission from Ref. 24. Copyright 2023, the authors. Published by Elsevier B.V.

## CHAPTER 5

### Optimization of the Highly Ordered Laser-Patterned Electrode Architecture Using Continuum-Level Simulations\*

#### 5.1 Introduction: Optimal design of the laser-patterned electrode for fast charging

As explained in Chapter 4, the Highly Ordered Laser-Patterned Electrode (HOLE) architecture improves the fast-charging performance of thick graphite electrode by enhancing the Li-ion transport and the homogeneity of the reaction distribution within the electrode volume. However, there is a lack of understanding of the effect of HOLE design parameters on the fast-charging performance. Until now, only a limited number of studies have carried out such an investigation. In the report by Lauri et al.,<sup>94</sup> the authors simulated the effect of the cone angle of the HOLE channel and the misalignment of the channels in the cathode and anode on the fast-charging performance (up to 4C) of NMC-111/Graphite cells. In the report by Schweighofer et al.,<sup>96</sup> the effect of inter-channel spacing for various patterned electrode geometries (line, grid, and cylindrical channels) on the fast-discharging performance (up to 3C) of NMC-811/Graphite cells was simulated. Additionally, all the reported studies so far use the computationally expensive 3D simulations to study HOLE architectures. Thus, a theoretical framework for predicting the effect of various HOLE design parameters on the high C-rate performance of the thick electrodes is also missing.

---

\* This chapter is adapted from V. Goel et al., *Energy Storage Materials*, 57 (2023), 44<sup>24</sup>; and V. Goel et al., *MethodsX*, 8 (2021), 101425.<sup>30</sup>



In this chapter, we bridge the aforementioned knowledge gaps by investigating the effect of the HOLE architecture parameters like the inter-channel spacing at a fixed volume retention on the fast-charging performance with continuum-level simulations. Note that the parameterized model obtained in Chapter 4 is used for this work. Our results reveal that while closer (and smaller) channels improved fast-charging performance compared to those with larger spacings and diameters, there exists an optimal spacing below which the marginal gain in the performance falls rapidly. We also define the second Damköhler number,  $Da_{II}$ , as a metric to quantify the effect of the channel size/spacing on the electrode performance and to provide a metric for optimizing the HOLE design. Our results show that the optimal configuration has  $Da_{II} \approx 1$  throughout charging. Based on this finding, we develop a semi-analytical method to obtain a time-averaged value of  $Da_{II}$ , which can be used for high-throughput screening of various candidate electrode architectures, thereby reducing the computational cost of the overall optimization process.

## 5.2 Optimization of the HOLE architecture

As discussed in Chapter 4, HOLE architecture enhances fast-charging performance of thick graphite anodes by improving the homogeneity of the electrolyte concentration and reaction current density distribution within the anode. We now optimize the HOLE geometry. The geometric optimization aims to maximize the accessible capacity during 4C and 6C galvanostatic charging, with a fixed amount of electrode volume that is removed in the HOLE pattern. The results for 4C charging are presented first followed by that for 6C (Section 5.2.3). Moreover, to reduce the computational cost of the 3D simulations required for the optimization, we only consider half cells of a graphite electrode with a Li metal electrode. The details of the half-cell configuration are provided in the in Figure 5.8 and the associated text in Section 5.4.

For this study, we considered the shape of the channels to be cylindrical (instead of conical, which was considered in the results discussed in Chapter 4). This change was made to facilitate the theoretical work that will be described in Section 5.2.2. The geometry of a HOLE anode with cylindrical channels can be characterized in terms of three parameters – the inter-channel spacing,  $d_h$ ; the channel radius,  $\mu_h$ ; and the electrode volume fraction retained,  $\Omega_R$ . For a hexagonal arrangement of the channels, these parameters are related by

$$\Omega_R = 1 - \frac{2\pi}{\sqrt{3}} \left( \frac{\mu_h}{d_h} \right)^2. \quad (5.1)$$

Therefore, only two independent parameters govern the geometry of a HOLE anode. For our study, we chose  $d_h$  and  $\Omega_R$  as the independent parameters. We then set  $\Omega_R \approx 0.895$ , as mentioned in Table 4.6. By fixing the value of  $\Omega_R$ , we maintain a value of the N:P ratio for the full cell to be greater than 1, which is typical of commercial Li-ion batteries. Therefore, as in commercial LIBs, the battery capacity remains limited by the cathode, and not the anode. As a result, the HOLE architecture enables improved power density without sacrificing energy density of the battery, since the accessible cell capacity remains lower than the theoretical capacity of the anode, and thus the energy density does not change after HOLE patterning. Under these conditions,  $\mu_h$  and  $d_h$  are related as

$$\mu_h = \left( \sqrt{\frac{\sqrt{3}}{2\pi} (1 - 0.895)} \right) d_h. \quad (5.2)$$

Thus, the channel radius is directly proportional to the inter-channel spacing for a fixed  $\Omega_R$ .

Furthermore,  $d_h$  also determines the maximum distance,  $\delta_h$ , to the nearest channel wall within the electrode. This distance is of interest because it sets the time it takes for Li-ion transport from the channel wall to reach the entire electrode volume. For the hexagonal symmetry of the

channels, the furthest point from the channel walls lies at the centroid of the triangle formed by the three adjacent channel centers, as shown in Figure 5.1a. Thus,

$$\delta_h = \frac{\sqrt{3}}{3}d_h - \mu_h = 0.407d_h. \quad (5.3)$$

As seen above, the relevant design parameters for a hexagonal arrangement of the channels can be directly obtained from  $d_h$ . Therefore, to find the optimal HOLE architecture for 4C charging, we considered 10 values of  $d_h$  ranging from 15 to 235  $\mu m$ . Table 5.1 lists the values of  $d_h$  examined along with corresponding values of  $\mu_h$  and  $\delta_h$ . Here, we focus on the performance quantified by the *accessible capacity*, which is defined as the SOC achieved when the anode voltage reaches 0 V vs. Li/Li<sup>+</sup>, below which there is a risk of Li plating. We also considered a loading-adjusted control anode, which has the same loading as the HOLE anodes, and discuss its fast-charging performance in Section 5.4 (see Figure 5.9 and associated text). Note that the loading-adjusted anode is the same as the new control anode in Chapter 4 (Figure 4.2f and the associated text). Since we have previously shown (Figure 4.2f and the associated text ) that simply adjusting the loading of the control electrode to match that of the HOLE electrode does not result in a significant improvement in its performance, it does not merit further investigation.

Table 5.1. List of values of  $d_h$  used in the 4C optimization study along with corresponding values of  $\mu_h$  and  $\delta_h$ . Reproduced with permission from Ref. 24. Copyright 2023, the authors. Published by Elsevier B.V.

$d_h$ ( $\mu\text{m}$ )	$\mu_h$ ( $\mu\text{m}$ )	$\delta_h$ ( $\mu\text{m}$ )
15	2.55	6.11
25	4.25	10.18
40	6.81	16.28
55	9.36	22.39
85	14.46	34.60
115	19.57	46.81
145	24.67	59.02
175	29.77	71.23
205	34.88	83.44
235	39.98	95.65

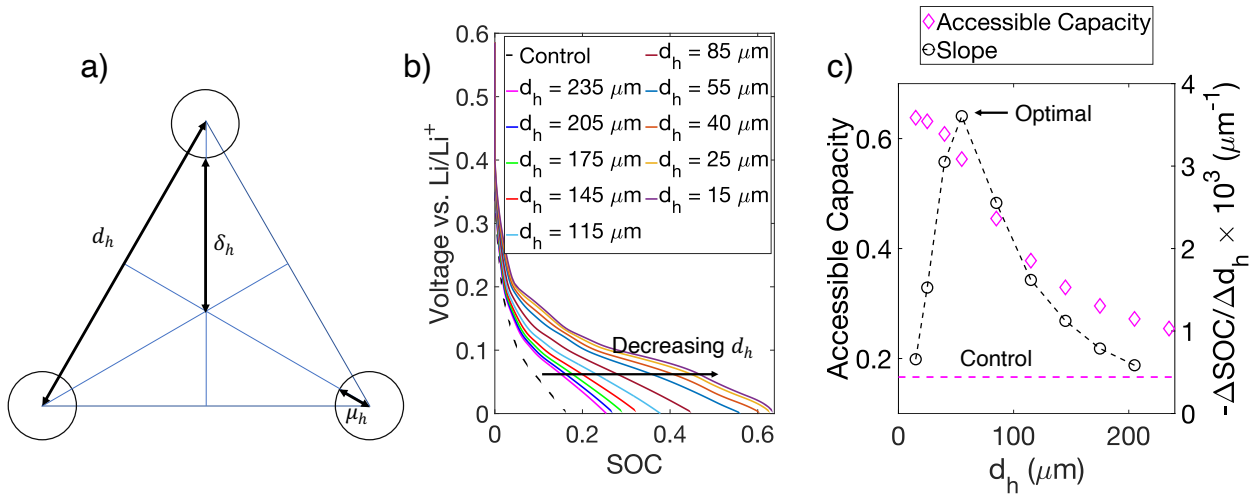


Figure 5.1. Schematic of a triangle formed by three adjacent channels, simulated voltage vs. SOC plots and the accessible capacity as a function of  $d_h$  at 4C for all HOLE configurations considered here. Schematic of a single triangle from the hexagonal arrangement of channels in the HOLE architecture. (b) Voltage vs. SOC plots for the control anode and the HOLE anodes considered in this optimization study at 4C charging. (c) Accessible capacity vs.  $d_h$  curve for the HOLE configurations (magenta diamonds, left y-axis), and the magnitude of its discrete derivate (black circles connected with a dashed line, right y-axis); the accessible capacity observed for the control anode is provided as a reference, using the magenta dashed line. The optimal configuration among the simulations conducted,  $d_h = 55 \mu\text{m}$ , is noted in (c). Reproduced with permission from Ref. 24. Copyright 2023, the authors. Published by Elsevier B.V.

Figure 5.1b and c show the anode voltage vs. SOC and the accessible capacity vs.  $d_h$ , respectively, for all  $d_h$  values (including the control anode). We also provide the magnitude of the discrete derivative of the accessible capacity vs.  $d_h$  curve on the right y-axis in Figure 5.1c, which signifies the marginal gain in the accessible capacity. As can be seen, all the HOLE configurations perform better, i.e., access a higher SOC under fast-charge conditions, than the control anode (magenta diamonds vs. magenta dashed line in Figure 5.1c). In addition, the performance of the HOLE configuration improves with decreasing  $d_h$ ; closer spaced (and smaller diameter) channels deliver better fast-charging performance than the larger-spaced (and larger diameter) channels, under the constraint of retaining a fixed volume fraction. This finding is consistent with a previous study that examined a smaller range of parameters in another system (an NCA cathode with a hard carbon anode).<sup>152</sup>

We observe that the derivative of the accessible capacity vs.  $d_h$  curve is nonmonotonic, as shown by the black curve in Figure 5.1c. The magnitude of the derivative increases up to  $d_h = 55 \mu m$ , below which it rapidly decreases. Therefore,  $d_h = 55 \mu m$  acts as the point of diminishing return, i.e., any progressive decrease in  $d_h$  leads to an increasingly smaller improvement in the accessible capacity. Mechanistically, this diminishing improvement is observed because at a sufficiently small  $d_h$  value, the transport in the electrolyte is no longer the limiting mechanism and other phenomena such as Li diffusion in graphite particles limit the charging process. We provide more insights into this diminishing return in the following sections (Sections 5.2.1). We define the  $d_h$  value corresponding to the point of diminishing return as the optimal configuration, as noted in Figure 5.1c. Thus,  $d_h = 55 \mu m$  is identified as the optimal configuration for 4C charging for  $\Omega_R \approx 0.895$  among the simulations conducted. Quantitatively, this configuration provides a 3.4 times larger value in the accessible SOC than the control anode.

We now offer additional insights into the enhancement of fast-charging performance observed above in the HOLE anodes by examining the distribution of the reaction current density (RCD),  $\xi$  (A/m<sup>3</sup>), at separate times during charging. Figure 5.2 shows the evolution of the RCD distribution in the control anode during 4C charging. The RCD is highly concentrated near the anode-separator interface throughout charging, which is associated with a large overpotential at the interface. Owing to this large overpotential, the anode reaches the cut-off voltage (0 V vs. Li/Li<sup>+</sup>) well before a full charge is completed (149.5 s vs. 900 s). On the other hand, the RCD distribution is much more uniform in the HOLE anode ( $d_h = 85 \mu\text{m}$ ), as shown in Figure 5.2. Note that the effect of the HOLE architecture on the homogeneity on the RCD and the voltage vs. SOC plot is consistent with the results presented in Figure 4.10 and the associated text.

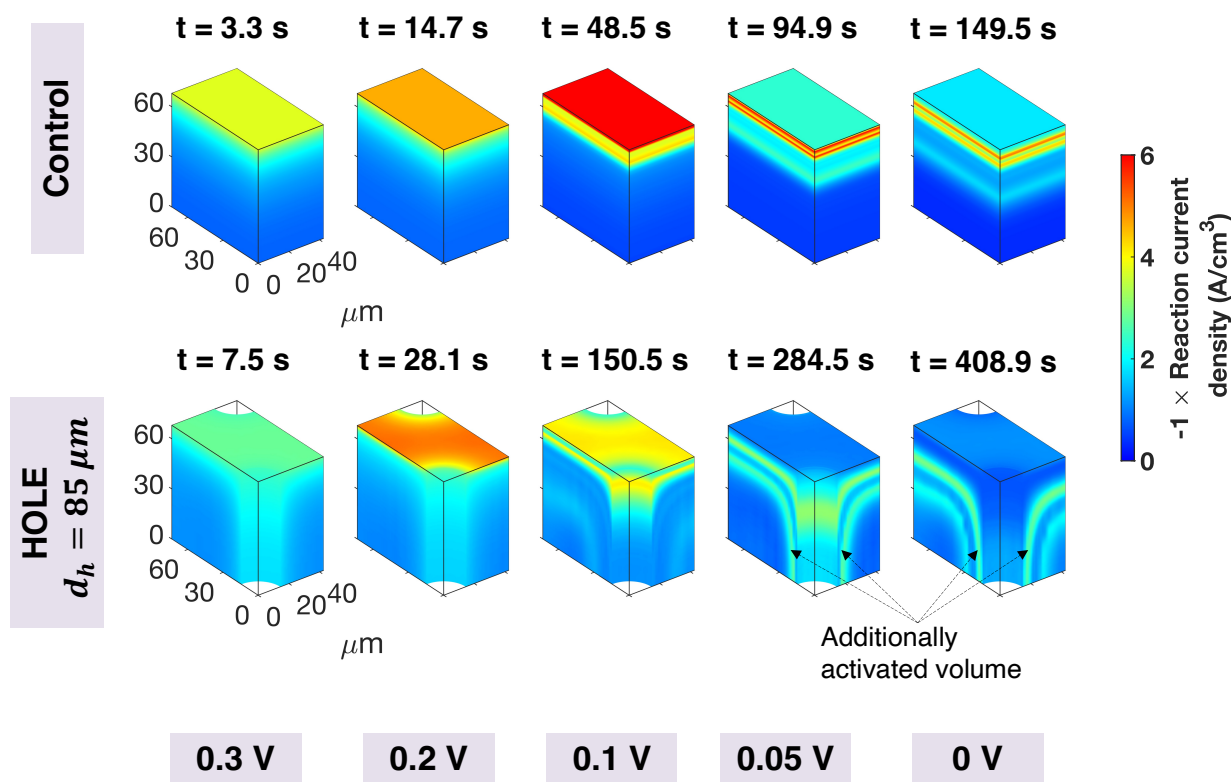


Figure 5.2. Time series of the simulated reaction current density distribution (RCD) for the control and HOLE anode ( $d_h = 85 \mu\text{m}$ ) during 4C charging. The times for the images were selected when the anode voltage is 0.3V, 0.2V, 0.1V, 0.05V, and 0V, as noted at the bottom of the figure. The color indicates the RCD value according to the color bar on the right. The maximum magnitude of the RCD observed in the control anode is  $\sim 10.7 \text{ A/cm}^3$ ; however, the maximum value of color bar is set to  $6 \text{ A/cm}^3$  to enable a better visual comparison with the HOLE anodes. Dashed arrows indicate the additional regions activated in the HOLE anode near the channel wall. Reproduced with permission from Ref. 24. Copyright 2023, the authors. Published by Elsevier B.V.

This improvement in homogeneity arises because the HOLE architecture increases the electrochemically active fraction of the anode volume in two ways. First, it activates the volume near the channel walls, as highlighted in Figure 5.2. Second, to a lesser degree, it activates the volume away from the wall by decreasing the distance over which Li ions must be transported to reach the active particles that are located far from the separator. Consequently, a more uniform distribution of the current density is achieved in the HOLE anode, allowing it to sustain 4C charging for a longer time and to reach a higher SOC than the control anode. We note that the

presence of local regions with a high RCD in the anodes studied here, such as the red bands in the control anode at  $t = 94.9\text{s}$  and the green bands in the HOLE anode at  $t = 284.5\text{s}$  and  $t = 408.9\text{s}$  in Figure 5.2, is caused by a complex interplay between thermodynamics and kinetics.<sup>22,23,133</sup> The bands originate because of the plateaus in the graphite OCV (which is the function of Li concentration in graphite; see Figure 4.11 and the associated text), and transport limitations in the electrolyte render them to be more pronounced<sup>104,132,133</sup> (further details are found in Section 4.7; see Figure 4.14 and the associated text). Hereafter, we refer to these bands as *peaks* because they are analogous to the RCD peaks observed in pseudo-1D simulations in a previous study<sup>23</sup> and later in Figure 5.5a. We discuss the effect of these peaks in detail in Section 5.2.1.

Figure 5.3 compares the RCD distribution for  $d_h = 55, 145, \text{ and } 235 \mu\text{m}$  at separate times during charging. Note that the anode voltages corresponding to these times are the same as in Figure 5.2. As can be seen, the reaction distribution is much more homogeneous for  $d_h = 55 \mu\text{m}$  than  $d_h = 235 \mu\text{m}$ , which underlies the superior performance of  $d_h = 55 \mu\text{m}$ . The details on the mesh required to sufficiently resolve the spatial distribution of the reaction current density are provided in Figure 5.10 and the associated text in Section 5.4. In the next section, we propose a metric for homogeneity of the RCD to quantify the effect of  $d_h$  on the current homogeneity and the resulting electrode performance.



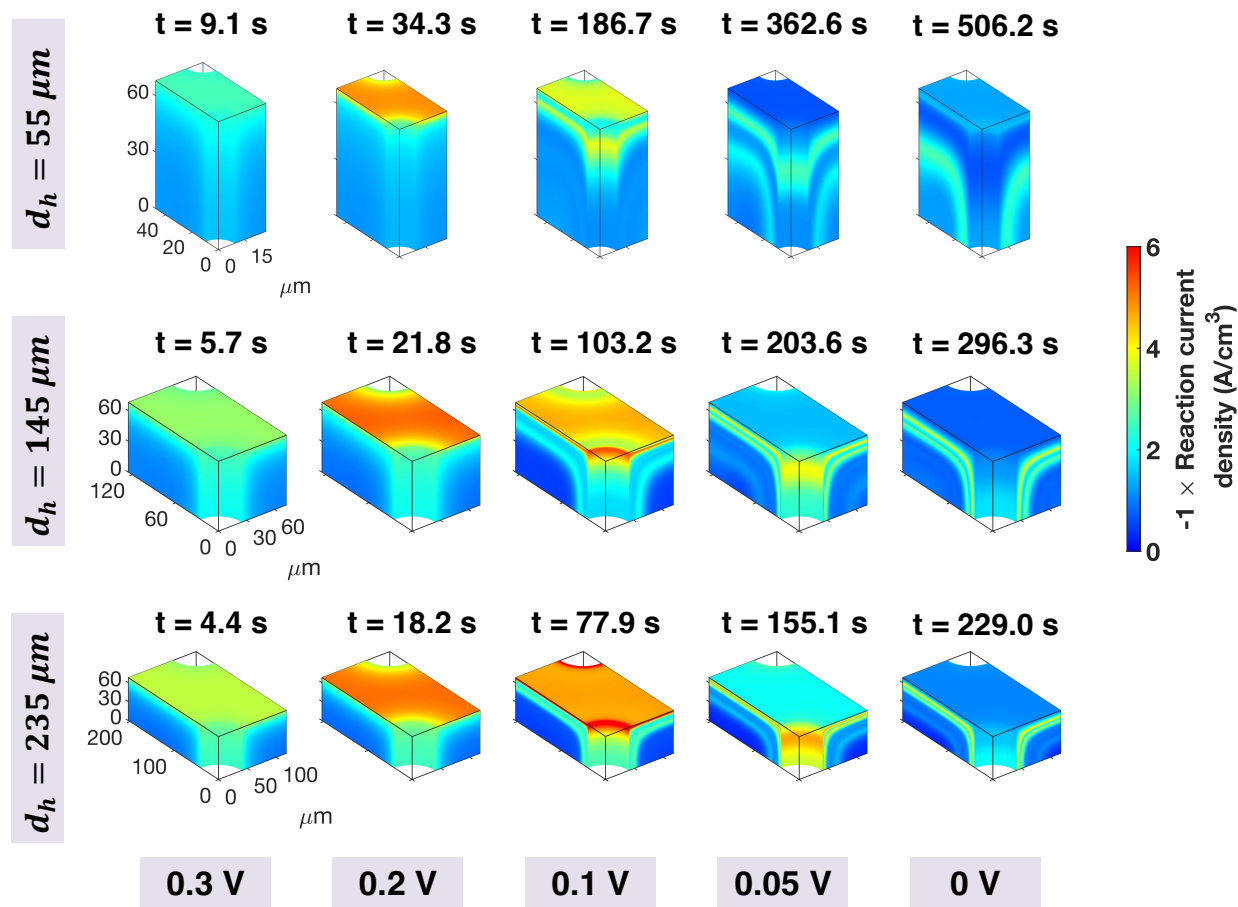


Figure 5.3. Time series of the simulated RCD distribution in three HOLE anodes with  $d_h = 55, 145,$  and  $235 \mu\text{m}$  during 4C charging. The times for the images were selected when the anode voltage is 0.3V, 0.2V, 0.1V, 0.05V, and 0V, as noted at the bottom of the figure. Note that the times corresponding to these voltages vary significantly among the anodes. The range of the color bar is the same as Figure 5. Note that, while the thickness is the same for the three HOLE configurations, the lateral size is different since the channel spacings are different. Reproduced with permission from Ref. 24. Copyright 2023, the authors. Published by Elsevier B.V.

### 5.2.1 Quantification of the current homogeneity and $Da_{II}$

As discussed above, the HOLE configuration with a smaller  $d_h$  value exhibits a more homogeneous RCD distribution and thus improved fast-charging performance. However, a quantification of this effect is needed to fully understand the relation between the geometry and the electrode performance. We achieved this quantification by determining the contribution of the

peaks in the RCD distribution to the applied current and the corresponding volume occupied by them in the anode. In addition, we defined the second Damköhler number,  $Da_{II}$ , for the anodes to provide insights into the effect of  $d_h$  on the HOLE performance, and to identify the distinct features of the optimal HOLE configuration. We selected  $Da_{II}$  because it captures the effects of both the reaction rate and the diffusion dynamics, and thus serves as a suitable metric to identify the optimal HOLE configuration.

In general, the Damköhler number,  $Da_{II}$ , for any system is defined as the ratio between the characteristic diffusion time and the characteristic reaction time. It is then analytically expressed by using the known properties of the system such as its geometry, the diffusivity of the mobile species, and the rate constant for the underlying reaction. Such an analytical method has been used previously to obtain  $Da_{II}$  for Li-ion-battery electrodes<sup>153–155</sup> and Li-metal electrodes,<sup>156</sup> where the value of the exchange current density,  $i_{0,\psi}$ , or the reaction-rate constant,  $k_\psi$ , was used to calculate the characteristic reaction time. However, this method does not account for the effects of the applied current and the inhomogeneity in the RCD distribution. Since significant inhomogeneity is observed in the RCD distribution for the anodes studied here (see Figure 5.2 and Figure 5.3), it cannot be used to obtain a relevant  $Da_{II}$  value. Furthermore, obtaining a fully analytical expression for  $Da_{II}$  that accounts for the inhomogeneity is challenging because of the 3D nature of the RCD distribution in the HOLE anodes. Thus, we first obtained the  $Da_{II}$  value using the simulation results as described below. Then, using the insights generated from the simulation-based  $Da_{II}$ , we developed a semi-analytical method for obtaining the time-averaged value of  $Da_{II}$  that only requires 1D simulations. Details are provided below, along with the definition of  $Da_{II}$ . All the symbols used in the analysis below are provided in Table 5.2.

Table 5.2. The list of symbols used in Section 5.2 along with their description. Reproduced with permission from Ref. 24. Copyright 2023, the authors. Published by Elsevier B.V.

Symbol	Description
$d_h$	Inter-channel spacing, m
$\mu_h$	Channel radius, m
$\delta_h$	Distance between the centroid of the triangle, formed by three adjacent channel centers, and one of the channel walls, m
$\Omega_R$	Fraction of the electrode volume retained after laser patterning
$Da_{II}$	Second Damköhler number, which is the ratio between the characteristic diffusion time and the characteristic reaction time for Li ions in an electrode
$l_D$	Characteristic diffusion length for Li ions in an electrode, m
$c_{e,a}^0$	Initial concentration of Li ions in the electrolyte, mol/m <sup>3</sup>
$\xi^{peak}$	Reaction current density (RCD) contributed by the peaks, A/m <sup>3</sup>
$A_C$	Nominal cross-sectional area, i.e., the in-plane cross-section area of the anodes, including the channel area, m <sup>2</sup>
$A_H$	In-plane cross-section area of the HOLE anodes excluding the channel area, m <sup>2</sup> . It is related to $A_C$ via $A_H = \Omega_R A_C$ .
$f_\xi$	For the control anode – Fraction of the anode volume occupied by the peaks in the RCD For the HOLE anodes – Fraction of the anode volume contributing to a current value of $\langle \gamma_{\xi,C} \rangle_t i_{app} A_C$
$\gamma_\xi$	Fractional contribution of the RCD peaks to the applied current in the control anode
$V_E$	Volume of an electrode, m <sup>3</sup> ; subscript $E = C, H$ represents the control and HOLE anodes, respectively.
$l_\xi$	Characteristic reaction length for Li ions in an electrode, m
$\lambda$	Width of a peak in the RCD, m
$\Delta U_\psi$	Potential drop across an OCV plateau, V
$V_1$	Volume of the active region that is close to the anode-separator interface in the HOLE anode, m <sup>3</sup>
$V_2$	Volume of the active region in the shape of an annular cylinder near the channel wall, m <sup>3</sup>
$\langle \cdot \rangle_t$	Represents the time-averaged value of the quantity inside the angular brackets
$\langle f_\xi \rangle_t^{int}$	Intermediate form of $\langle f_\xi \rangle_t$ obtained during the semi-analytical estimation of $\langle f_\xi \rangle_t$

For the anodes studied here, we define the characteristic diffusion time for Li ions as  $l_D^2/D_{eff,a}^0$ , and the characteristic reaction time for Li ion as  $(Fc_{e,a}^0)/\xi^{peak}$ , where  $\xi^{peak}$  is the

characteristic RCD within the peaks,  $c_{e,a}^0 = 1M$  is the initial concentration of Li ions in the electrolyte,  $F$  is Faraday's constant,  $l_D$  is the characteristic diffusion length, and  $D_{eff,a}^0$  is the effective electrolyte diffusivity corresponding to  $c_{e,a}^0$ . Thus,  $Da_{II}$  becomes

$$Da_{II} = \left( \frac{l_D^2}{D_{eff,a}^0} \right) \left( \frac{F c_{e,a}^0}{\xi^{peak}} \right)^{-1}. \quad (5.4)$$

A large value of  $Da_{II}$  ( $\gg 1$ ) signifies a diffusion-limited condition, i.e., the reaction current is limited by the rate of diffusive transport of Li ions in the electrolyte rather than reaction kinetics. Thus, an anode with a high  $Da_{II}$  value will exhibit poor fast-charging performance. On the other hand, a  $Da_{II}$  value of much less than 1 signifies a reaction-limited condition, in which the reaction current is set by the reaction kinetics that is unhindered by ionic transport. Finally, a  $Da_{II} \approx 1$  signifies a mixed-control condition.

As can be seen from Eq. 5.4, we have two unknowns in the calculation of  $Da_{II}$ , namely, the reaction current density contributed by the peaks,  $\xi^{peak}$ , and the characteristic diffusion length,  $l_D$ . The length  $l_D$  can be obtained straightforwardly as the lesser value of  $L_a$  and  $\delta_h$  for the HOLE anode and as  $L_a$  for the control anode. However, the calculation of  $\xi^{peak}$  is more complex, especially for the HOLE anode due to the 3D nature of reaction distribution observed in the simulations. In general,  $\xi^{peak}$  can be defined as

$$\xi^{peak} \equiv \frac{(\text{current contributed by the peaks})}{(\text{volume occupied by the peaks})} = \frac{\gamma_\xi i_{app} A_C}{f_\xi V_E}, \quad (5.5)$$

where  $\gamma_\xi$  represents the fraction of the applied current contributed by the peaks and  $f_\xi$  denotes the fraction of the anode volume occupied by the peaks. Note that the subscript  $\xi$  indicates that the corresponding quantity is characteristic of the electrochemical reaction occurring within the peaks. The variable  $A_C$  represents the nominal cross-sectional area, i.e., the in-plane cross-section area of

the anodes, including the channel area. Additionally,  $V_E$  represents the volume of the electrode, and the subscript  $E = C, H$  refers to the control anode and the HOLE anode, respectively. Since  $i_{app}$  represents the applied current density,  $i_{app}A_C$  represents the total applied current. Note that both the control and HOLE anodes have the same total applied current.

Below, we describe our methodology for determining  $\gamma_\xi$  and  $f_\xi$  for both the control and HOLE anodes. In brief, we first determine  $f_\xi$  for the control anode by using the work of Wang et al.,<sup>132</sup> and then we obtain  $\gamma_\xi$  using the simulation results. Subsequently, the time-average  $\gamma_\xi$  for the control anode is set equal to the fractional contribution of the peaks in the HOLE anode and the corresponding volume of the peaks is determined.

### ***Calculation of $\xi^{peak}$ for the Control Anode***

Using Eq. 5.5, the expression for  $\xi^{peak}$  for the control anode can be written as

$$\xi^{peak} = \frac{\gamma_\xi i_{app} A_C}{f_\xi V_C} = \frac{\gamma_\xi i_{app} A_C}{f_\xi A_C L_a}, \quad (5.6)$$

where  $L_a$  is the anode thickness. Since there are no in-plane variations in the RCD distribution in the control anode, the volume occupied by the peaks can also be written as  $l_\xi A_C$ , where  $l_\xi$  is the sum of the width of peaks in the RCD distribution. Therefore, the expression for  $\xi^{peak}$  becomes

$$\xi^{peak} = \frac{\gamma_\xi i_{app} A_C}{l_\xi A_C} = \frac{\gamma_\xi i_{app}}{l_\xi}. \quad (5.7)$$

We note that Eq. 5.7 is only valid when the peaks in the RCD distribution are nonoverlapping, which is true for the anodes studied here (see Figure 5.5a and Figure 5.3). To obtain the width of each peak, we employ the expression derived by Wang et al.,<sup>132</sup> who showed that the width of a peak in the RCD distribution,  $\lambda$ , in a conventional electrode is related to its effective ionic and

electronic conductivities ( $\kappa_{eff,\psi}$  and  $\sigma_{eff,\psi}$ , respectively) and the potential drop across the corresponding OCV plateau,  $\Delta U_\psi$ , via <sup>132</sup>

$$\lambda = \frac{2\Delta U_\psi}{i_{app} |\kappa_{eff,\psi}^{-1} - \sigma_{eff,\psi}^{-1}|}. \quad (5.8)$$

Using Eq. 5.8, Wang et al. showed that the uniformity of reaction distribution can be achieved through increasing  $\lambda$ , i.e., by reducing  $i_{app}$ , by selecting a material with a large  $\Delta U_\psi$  (sloping OCV profile or absence of plateaus), and/or by reducing the difference between  $\kappa_{eff,\psi}$  and  $\sigma_{eff,\psi}$ . Next, we extend the work of Wang et al.<sup>132</sup> by applying Eq. 5.8 to graphite, which has three plateau-like regions (where the slope is shallow) in its OCV (see Figure 4.11 and the associated text). We hereafter refer to these plateau-like regions as plateaus. Figure 5.5a shows the three peaks in the RCD that originate due to the presence of three plateaus in the graphite OCV.

To determine the size of drop in OCV across a plateau-like region,  $\Delta U_a$ , for each plateau, we first calculated the derivative of the OCV with respect to Li-site fraction within and near the plateau. We then determined the difference in OCV over a symmetric range of the derivative around the average value of the derivative. Mathematically, the range of each plateau were selected such that within the plateau,  $\left| \frac{dU_a}{d(c_{p,a}^{surf}/c_{p,a}^{max})} - \text{mean} \left( \frac{dU_a}{d(c_{p,a}^{surf}/c_{p,a}^{max})} \right) \right| \leq 0.105 \text{ V}$ . The derivative range of  $\sim \pm 0.105 \text{ V}$  was chosen because it yielded a good agreement with visual inspection of the plateaus. Figure 5.4 shows the graphite OCV vs. Li-site fraction (with its y-axis on the left) and its derivative (with y-axis on the right). As described in Section 4.7 (Figure 4.11a and the associated text), the OCV was obtained experimentally. The red, purple, and blue shaded areas represent the regions corresponding to the first, second, and third plateau, respectively. The corresponding Li-site fractions for the plateaus are provided in Table 5.3. The  $\Delta U_a$  value for the three plateaus is determined to be  $\sim 6, 15, \text{ and } 14 \text{ mV}$ . Thus, the corresponding values of  $\lambda$  from Eq. 5.8 are  $\sim$

2.6  $\mu m$ , 6.6  $\mu m$ , and 6.1  $\mu m$ , which result in the total peak width,  $l_\xi = 15.4 \mu m$ . We note that, in this calculation, a constant value of  $\kappa_{eff,a} = 0.0204 S/m$  was assumed, which corresponds to its value at Li-ion concentration of  $c_{e,a}^0 = 1M$ .

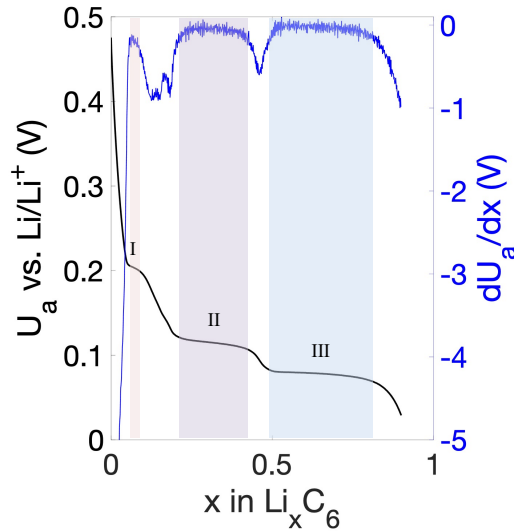


Figure 5.4. The OCV vs. Li-site fraction plot (black, left y-axis) and its derivative (blue, right y-axis). The red, purple, and blue shaded areas represent the regions corresponding to the first, second, and third plateau, respectively. Reproduced with permission from Ref. 24. Copyright 2023, the authors. Published by Elsevier B.V.

Table 5.3. List of Li-site fraction ranges corresponding to graphite OCV plateaus. Reproduced with permission from Ref. 24. Copyright 2023, the authors. Published by Elsevier B.V.

Plateau	Min Li-site fraction	Max Li-site fraction
I	0.056	0.087
II	0.210	0.427
III	0.492	0.815

Next, we determined  $\gamma_\xi$  by integrating the current contributed by the most active regions in the simulation until a threshold thickness of 15.4  $\mu m$  is reached. Figure 5.5b shows the plot of  $\gamma_\xi$  vs. SOC for the control anode during 4C charging. The RCD distribution is highly inhomogeneous in the control anode, as  $\sim 23\%$  of the volume (15.4  $\mu m$  out of 68  $\mu m$  thickness)

contributes to ~55% of the applied current density (on average) throughout charging. The decreasing behavior of  $\gamma_\xi$  in the beginning can be attributed to the fact that only migration can facilitate transport of ions, because the initial ionic concentration is constant, but  $\kappa_{eff,a}$  is not sufficiently large to keep pace with the reaction. When a sufficiently large concentration gradient develops and diffusion starts to complement the migration current,  $\gamma_\xi$  drops, before rising again when the first RCD peak emerges. With  $\gamma_\xi$  and  $l_\xi$  obtained, we used Eqs. 5.4 and 5.7 to calculate  $D\alpha_{II}$  as a function of SOC for the control anode during 4C charging, as shown in Figure 5.5b. The results are discussed later, along with the results for the HOLE anodes.



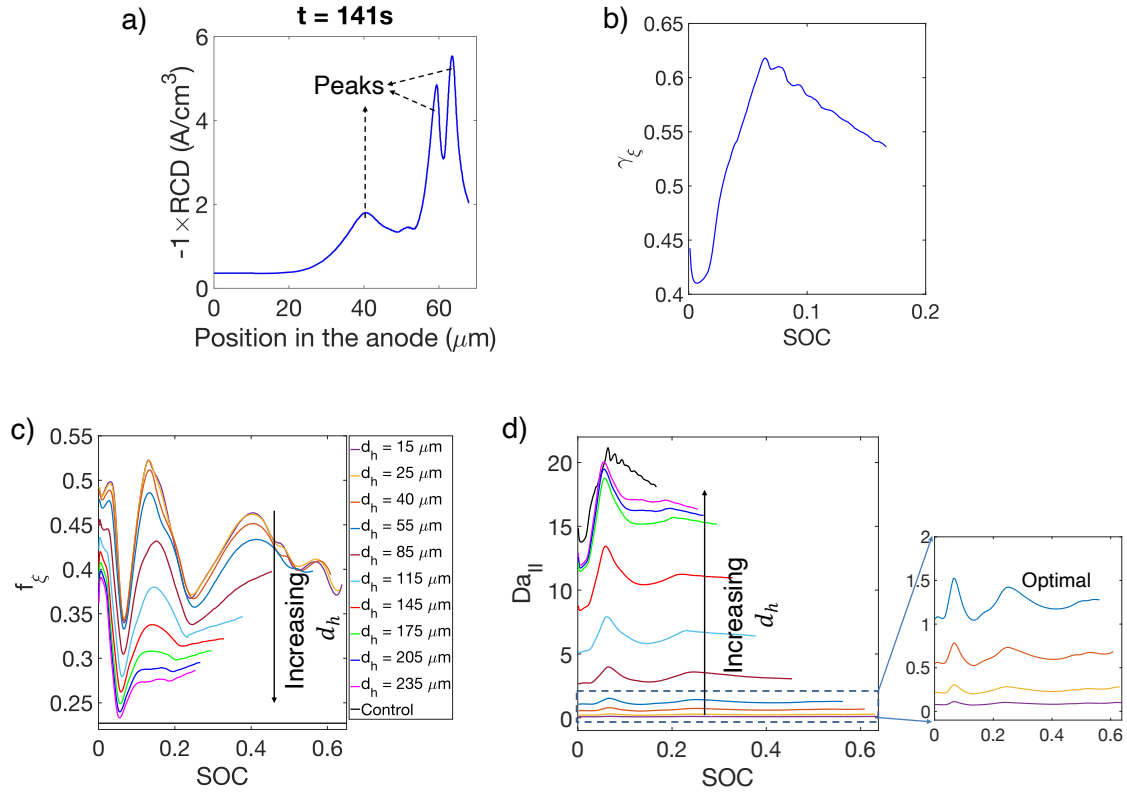


Figure 5.5. Simulated reaction current density (RCD), fractional contribution to current from the peak and the corresponding volume, and the Damköhler number. A snapshot of the reaction current density (RCD) distribution in the control anode; the arrows indicate the location of peaks. (b) Fractional contribution of the peaks in the RCD to the applied current,  $\gamma_\xi$ , vs. SOC plot for the control anode. (c) Fractional volume that contributes to a current value of  $\langle \gamma_{\xi,C} \rangle_t i_{app} A_C$ ,  $f_\xi$ , vs. SOC plot for the HOLE configurations; the control data (black line) is added for reference. (d)  $Da_{II}$  vs. SOC plot for the control anode and the HOLE anodes considered in this work; the section highlighted using the dashed box is magnified in the adjacent subfigure. Each curve in (c) and (d) corresponds to a different inter-channel spacing,  $d_h$ , ranging from 15  $\mu\text{m}$  to 235  $\mu\text{m}$ , as noted in the legend in (c). The optimal configuration among the simulations conducted,  $d_h = 55 \mu\text{m}$ , is noted in the subfigure of (d). Reproduced with permission from Ref. 24. Copyright 2023, the authors. Published by Elsevier B.V.

### Calculation of $\xi^{peak}$ for the HOLE Anodes

Using Eq. 5.5, the expression of  $\xi^{peak}$  for the HOLE anodes can be written as

$$\xi^{peak} = \frac{\gamma_{\xi} i_{app} A_C}{f_{\xi} V_H}. \quad (5.9)$$

However, owing to the three-dimensional nature of the reaction distribution, the definition of  $f_{\xi}$  is not as straightforward as for the control anode. For the HOLE anodes, we define  $f_{\xi}$  as the volume fraction that contributes to a specific amount of the applied current, and to enable a direct comparison with the control anode, we set that specific quantity to be equal to the time-averaged contribution of the peaks in the applied current of the control anode. Therefore, the current amount is set equal to  $\langle \gamma_{\xi, C} \rangle_t i_{app} A_C$ , where  $\langle \gamma_{\xi, C} \rangle_t$  is the time-averaged value of  $\gamma_{\xi}$  in the control anode. Moreover,  $V_H$  can be written as  $A_H L_a$ , where  $A_H$  is the in-plane cross-sectional area of the HOLE anodes, i.e., not including the channel area. As mentioned above for the control anode,  $\langle \gamma_{\xi, C} \rangle_t = 0.55$ . Furthermore, due to the cylindrical morphology of the channels,  $A_H$  is related to  $A_C$  via  $A_H = \Omega_R A_C$ . Thus,  $\xi^{peak}$  for the HOLE anodes can be written as

$$\xi^{peak} = \frac{\langle \gamma_{\xi, C} \rangle_t i_{app} A_C}{f_{\xi} A_H L_a} \approx \frac{0.55 i_{app} A_C}{f_{\xi} \Omega_R A_C L_a} = \frac{0.55 i_{app}}{f_{\xi} \Omega_R L_a}. \quad (5.10)$$

Figure 5.5c shows the  $f_{\xi}$  vs. SOC plot for the HOLE configurations (with different  $d_h$  at a constant  $\Omega_R$ ) studied in this work. As can be seen,  $f_{\xi}$  for HOLE anodes increases with decreasing channel spacing, with a concomitant decrease of the channel size. Therefore, reducing the inter-channel spacing with a constant volume retention increases the homogeneity of the RCD distribution, which was also qualitatively observed in Figure 5.3. Moreover, all the HOLE configurations have a higher value of  $f_{\xi}$  than the control anode, which is consistent with the superior performance of every HOLE anode over the control anode discussed in the text associated

with Figure 5.2 and Figure 5.3. We note that the dips in the  $f_\xi$  vs. SOC plot in Figure 5.5c occur with the change in the inhomogeneity in the RCD distribution, which can be observed in Figure 5.3.  $Da_{II}$  is obtained by substituting the value of  $\xi^{peak}$  into Eq. 5.4. Figure 5.5d shows the  $Da_{II}$  vs. SOC plot for HOLE anodes with different  $d_h$  values; the result for the control anode (black curve) is also provided for comparison. Two key trends can be observed in the figure. First, the control anode has the highest value of  $Da_{II}$  throughout charging, and thus, it exhibits the lowest accessible capacity among the anodes examined. In fact,  $Da_{II}$  for the control anode is greater than 13 throughout the 4C charging. This means that the characteristic diffusion time is over 13 times higher than the characteristic reaction time for the control anode during 4C charging, which results in severe depletion of Li ions within the control anode during charging.

Second,  $Da_{II}$  for the HOLE anodes monotonically decreases with a reduction in  $d_h$  (see non-black curves in Figure 5.5d), which is consistent with our finding in Figure 5.1c that the performance of HOLE configurations improves with closer (and smaller) channels. However, the marginal decrease in  $Da_{II}$  with respect to the reduction in the inter-channel distance ( $d_h$ ) is not constant. As can be seen in Figure 5.5d,  $Da_{II}$  for the HOLE anodes with  $d_h \geq 175 \mu m$  (green, blue, and magenta curves) does not vary significantly with a change in  $d_h$  and is similar to the control anode's (the black curve), whereas it decreases significantly with a reduction in  $d_h$  for the HOLE anodes when  $d_h \leq 145 \mu m$  (below the green curve). This behavior can be explained based on the characteristic diffusion length,  $l_D$ . For the HOLE anodes with  $d_h \geq 175 \mu m$ , the channels are too far apart to affect the ionic concentration in most of the anode volume, and thus,  $l_D$  is set by the anode thickness,  $L_a$ . Furthermore, varying  $d_h$  does not strongly affect the RCD or the  $Da_{II}$  value for such anodes, and only a minor increase in  $f_\xi$  with decreasing  $d_h$  was observed in Figure 5.5c (indicating a minor reduction in RCD peaks). On the other hand,  $l_D$  is equal to the maximum

distance to the nearest channel wall,  $\delta_h$ , for the HOLE anodes with  $d_h \leq 145 \mu\text{m}$ , and thus a decrease in  $d_h$  (and consequently  $\delta_h$  following Eq. 5.3) leads to a significant decrease in the  $Da_{\text{II}}$  value. This is the greatest advantage of applying the HOLE architecture, because doing so makes  $l_D$  independent of  $L_a$ . Thus, the HOLE architecture offers a method to decouple the energy density and power density of an electrode, and consequently, to overcome the inherent tradeoff that exists in the conventional electrode design.

Figure 5.5 also shows that  $Da_{\text{II}}$  for the HOLE configuration with  $d_h = 55 \mu\text{m}$  is  $\approx 1$  (see Figure 5.5d inset, light-blue curve). This indicates that the value of the characteristic diffusion time for Li ions is similar to that of the characteristic reaction time. Therefore, the diffusion in the electrolyte phase is no longer the limiting mechanism during 4C charging, and thus any further reduction in the  $d_h$  value does not yield any substantial gains in the accessible capacity of the HOLE anode. This is the reason behind the decreasing behavior of the magnitude of the slope as  $d_h$  is decreased below  $55 \mu\text{m}$ , as seen in Figure 5.1c. Thus, it can be inferred that the optimal configuration has the  $Da_{\text{II}}$  value  $\approx 1$ .

In summary, we showed that the inter-channel spacing at a constant volume retention has a direct effect on fast-charging performance of a HOLE anode. This effect can be quantified using  $Da_{\text{II}}$ , which is the ratio between the characteristic diffusion and reaction times for Li ions. We also showed that  $Da_{\text{II}}$  serves as a suitable quantitative metric for comparing different configurations of the HOLE architecture and the optimal configuration has the  $Da_{\text{II}}$  value  $\approx 1$ . However, we note that the calculation of  $Da_{\text{II}}$  so far has been based on the simulation results, which are costly to obtain, especially for the HOLE anodes. To reduce this cost, we developed a semi-analytical method for estimating the time-averaged value of  $Da_{\text{II}}$ ,  $\langle Da_{\text{II}} \rangle_t$ , which is discussed in the following

section (Section 5.2.2). Furthermore, we demonstrate the utility of this method and  $\langle Da_{II} \rangle_t$  to screen the HOLE candidates for optimal performance during 6C charging in Section 5.2.3

### 5.2.2 Semi-analytical estimation of the time-averaged $f_\xi$ and $Da_{II}$

As mentioned earlier, our calculations of  $Da_{II}$  for the HOLE anodes are based on the results from the 3D simulations, which are computationally expensive. However, it can be seen using Eqs. 5.4 and 5.10 that only  $f_\xi$  needs to be obtained from the 3D simulations; all other quantities are either known analytically or can be obtained from 1D simulations for the control anode, which are computationally inexpensive. Therefore, the computational cost of the optimization process can be significantly reduced if  $f_\xi$  is analytically estimated. Such an estimation would enable an exploration of a much larger parametric space for the HOLE design, which includes volume retention ( $\Omega_R$ ), pattern, channel depth, C-rate, and the electrode material properties as independent parameters. With the initial screening processes enabled by such a method, 3D simulations would only be required to examine a small range of the parameters for refinement. To achieve such an estimation, we propose a semi-analytical method for obtaining the time-averaged  $f_\xi$ ,  $\langle f_\xi \rangle_t$ , for a given HOLE configuration. As shown in Figure 5.6a, the volume of active region in a HOLE anode can be treated as the sum of two volumes,  $V_1$  and  $V_2$ . The volume  $V_1$  is the portion of the active region that is close to the anode-separator interface and can be obtained as

$$V_1 = \frac{\sqrt{3}}{4} d_h^2 l_\xi - \frac{1}{2} \pi \mu_h^2 l_\xi, \quad (5.11)$$

where the first term on the right-hand side represents the active volume region for the corresponding control anode and the second term represents the anode volume removed by laser patterning through the depth of  $l_\xi$ .

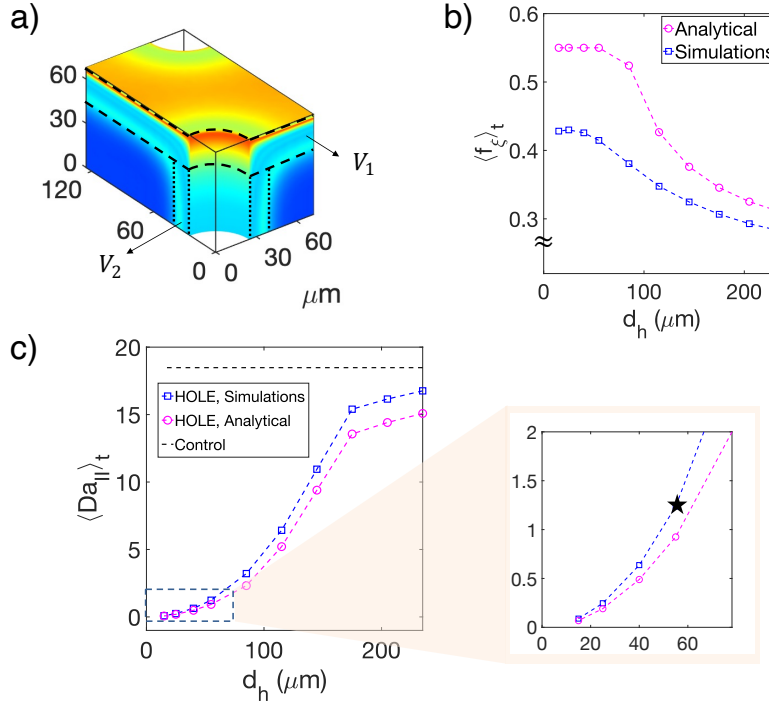


Figure 5.6. Comparison of the simulated and semi-analytically obtained time-averaged active volume fraction ( $f_{\xi}$ ) and Damköhler number. (a) Illustration of the division of the active volume into  $V_1$ , the volume enclosed within the dashed lines, and  $V_2$ , the volume enclosed within the dotted lines. The comparison of (b)  $\langle f_{\xi} \rangle_t$  and (c)  $\langle Da_{II} \rangle_t$  obtained from the simulations (squares) and analytically (circles) as functions of  $d_h$ . The subfigure on the right side of (c) shows the magnified view of the region highlighted by the dashed box in (c). The star in the subfigure corresponds to  $d_h = 55 \mu\text{m}$ , where  $\langle Da_{II} \rangle_t \approx 1$ . Note that the apparent match between the  $\langle Da_{II} \rangle_t$  values at small  $d_h$  values is due to the large range of the y-axis. Reproduced with permission from Ref. 24. Copyright 2023, the authors. Published by Elsevier B.V.

The volume  $V_2$  is the additional volume activated by the HOLE architecture in the shape of quarter annular cylinders next to the channels, as shown in Figure 5.6a. Since both the anode/channel interface and the anode/seperator interface act as unrestricted sources of Li ions, the penetration depth of the electrochemical reaction (or the characteristic reaction length) when measured radially from the anode-channel interface is also assumed to be equal to  $l_{\xi}$ . Thus, the difference between the inner and outer radii of the annular cylinders shown in Figure 5.6a can be approximated as  $l_{\xi}$ . We note that by making this assumption, we ignore the variation in  $\phi_{e,a}$  along the anode thickness,

which affects the characteristic reaction length in the radial direction. Next, by setting the length of the annular cylinders equal to  $L_a - l_\xi$ , we can compute  $V_2$  as

$$V_2 = \frac{1}{2}\pi \left( (\mu_h + l_\xi)^2 - \mu_h^2 \right) (L_a - l_\xi). \quad (5.12)$$

With the volume of the active region obtained, we can express an intermediate form of  $\langle f_\xi \rangle_t$ ,  $\langle f_\xi \rangle_t^{int}$ , as

$$\langle f_\xi \rangle_t^{int} = \frac{V_1 + V_2}{V_H} = \frac{\left( \frac{\sqrt{3}}{4} d_h^2 l_\xi - \frac{1}{2} \pi \mu_h^2 l_\xi + \frac{1}{2} \pi \left( (\mu_h + l_\xi)^2 - \mu_h^2 \right) (L_a - l_\xi) \right)}{\left( \frac{\sqrt{3}}{4} \Omega_R d_h^2 L_a \right)}, \quad (5.13)$$

where  $V_H$  is the total volume of the HOLE anode. We note that  $\langle f_\xi \rangle_t$  is physically bounded by an upper limit. This limit corresponds to the case when the RCD distribution is uniform, in which case the volume fraction  $\langle f_\xi \rangle_t$  becomes equal to the current fraction  $\langle \gamma_{\xi,C} \rangle_t$ . Thus,  $\langle f_\xi \rangle_t$  has an upper threshold of 0.55 in this analysis. Therefore, we define  $\langle f_\xi \rangle_t$  as

$$\langle f_\xi \rangle_t = \min \left( \langle f_\xi \rangle_t^{int}, 0.55 \right). \quad (5.14)$$

Figure 5.6b shows the comparison of  $\langle f_\xi \rangle_t$  obtained from the analytical estimation and simulations as a function of  $d_h$  for  $\Omega_R = 0.895$  during 4C charging. Both plots exhibit the same dependence on  $d_h$ , i.e.,  $\langle f_\xi \rangle_t$  monotonically increases with decreasing  $d_h$ . Quantitatively, there exists up to a  $\approx 38\%$  difference between the simulation and analytical results (the analytical method overestimates the value of  $\langle f_\xi \rangle_t$ ). We note that this error is caused by the simplifying assumption that the anode volume corresponding to  $\langle f_\xi \rangle_t$  can be considered as the sum of two regular volumes,  $V_1$  and  $V_2$ , as shown in Figure 5.6a. However, in a physical system, the shape of the electrochemically active volume is more complex due to, for example, the variation of the

electrolyte potential and concentration along the anode thickness. The analytical estimate of  $\langle f_{\xi} \rangle_t$  might be further improved by an explicit consideration of the variation of the electrolyte potential and concentration along the anode thickness, which may be of interest for future work. Nonetheless, given the analytical estimates are used as a first step for determining the optimal  $d_h$  range, and that a significant reduction in the required computation is achieved, this error is acceptable. For instance, every  $d_h$  value that can be rejected based on the analytical estimate eliminates  $\approx 36$  hrs of computation carried out using 16 cores of a 3.0 GHz Intel Xeon Gold 6154 processor.

With the estimates for  $\langle f_{\xi} \rangle_t$ , Eqs. 5.4 and 5.10 can be used to determine the time-averaged value of  $Da_{II}$ , defined as  $\langle Da_{II} \rangle_t$ , for various HOLE configurations. Figure 5.6c, shows  $\langle Da_{II} \rangle_t$  vs.  $d_h$  obtained both from the simulations and analytical estimation. The value of  $\langle Da_{II} \rangle_t$  for the control anode is also plotted for reference. Both the curves exhibit the same qualitative dependence on  $d_h$ , i.e.,  $\langle Da_{II} \rangle_t$  increases monotonically with  $d_h$ . The change in the slope of the curve for  $d_h \geq 175 \mu m$  is caused by the change in the characteristic diffusion length,  $l_D$ , as discussed above. The quantitative difference between the two plots is caused by the difference in the estimation of  $\langle f_{\xi} \rangle_t$ . The apparent match between the  $\langle Da_{II} \rangle_t$  values obtained at small  $d_h$  values is caused by the large range of the y-axis compared to those values; the percentage error is still around 38%. Due to the acceptable qualitative and quantitative agreement between the analytical estimate and the simulation results, we conclude that our proposed method can be used for the preliminary screening of various HOLE configurations to reduce the computational cost. In the next section (Section 5.2.3), we demonstrate the application of the semi-analytical method to identify the optimal HOLE configuration for 6C charging.



### 5.2.3 Optimal HOLE configuration for 6C charging

To demonstrate the utility of the semi-analytical method, we employ it to screen HOLE configurations for 6C charging and verify the results using simulations. The method can be broadly summarized as a two-step process. In the first step,  $l_\xi$  is calculated in the same manner as the 4C case by calculating the sum of  $\lambda$  values;  $l_\xi \approx 10.3 \mu m$  for 6C. Subsequently,  $\langle \gamma_{\xi,c} \rangle_t$  (corresponding to  $l_\xi$ ) is determined to be 0.47 from the 1D simulation of the control anode at 6C. In the second step,  $\langle f_\xi \rangle_t$  (and subsequently  $\langle Da_{II} \rangle_t$ ) are obtained as a function of  $d_h$  using Eqs. 5.4 and 5.10. Figure 5.7a shows the analytically determined  $\langle Da_{II} \rangle_t$  vs.  $d_h$ , for  $d_h$  values ranging from 15 to 75  $\mu m$ . We note that this semi-analytical estimate of  $\langle Da_{II} \rangle_t$  took  $\sim 180$  s (including the 1D simulation) on the same processor as described in Section 5.2.2, while each 3D simulation for 6C charging current took  $\approx 24$  hrs. Thus, the semi-analytical method offers at least two orders of magnitude reduction in the computational cost.

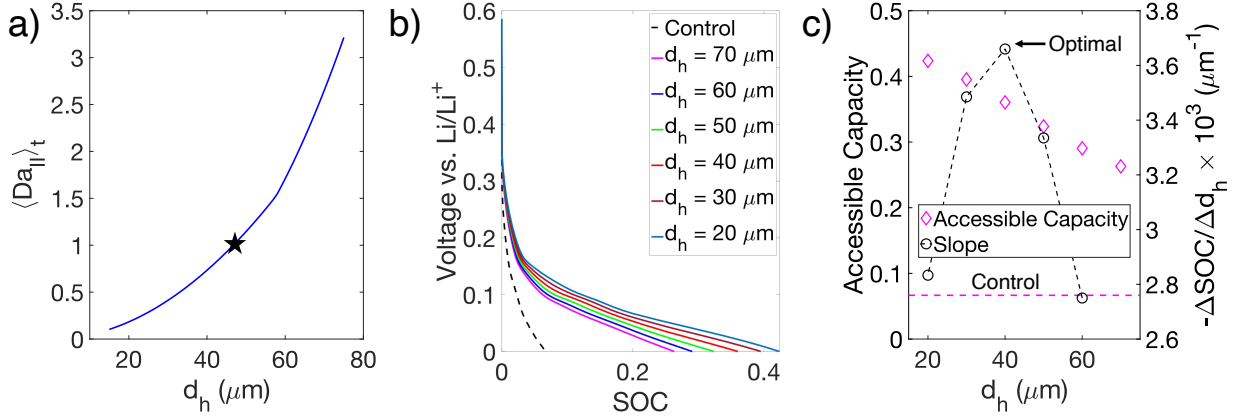


Figure 5.7. 6C results for semi-analytically obtained time-averaged Damköhler number, simulated voltage vs. SOC plot for six HOLE anodes, and the simulated accessible capacity. (a) The analytically obtained dependence of  $\langle Da_{II} \rangle_t$  on  $d_h$  for 6C charging. The star corresponds to  $d_h = 47 \mu\text{m}$ , where  $\langle Da_{II} \rangle_t \sim 1$ . (b) The simulated voltage vs. SOC plot for six HOLE anodes (different  $d_h$ ) at 6C charging; the dashed black curve represents the result for the control anode. The six values of  $d_h$ , range from  $20 \mu\text{m}$  (light blue) to  $70 \mu\text{m}$  (magenta). (c) The accessible capacity vs.  $d_h$  plot (magenta diamonds, left y-axis) and the magnitude of its discrete derivative vs.  $d_h$  plot (black circles connected with a black dashed line, right y-axis) obtained from simulations for 6C charging. The accessible capacity for the control anode is included for reference (magenta dashed line). The optimal configuration among the simulations conducted,  $d_h = 40 \mu\text{m}$ , is noted in (c). Reproduced with permission from Ref. 24. Copyright 2023, the authors. Published by Elsevier B.V.

Based on our discussion in the Section 5.2.2, the optimal HOLE configuration has a  $\langle Da_{II} \rangle_t$  value  $\approx 1$ , which corresponds to  $d_h \approx 47 \mu\text{m}$  for 6C charging (predicted using the semi-analytical method). To validate this prediction, we conducted six 3D simulations for the HOLE anode corresponding to the six equally spaced  $d_h$  values, ranging from 20 to  $70 \mu\text{m}$ . The voltage vs. SOC curves for the six configurations, along with that of the control anode, are shown in Figure 5.7b. Figure 5.7c summarizes the results by plotting accessible capacity vs.  $d_h$  (magenta diamonds, left y axis) and the magnitude of its discrete derivative (black dashed curve, right y axis). As can be seen, a reduction in  $d_h$  improves the accessible capacity in this case also. However, the point of diminishing return (based on the magnitude of the derivative) falls at  $d_h = 40 \mu\text{m}$ , below which the magnitude of the derivative decreases (see the black dashed curve in Figure 5.7c). Hence, we conclude that  $d_h = 40 \mu\text{m}$  is the optimal configuration (as noted in Figure 5.7c) among the

candidates investigated (for  $\Omega_R \approx 0.895$ ), which is close to the value estimated by the analytical method ( $\sim 47 \mu\text{m}$ ). Furthermore, we note that the optimal  $d_h$  value for 6C charging is smaller than that for 4C charging ( $40 \mu\text{m}$  vs.  $55 \mu\text{m}$ ). Such a trend is expected as the rate of Li-ion consumption increases with an increase in the C-rate, and therefore, the rate of ionic transport must be increased (by the means of decreasing  $d_h$ ) to sustain the charging process.

The demonstration above illustrates the strength of the analytical method to screen the HOLE candidates in the search for an optimal configuration at a given C-rate with a computational cost smaller by two orders of magnitude compared if only 3D simulations were used. We note that, in practice, a narrower range of  $d_h$  values needs to be examined to validate the result obtained from the analytical method. We deliberately chose such a wide range to show that the optimal configuration does not lie far from the estimate obtained using the analytical method. Finally, we also note that the method is not just limited to account for the effect of the C-rate but can also be used to perform initial screening for other design parameters by changing the corresponding variable in different equations used above. The design parameters include  $\Omega_R$ , pattern symmetry, channel depth, electrode loading, active material, and electrolyte properties.

#### ***5.2.4 Effect of materials properties and electrode design on $Da_{II}$ and the optimal configuration***

In the sections above, our discussion has been focused on the graphite anodes. However, the semi-analytical approach employed here can be used for any porous electrode for Li-ion batteries when the active material has at least one plateau-like region in its OCV. To further demonstrate the effect of the material properties and electrode design on  $Da_{II}$  (for an unmodified electrode), and thus fast charging performance we rearrange Eqs. 5.4, 5.7, and 5.8, as follows. The length  $l_\xi$  is the sum of the peak widths in the RCD distribution. Thus,

$$l_\xi = \sum_j \lambda_j = \sum_j \frac{2(\Delta U_\psi)_j}{i_{app} |\kappa_{eff,\psi}^{-1} - \sigma_{eff,\psi}^{-1}|}, \quad (5.15)$$

where the subscript  $j$  represents the number of the plateau. For instance, for the graphite electrodes,  $j$  goes from 1 to 3. Furthermore,  $(\Delta U_\psi)_j$  can be written as the product of the slope,  $\left(\frac{dU_\psi}{dc_{p,\psi}^{surf}}\right)_j$ , and the width,  $(\Delta c_{p,\psi}^{surf})_j$ , of the  $j^{\text{th}}$  plateau. Thus, by combining this form of  $(\Delta U_\psi)_j$  with Eqs. 5.7 and 5.15, we can write  $\xi^{peak}$  as

$$\xi^{peak} = \gamma_\xi i_{app}^2 (|\kappa_{eff,\psi}^{-1} - \sigma_{eff,\psi}^{-1}|) \left( \sum_j 2 \left( \frac{dU_\psi}{dc_{p,\psi}^{surf}} \right)_j (\Delta c_{p,\psi}^{surf})_j \right)^{-1}. \quad (5.16)$$

Now, using Eqs. 5.4 and 5.16,  $Da_{II}$  can be written as

$$Da_{II} = \frac{l_D^2}{D_{eff,\psi}} \left( \frac{\gamma_\xi i_{app}^2 (|\kappa_{eff,\psi}^{-1} - \sigma_{eff,\psi}^{-1}|) \left( \sum_j 2 \left( \frac{dU_\psi}{dc_{p,\psi}^{surf}} \right)_j (\Delta c_{p,\psi}^{surf})_j \right)^{-1}}{Fc_{e,\psi}^0} \right). \quad (5.17)$$

Note that  $l_D = L_\psi$  (the electrode thickness) for an unmodified electrode. Additionally, if  $\kappa_{eff,\psi} \ll \sigma_{eff,\psi}$ , which is observed for many Li-ion battery electrodes, the expression for  $Da_{II}$  becomes

$$Da_{II} = \frac{L_\psi^2}{D_{eff,\psi}} \left( \frac{\gamma_\xi i_{app}^2 \left( \sum_j 2 \left( \frac{dU_\psi}{dc_{p,\psi}^{surf}} \right)_j (\Delta c_{p,\psi}^{surf})_j \right)^{-1}}{Fc_{e,\psi}^0 \kappa_{eff,\psi}} \right). \quad (5.18)$$

By substituting the effective transport properties in terms of intrinsic values and the electrode porosity and tortuosity,  $Da_{II}$  can be written as

$$Da_{II} = \frac{\tau_{\psi}^4 L_{\psi}^2 \gamma_{\xi} i_{app}^2}{\varepsilon_{\psi}^2 D_L \kappa_L F c_{e,\psi}^0} \left( \sum_j 2 \left( \frac{dU_{\psi}}{dc_{p,\psi}^{surf}} \right)_j (\Delta c_{p,\psi}^{surf})_j \right)^{-1}. \quad (5.19)$$

Eq. 5.19 provides some interesting insights on the effect of material properties, electrode design, and operating conditions on  $Da_{II}$  for an unmodified electrode and its corresponding optimal HOLE configuration. As can be seen,  $Da_{II}$  is directly proportional to  $L_{\psi}^2$ ,  $\tau_{\psi}^4$ , and  $i_{app}^2$ . Therefore, increasing the electrode thickness, or tortuosity, or the applied current density nonlinearly increases  $Da_{II}$ . Such nonlinear dependence explains the rapid decrease in accessible capacity that is observed experimentally when either the electrode thickness is increased at a fixed C-rate, or the C-rate is increased for a fixed electrode thickness.<sup>77</sup> Thus, for such an electrode design or operating condition, the optimal inter-channel spacing for the corresponding HOLE configuration is expected to decrease from the values determined in previous sections.

On the other hand,  $Da_{II}$  is inversely proportional to  $\varepsilon_{\psi}^2$ ,  $D_L$ ,  $\kappa_L$ , and  $c_{e,\psi}^0$ , as well as the sum of the OCV drop across the plateaus. Therefore, increasing the electrode porosity or the intrinsic electrolyte diffusivity and conductivity or the initial electrolyte concentration nonlinearly decreases  $Da_{II}$ . Furthermore, selecting an active material with a sloping OCV, i.e., larger  $\left( \frac{dU_{\psi}}{dc_{p,\psi}^{surf}} \right)_j$ , will decrease  $Da_{II}$ . Note that in the absence of such plateaus, the reaction distribution will be more homogeneous, and the width of the electrochemically active region becomes comparable to the thickness of the electrode. This inverse relationship between  $Da_{II}$  and the aforementioned quantities explains the improvement observed in the fast-charging performance when any of following strategies is employed in previous studies: electrolyte with high intrinsic diffusivity and conductivity<sup>157</sup>; electrolyte with high initial concentration<sup>158</sup>; active material with a sloping OCV<sup>23</sup>; and electrode with high porosity.<sup>157</sup> In addition to the improvement of fast-

charging performance of unmodified electrodes, the optimal inter-channel spacing of the corresponding HOLE configuration is expected to decrease from the values determined in previous section.

### 5.3 Chapter 5 Summary

In this chapter, we employed continuum-scale modeling to determine the optimal inter-channel spacing for a hexagonal HOLE pattern. The key findings are summarized below:

1. In general, a decrease in the inter-channel spacing,  $d_h$ , improves fast-charging performance of the HOLE architecture for a constant volume retention,  $\Omega_R$ . However, there exists an optimal value of  $d_h$ , below which there is no significant marginal increase in the performance. This is because at this optimal  $d_h$ , the Li-ion transport is no longer the limiting factor, and other factors such as solid-state diffusion limit the performance. We found the optimal spacing at  $\Omega_R \approx 0.895$  for 4C and 6C charging is  $55 \mu m$  and  $40 \mu m$ , respectively.
2. The effect of  $d_h$  on the performance of the HOLE anode can be quantified in terms of the second Damköhler number,  $Da_{II}$ , which is defined as the ratio between the characteristic diffusion time and characteristic reaction time.  $Da_{II}$  decreases monotonically with  $d_h$ , and the optimal HOLE configuration has  $Da_{II} \sim 1$  throughout charging.
3. A semi-analytical method is also developed to estimate the time-averaged value of  $Da_{II}$ ,  $\langle Da_{II} \rangle_t$ , for a given combination of active material, electrolyte, electrode loading, pattern design,  $\Omega_R$ , channel depth, and C-rate. This method allows an initial screening of the HOLE candidates during the optimization process, and thereby significantly reduces the

computational cost of the overall process. The optimization of the HOLE architecture for 6C charging is provided as an example of the method application.

In summary, this modeling and analytical study provides a detailed mechanistic understanding of the influence of the HOLE design parameters on fast-charging performance of energy-dense electrodes. Through this understanding, the architectures that achieve optimal performance at 4C and 6C have been identified. Although only graphite anodes were considered in this work, the simulation approach employed here can be applied to any porous electrodes for Li-ion batteries. The implications of changes in material properties, electrode design, and operating conditions on the optimal configuration are also discussed. Moreover, the method used here to estimate the second Damköhler number,  $Da_{II}$ , both using the simulation data and the semi-analytical method, can be used for any other active material with at least one plateau in its OCV curve. Further extension that considers local conditions, rather than the cutoff voltage, will enable more a precise determination of optimal architecture and material properties, as well as charging protocols, to achieve fast charging while avoiding Li plating.

## **5.4 Chapter 5 Appendix**

### ***Half-cell configuration***

The half-cell configuration used for the optimization study is shown in Figure 5.8. The details about the Li-metal electrode can be found elsewhere.<sup>159</sup> The thickness of the Li-metal electrode used here is 10  $\mu\text{m}$ .

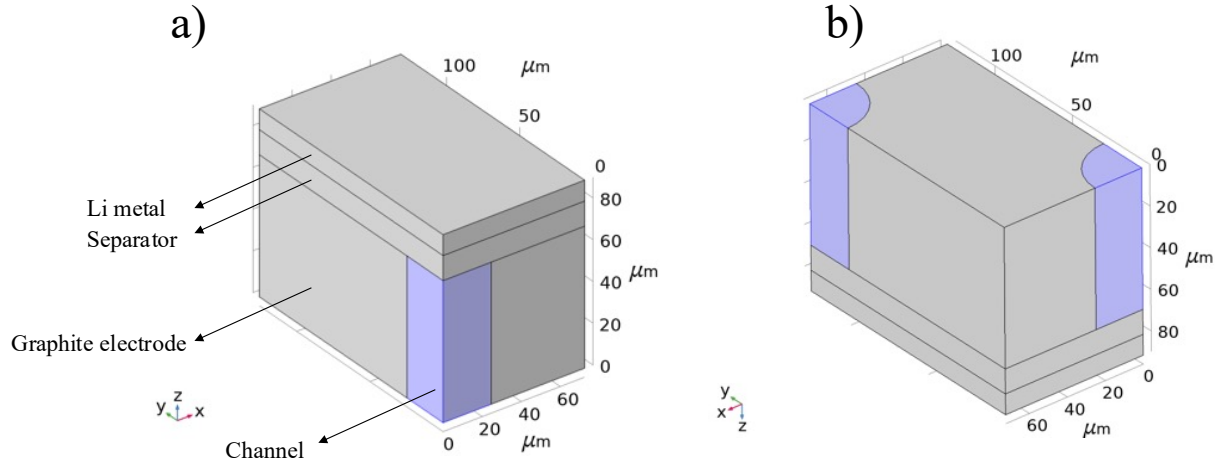


Figure 5.8. The half-cell configuration used in the 3D simulations for the optimization study. The view in (a) shows Li electrode on the top, and (b) shows the graphite electrode on top. The channels are highlighted in blue. Reproduced with permission from Ref. 24. Copyright 2023, the authors. Published by Elsevier B.V.

### ***Results for loading-adjusted (LA) control anode***

Figure 5.9 supplements the results provided in Figure 5.1 with the results for the LA control anode, which has the same active material loading as the HOLE anodes. The loading is adjusted by reducing the volume fraction of the active material (at the fixed volume fraction of fillers), which resulted in an increase in the porosity ( $\approx 39\%$  vs.  $\approx 31.3\%$  of the control anode). Correspondingly,  $\chi_a$  for the LA control anode was adjusted according to the relationship  $\frac{\varepsilon_a}{\tau_a^2}$  and the dependence of  $\tau_a$  on  $\varepsilon_a$  was obtained from the work of Malifarge et al.,<sup>160</sup> who used the impedance data to obtain this dependence. We note that the authors provided a range of relationships between  $\tau_a$  and  $\varepsilon_a$ , and we selected the one that resulted in the smallest value of  $\tau_a$  to obtain the upper bound on the performance of the LA control anode, i.e.,  $\tau_a \propto \varepsilon_a^{-0.25}$ . Note that Malifarge et al.<sup>160</sup> used  $\tau$  to represent the tortuosity factor instead of the tortuosity, which is a square root of the tortuosity factor. Therefore,  $\chi_a \propto \varepsilon_a^{1.5}$ , and thus we estimated  $\chi_a$  to increase by  $\approx 40\%$  upon a  $\approx 25\%$  increase in the porosity. The voltage vs. SOC plot for the LA control anode is provided in Figure 5.9 along with the results for other anodes considered in this work. As can



be seen, the LA anode performs better than the control anode (SOC at the cutoff voltage of 0.215 vs. 0.167) because of the increase in  $\chi_a$ . However, it still performs worse than the HOLE anode with  $d_h = 235 \mu\text{m}$  (the worst performing HOLE anode among the ones studied here). Thus, we conclude that the benefits of the HOLE architecture cannot be realized by increasing the anode porosity to match the overall loading of the HOLE anode.

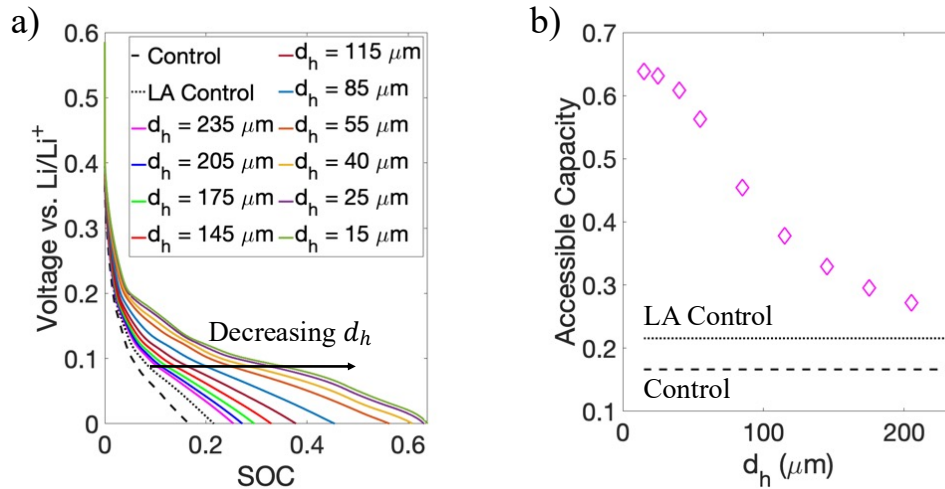


Figure 5.9. Comparison of the 4C results (voltage vs. SOC and the accessible capacity) for the loading-adjusted anode with other anodes considered here. (a) Voltage vs. SOC plot for the two control anodes and HOLE anodes considered in the optimization study at 4C charging. (b) Accessible capacity vs.  $d_h$  for the HOLE anodes; the accessible capacities observed for the control anode and LA control anode are provided for reference using the black dashed and dotted lines, respectively. Reproduced with permission from Ref. 24. Copyright 2023, the authors. Published by Elsevier B.V.

### ***FEM mesh***

A combination of triangular prism and tetrahedral elements was used to discretize the half-cell geometry. To sufficiently resolve the spatial distribution of the RCD, the regions in the graphite electrode near the electrode/separator interface and the channel wall were discretized using a “very fine mesh” setting, as shown in Figure 5.10. If these regions are not sufficiently resolved, the peaks in the RCD exhibit discontinuous and sharply changing behavior. The maximum element size in the region near channel wall and elsewhere was set to  $\approx 2 \mu\text{m}$  and  $\approx 9$

$\mu\text{m}$ , respectively. A total of 35 elements in the direction of the thickness of the electrode were used to discretize the graphite electrode, and the element sizes were obtained using an exponential relation (termed as geometric sequence in COMSOL) with an element ratio of 20. Similarly, a total of 8 elements along the thickness of the separator with an element ratio of 14 were used. Finally, the Li metal domain was discretized using tetrahedral elements to avoid the unnecessary refinement of the corresponding regions in it, which would have resulted if the triangular prism elements were used.

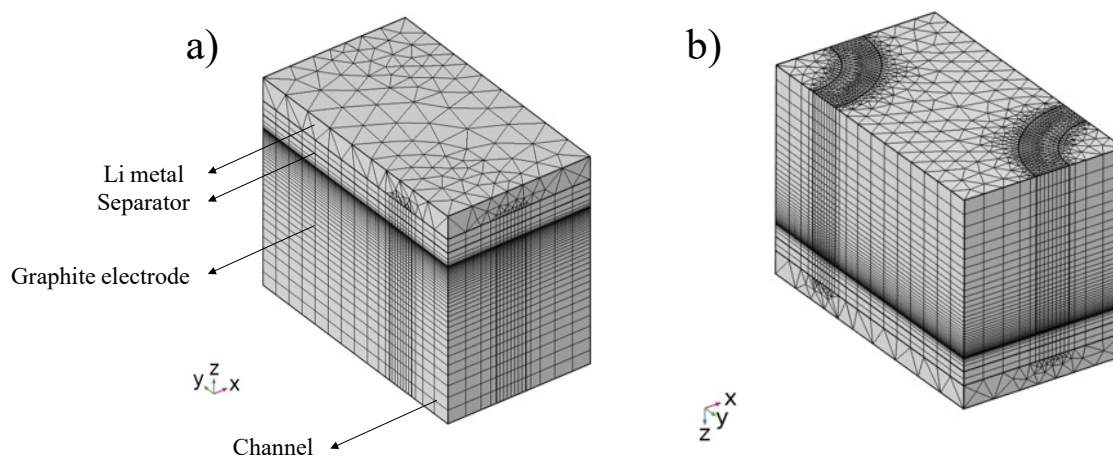


Figure 5.10. The custom mesh used in the 3D simulations for the optimization study. The view in (a) shows Li electrode on the top, and (b) shows the graphite electrode on top. Note that the regions near the anode-separator interface and the channel wall are discretized using a “very fine mesh” setting. Reproduced with permission from Ref. 24. Copyright 2023, the authors. Published by Elsevier B.V.

### ***Data availability***

The shared data for this chapter can be found at the following link:  
<https://doi.org/10.13011/m3-3agy-7y28>.

## CHAPTER 6

### Effect of Material Properties and Microstructure on the Microgalvanic Corrosion Behavior of Mg Alloys\*

#### 6.1 Introduction: Microgalvanic corrosion of Mg alloys

In this chapter, we apply a phase-field model to study the effect of electrochemical properties of the materials and their environment and the spatial distribution of second phases in a magnesium alloy. To this end, we perform sensitivity analyses in which we separately vary the exchange current density and corrosion potential of the second phase, as well as the electrolyte conductivity. We describe the effects of these parameters on the corrosion current and the resulting corrosion-front morphology. We also confirm that the ratio between the Wagner length, calculated for the anodic phase, and the initial width of the anodic domain is a good predictor of the morphological characteristic of the corroding surface. In addition, we examine the effect of the microstructure on the corrosion behavior in both 2D and 3D systems by varying the shape, size, and distribution of the second-phase regions. Our findings provide insights into the influence of the two-phase microstructure on the corrosion behavior in a magnesium alloy.

As described in Chapter 2 (Section 2.2), Mg alloys are of great technological interest for lightweight structural applications, especially in the automotive industry, for several reasons. First, they exhibit one of the highest strength-to-weight ratios among structural alloys.<sup>46,161</sup> Second, they

---

\* This chapter is adapted from V. Goel et al., 2023, submitted to Journal of the Electrochemical Society, in revision,<sup>31</sup> and V. Goel et al., MRS Communications, 12, (2022), 1050.<sup>26</sup>

exhibit relative ease of machining (milling and turning) compared to other lightweight structural materials like Al.<sup>46,161</sup> Third, they offer other desirable properties such as high thermal conductivity, high recyclability, and nontoxicity.<sup>46</sup> Despite these remarkable properties, structural applications of Mg alloys remain limited. One of the key reasons behind this limited use is the poor corrosion resistance of Mg alloys,<sup>46,162,163</sup> primarily due to the low standard reduction potential (-2.37 V) of Mg compared to most metals.<sup>46</sup> Even the corrosion behavior of pure Mg is quite complex due to anomalous hydrogen evolution during its anodic polarization (also known as the negative difference effect).<sup>164–166</sup> The corrosion behavior of Mg alloys are further complicated by different mechanisms that could lead to localized corrosion.<sup>46,167,168</sup> One of the leading mechanisms that cause localized corrosion is the microgalvanic coupling between the various phases in the alloy microstructure that have different electrochemical potentials.<sup>46,50,53,169–172</sup> Microgalvanic corrosion is highly dependent not only on the alloying elements, which influence the electrochemical properties of various phases, but also on the alloy processing, which determines the alloy microstructure, as well as on the surrounding environment. Thus, due to its dependence on multiple factors, understanding and mitigating microgalvanic corrosion is challenging.

Several experimental and modeling studies have examined the roles of the aforementioned factors on the corrosion behavior of Mg alloys, including the effect of alloying elements<sup>162,163,173,174</sup> and the microstructure.<sup>26,46,49,50,53,167,169–172,175–177</sup> Many alloys form a two-phase system: one is the solute-rich  $\beta$  phase (which is the minority/second phase), and the other is the solute-depleted  $\alpha$  phase. In most Mg alloys, a microgalvanic couple is formed between the  $\beta$  phase that acts as a cathode and the  $\alpha$  phase that acts as an anode.<sup>46,53,163,170–175</sup> An exception of this behavior occurs

for Mg-Ca alloys,<sup>46,49</sup> where the opposite is observed. Owing to such microgalvanic coupling between the  $\alpha$  and  $\beta$  phases, Mg alloys often exhibit a higher corrosion rate than pure Mg.<sup>46</sup>

Predicting the location and extent of the microgalvanic corrosion is not straightforward due to the strong dependence of the microgalvanic coupling on the microstructure. For instance, Song et al.<sup>50</sup> reported that the microgalvanic coupling in the AZ91 alloy is strong when large  $\alpha$  domains exist in the microstructure between  $\beta$  precipitates. However, they observed a significantly lower corrosion rate when the  $\beta$  phase forms a continuous network in the microstructure, acting as a barrier along the alloy surface. Deshpande further explained these results in their modeling study,<sup>177</sup> which showed that although the continuous network of  $\beta$  reduced the corrosion rate at later times, this reduction only happened once the  $\alpha$  phase present on the alloy surface corroded fully. These studies show that the effect of the microstructure on microgalvanic corrosion is quite complex and changes as corrosion progresses. Therefore, to understand the mechanisms involved, one needs to examine the effect of each underlying variable that affects corrosion separately. However, such examinations are challenging to conduct via experiments alone because of the difficulty in decoupling the effects of different variables. For instance, any heat treatment of alloys not only alters the microstructure but also changes the distribution of the alloying elements in various phases, which can affect their electrochemical properties.

To overcome the aforementioned challenge, we perform a series of phase-field simulations and study the effect of the exchange current density and corrosion potential of the  $\beta$  phase, as well as the electrolyte conductivity, on the microgalvanic corrosion behavior. Furthermore, we also investigate the effect of the microstructure on the corrosion behavior by varying the size/shape and spatial distribution of the  $\beta$  phase in both 2D and 3D systems; specifically, we provide insights

into the influence of the presence of an alternating arrangement of the  $\alpha$  and  $\beta$  domains (lamellar region) on the corrosion behavior.

## 6.2 Governing equations for microgalvanic corrosion

We employ the phase-field model<sup>26</sup> that describes the evolution of the anodic phase/electrolyte interface due to microgalvanic corrosion with a cathodic phase under the assumption that the electrolyte is well-stirred and under the condition of free immersion. We describe all model equations in the following text and provide a list of symbols used in the equations in Table 6.1, along with their description. The phase-field method is employed as a computational tool to track the evolution of microstructures formed by various phases present in the system. In this approach, the region occupied by each phase is described by a field variable known as the order parameter or phase field. The phase field takes a value of 1 within the corresponding phase and 0 outside. At the interface between the phase and another phase, its phase field smoothly transitions from 1 to 0.

Given  $\{\varphi_j\}$ , which are the phase fields for the metallic phases, and  $\psi$ , which is the phase field for the electrolyte, the free energy functional for a system can be written as<sup>178</sup>

$$\tilde{\mathcal{F}} = \int_{\Omega} \left( f_0(\{\varphi_j\}, \psi) + \frac{\tilde{\epsilon}^2}{2} \left( \sum_{j=1}^N (\nabla \varphi_j)^2 + (\nabla \psi)^2 \right) \right) d\Omega, \quad (6.1)$$

where  $\tilde{\epsilon}$  is the gradient energy coefficient and  $\Omega$  represents the system volume. Note that the quantities  $\tilde{\mathcal{F}}$  and  $\tilde{\epsilon}^2$  are normalized by the height of the double well that has units of J/m<sup>3</sup>. The bulk free energy  $f_0$  is given by<sup>178</sup>

$$f_0(\{\varphi_j\}, \psi) = \sum_{j=1}^N \left( \frac{\varphi_j^4}{4} - \frac{\varphi_j^2}{2} \right) + \left( \frac{\psi^4}{4} - \frac{\psi^2}{2} \right) + \frac{3}{2} \sum_{j=1}^N \sum_{k>j}^N \varphi_j^2 \varphi_k^2 + \frac{3}{2} \sum_{j=1}^N \varphi_j^2 \psi^2, \quad (6.2)$$

which is constructed to enforce that the value of phase fields in equilibrium states be either 0 or 1.

The evolution of the phase fields corresponding to the anodic phase and the electrolyte are modeled using the Cahn-Hilliard equation with a source term as<sup>179,180</sup>

$$\frac{\partial \varphi_1}{\partial t} = \nabla \cdot \left( M_{\varphi_1} \nabla \frac{\delta \tilde{\mathcal{F}}}{\delta \varphi_1} \right) + v |\nabla \psi|, \quad (6.3)$$

and

$$\frac{\partial \psi}{\partial t} = \nabla \cdot \left( M_{\psi} \nabla \frac{\delta \tilde{\mathcal{F}}}{\delta \psi} \right) - v |\nabla \psi|, \quad (6.4)$$

where  $M_{\varphi_1}$  and  $M_{\psi}$  are the mobilities for phases  $\varphi_1$  and  $\psi$ , respectively, and  $v$  is the normal component of the velocity of the anodic phase/electrolyte interface.

The velocity is related to the anodic reaction current density (RCD),  $i_{rxn,1}$ , and an interpolation function for the anodic phase,  $\xi_1$ , which is equal to 0 in the cathodic phase and 1 in the anodic phase, via<sup>181</sup>

$$v = - \frac{V_m \xi_1 i_{rxn,1}}{z_m F}, \quad (6.5)$$

where  $V_m$  is the molar volume of the corroding metal,  $z_m$  is the charge number of the corresponding metallic cation in the electrolyte, and  $F$  is Faraday's constant. The equations used to calculate  $i_{rxn,1}$  and  $\xi_1$  are described below. It is important to note that the terms proportional to  $v$  on the right-hand side Eqs. 6.3 and 6.4 are not due to the bulk motion. Rather, these terms are added as source terms to model the motion of the electrolyte/anodic phase interface due to the corrosion

reaction at the interface. Note that multiplication by the magnitude of the gradient of  $\psi$  confines the region where these terms are nonzero. In Eq. 6.3, the Cahn-Hilliard dynamics, rather than the Allen-Cahn dynamics, was chosen to describe the evolution of  $\varphi_1$  to ensure that the change in mass of anodic phase is due only to the corrosion reaction. We use the same approach for the electrolyte phase (Eq. 6.4) but with the opposite sign of the source term to ensure the direction of the interfacial displacement is correct.<sup>181</sup> We do not consider any deposition on the cathodic phase, and thus the evolution of  $\varphi_2$  is given by the Cahn-Hilliard equation<sup>180</sup> as

$$\frac{\partial \varphi_2}{\partial t} = \nabla \cdot \left( M_{\varphi_2} \nabla \frac{\delta \tilde{\mathcal{F}}}{\delta \varphi_2} \right), \quad (6.6)$$

where  $M_{\varphi_2}$  is the mobility for the phase  $\varphi_2$ . While corrosion does not affect the cathodic phase, it is important to evolve this equation so that the order parameters adjust accordingly to the free energy functional in Eq. 6.2 as other order parameters evolve; without doing so can lead to undesired numerical artifacts and instability.

Following the approach proposed by Chadwick et al.,<sup>181</sup> we assume the mobilities for all phases to be the same and dependent on the anodic reaction current density such that the Peclet number,  $v\delta/M$ , associated with the interfacial width,  $\delta = 2\sqrt{2\tilde{\epsilon}^2}$ , to be unity. This condition ensures that the moving interface maintains the profile required by the free energy functional:

$$M_{\varphi_1} = M_{\varphi_2} = M_{\psi} = M = 2 \frac{V_m |\xi_1 i_{rxn,1}| \psi}{z_m F} \sqrt{2\tilde{\epsilon}^2}. \quad (6.7)$$

We assume that the electrolyte remains electrically neutral, which ensures that the bulk motion of the electrolyte does not contribute to the electrolyte current density.<sup>35</sup> We also assume that the electrolyte concentration remains constant and uniform, which corresponds to a well-stirred system.<sup>35</sup> These assumptions are in line with previous modeling studies.<sup>26,176,177</sup> Under these



assumptions, where diffusive and convective contributions are absent, the ionic flux arises solely from the migration current, i.e.,  $\mathbf{i}_e = -\kappa_e \nabla \Phi_e$ . The governing equation for ionic transport is derived by combining this with the condition of charge conservation and charge neutrality in the electrolyte, i.e.,  $\nabla \cdot \mathbf{i}_e = 0$ . Finally, the resulting equation is formulated using the Smoothed Boundary Method (SBM)<sup>75</sup> to incorporate the flux boundary conditions at the metal/electrolyte interface arising from the electrochemical reaction and the zero-normal-flux boundary conditions at domain boundaries, as derived in a previous work<sup>26</sup>:

$$\nabla \cdot (\psi \kappa_e \nabla \Phi_e) = -|\nabla \psi| i_{rxn}, \quad (6.8)$$

where

$$i_{rxn} = \sum_{j=1}^2 \xi_j i_{rxn,j}, \quad (6.9)$$

where  $\xi_j$  is an interpolation function that varies from 0 to 1, which indicates the region of the corresponding phase. The interpolation functions,  $\xi_1$  and  $\xi_2$ , are used to combine the anodic and cathodic RCDs into a single spatially dependent field, are calculated by

$$\xi_2 = \frac{\varphi_2}{\max(\varphi_1 + \varphi_2, \zeta)}, \quad (6.10)$$

$$\xi_1 = 1 - \xi_2, \quad (6.11)$$

where  $\zeta$  is a small number added to the denominator to avoid division by zero. Note that even though  $i_{rxn}$  is calculated throughout the system, its value is only meaningful in the interfacial

regions and affects the electrolyte potential only where  $|\nabla\psi|$  is nonzero, i.e., at the metal/electrolyte interface.

The anodic reaction current density (RCD) is obtained by a modified Tafel relation that restricts the value as it approaches the limiting current<sup>182</sup>:

$$i_{rxn,1} = \frac{i_{corr,1}e^{\eta_1/A_1}}{1 + \frac{i_{corr,1}e^{\eta_1/A_1}}{i_{max}}}, \quad (6.12)$$

where  $i_{corr,1}$  is the corrosion current density for the anodic phase,  $\eta_1$  is the anodic overpotential given by  $\Phi_m - \Phi_e - E_{corr,1}$ ;  $\Phi_m$  and  $E_{corr,1}$  represent the applied electrostatic potential of the metal and the corrosion potential of the anodic phase, respectively; and  $A_1$  is the corresponding Tafel slope. In Eq. 6.12, the current density smoothly approaches  $i_{max}$  as  $i_{0,1}e^{\eta_1/A_1}$  becomes large, and thus  $i_{max}$  sets the maximum current density. This constraint is added to account for any kinetic limitations such as limiting ionic transport in the electrolyte or charge transfer current density that may exist in the system due to surface passivation or the deposition of the corrosion product.<sup>182</sup> We assume no such limitation on the cathode, and thus the cathodic RCD is obtained using the standard Tafel relation as<sup>182</sup>

$$i_{rxn,2} = -i_{corr,2}e^{\eta_2/A_2}, \quad (6.13)$$

where  $\eta_2 = \Phi_m - \Phi_e - E_{corr,2}$ , and the cathodic corrosion current density, the corrosion potential, and the Tafel slope for the cathodic phase are denoted by  $i_{corr,2}$ ,  $E_{corr,2}$ , and  $A_2$ , respectively. Note that we assume that the metallic conductivity is large enough to ensure that  $\Phi_m$  is constant throughout the metal. Additionally, we assume corrosion to advance under an unbiased condition, i.e., free immersion, and thus we set  $\Phi_m = 0$ . Furthermore, the use of natural (zero-normal-derivative) boundary conditions for  $\Phi_e$  on the borders of the system in contact with the electrolyte

ensures that the net current along the metal/electrolyte interfaces is zero. This can be shown by applying the divergence theorem on the volume (area in 2D) occupied by the electrolyte along with the equation for charge conservation in the electrolyte,  $\nabla \cdot \mathbf{i}_e = 0$ .

Table 6.1 List and description of the variables and symbols used in the model equations.<sup>31</sup>

Symbol	Description
$\bar{\mathcal{F}}$	Free energy functional of the system normalized by the double well height; $\text{m}^3$
$\Omega$	Volume of the computational domain; $\text{m}^3$
$\tilde{\epsilon}$	Energy penalty coefficient for the gradient in phase fields, which is normalized by the double well height; m
$f_0$	Nondimensionalized bulk free energy density function; unitless
$\psi$	Domain parameter and phase field for the electrolyte phase; unitless
$\varphi_j$	Phase field for the $j^{\text{th}}$ phase within the metal domain; unitless
$j$	Subscript for denoting the phase in metal; $j = 1$ represents the anodic phase, and $j = 2$ represents the cathodic phase
$M$	Mobility coefficients in the Cahn-Hilliard equations; $\text{m}^2/\text{s}$
$v$	Normal velocity of the $\varphi_1/\psi$ interface; $\text{m}/\text{s}$
$i_{rxn}$	Reaction current density; $\text{A}/\text{m}^2$
$V_m$	Molar volume of the corroding metal; $\text{m}^3/\text{mol}$
$z_m$	Charge number of the corroding-metal ion in the electrolyte
$F$	Faraday's constant; $\text{C}/\text{mol}$
$\kappa_e$	Electrolyte conductivity; $\text{S}/\text{m}$
$\Phi_e$	Electrostatic potential of the electrolyte; V
$\mathbf{i}_e$	Ionic current density in the electrolyte; $\text{A}/\text{m}^2$
$\xi_j$	Interpolation factor for the reaction current density; unitless
$i_{rxn,j}$	Reaction current density for the $j^{\text{th}}$ phase; $\text{A}/\text{m}^2$
$i_{corr,j}$	Exchange current density for the $j^{\text{th}}$ phase; $\text{A}/\text{m}^2$
$\eta_j$	Overpotential for the $j^{\text{th}}$ phase; V
$E_{corr,j}$	Equilibrium corrosion potential for the $j^{\text{th}}$ phase; V
$A_j$	Tafel slope for the $j^{\text{th}}$ phase; V

$i_{max}$	Maximum reaction current density; A/m <sup>2</sup>
$\phi_m$	Electrostatic potential of the metal; V
$\zeta$	A small number that is added to the denominator of the expression for $\xi_2$ (Eq. 6.10) to avoid division by zero; unitless

In this study, the subscripts 1 and 2 are replaced by  $\alpha$  and  $\beta$ , respectively, to make it easier for the reader to follow which phase a quantity belongs to. For example,  $i_{corr,\beta}$  represents the exchange current density of the  $\beta$  phase. The values of the model parameters are obtained from literature and are listed in Table 6.2. All simulations in this study are conducted for unbiased conditions, i.e., corrosion occurs only because of the microgalvanic coupling between the anodic and cathodic phases, and the net current in the system is zero. Furthermore, natural (zero-normal-derivative) boundary conditions are applied for all fields at every boundary of the computational domain. Finally, the model equations were implemented in the PRISMS-PF framework,<sup>27</sup> an open-source phase-field solver, as described elsewhere.<sup>26</sup>

Table 6.2. Parameter values used in the simulations presented here, unless specified otherwise, along with their sources.<sup>31</sup>

Parameter	Value	Units	Source
$V_m$	$1.37 \times 10^{-5}$	m <sup>3</sup> /mol	Literature <sup>183</sup>
$z_m$	2	--	--
$\kappa_e$	$5 \times 10^{-3}$	S/m	Literature <sup>184</sup>
$i_{\text{corr},\alpha}$	$8.1 \times 10^{-2}$	A/m <sup>2</sup>	Literature <sup>176</sup>
$i_{\text{corr},\beta}$	$1.7 \times 10^{-2}$	A/m <sup>2</sup>	Literature <sup>176</sup>
$i_{\text{max}}$	100	A/m <sup>2</sup>	--
$A_\alpha$	$3.474 \times 10^{-3}$	V	Literature <sup>176</sup>
$A_\beta$	$-3.626 \times 10^{-2}$	V	Literature <sup>176</sup>
$E_{\text{corr},\alpha}$	-1.424	V (SCE)	Literature <sup>176</sup>
$E_{\text{corr},\beta}$	-1.151	V (SCE)	Literature <sup>176</sup>
$\zeta$	$1 \times 10^{-3}$	--	--

### 6.3 Simulation results for the effect of the material properties of the $\beta$ phase, the electrolyte, and the alloy microstructure on corrosion behavior

#### 6.3.1 Sensitivity analyses

Sensitivity analyses were performed to understand the effect of model input parameters on the predicted microgalvanic-corrosion behavior in Mg alloys, where we considered three parameters:  $i_{\text{corr},\beta}$ ,  $E_{\text{corr},\beta}$ , and  $\kappa_e$ . Values of  $i_{\text{corr},\beta}$  and/or  $E_{\text{corr},\beta}$  depends on the material composition of the alloy and/or the electrolyte surrounding the alloy. On the other hand,  $\kappa_e$  is a property of the surrounding electrolyte. To ensure that the change in  $i_{\text{corr},\beta}$  and  $E_{\text{corr},\beta}$  is only due to the change in the material composition, we chose these values from the experiments performed using the same electrolyte, 0.1 M NaCl aqueous solution.<sup>46,163,183</sup> We chose this electrolyte because

of the abundance of studies<sup>46,163,183</sup> carried out using this solution. We performed the sensitivity analyses in a 2D system containing a  $\beta$  precipitate embedded in an  $\alpha$  matrix, as described elsewhere,<sup>26</sup> in order to reduce the computational cost. The computational details, such as the element size, the element order, and the time step size, used for the sensitivity analyses are provided in Section 6.5 (see Table 6.5 and the associated text).

To perform the sensitivity analysis, we only altered the value of one model parameter (out of  $i_{\text{corr},\beta}$ ,  $E_{\text{corr},\beta}$ , and  $\kappa_e$ ) and kept all other model parameters fixed. The values for each of the parameters studied are obtained from the ranges reported in the literature – Ref. 46,163,183 are used for  $i_{\text{corr},\beta}$ ,  $E_{\text{corr},\beta}$ , and Ref. 184 is used for  $\kappa_e$ . The effect of each physical parameter is then studied in terms of *corrosion current*, as defined by the integration of the corrosion current density over the  $\alpha$ /electrolyte interface in the computational domain, which varies with time. Additionally, the morphology and position of the  $\alpha$ /electrolyte interface are qualitatively examined. Finally, we use the ratio between the Wagner length for the  $\alpha$  phase and the initial width of the  $\alpha$  phase as a metric to study the uniformity of corrosion along the  $\alpha$ /electrolyte interface, as explained in the following section.

### ***6.3.1.1 Sensitivity analysis with respect to $i_{\text{corr},\beta}$***

In this section, we examine the effect of  $i_{\text{corr},\beta}$ , which is the exchange current density for the  $\beta$  phase. As can be seen in Eq. 6.13 (with subscript 2 being  $\beta$ ), the corrosion current density on the  $\beta$  phase is directly proportional to  $i_{\text{corr},\beta}$ . Thus, the corrosion current is also expected to be proportional to  $i_{\text{corr},\beta}$  if the electrolyte potential is assumed to remain constant. It is reported in the literature that  $i_{\text{corr},\beta}$  ranges between  $10^{-3}$  to  $1 \text{ A/m}^2$  for most second phases of Mg alloys

immersed in 0.1 M NaCl aqueous solution.<sup>46,163,183</sup> Therefore, we chose five values of  $i_{\text{corr},\beta}$  in this range:  $5 \times 10^{-3}$ ,  $1.7 \times 10^{-2}$ ,  $5 \times 10^{-2}$ ,  $1 \times 10^{-1}$ , and  $1 \text{ A/m}^2$ . The value of  $1.7 \times 10^{-2} \text{ A/m}^2$  represents the baseline value, which was used in a previous study<sup>26</sup> and corresponds to the AM30 alloy.<sup>176,177</sup> The remaining model parameters were kept the same, which are listed in Table 6.2. The results of the sensitivity analysis are summarized in Figure 6.1.

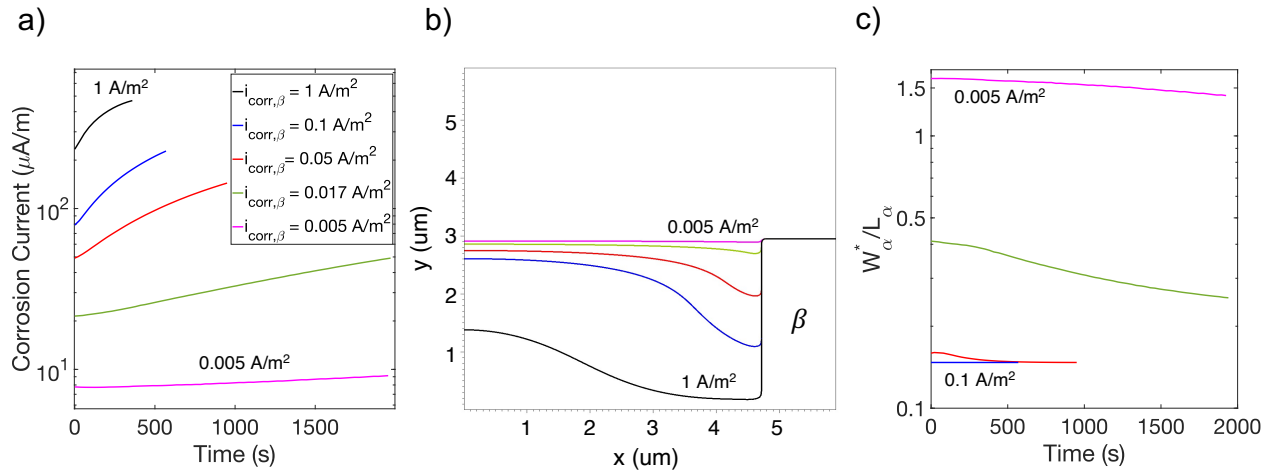


Figure 6.1. Results for the corrosion current, morphology of the corroded surface, and the Wagner length from the sensitivity analysis with respect to the exchange current density of the  $\beta$  phase. (a) The log-linear plot of the corrosion current vs. time. (b) The metal/electrolyte interface at  $t = 390 \text{ s}$ . (c) The log-linear plot of  $W_{\alpha}^*/L_{\alpha}$  vs. time. The values of  $i_{\text{corr},\beta}$  varies from  $0.005 \text{ A/m}^2$  to  $1 \text{ A/m}^2$ , as presented in the legend provided in (a), which applies to all subfigures.<sup>31</sup>

Figure 6.1a shows the plot of the corrosion current vs. time for the values of  $i_{\text{corr},\beta}$  examined. Two trends can be observed. First, for a fixed  $i_{\text{corr},\beta}$  value, the corrosion current increases with time. This occurs because, for the given system and condition (e.g., the  $\beta$  fraction), the corrosion reaction is limited by the cathode. Hence, when more  $\beta$  is exposed to the electrolyte upon the corrosion of the  $\alpha$  phase, the corrosion current increases. Second, increasing  $i_{\text{corr},\beta}$  monotonically increases the corrosion current. In fact, when  $i_{\text{corr},\beta}$  is increased from  $1.7 \times 10^{-2}$  to  $1 \times 10^{-1}$  (by a factor of  $\sim 5.9$ ), the initial corrosion current (at  $t = 0 \text{ s}$ ) increases by a factor of

~3.7. Similarly, when  $i_{\text{corr},\beta}$  is reduced from  $1.7 \times 10^{-2}$  to  $5 \times 10^{-3}$  (a reduction by a factor of ~3.4), the initial corrosion current (at  $t = 0$  s) decreases by ~2.7 times. This result shows that although the corrosion current monotonically increases with  $i_{\text{corr},\beta}$ , it does not depend linearly on  $i_{\text{corr},\beta}$ ; rather, it scales sublinearly with  $i_{\text{corr},\beta}$ , i.e., the corrosion current  $\propto (i_{\text{corr},\beta})^p$ , where  $p < 1$ . The observed sublinearity arises because of the spatial distribution of the electrolyte potential changes when  $i_{\text{corr},\beta}$  is altered, as shown in Figure 6.2, which is nonlinearly related to the reaction current density through the exponential term in the Tafel relations (see Eqs. 6.8, 6.9, and 6.12).

Figure 6.1b shows the metal/electrolyte interface for all cases at  $t = 390$  s, which is the time when the  $\alpha$  domain near  $\alpha/\beta$  interface is almost fully corroded within the simulation domain for  $i_{\text{corr},\beta} = 1$  A/m<sup>2</sup>. Three distinct features emerge from the plot. First, as expected from the above discussion of the observed increase in the corrosion current with  $i_{\text{corr},\beta}$ , the depth of corrosion increases as  $i_{\text{corr},\beta}$  is increased. Second, the morphology of the interface for  $i_{\text{corr},\beta} = 1$  A/m<sup>2</sup> is distinct from the other cases. This occurs because, for this case, the corrosion current density near the  $\alpha/\beta$  interface calculated by the standard Tafel relationship would exceed the maximum corrosion current density,  $i_{\text{max}}$ . Therefore, the corrosion current density in the region becomes relatively uniform with the limiting value of  $i_{\text{max}}$  per the modified Tafel relationship (Eq. 6.12). Figure 6.3a shows that the morphology of the corroding surface for  $i_{\text{corr},\beta} = 1$  A/m<sup>2</sup> reverts to one that resembles those of smaller  $i_{\text{corr},\beta}$  values when a sufficiently large  $i_{\text{max}}$  is used. Lastly, all cases with  $i_{\text{corr},\beta} > 5 \times 10^{-3}$  A/m<sup>2</sup> exhibit nonuniform corrosion, where a greater extent of corrosion is observed near the  $\alpha/\beta$  interface than elsewhere. Note that for  $i_{\text{corr},\beta} = 5 \times 10^{-3}$  A/m<sup>2</sup> relatively uniform corrosion is observed even at later times, as shown in Figure 6.3b.



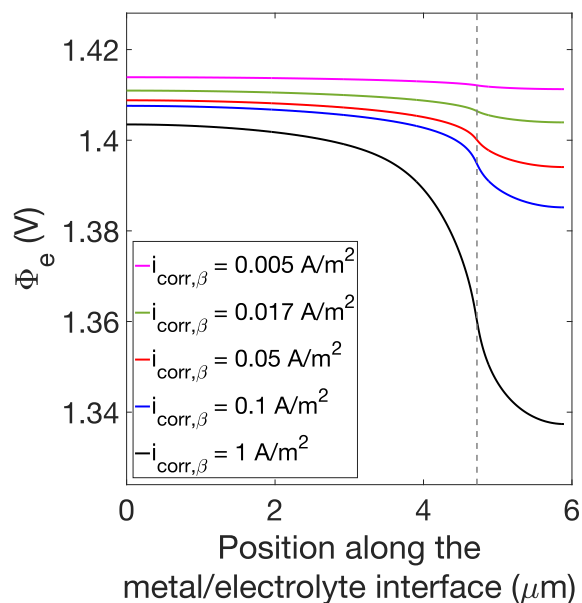


Figure 6.2. The plot of the electrolyte potential,  $\Phi_e$ , along the metal/electrolyte interface at  $t = 0$  s for different values of  $i_{\text{corr},\beta}$  considered in the sensitivity analysis. The grey dashed line represents the  $\alpha/\beta$  interface; the  $\beta$  domain lies on the right side of the line.<sup>31</sup>

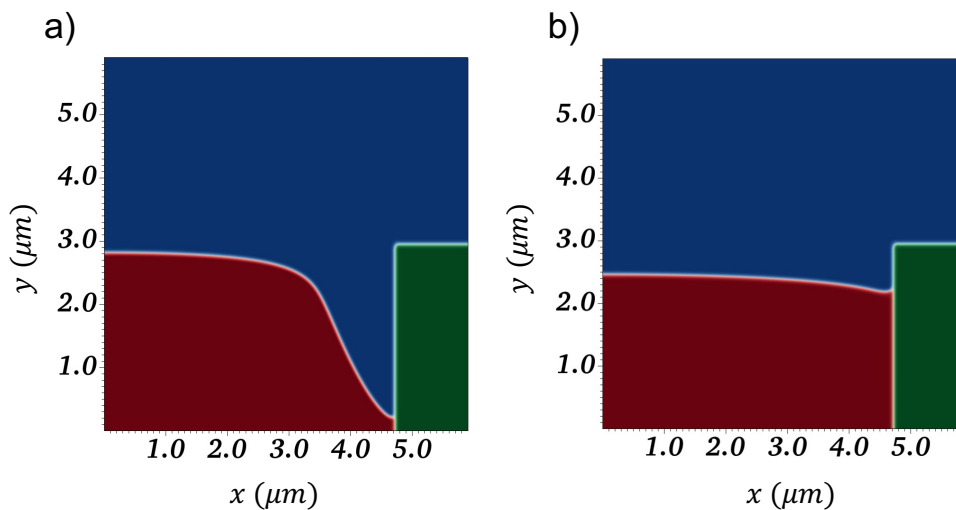


Figure 6.3. The simulated morphology of the metal/electrolyte interface for (a)  $i_{\text{corr},\beta} = 1 \text{ A/m}^2$  and  $i_{\text{max}} = 1 \times 10^3 \text{ A/m}^2$  at  $t = 72\text{s}$  and (b)  $i_{\text{corr},\beta} = 5 \times 10^{-3} \text{ A/m}^2$  and  $i_{\text{max}} = 1 \times 10^2 \text{ A/m}^2$  at  $t = 4000 \text{ s}$ . The red, green, and blue regions correspond to the  $\alpha$ ,  $\beta$ , and electrolyte phases, respectively.<sup>31</sup>

To explain the differences in the uniformity of corrosion along the  $\alpha$ /electrolyte interface observed for different  $i_{\text{corr},\beta}$  values, we examined the Wagner length corresponding to the  $\alpha$  phase. The Wagner length,  $W$ , for any electrode is defined as<sup>185</sup>

$$W = \kappa_e \frac{\partial \eta}{\partial i_{rxn}}, \quad (6.14)$$

where  $\eta$  and  $i_{rxn}$  are the electrode overpotential and reaction current density, respectively. Wagner<sup>185</sup> showed that the ratio between the Wagner length and the characteristic length of the electrode determines the uniformity of the current density distribution over the electrode. Specifically, when the ratio is significantly larger than 1 (i.e., large  $W$  compared to the characteristic length), the current density distribution is expected to be uniform over the electrode.<sup>185</sup> Conversely, when the ratio is significantly smaller than 1, the current density distribution is expected to be nonuniform.<sup>185</sup> Furthermore, Wagner<sup>185</sup> also showed for a planar electrode, the characteristic length is the width of the electrode.

Following Wagner's formulation, we obtained the Wagner length for the  $\alpha$  phase,  $W_\alpha$ , using Eq. 6.14. Note that  $\frac{\partial \eta}{\partial i_{rxn}}$  for the  $\alpha$  phase was calculated using the numerical solution obtained from the simulations. Moreover, we set the characteristic length equal to the initial width of the  $\alpha$  phase,  $L_\alpha$ , and thus the ratio  $W_\alpha/L_\alpha$  was used to examine the effect of  $i_{\text{corr},\beta}$  on the uniformity of corrosion along the  $\alpha$ /electrolyte interface. We note that the Wagner length for only the  $\alpha$  phase was calculated since it is the corroding phase.

The calculated value of  $W_\alpha$  for  $i_{\text{corr},\beta} = 1.7 \times 10^{-2}$  A/m<sup>2</sup> is provided at  $t = 1110$  s in Figure 6.4. As can be seen, the value of  $W_\alpha$  varies along the  $\alpha$ /electrolyte interface, with the smallest value occurring near the  $\alpha/\beta$  interface where the corrosion current density is largest.

Thus, the most stringent condition, given by taking the minimum value of  $W_\alpha$  (or the minimum value of the ratio, as  $L_\alpha$  is a constant) over the  $\alpha$ /electrolyte interface, is used to determine the expected degree of uniformity in the corrosion current density distribution. We denote the minimum of  $W_\alpha$  as  $W_\alpha^*$  hereafter. Figure 6.1c shows the plot of  $W_\alpha^*/L_\alpha$  vs. time for all cases, except for  $i_{\text{corr},\beta} = 1 \text{ A/m}^2$ , where the current density is limited by  $i_{\text{max}}$ , as discussed above. The  $W_\alpha^*/L_\alpha$  value for all cases, except  $i_{\text{corr},\beta} = 5 \times 10^{-3} \text{ A/m}^2$ , is much smaller than 1 throughout corrosion. Correspondingly, nonuniform corrosion is observed along the  $\alpha$ /electrolyte interface for these values of  $i_{\text{corr},\beta}$  in Figure 6.1b. Conversely, the  $W_\alpha^*/L_\alpha$  value for  $i_{\text{corr},\beta} = 5 \times 10^{-3}$  is larger than 1, and the simulation shows a relatively uniform corrosion along the  $\alpha$ /electrolyte interface in this case, as compared to the larger values of  $i_{\text{corr},\beta}$ . Finally, the monotonic decrease in  $W_\alpha^*/L_\alpha$  with time suggests an increase in the nonuniformity of the current density distribution over the  $\alpha$ /electrolyte interface with time according to the Wagner theory.

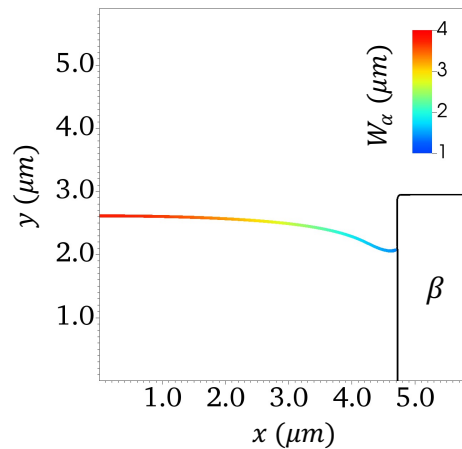


Figure 6.4. The plot of  $W_\alpha$  along the  $\alpha$ /electrolyte interface for  $i_{\text{corr},\beta} = 1.7 \times 10^{-2} \text{ A/m}^2$  at  $t = 1110 \text{ s}$ . The color indicates the value of  $W_\alpha$  according to the color bar on the right.<sup>31</sup>

In summary, this sensitivity analysis shows that  $i_{\text{corr},\beta}$  strongly affects the microgalvanic corrosion behavior and that decreasing it reduces localized corrosion, both by reducing the overall rate and enhancing the uniformity. However, the change in the corrosion current is sublinearly dependent on  $i_{\text{corr},\beta}$ . Thus, a significantly larger reduction in  $i_{\text{corr},\beta}$  is required to achieve the reduction in the corrosion current. This result could potentially have a direct consequence on passivation techniques<sup>186</sup> that aim at reducing  $i_{\text{corr},\beta}$  to mitigate localized corrosion.

### 6.3.1.2 Sensitivity analysis with respect to $E_{\text{corr},\beta}$

The parameter  $E_{\text{corr},\beta}$  represents the equilibrium corrosion potential for the  $\beta$  phase, which is the cathodic phase in this study. In a galvanic couple, increasing the difference between the equilibrium potentials of the anode and the cathode amplifies the strength of the coupling, which increases the corrosion current. Therefore, given that we limit our studies to cases where  $E_{\text{corr},\beta} > E_{\text{corr},\alpha}$ , raising  $E_{\text{corr},\beta}$  increases the difference between  $E_{\text{corr}}$  of the two phases and is thus expected to increase the corrosion current. As reported in the literature,<sup>46,163,183</sup> the value of  $E_{\text{corr},\beta}$  ranges from -1.6 V to -1 V vs. the standard calomel electrode (SCE) for most second phases in Mg alloys immersed in 0.1 M NaCl aqueous solution. Since we restrict the cases to  $E_{\text{corr},\beta} > E_{\text{corr},\alpha}$  and  $E_{\text{corr},\alpha} = -1.424$  V vs. SCE in this study (see Table 6.2), we chose five values of  $E_{\text{corr},\beta}$ , namely, -1.3, -1.25, -1.2, -1.151, and -1.1 V. We did not examine values above -1.1 V because the resulting reaction current density would be limited by  $i_{\text{max}}$ , which leads to a similar result seen for  $i_{\text{corr},\beta} = 1$  A/m<sup>2</sup> in Section 6.3.1.1. Note that the value of -1.151 V represents the baseline case, which was used in a previous work<sup>26</sup> and corresponds to the AM30 alloy.<sup>176,177</sup> The remaining

model parameters were kept the same as listed in Table 6.2. The results are summarized in Figure 6.5.

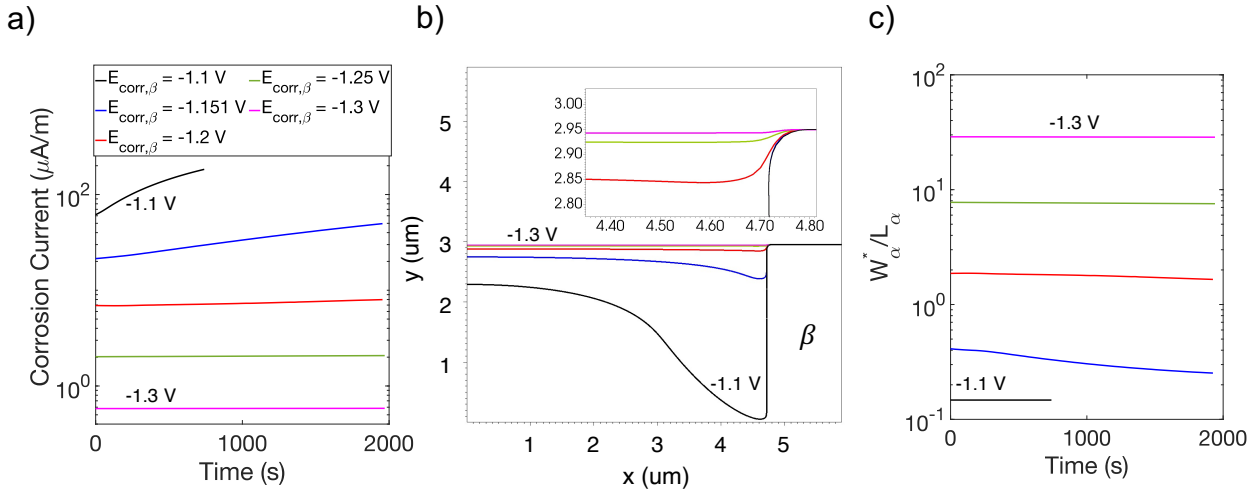


Figure 6.5. Results for the corrosion current, morphology of the corroded surface, and the Wagner length from the sensitivity analysis with respect to the corrosion potential of the  $\beta$  phase. (a) The log-linear plot of the corrosion current vs. time. (b) The metal/electrolyte interface at  $t = 755$  s. The inset shows an expanded view of (b) near the  $\alpha/\beta$  interface to enable visual delineation of cases in which corrosion is limited. (c) The log-linear plot of  $W_{\alpha}^*/L_{\alpha}$  vs. time. The values of  $E_{\text{corr},\beta}$  varies from  $-1.3$  V to  $-1.1$  V, as presented in the legend provided in (a), which applies to all subfigures.<sup>31</sup>

The plot of the corrosion current vs. time for different values of  $E_{\text{corr},\beta}$  is presented in Figure 6.5a. Two trends can be observed in the figure. First, for a fixed  $E_{\text{corr},\beta} > -1.25$  V (vs. SCE), the corrosion current increases with time. For  $E_{\text{corr},\beta} \leq -1.25$  V (vs. SCE), the corrosion current remains almost constant in time because the amount of the  $\beta$  phase exposed to the electrolyte does not change significantly. Second, increasing  $E_{\text{corr},\beta}$  increases the corrosion current. In fact, increasing  $E_{\text{corr},\beta}$  from  $-1.151$  V to  $-1.1$  V (i.e., the change in  $E_{\text{corr},\beta}$  with respect to the baseline case,  $\Delta E_{\text{corr},\beta} = \sim 0.05$  V) causes the corrosion current (at  $t = 0$  s) to increase by a factor of  $\sim 2.9$ . Similarly, decreasing the  $E_{\text{corr},\beta}$  from  $-1.151$  V to  $-1.2$  V (i.e.,  $\Delta E_{\text{corr},\beta} \sim -0.05$  V) reduces the corrosion current (at  $t = 0$  s) by a factor of  $\sim 3.1$ . While these factors are

similar ( $\sim 3$ ), they differ from  $\exp\left(\left|\frac{\Delta E_{\text{corr},\beta}}{A_\beta}\right|\right) \sim 4$ , obtained theoretically by assuming that the electrolyte potential at  $t = 0$  s remains the same for different  $E_{\text{corr},\beta}$  cases. This result exemplifies the need for simulations when more precise predictions are required because the assumption of the invariant electrolyte potential is not applicable for the system under consideration (see Figure 6.12 in Section 6.5 for additional data). Nevertheless, the theoretical value is still useful as it provides an approximate change expected in the corrosion current at  $t = 0$  s for consecutive values of  $E_{\text{corr},\beta}$ .

Finally, the effects of  $E_{\text{corr},\beta}$  on the interface position and morphology (shown in Figure 6.5b) and the uniformity of corrosion along the  $\alpha$ /electrolyte interface (in terms of  $W_\alpha^*/L_\alpha$ , shown in Figure 6.5c) are analogous to the effects of  $i_{\text{corr},\beta}$  discussed above. In short, increasing  $E_{\text{corr},\beta}$  increases the corrosion current, which results in more corrosion (e.g., magenta vs. black curves in Figure 6.5b) and decreases the  $W_\alpha^*/L_\alpha$  value (e.g., blue vs. green curves in Figure 6.5c), which explains the corresponding corrosion morphologies found in Figure 6.5b. Thus, this sensitivity analysis shows that  $E_{\text{corr},\beta}$  significantly affect the microgalvanic corrosion behavior and should be considered as a parameter in the alloy design. Furthermore, the analysis shows that keeping the difference between  $E_{\text{corr},\beta}$  and  $E_{\text{corr},\alpha}$  below  $\sim 0.22$  V significantly reduces localized corrosion in the AM30 alloy for the assumed model parameters, both by decreasing the overall rate and enhancing the uniformity.

### **6.3.1.3 Sensitivity analysis with respect to $\kappa_e$**

The parameter  $\kappa_e$  is the ionic conductivity of the electrolyte. Thus, changing  $\kappa_e$  in the model represents a change in the corrosion environment. Facile ionic transport in the electrolyte

(i.e., larger  $\kappa_e$ ) is expected to increase the corrosion current; below, we will quantify this effect. We note that changing the electrolyte can potentially alter the  $i_{\text{corr},\beta}$  and  $E_{\text{corr},\beta}$  values in a physical system; however, here we isolate the effect of  $\kappa_e$  on the corrosion behavior. The  $\kappa_e$  value for various aqueous electrolytes can vary from  $1 \times 10^{-3}$  S/m (for distilled water) to 1 S/m (sea water).<sup>184</sup> Thus, we chose five values of  $\kappa_e$  within this range, namely  $5 \times 10^{-3}$ ,  $1 \times 10^{-2}$ ,  $2 \times 10^{-2}$ ,  $1 \times 10^{-1}$ , and 1 S/m, for the sensitivity analysis. Again, the remaining model parameters were kept the same as listed in Table 6.2. The results are summarized in Figure 6.6.

The plot of corrosion current vs. time for all cases is shown in Figure 6.6a. As can be seen, for a fixed  $\kappa_e$  value, the corrosion current increases with time, which occurs due to an increase in the amount of the  $\beta$  phase exposed to the electrolyte. However, the effect of  $\kappa_e$  on the corrosion current is not as straightforward. An increase in the corrosion current is observed during early times ( $t < 600$  s) as  $\kappa_e$  is increased, which is in line with our expectation. However, the increase is minor considering the large change in  $\kappa_e$ ; for example, the corrosion current at  $t = 0$  s increased by  $\sim 15\%$  when  $\kappa_e$  is raised from  $5 \times 10^{-3}$  to 0.1 S/m, at which point no significant change in the corrosion current is observed with a further increase in  $\kappa_e$ . This result indicates that the ionic transport is not a limiting factor for  $\kappa_e > 0.1$  S/m even when the reaction current density is large for this system. Furthermore, we note that it is challenging to theoretically predict the nonlinear effect of  $\kappa_e$  on the corrosion current observed here even at  $t = 0$  s. The challenge arises because changing  $\kappa_e$  alters  $\Phi_e$  through the current continuity equation with corrosion current density boundary condition (see its SBM formulation, Eq. 6.8), which in turn changes the corrosion current density (Eqs. 6.9 to 6.13), making it difficult to solve them analytically.

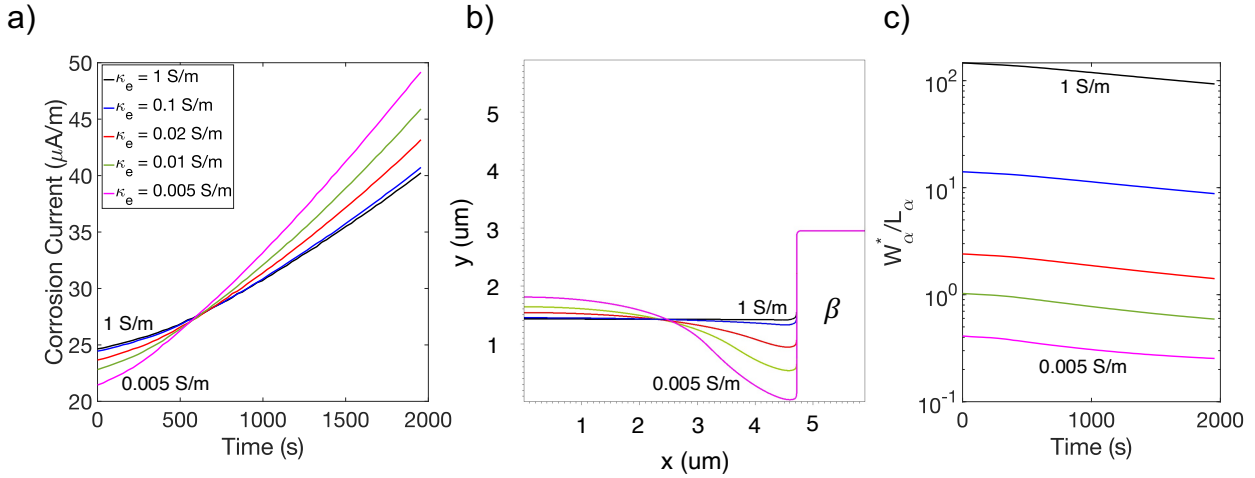


Figure 6.6. Results for the corrosion current, morphology of the corroded surface, and the Wagner length from the sensitivity analysis with respect to the electrolyte conductivity. (a) The log-linear plot of the corrosion current vs. time. (b) The metal/electrolyte interface at  $t = 2825 \text{ s}$ . (c) The log-linear plot of  $W_\alpha^*/L_\alpha$  vs. time. The values of  $\kappa_e$  varies from  $0.005 \text{ S/m}$  to  $1 \text{ S/m}$ , as presented in the legend provided in (a), which applies to all subfigures.<sup>31</sup>

At later times ( $t > 600 \text{ s}$ ), the trend observed above reverses: the smallest  $\kappa_e$  value exhibits the highest corrosion current. To understand this reversal, we need to examine the morphology of the corroding interface ( $\alpha$ /electrolyte), which is shown in Figure 6.6b for all cases at  $t = 2825 \text{ s}$  (the final time for the case with  $\kappa_e = 5 \times 10^{-3} \text{ S/m}$  when the corroding interface reaches the bottom end of the domain). As can be seen, the interface is almost flat for the cases of  $\kappa_e = 0.1$  and  $1 \text{ S/m}$ , but the interface becomes increasingly curved as the conductivity is decreased, with more corrosion near the  $\alpha/\beta$  interface than elsewhere. This rapid corrosion near the  $\alpha/\beta$  interface exposes a larger amount of the  $\beta$  phase to the electrolyte than in the case of a higher  $\kappa_e$ , and thus leads to a higher corrosion current. These results show that although the corrosion current is not as sensitive to  $\kappa_e$  as it is to  $i_{\text{corr},\beta}$  and  $E_{\text{corr},\beta}$ ,  $\kappa_e$  has an impact on the morphology of corroding interface.



We further analyze the results based on the Wagner length. Figure 6.6c shows the plot of  $W_\alpha^*/L_\alpha$  vs. time for all cases. As can be seen,  $W_\alpha^*/L_\alpha \gg 1$  for  $\kappa_e = 0.1$  and 1 S/m throughout the simulation, and, correspondingly, uniform corrosion is observed in these cases. Additionally, two more trends are observed: first, a monotonic decrease in  $W_\alpha^*/L_\alpha$  is observed as  $\kappa_e$  is decreased, which is consistent with an increase in the nonuniformity of corrosion along the  $\alpha$ /electrolyte interface. Second,  $W_\alpha^*/L_\alpha$  decreases with time, and the Wagner theory suggests an increase in the nonuniformity of the current density distribution over the  $\alpha$ /electrolyte interface with time. Thus, in summary, this sensitivity analysis showed that although  $\kappa_e$  does not strongly influence the overall rate of corrosion, especially during the early times, it significantly affects the uniformity of corrosion. These results have a direct implication for the strategies to mitigate localized corrosion, as they show that it is beneficial to have the ionic conductivity of the electrolyte to be greater than 0.1 S/m to maintain the uniformity of corrosion and reduce the corrosion current at later times.

### ***6.3.2 Effect of microstructure on corrosion behavior***

Next, we examine the influence of the microstructure on the corrosion behavior of Mg alloys by studying the effect of geometric features of second phase particles and lamellar regions, i.e., an alternate arrangement of  $\alpha$  and  $\beta$  domains. We note that the presence of such a region and its characteristic features are dependent on the alloy processing and is usually observed in various alloys during eutectic solidification or eutectoid (solid-state) phase transformation. We conducted this investigation in both 2D and 3D systems, which we discuss separately below. Note that the initial widths of the  $\alpha$  and  $\beta$  domains for one in both 2D and 3D systems are extracted from the literature.<sup>171</sup> The widths for the remainder of the cases are calculated based on the number of lamellar pairs under the constraint of fixed  $\beta$  volume fraction (at  $t = 0$  s), as explained in the following subsections. We also note that the use of natural boundary conditions (zero-normal-derivative) for all fields, as described in Section 6.2, corresponds to mirroring of the computational domain across each boundary. Other computational details, such as the time step size and the element size and order, are provided in Section 6.5 (see Table 6.5 and the associated text).

#### ***6.3.2.1 2D systems***

In this section, we describe the simulation results the microgalvanic corrosion in 2D systems that physically represent 3D systems, which have uniform microstructure along the direction perpendicular to the simulation plane. We considered four microstructures of the same dimensions but different distribution of the  $\beta$  phase for this investigation. The key distinguishing features among the four microstructures (referred to as Case 1 through Case 4) are summarized in Table 6.3, along with figures of the microstructures, and are discussed further below. Note that the

red, green, and blue regions in each figure correspond to the  $\alpha$ ,  $\beta$ , and the electrolyte domains, respectively.

Case 1, Case 2, and Case 3 represent a microstructure with only a lamellar region in the same cross-sectional area ( $2.810 \mu\text{m}$  by  $1.405 \mu\text{m}$ ), but they differ from each other in terms of number of lamellar pairs present in them, as listed in Table 6.3. Case 4, on the other hand, represents a microstructure with a lamellar region with 3 lamellar pairs along with a larger  $\alpha$  domain (hereafter referred to as the bulk  $\alpha$  domain for short), similar to what may be expected when primary  $\alpha$  forms before the lamellar region. The initial widths of the  $\alpha$  and  $\beta$  domains in the lamellar region in Case 4 are extracted from the microstructures reported in the literature.<sup>171</sup> Note that two values for the width of the  $\alpha$  domain in Case 4 are provided in Table 6.3; the values  $0.40 \mu\text{m}$  and  $1.21 \mu\text{m}$  correspond to the  $\alpha$  domain within the lamellar region and the bulk  $\alpha$  domain, respectively. The initial widths of the  $\alpha$  and  $\beta$  domains in all other cases are determined based on the number of lamellar pairs under the constraint of fixed  $\beta$  volume fraction (at  $t = 0$  s), which was set to  $\sim 21\%$  in all cases (like the value used in the sensitivity analyses above and a previous study<sup>26</sup>). Note that in the microstructures studied here, the  $\beta$  volume fraction is the same as the  $\beta$  area fraction at any given time due to the assumed uniformity of the microstructures along the direction perpendicular to the simulation plane. The remaining model parameters were kept the same as listed in Table 6.2.

Table 6.3. A comparison of the four microstructures used for the 2D system. In all cases, the area fraction of the  $\beta$  phase is set to 21%.<sup>31</sup>

Case	Figure	Description	No. of lamellar pairs per domain	Width of $\alpha$ regions ( $\mu\text{m}$ )	Width of $\beta$ regions ( $\mu\text{m}$ )
1		Wide lamellar	1	2.210	0.600
2		Medium lamellar	2	1.105	0.300
3		Narrow lamellar	3	0.737	0.200
4		Lamellar region next to a larger $\alpha$ region	3	0.400 (lamella) 1.210 (bulk)	0.200

The plot of the corrosion current vs. time for all cases is provided in Figure 6.7a. Three distinct features can be observed in the figure: first, the corrosion currents for all cases are the same at  $t = 0$  s; second, for each case, the corrosion current increases with time; and third, at  $t > 0$  s, the corrosion current is influenced by the microstructure. Specifically, we observe that increasing the number of lamellar pairs with a fixed initial  $\beta$  fraction (which decreases the lamellar width) increases the corrosion current at  $t > 0$  s. Furthermore, by comparing Case 3 and Case 4, we find that, for a fixed number of lamellar pairs at a fixed initial  $\beta$  fraction, decreasing the spacing between the  $\beta$  domains (i.e., the width of the  $\alpha$  domains in the lamellar region) increases the corrosion current at  $t > 0$  s.

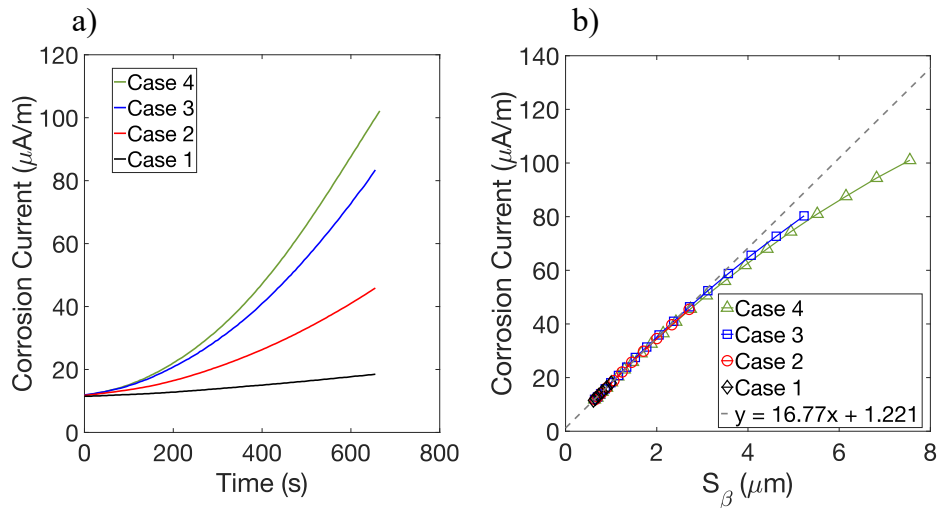


Figure 6.7. Corrosion current as a function of time and cathode surface area per unit length for the 2D microstructures. (a) The plot of the corrosion current vs. time for the 2D microstructures studied here. (b) The relation between the corrosion current and  $S_\beta$  (the cathode surface area per unit length perpendicular to the simulation plane) for the microstructures. In both plots, the same color corresponds to the same case, namely, black for Case 1; red for Case 2; blue for Case 3; and green for Case 4. The best fit to the linear portion of the data is also shown in (b) by a grey dash line.<sup>31</sup>

The underlying reason behind the three features discussed above for Figure 6.7a is the amount of the  $\beta$  phase exposed to the electrolyte at any given time because the corrosion current is limited by the cathodic phase. When the area of the exposed  $\beta$  phase is the same, the same

corrosion current is obtained. This is why all cases have the same corrosion current at  $t = 0$  s. It also explains why the current increases with time as more  $\beta$  surface area becomes exposed to the electrolyte and why the cases with more (and finer) lamellas (e.g., Case 3) have a higher corrosion current over those with fewer (and coarser) lamellas (e.g., Case 1) at a given time. The amount of the exposed  $\beta$  phase can be quantified in terms of the surface area of the  $\beta$  phase exposed to the electrolyte. Given the 2D nature of the microstructures studied here, we use the cathode surface area per unit length perpendicular to the simulation plane, or  $S_\beta$ , as the quantifying metric instead of the surface area. Figure 6.8 shows the plot of  $S_\beta$  vs. time for all cases. The evolution of  $S_\beta$  is similar to that observed in the plot of corrosion current vs. time (Figure 6.7a) in three ways. First,  $S_\beta$  is the same for all cases at  $t = 0$  s because the initial  $\beta$  fraction is the same in all the cases. Second,  $S_\beta$  increases with time in all cases. Third,  $S_\beta(\text{Case 4}) > S_\beta(\text{Case 3}) > S_\beta(\text{Case 2}) > S_\beta(\text{Case 1})$  at  $t > 0$  s. This dependence of the corrosion current on the surface area of the cathode is also reported by Raman<sup>167</sup> based on potentiodynamic and weight loss measurements of AZ91 alloy samples that underwent a heat treatment for different durations.

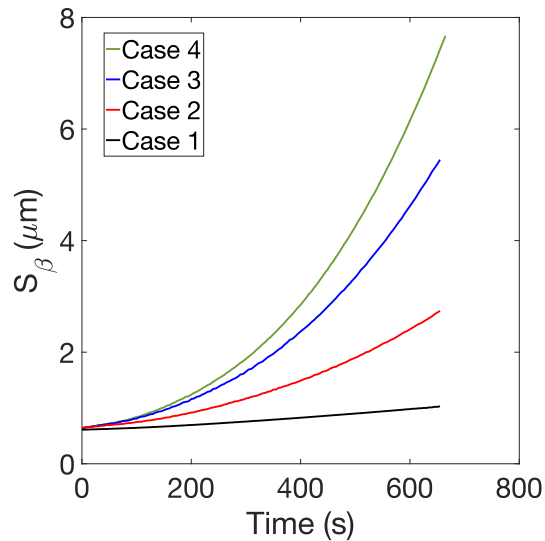


Figure 6.8. The plot of  $S_\beta$  (the cathode surface area per unit length perpendicular to the simulation plane) vs. time for the 2D microstructures studied in this work. Note that different curves correspond to various microstructures, namely, black for Case 1; red for Case 2; blue for Case 3; and green for Case 4.<sup>31</sup>

To further highlight the relationship between the corrosion current and  $S_\beta$ , we plot the corrosion current vs.  $S_\beta$  in Figure 6.7b. As can be seen, the corrosion current increases with  $S_\beta$  for all cases. More interestingly, all plots in Figure 6.7b approximately overlap onto a single curve for the duration of the simulations performed. Note that the agreement is excellent up to  $S_\beta \sim 3 \mu\text{m}$ , where a linear relationship is observed, as shown by the grey dashed line in Figure 6.7b. This result illustrates that  $S_\beta$  is the rate-defining quantity in the microstructures studied here. The deviation observed between the linear relationship and the simulated result at larger  $S_\beta$  is caused by the ionic-transport limitation (due to a small  $\kappa_e$  value) and the current-density limitation on the  $\alpha$  phase (due to a small  $i_{max}$  value). When sufficiently large  $\kappa_e$  and  $i_{max}$  values are used, the simulated result matches well with the linear relationship, as shown in Figure 6.13 and discussed in the associated text in Section 6.5.

The evolution of the metal/electrolyte interface is consistent with the corrosion behavior discussed above, which shows that the corrosion current is strongly correlated to  $S_{\beta}$ . Figure 6.9 shows the metal/electrolyte interface for each case (in each row) at three times (in different columns) during corrosion. As can be seen, the largest amount of corrosion at any given time is observed in Case 4, followed by Case 3, Case 2, and Case 1 in this order. In addition to the extent of corrosion, the uniformity of corrosion is also highly dependent on the microstructure. For Case 1, we observe nonuniform corrosion along the  $\alpha$ /electrolyte interface, with more corrosion near the  $\alpha/\beta$  interface than elsewhere. This nonuniform corrosion behavior is consistent with that described in the Sensitivity Analyses section and in a previous work.<sup>26</sup> Specifically, the observed nonuniformity suggests there exist two length scales for corrosion: one associated with a high corrosion current density that decays rapidly from the  $\alpha/\beta$ /electrolyte triple junction, and another, associated with a low corrosion current density that persists for a length scale comparable or longer than the domain size.<sup>26</sup> The length scale of the first type determines the extent of the *field of influence* of the  $\beta$  domain on the surrounding  $\alpha$  region.

For Case 2 and Case 3, we still observe some nonuniform corrosion in each  $\alpha$  domain, i.e., more corrosion near the  $\alpha/\beta$  interface. However, the depth of corrosion in the middle of each  $\alpha$  domain is not much behind that near the  $\alpha/\beta$  interfaces at all times. This happens because the spacing between two adjacent  $\beta$  domains, i.e., the width of each  $\alpha$  domain, is small enough such that the fields of influence of the two  $\beta$  domains overlap and act together on the  $\alpha$  domain in between. Furthermore, the overlap of the fields of influence becomes stronger as  $\beta$  domains are brought closer. This is the reason behind the faster corrosion observed in Case 3 than in Case 2. Finally, due to the symmetry of the microstructure, we observe the same corrosion extent in each  $\alpha$  domain for both Case 2 and Case 3. In Case 4, we observe a combination of behaviors observed



in the cases discussed above. A behavior like that of Case 1 can be seen for the bulk  $\alpha$  domain (right-most domain), where the two distinct length scale discussed for Case 1 are apparent. Within the lamellar region, we observe an overlap of the fields of influence of multiple  $\beta$  domains, like Case 2 and Case 3, which leads to a relatively uniform but faster corrosion within the lamellar region than the bulk  $\alpha$  phase. However, unlike Case 2 and Case 3, the extent of corrosion in Case 4 is not uniform among the  $\alpha$  domains within the lamellar region. In fact, the innermost  $\alpha$  domain (i.e., the left-most  $\alpha$  domain) exhibits the greatest extent of corrosion because of the asymmetry of the microstructure.

The results presented here show that when the corrosion current is limited by the cathodic phase, the presence of the lamellar region, in addition to the bulk  $\alpha$  phase, not only increases the corrosion current, but also increases the difference in the extent of corrosion among  $\alpha$  domains. A larger extent of corrosion is observed in the  $\alpha$  domain that lies in the center of the lamellar region, and the extent decreases monotonically as one moves to the domains that are away from the center. These results agree well with the experimental results reported by Song et al.<sup>50</sup> for the AZ91 alloy, where a greater extent of corrosion was observed within the lamellar region than the bulk  $\alpha$  phase. Although Song et al.<sup>50</sup> attributed this behavior to the difference in the electrochemical properties of the  $\alpha$  phase present within the lamellar region and in bulk (due to the difference in the solute concentration), our results here show that the same effect can be observed even in the absence of such differences. Moreover, the phenomenon of accelerated corrosion of the anodic phase within the lamellar region is also observed in other alloys.<sup>49,187</sup> In the next section (Section 6.3.2.2), we study the corrosion behavior in 3D microstructures, where the  $\beta$  phase is either present as a precipitate or within a lamellar region.

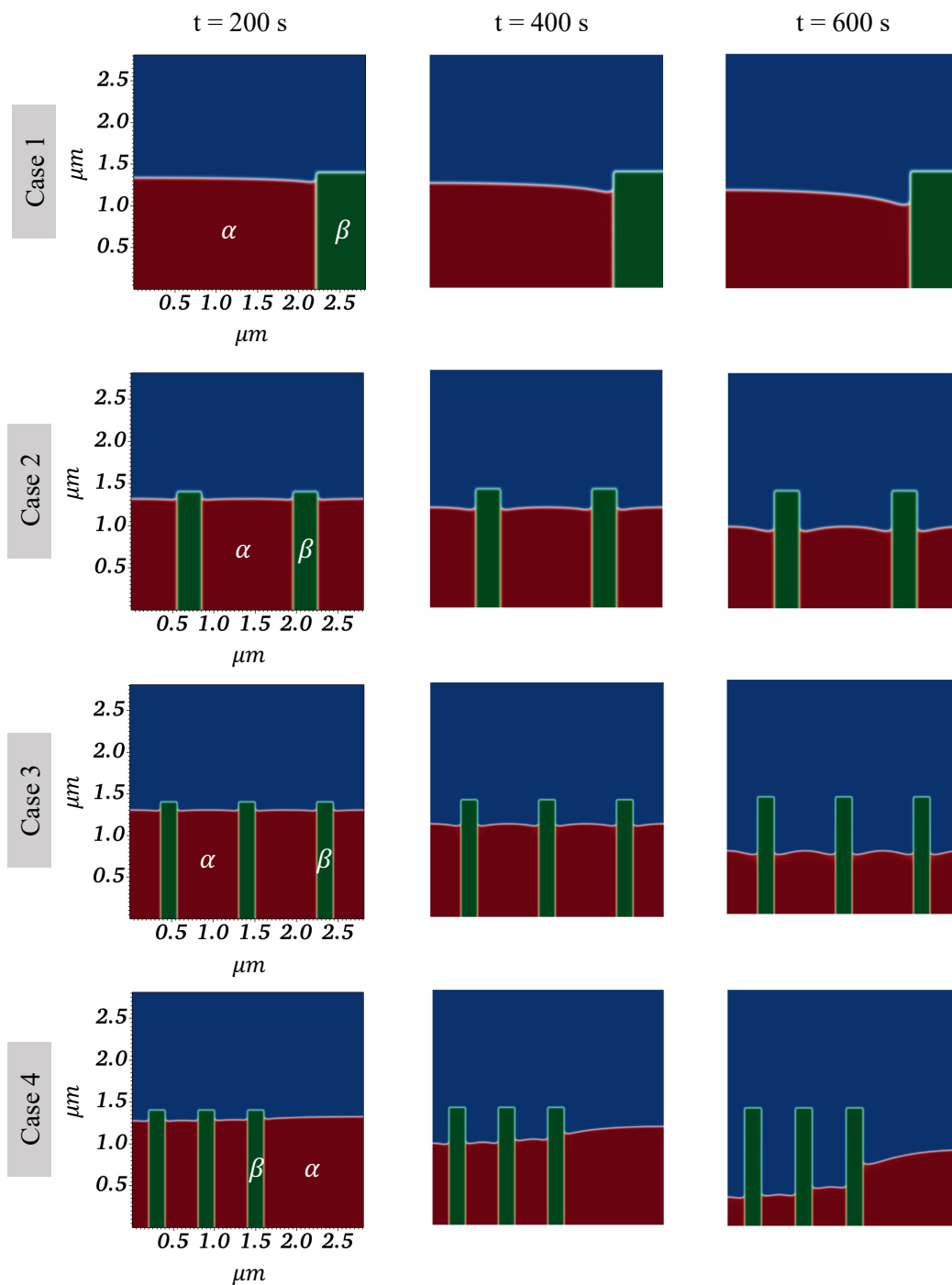
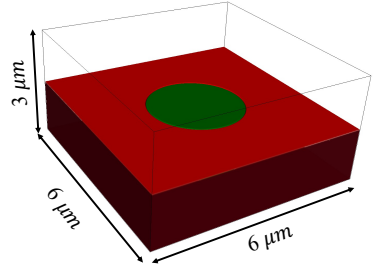
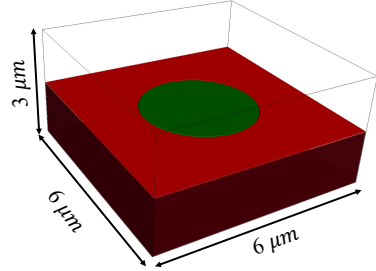
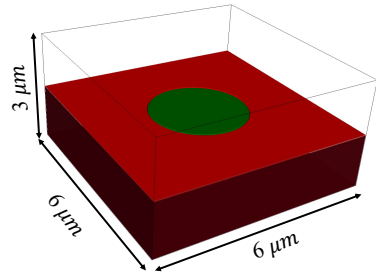
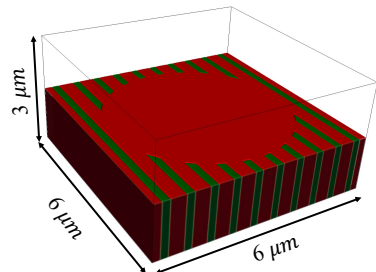


Figure 6.9. Time series of the corrosion evolution in the four 2D microstructures investigated here, which are presented in different rows. Times selected are 200s (the first column), 400s (the second column), and 600s (the third column). Axes labels are omitted for the latter two since they are identical to the first set. As noted in the main text, the red, green, and blue regions represent the  $\alpha$ ,  $\beta$ , and electrolyte domains, respectively.<sup>31</sup>

### 6.3.2.2 3D systems

We simulated the corrosion behavior in four 3D microstructures, which are listed in Table 6.4, along with their description and distinguishing features. The microstructures in Cases A to C differ in terms of the size and shape of the  $\beta$  precipitate, and none of them have any lamellar region in them. Case D, on the other hand, places approximately the same amount of the  $\beta$  phase as Cases A and B in lamellar region that surrounds a cylindrically shaped  $\alpha$  domain. The initial widths of the  $\alpha$  and  $\beta$  domains in the lamellar region of Case D are exactly the same as in Case 4 in the 2D system and are obtained from the literature.<sup>171</sup> The initial volume fractions (at  $t = 0$  s) of the  $\beta$  phase in Case A, Case B, and Case D are set to be the same at  $\sim 15\%$ . Note that due to the uniformity of the microstructures along the thickness in Cases A and D, the initial surface fraction of the  $\beta$  phase is also the same as the initial volume fraction (at  $\sim 15\%$ ). Since corrosion is a surface phenomenon, we included Case C to study corrosion for the same initial surface  $\beta$  fraction as cases A and D, but with a hemispherical  $\beta$  precipitate. Finally, we note that the symmetry of the setup in all four microstructures allowed us to perform simulations for only a quarter of the system; however, the simulation results are reflected to provide the full view of the microstructure.

Table 6.4. A comparison of the four microstructures used for the 3D system. Note that the red and green regions in the figures represent the  $\alpha$  and  $\beta$  domains, respectively.<sup>31</sup>

Case	Figure	Description	Dimensions of the $\alpha$ domain ( $\mu\text{m}$ )	Dimensions of the $\beta$ domain ( $\mu\text{m}$ )	Initial volume (surface) fraction of $\beta$
A		Cylindrical $\beta$ precipitate in an $\alpha$ matrix	Length = 6.0, Width = 6.0, Depth = 1.5	Radius = 1.32, Depth = 1.50	15.2% (15.2%)
B		Hemispherical $\beta$ precipitate in an $\alpha$ matrix	Length = 6.0, Width = 6.0, Depth = 1.5	Radius = 1.57	15.0% (21.5%)
C		Hemispherical $\beta$ precipitate in an $\alpha$ matrix	Length = 6.0, Width = 6.0, Depth = 1.5	Radius = 1.32	8.9% (15.2%)
D		Cylindrical $\alpha$ precipitate in lamellar region	Width in the lamellae = 0.4, Precipitate radius = 2.5, Depth = 1.5	Width = 0.2, Depth = 1.5	15.2% (15.2%)

The plot of the corrosion current vs. time for all four microstructures is shown in Figure 6.10a; supplementary results are provided in Figure 6.14 in Section 6.5. As in the 2D systems, the corrosion behavior observed in the 3D microstructures can be explained based on the amount of the  $\beta$  surface exposed to the electrolyte, referred to as cathode area hereafter, as shown in Figure 6.10b. For instance, at  $t = 0$  s, the corrosion current is the same for Case A, Case C, and Case D because in all three cases, the cathode areas are nearly equal. The small difference between the cathode area of Case D and that of Cases A and C at  $t = 0$  s is caused by the difference in the geometry. The larger cathode area in Case B (at  $t = 0$  s) than other microstructures also explains the larger corrosion current observed in that case.

The evolution of the corrosion current can also be explained based on the cathode area. The close match between the corrosion currents for Cases A and C, especially during the early the times, can be traced to the fact that the cathode areas of these two cases evolve very similarly (see black and red curves in Figure 6.10a and Figure 6.10b). The match between the cathode areas for Cases A and C, despite the difference in the geometry and the volume of the  $\beta$  precipitate, is observed because the initial area of the  $\beta$  surface is set to be the same and the geometry effect is negligible when corrosion has not advanced significantly. At later times, Case C exhibits lower cathode area (and thus corrosion current) than Case A, due to the tapering profile of the hemispherical precipitate, as shown in the inset of Figure 6.10b. The corrosion current in Case B remains higher than Cases A and C because of the larger cathode area in Case B throughout the simulation. Similarly, the corrosion current in Case D exhibits rapid increase and becomes the largest after 240 s of corrosion among the simulations conducted, which is caused by the faster increase in the cathode area, as shown in Figure 6.10b. Thus, as observed in the 2D systems, the

simulations show that the presence of the lamellar region in addition to a larger (e.g., primary)  $\alpha$  region accelerates corrosion in 3D systems.

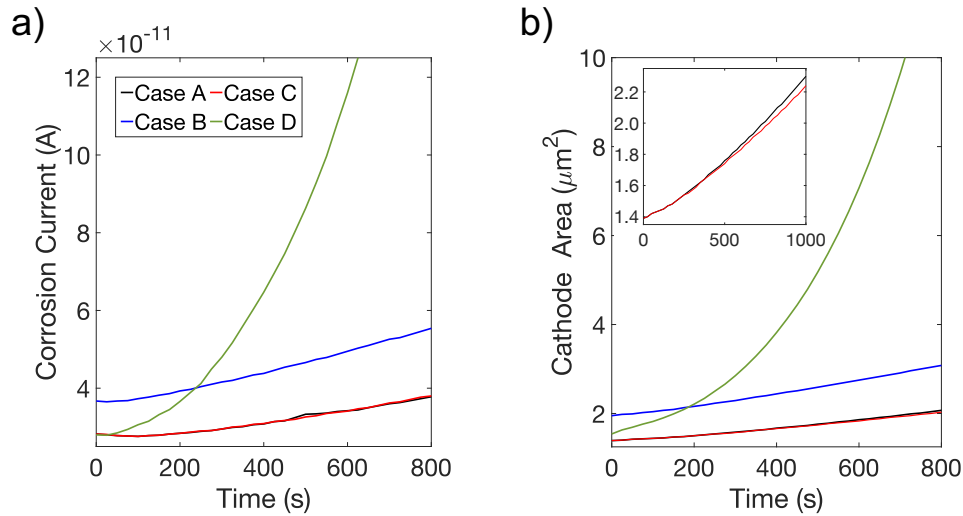


Figure 6.10. Corrosion current as a function of time and cathode surface for the 3D microstructures. The plot of (a) the corrosion current vs. time and (b) the cathode area vs. time for the 3D microstructures studied in this work. The inset of (b) shows the plot of the cathode vs. time for Case A and Case C for a longer duration than (b), which is added to highlight the difference in the cathode area for the two cases. The legends are provided in (a) for both plots (black, Case A; blue, Case B; red, Case C; and green, Case D). Note that the black curve (Case A) mostly overlaps the red curve (Case C) in the main subfigure (b); see the inset for a magnified view.<sup>31</sup>

Figure 6.11 shows the evolution of the metal/electrolyte interface for each case (in different rows) at three times (250 s, 500 s, and 750 s in different columns). For Case A, Case B, and Case C, we observe faster corrosion near the  $\alpha/\beta$  interface and slower corrosion far from the interface, which leads to the formation of a circular trench around the  $\beta$  precipitate (see the last column in Figure 6.11). Thus, we again observe the presence of the two length scales that were discussed for Case 1 of the 2D system: one over which the current density decays from the  $\alpha/\beta$ /electrolyte triple junction and another over which the current density is smaller but persists for a length scale comparable or longer than the domain size. The evolution of the interface in Case D is also

analogous to that of Case 4 for the 2D system. In the cylindrical  $\alpha$  region, we observe the presence of the two length scales for the corrosion: one associated with faster corrosion near the  $\alpha/\beta$ /electrolyte triple junction and the other associated with slower corrosion near the center of the region, which causes the initially flat surface to evolve into a dome shape (see the last row in Figure 6.11). Furthermore, corrosion in each  $\alpha$  domain within the lamellar region is more uniform than in the cylindrical region due to the overlap of the fields of the influence of multiple  $\beta$  domains, as discussed above for the 2D systems. However, the extent of corrosion among  $\alpha$  domains in the lamellar region varies. Faster corrosion is observed in the  $\alpha$  domains surrounded by the  $\beta$  domains that run through the entire length of the microstructure (i.e., the  $\alpha$  domains at the edges of the microstructure; an example is noted by a black arrow in Figure 6.11). The extent of corrosion decreases towards the centerline of the domain in the lamellar region. This behavior is analogous to Case 4 for the 2D system, where the greatest extent of corrosion was observed in the left-most  $\alpha$  domain. In summary, the 3D simulations show that the trends observed in the 2D systems are also valid in 3D systems.

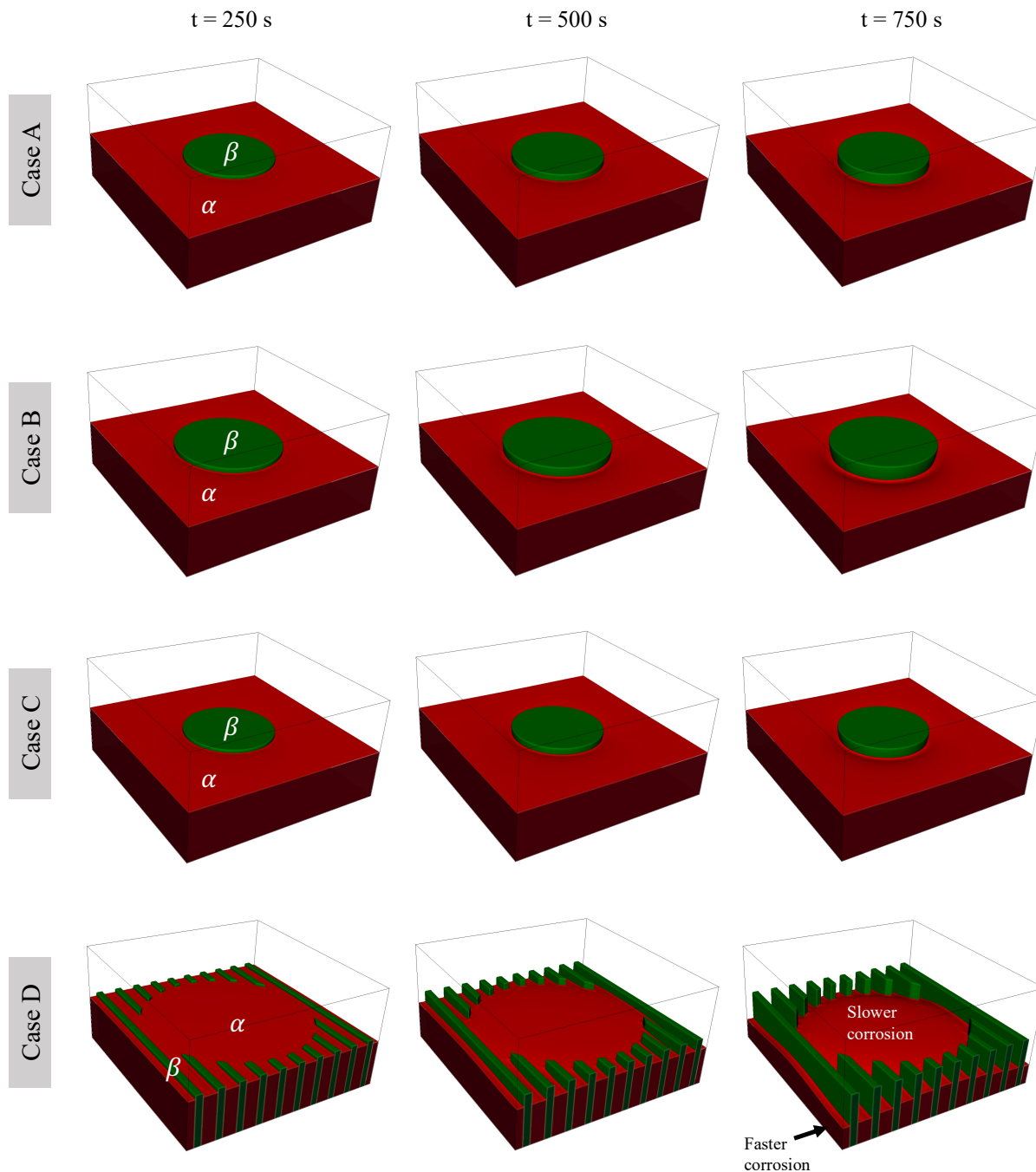


Figure 6.11. Time series of the corrosion evolution in the four 3D microstructures investigated, which are presented in different rows. Times selected are 250 s (the first column), 500 s (the second column), and 750 s (the third column). In Case D, the regions with slower and faster corrosion are noted in the third column. As noted in the main text, the red and green regions represent the  $\alpha$  and  $\beta$  domains, respectively. Note that the symmetry of the setup in all four microstructures allowed us to perform simulations in only a quarter of the system.<sup>31</sup>



## 6.4 Chapter 6 Summary

In this work, we performed phase-field simulations to individually study the effect of the electrochemical properties of the  $\beta$  phase and electrolyte, as well as that of the alloy microstructure on the microgalvanic-corrosion behavior of Mg alloys. These simulations enable the decoupling of the effect of the aforementioned factors on the microgalvanic corrosion, which is challenging to achieve solely by experiment. Based on the results from the sensitivity analyses, we showed that decreasing either  $i_{\text{corr},\beta}$  or  $E_{\text{corr},\beta}$  reduces the corrosion current and promotes more uniform corrosion. We also confirmed that the ratio between the minimum Wagner length for the  $\alpha$  phase (corroding phase),  $W_{\alpha}^*$ , and the initial width of that phase,  $L_{\alpha}$ , is an excellent metric for determining the uniformity of corrosion along the corroding interface. In short, when the ratio is significantly larger than 1, the corrosion is found to be uniform, and the opposite behavior is observed when the ratio is significantly smaller than 1. Furthermore, the sensitivity analyses also revealed that increasing  $\kappa_e$  improves the corrosion resistance at longer times due to the improved uniformity of corrosion. However, the corrosion current is not as sensitive to  $\kappa_e$  as it is to  $i_{\text{corr},\beta}$  and  $E_{\text{corr},\beta}$  for the range of parameter values and the system sizes studied here.

Additionally, we showed that the microstructure has a strong effect on corrosion behavior. Specifically, the presence of a lamellar region in addition to a bulk  $\alpha$  domain in the microstructure proves to be detrimental to the corrosion resistance in both 2D and 3D microstructures, which qualitatively agrees with experimental studies.<sup>49,50,187</sup> Furthermore, increasing the number of lamellar pairs in the microstructure for a fixed initial volume and surface fraction of the  $\beta$  phase increases the corrosion current. Thus, finer microstructure is detrimental to corrosion resistance. In the case where a lamellar region is present next to a bulk  $\alpha$  domain, we observed differences in the extent of corrosion among  $\alpha$  domains present in the system. We note that some experimental

studies about the influence of the lamellar region on the corrosion current contradict our simulation results. For example, Zhao et al.<sup>171</sup> and Zhao et al.<sup>46</sup> reported that for AZ91, the presence of the lamellar region is beneficial to the corrosion resistance of the alloy. This discrepancy may be due to the difference in the composition (and resulting difference in the electrochemical properties) of the  $\alpha$  phase in the lamellar region as compared to the bulk  $\alpha$  phase. To further investigate this discrepancy, the properties of the  $\alpha$  phase should also be examined systematically, which will be left for future work. Moreover, the deposition of the corrosion product on the metal/electrolyte interface can play a significant role in reducing the corrosion rate. The present model does not account for the deposition of the product phase, and thus the model needs to be extended to study corrosion involving product deposition. Nevertheless, this systematic investigation provides guidance to the design of alloys and processing approaches to mitigate localized corrosion.

## **6.5 Chapter 6 Appendix**

### ***Computational details for the sensitivity analyses***

The numerical parameters used for performing the sensitivity analyses are listed in Table 6.5. In addition, the tolerance for the nonlinear solver was kept at  $1 \times 10^{-10}$  for the simulations pertaining to the sensitivity analyses. The mesh was refined where the order parameters were between  $\epsilon$  and  $1 - \epsilon$ , where  $\epsilon = 1 \times 10^{-2}$  and  $1 \times 10^{-3}$  for quadratic and linear elements, respectively, to ensure sufficient refinement of the interface. The wider range was used for linear elements due to their lower accuracy than quadratic elements. Finally, the interfacial thickness was set at approximately 5% of the thickness of the  $\beta$  phase to ensure the error introduced by the diffused interface approach is sufficiently small.

Table 6.5. Numerical parameters used in the sensitivity analyses.<sup>31</sup>

<b>Sensitivity analysis with respect to <math>i_{\text{corr},\beta}</math></b>						
$i_{\text{corr},\beta}$ (A/m <sup>2</sup> )	Time step (s)	Element Order	Sub-divisions in each direction	Max Refinement Level	Min Refinement Level	Tolerance of the linear solver
$5 \times 10^{-3}$	$2.5 \times 10^{-3}$	1	3	8	4	$1 \times 10^{-8}$
$1.7 \times 10^{-2}$	$2.5 \times 10^{-3}$	1	3	8	4	$1 \times 10^{-8}$
$5 \times 10^{-2}$	$1 \times 10^{-3}$	1	3	8	4	$1 \times 10^{-8}$
$1 \times 10^{-1}$	$1 \times 10^{-4}$	1	3	8	4	$1 \times 10^{-8}$
1	$1 \times 10^{-4}$	1	3	8	4	$1 \times 10^{-8}$
<b>Sensitivity analysis with respect to <math>E_{\text{corr},\beta}</math></b>						
$E_{\text{corr},\beta}$ vs. SCE (V)	Time step (s)	Element Order	Sub-divisions in each direction	Max Refinement Level	Min Refinement Level	Tolerance of the linear solver
-1.3	$2.5 \times 10^{-3}$	2	3	6	1	$1 \times 10^{-10}$
-1.25	$2.5 \times 10^{-3}$	2	3	6	1	$1 \times 10^{-10}$
-1.2	$2.5 \times 10^{-3}$	2	3	6	1	$1 \times 10^{-8}$
-1.151	$2.5 \times 10^{-3}$	2	3	6	1	$1 \times 10^{-8}$
-1.1	$2.5 \times 10^{-3}$	2	3	6	1	$1 \times 10^{-8}$
<b>Sensitivity analysis with respect to <math>\kappa_e</math></b>						
$\kappa_e$ (S/m)	Time step (s)	Element Order	Sub-divisions in each direction	Max Refinement Level	Min Refinement Level	Tolerance of the linear solver
$5 \times 10^{-3}$	$2.5 \times 10^{-3}$	1	3	8	4	$1 \times 10^{-8}$
$1 \times 10^{-2}$	$2.5 \times 10^{-3}$	1	3	8	4	$1 \times 10^{-8}$
$2 \times 10^{-2}$	$2.5 \times 10^{-3}$	1	3	8	4	$1 \times 10^{-8}$
$1 \times 10^{-1}$	$2.5 \times 10^{-3}$	1	3	8	4	$1 \times 10^{-8}$
1	$2.5 \times 10^{-3}$	1	3	8	4	$1 \times 10^{-8}$

### *Computational details for the microstructure studies*

The numerical parameters used in the simulations pertaining to the microstructure-based study for both 2D and 3D systems are listed in Table 6.6. All these simulations used quadratic elements with 3 subdivisions in each dimension, except for cases A to C in the 3D microstructures, where 4 subdivisions were used. Furthermore, the tolerance for the nonlinear solver was set as  $1 \times 10^{-10}$  for these simulations. Finally, the mesh was refined where the order parameters were between  $\epsilon$  and  $1 - \epsilon$ , where  $\epsilon = 1 \times 10^{-3}$  and  $1 \times 10^{-2}$  for 2D and 3D microstructures, respectively.

Table 6.6. Numerical parameters used in the simulations performed to study the effect of the microstructure.<sup>31</sup>

<b>2D Systems</b>					
<b>Case</b>	<b>Time step (s)</b>	<b>Interfacial thickness (m)</b>	<b>Max Refinement Level</b>	<b>Min Refinement Level</b>	<b>Tolerance of the linear solver</b>
1	$1 \times 10^{-3}$	$3.67 \times 10^{-8}$	6	1	$1 \times 10^{-8}$
2	$1 \times 10^{-3}$	$3.14 \times 10^{-8}$	6	1	$1 \times 10^{-8}$
3	$1 \times 10^{-3}$	$2.09 \times 10^{-8}$	6	1	$1 \times 10^{-8}$
4	$1 \times 10^{-3}$	$2.09 \times 10^{-8}$	6	1	$1 \times 10^{-8}$
<b>3D Systems</b>					
<b>Case</b>	<b>Time step (s)</b>	<b>Interfacial thickness (m)</b>	<b>Max Refinement Level</b>	<b>Min Refinement Level</b>	<b>Tolerance of the linear solver</b>
A	$5 \times 10^{-4}$	$3.16 \times 10^{-8}$	6	1	$1 \times 10^{-14}$
B	$5 \times 10^{-4}$	$3.16 \times 10^{-8}$	6	1	$1 \times 10^{-14}$
C	$5 \times 10^{-4}$	$3.16 \times 10^{-8}$	6	1	$1 \times 10^{-14}$
D	$5 \times 10^{-4}$	$3.14 \times 10^{-8}$	6	1	$1 \times 10^{-14}$

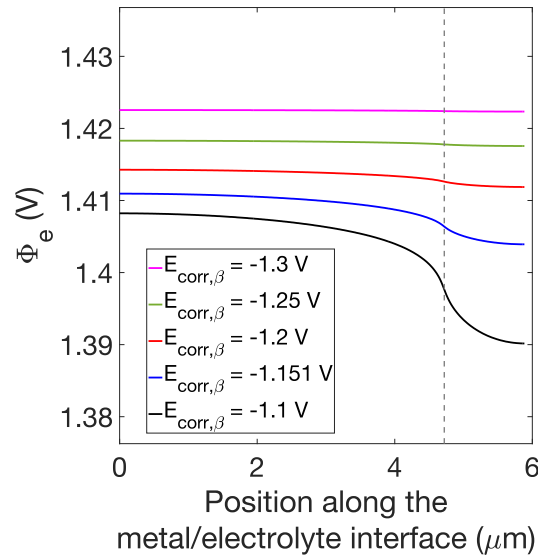


Figure 6.12. The plot of the electrolyte potential,  $\Phi_e$ , along the metal/electrolyte interface at  $t = 0$  s for different values of  $E_{\text{corr},\beta}$  considered in the sensitivity analysis. The grey dashed line represents the  $\alpha/\beta$  interface; the  $\beta$  domain lies on the right side of the line.<sup>31</sup>

To show that the deviation from the linear relationship observed for the Corrosion Current vs.  $S_\beta$  plot (Figure 6.7b) is caused by the spatial variation in the electrolyte potential along the  $\beta$ /electrolyte interface and  $i_{\text{max}}$ , we performed two additional simulations for Case 4, as follows. In the first simulation,  $\kappa_e$  was increased to 1S/m (from the baseline value of  $5 \times 10^{-3}$  S/m) to significantly reduce the spatial variation of the electrolyte potential. In the second simulation,  $i_{\text{max}}$  was increased to  $1 \times 10^3$  A/m<sup>2</sup> (from the baseline value of  $1 \times 10^2$  A/m<sup>2</sup>) to reduce the limiting effect of  $i_{\text{max}}$ , along with an increase of  $\kappa_e$  to 1S/m. The resulting corrosion current vs.  $S_\beta$  relationships are summarized in Figure 6.13, along with the result reported for Case 4 in Section 6.3.2.1. As can be seen, only increasing  $\kappa_e$  brings the relationship between corrosion current and  $S_\beta$  closer to the grey dashed line (compare the blue and green curves in Figure 6.13). Furthermore, upon a simultaneous increase in  $\kappa_e$  and  $i_{\text{max}}$ , the resulting relationship resembles the grey dashed line (see the purple curve in Figure 6.13). Thus, these results suggest that the linear relationship

between the corrosion current and  $S_\beta$  would be retained if sufficiently large values of  $\kappa_e$  and  $i_{max}$  are used to avoid any significant spatial variation in the electrolyte potential and severe limiting effect caused by  $i_{max}$ .

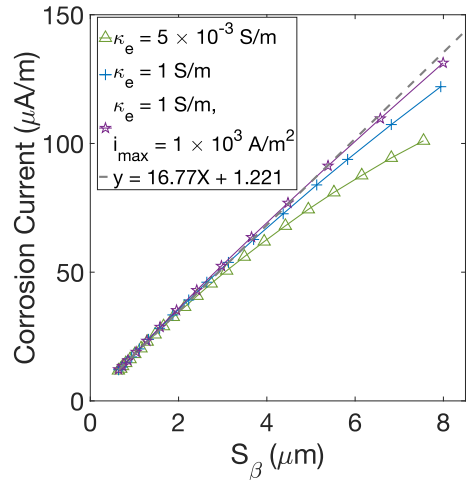


Figure 6.13. The relation between the corrosion current and  $S_\beta$  (the cathode surface area per unit length perpendicular to the simulation plane) for Case 4 with different values of  $\kappa_e$  and  $i_{max}$ . The green curve represents the result reported in the main text; the blue curve represents the result with increased  $\kappa_e$ ; the purple curve represents the result with both increased  $\kappa_e$  and  $i_{max}$ .<sup>31</sup>

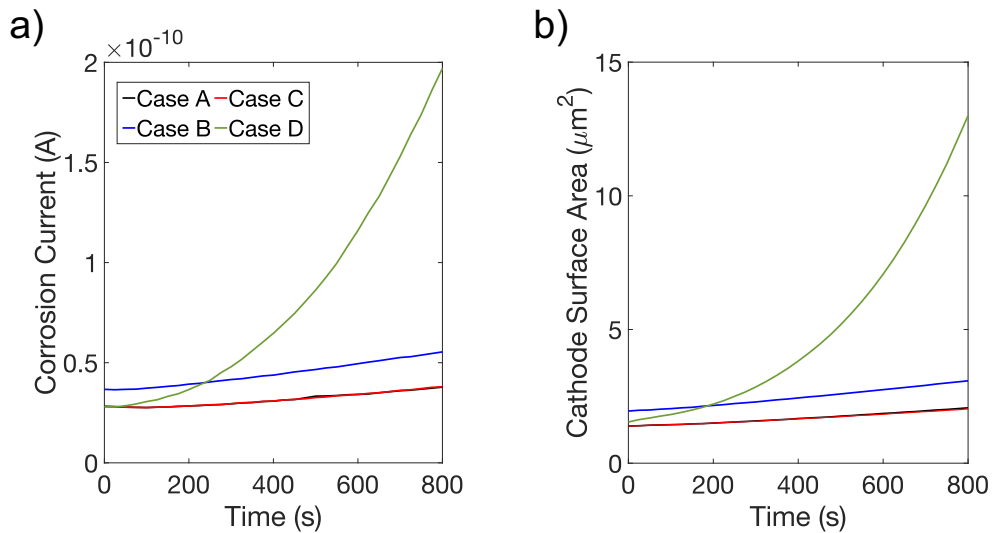


Figure 6.14. The plot of (a) the corrosion current vs. time and (b) the cathode area vs. time for the 3D microstructures studied here. The legends are provided in (a) for both plots (black, Case A; blue, Case B; red, Case C; and green, Case D). Note that the black curve (Case A) mostly overlaps the red curve (Case C).<sup>31</sup>

***Data availability***

The shared data for this chapter can be found at the following link:

<https://doi.org/10.13011/m3-ffgq-d561>.

## CHAPTER 7

### Effect of Material Properties on the Impedance Behavior and Tortuosity of SOFC

#### Cathodes\*

#### 7.1 Introduction: Application of electrochemical impedance spectroscopy to characterize SOFC cathodes

Electrochemical impedance spectroscopy (EIS) is a powerful technique for material characterization and diagnosis of the solid oxide fuel cells (SOFC) as it enables the separation of different phenomena, such as bulk diffusion and surface reaction, that occur simultaneously in the SOFC. In this chapter, the electrochemical impedance in an experimentally determined, three-dimensional (3D) microstructure of a mixed ion-electron conducting (MIEC) SOFC cathode is simulated. The impedance response is determined by solving the mass conservation equation in the cathode under the conditions of an AC load across the cathode's thickness and surface reaction at the pore/solid interface. The simulation results reveal a need for modifying the Adler-Lane-Steele model, which is widely used for fitting the impedance behavior of an MIEC cathode, to account for the difference in the oscillation amplitudes of the oxygen vacancy concentration at the pore/solid interface and within the solid bulk. Moreover, the results demonstrate that the effective tortuosity is dependent on the frequency of the applied AC load as well as the material properties, and thus the prevalent practice of treating tortuosity as a constant for a given cathode should be

---

\*This chapter is adapted from V. Goel et al., *Frontiers in Chemistry*, 9 (2021), 627699.<sup>32</sup>



revised. Finally, a method of determining the dependence of tortuosity on material properties and frequency by using the EIS data is proposed.

As described in Chapter 2 (Section 2.3), SOFCs are an important technology in enabling the rapid integration of renewable energy sources into the energy mix of the modern world. Their importance stems from their versatility because they can be used to produce electricity or, when used in reverse (as a solid oxide electrolyzer cell), to produce fuel, depending upon their applied polarization. Specifically, anodically polarized cells act as low-emission fuel-flexible electrochemical engines, and cathodically polarized cells store energy in the form of stable chemical bonds in H<sub>2</sub>, CO, or CH<sub>4</sub> through electrolysis.<sup>6,7</sup> However, conventional high-temperature SOFCs run at 800–1000 °C, which makes their operation and maintenance highly cost-ineffective.<sup>55</sup> The operating temperature has been reduced using electrocatalytically active mixed ion-electron conducting (MIEC) cathodes such as (La,Sr)(Co,Fe)O<sub>3-δ</sub> (LSCF)<sup>188–190</sup> and Sr(Ti,Fe)O<sub>3-δ</sub> (STF),<sup>191–193</sup> wherein the oxygen evolution reactions (OERs) and oxygen reduction reactions (ORRs) occur over the entire surface. To take advantage of this behavior, SOFC cathodes are designed to have complex and porous microstructures with a large specific surface area; however, such designs result in a high degree of tortuosity for ion transport, which limits the performance of SOFCs. Thus, it is important to accurately determine the tortuosity of a cathode microstructure and optimize it to enable high performance at low operating temperatures.

Several methods have been reported in the literature for determining the tortuosity of a porous electrode. These methods include: porosity-tortuosity relations, such as Bruggeman's relations<sup>194</sup>; calculations of the tortuous path length either through the distance propagation method<sup>118</sup> or the shortest path search method<sup>195</sup>; and calculations of tortuosity based on the effective diffusivity.<sup>196</sup> Bruggeman's relations are known to be less suitable for a domain with

connected solid phases and complex porous networks (as in an MIEC cathode).<sup>197</sup> The methods involving the calculations of tortuous path length, or the effective diffusivity require three-dimensional microstructural data as input, which is obtained through tomography.<sup>123,196</sup> Unfortunately, the availability of the necessary equipment to obtain tomographic data is not ubiquitous, sample preparation is time consuming, and the calculations are computationally expensive. Furthermore, these approaches provide tortuosity values associated with steady-state diffusion, yielding a single value, and do not describe the tortuosity relevant to the oscillating load or when the surface reaction is present. Therefore, there is a need for alternate methods for determining the tortuosity of a given SOFC electrode. Yu et al.<sup>59</sup> showed that in systems limited by only bulk diffusion, the diffusional impedance data can be used to characterize a given microstructure in terms of tortuosity and the area of the loading boundary. They also showed that tortuosity is a function of the AC load frequency, which they define as effective tortuosity. Such use of impedance data to characterize the microstructure of a SOFC cathode is valuable to SOFC researchers since they widely use electrochemical impedance spectroscopy (EIS) to test SOFC performance.

In this chapter, it is shown that the EIS data of a SOFC MIEC cathode can be used to determine the tortuosity of the solid phase within the cathode. For this purpose, we use a statistically representative<sup>198</sup> portion of an experimentally determined complex three-dimensional microstructure of an unbiased SOFC cathode. The microstructure is reconstructed by Yu et al.<sup>59</sup> from the focused-ion-beam (FIB) SEM images obtained by the Barnett group at Northwestern University. In the microstructure, the amplitude of the concentration response to an applied AC load under the influence of surface reaction and bulk diffusion is numerically obtained, and subsequently, the solution is used to determine the impedance behavior. Furthermore, the effect of

different material properties (bulk diffusion coefficient and reaction rate constant) on the impedance behavior and the effective tortuosity of the microstructure is investigated. From the simulations, it is found that due to the presence of surface reaction, the amplitude of oscillations in the oxygen vacancy concentration at the pore/solid interface of the cathode is lower than the amplitude within the bulk of the solid phase. Moreover, the difference between the two concentration amplitudes increases with an increase in the ratio between the reaction rate constant and the bulk diffusion coefficient. Such a difference is not considered by the widely used Adler-Lane-Steele (ALS) model, a macrohomogeneous model developed by Adler, Lane, and Steele to predict the impedance data of a SOFC MIEC cathode.<sup>28,29</sup> Thus, an extension to the ALS model to account for the aforementioned difference is proposed.

Furthermore, a method of extracting the effective tortuosity from the impedance data is developed, which involves a comparison between the macrohomogeneous (modified ALS) and 1D Finite Length Gerischer relations for the impedance. The calculations for tortuosity determination reveal that the effective tortuosity is a function of the microstructure, frequency of the applied AC load, and the material properties such as the reaction rate constant and bulk diffusion constant. Additionally, the effective tortuosity of a microstructure in the low-frequency regime (where the tortuosity approaches the DC value) decreases with an increase in the ratio between the reaction rate constant and the bulk diffusion coefficient due to a decreased penetration depth of the electrode reactions. This finding suggests that the prevalent practice of using a single tortuosity value for a given electrode for extracting the material properties by employing the ALS model<sup>29,199,200</sup> should be reviewed and revised. Additionally, the finding suggests that both the intrinsic material properties and the microstructure should be considered concurrently in designing

a cathode with enhanced performance. These findings open a new array of applications for the EIS technique in characterizing and optimization of the microstructure of a SOFC cathode.

All the previous reports primarily consider artificially generated microstructures,<sup>201–203</sup> which are designed to match given macrohomogeneous properties and thus may not be representative of the local microstructural morphologies and topologies. Only a few three-dimensional impedance calculations have been reported with consideration of experimentally determined microstructures that are statistically representative of the cathode.<sup>204,205</sup> The report by Kreller et al.<sup>205</sup> only explicitly considered the three-dimensional microstructure near the electrode/electrolyte interface and assumed a one-dimensional macrohomogeneous domain beyond a certain distance from the interface. On the other hand, the investigation by Lynch et al.<sup>204</sup> focused on the method of calculating impedance in a microstructure where the ORR occurs either through bulk or surface pathways. However, it did not propose the utilization of the computed impedance data for characterizing the microstructure, nor did it consider the difference between the concentration amplitudes at the pore/solid interface and within the bulk of the solid, which are the two focuses of this chapter.

## 7.2 Model equations for impedance calculation

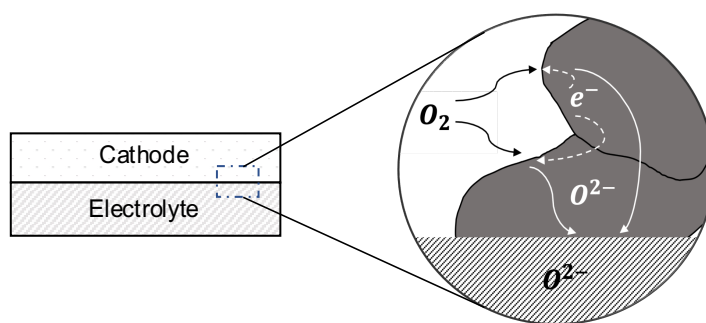


Figure 7.1. A schematic of oxygen transport within the solid phase (grey region) of a MIEC SOFC cathode. The schematic is based on Kreller et al.<sup>206</sup> Reproduced with permission from Ref. 32. Copyright 2021, the authors. Published by Frontiers Media SA.

MIEC cathodes are known to have much higher electronic conductivity as compared to the ionic conductivity<sup>207</sup>; thus, we ignore any impedance contribution due to electronic resistance. Moreover, due to the high electronic conductivity, it is reasonable to assume that the electrostatic potential of the solid phase is spatially invariant. Thus, in the absence of any gas phase transport limitation, the cathode impedance can be entirely attributed to the reduction of oxygen at the pore/solid interface and the transport of the resulting oxygen ions through the solid in the cathode, which is shown in Figure 7.1. The oxygen ions diffuse inside the solid phase of the cathode through a vacancy mechanism. Hence, the ionic current can be calculated from the flux of the oxygen vacancies. The mass transport equation for the oxygen vacancies inside the cathode can be written as

$$\frac{\partial C_v}{\partial t} = \nabla \cdot (AD_v \nabla C_v) \quad \in \Omega, \quad (7.1)$$

where  $C_v$  represents the concentration of oxygen vacancies,  $A$  represents the thermodynamic factor, which is defined by Adler, Lane, and Steele<sup>28</sup> as a factor relating the oxygen vacancy concentration to the partial pressure of oxygen gas in the pore phase,  $A = (1/2) \partial \ln(P_{O_2}) / \partial \ln(C_v)$ . The diffusivity of the vacancies inside the cathode is denoted by  $D_v$ , whereas  $t$  represents time, and  $\Omega$  represents the solid phase region within the cathode where the vacancy transport takes place. The reaction at the pore/solid interface within the cathode can be modeled as a first-order chemical reaction as

$$-AD_v \nabla C_v = \kappa^{3D} (C_v - C_v^0) \quad \in \delta\Omega, \quad (7.2)$$

where  $\kappa^{3D}$  is the reaction rate constant,  $C_v^0$  is the equilibrium vacancy concentration and  $\delta\Omega$  represents the pore/solid interface.

We employ the smoothed boundary method (SBM)<sup>75</sup> to solve Eq. 7.1 within an experimentally determined, complex microstructure of the MIEC cathode, along with the boundary condition set in Eq. 7.2. Using SBM, these equations can be reformulated as

$$\psi \frac{\partial C_v}{\partial t} = \nabla \cdot (\psi AD_v \nabla C_v) - |\nabla \psi| \kappa^{3D} (C_v - C_v^0), \quad (7.3)$$

where  $\psi$  is a domain parameter that represents the geometry of the complex microstructure. Within the pores,  $\psi$  has a value of zero, and within the solid phase, it has a value of one. At the pore/solid interface, it smoothly transitions between zero and one. Further details about the process of obtaining  $\psi$  for a complex microstructure can be found in a previous work.<sup>59</sup> The application of an AC load causes the vacancy concentration,  $C_v$ , to oscillate about  $C_v^0$ . The oscillating perturbation is denoted by  $\Delta C$ , and thus, the relation between  $C_v$ ,  $C_v^0$ , and  $\Delta C$  can be written as

$$C_v = C_v^0 + \Delta C. \quad (7.4)$$

Since  $C_v^0$  is constant throughout space at a given temperature, the spatial variation of  $C_v$  can be described entirely in terms of  $\Delta C$  as

$$\psi \frac{\partial \Delta C}{\partial t} = \nabla \cdot (\psi AD_v \nabla (\Delta C)) - |\nabla \psi| \kappa^{3D} \Delta C. \quad (7.5)$$

Furthermore,  $AD_v$  can be assumed to be a constant for a MIEC cathode at a given temperature and for a small value of  $\Delta C$ .<sup>208</sup> Therefore, Eq. 7.5 can be written as

$$\psi \frac{\partial \Delta C}{\partial t} = AD_v \nabla \cdot (\psi \nabla (\Delta C)) - |\nabla \psi| \kappa^{3D} \Delta C. \quad (7.6)$$

Eq. 7.6 can be further simplified by expressing the time dependent part of the oscillations as complex exponential functions, i.e.,

$$\Delta C = \frac{\tilde{C} e^{i\omega t} + \tilde{C}^* e^{-i\omega t}}{2}, \quad (7.7)$$

where  $\tilde{C}$  is a complex quantity that varies in space with  $\tilde{C}^*$  as its complex conjugate,  $\omega$  is the frequency of the AC load, and  $i$  is the imaginary unit. Let  $C_R$  and  $C_I$  be the real and imaginary components of  $\tilde{C}$ . Upon the substitution of Eq. 7.7 into Eq. 7.6, the subsequent collection of real and imaginary terms, and the cancellation of the exponential functions, we obtain

$$AD_v \nabla \cdot (\psi \nabla C_R) - |\nabla \psi| \kappa^{3D} C_R = -\psi \omega C_I, \quad (7.8)$$

$$AD_v \nabla \cdot (\psi \nabla C_I) - |\nabla \psi| \kappa^{3D} C_I = \psi \omega C_R. \quad (7.9)$$

The above pair of equations is then solved to determine the  $C_R$  and  $C_I$  as functions of space and  $\omega$ . Once  $C_R$  and  $C_I$  are known, the impedance,  $Z(\omega)$ , of the cathode can be calculated as<sup>57,209</sup>

$$Z(\omega) = \frac{RTL}{(-n^2 F^2 D_v C_v^0)} \frac{\tilde{C}|_{x=0}/L}{\langle \partial \tilde{C} / \partial x|_{x=0} \rangle}, \quad (7.10)$$

where  $R$  is the universal gas constant,  $T$  is temperature,  $n$  is the number of moles of electrons consumed in the reaction,  $F$  is Faraday's constant,  $L$  is the thickness of the cathode, and  $\langle \partial \tilde{C} / \partial x|_{x=0} \rangle$  is the gradient of the concentration amplitude in the primary diffusion direction,  $x$ , averaged over the loading boundary located at  $x = 0$ , which represents the electrolyte/cathode interface. Furthermore, the first term on the right-hand side of Eq. 7.10 is the product of the material resistivity and thickness of the cathode, and it can be defined as  $Z_0$ . Therefore, Eq. 7.10 becomes

$$Z(\omega) = Z_0 \frac{\tilde{C}|_{x=0}/L}{\langle \partial \tilde{C} / \partial x|_{x=0} \rangle}. \quad (7.11)$$

For numerically solving Eq. 7.8 and Eq. 7.9, we chose to make them nondimensional by defining a length scale,  $l$ ; then,  $\hat{\nabla} = l \nabla$ . Hereafter, the circumflex ( $\hat{\cdot}$ ) symbol denotes that the associated operator or quantity is nondimensional. Substituting  $\hat{\nabla}/l$  in place of  $\nabla$ , and multiplying both sides with  $(l^2/(AD_v))$  gives

$$\widehat{\nabla} \cdot (\psi \widehat{\nabla} C_R) - |\widehat{\nabla} \psi| \kappa^{3D} \frac{l}{AD_v} C_R = -\psi \omega \frac{l^2}{AD_v} C_I, \quad (7.12)$$

$$\widehat{\nabla} \cdot (\psi \widehat{\nabla} C_I) - |\widehat{\nabla} \psi| \kappa^{3D} \frac{l}{AD_v} C_I = \psi \omega \frac{l^2}{AD_v} C_R. \quad (7.13)$$

By defining  $\widehat{\kappa}^{3D} = \kappa^{3D} l / (AD_v)$  and  $\widehat{\omega} = \omega l^2 / (AD_v)$  we obtain

$$\widehat{\nabla} \cdot (\psi \widehat{\nabla} C_R) - |\widehat{\nabla} \psi| \widehat{\kappa}^{3D} C_R = -\psi \widehat{\omega} C_I, \quad (7.14)$$

$$\widehat{\nabla} \cdot (\psi \widehat{\nabla} C_I) - |\widehat{\nabla} \psi| \widehat{\kappa}^{3D} C_I = \psi \widehat{\omega} C_R, \quad (7.15)$$

which are solved for two different sets of boundary conditions (BCs) as listed in Table 7.1.

Table 7.1. Sets of boundary conditions applied to the system of equations, Eqs. 7.14 and 7.15. Reproduced with permission from Ref. 32. Copyright 2021, the authors. Published by Frontiers Media SA.

Set of BCs\Location	$\widehat{\mathbf{x}} = \mathbf{0}$	$\widehat{\mathbf{x}} = \widehat{\mathbf{L}}$
Blocking current collector (BCC) BC	$C_R = 1, C_I = 0$	$\partial C_R / \partial \widehat{\mathbf{x}} = 0, \partial C_I / \partial \widehat{\mathbf{x}} = 0$
Transmissive current collector (TCC) BC	$C_R = 1, C_I = 0$	$C_R = 0, C_I = 0$

The two sets of the BCs differ only in those at the cathode/current collector interface ( $\widehat{\mathbf{x}} = \widehat{\mathbf{L}}$ ), as shown in Table 7.1. The blocking current collector (BCC) BC represents the case of a foil-like current collector, which blocks the ionic current at the cathode/current collector interface. This condition is more representative of the SOFC cathodes and is also used by the ALS model.<sup>28</sup> However, in some reports<sup>210–212</sup> the impedance behavior of MIEC oxides has also been fit with the relation that is applicable to the transmissive boundary condition. Under this boundary condition, the vacancy concentration is set to be zero at the cathode/current collector interface, and it is referred to as transmissive current collector (TCC) BC, which may correspond to a porous or mixed conducting current collector. We simulate the impedance behavior for both sets of boundary



conditions to cover the scenarios reported in the literature. The results for TCC BC are provided in the Section 7.8 (Figure 7.11 to Figure 7.15 and the associated text). Moreover, a list of the variables and symbols used in this chapter is provided in Table 7.2.

Table 7.2. List and description of the variables and symbols used in this chapter. Reproduced with permission from Ref. 32. Copyright 2021, the authors. Published by Frontiers Media SA.

Symbol	Description
$C_v$	Concentration of oxygen vacancies
$A$	The thermodynamic factor relating the oxygen vacancy concentration to the partial pressure of oxygen gas in the pore phase, $A = (1/2)\partial\ln(P_{O_2})/\partial\ln(C_v)$
$D_v$	Diffusivity of the oxygen vacancies within the solid bulk
$\Omega$	Solid phase region within the cathode
$\delta\Omega$	Pore/solid interface
$\kappa^{3D}$	Reaction rate constant
$\psi$	Domain parameter that represents the geometry of the complex microstructure. Within the pores, $\psi$ has a value of zero, and within the solid phase, it has a value of one
$\Delta C$	Perturbation in the oxygen vacancy concentration caused by the applied AC load
$\tilde{C}$	Complex quantity that varies in space
$\tilde{C}^*$	Complex conjugate of $\tilde{C}$
$\omega$	Frequency of the AC load
$i$	Imaginary unit
$C_R$	Real Component of $\tilde{C}$
$C_I$	Imaginary Component of $\tilde{C}$
$Z(\omega)$	Impedance
$R$	Universal gas constant
$T$	Temperature
$n$	Number of moles of electrons consumed in the electrochemical reaction
$F$	Faraday's constant
$L$	Thickness of the cathode
$Z_0$	Product of the material resistivity and thickness of the cathode
$(\cdot)$	The circumflex symbol denotes that the associated operator or quantity is nondimensional

$Z^{3D}$	Impedance of a finitely thick MIEC SOFC cathode
$R_{chem}$	Characteristic resistance describing the chemical contributions to the cathode impedance, as defined in the ALS model
$t_{chem}$	Relaxation time related to the chemical processes of solid-state diffusion and oxygen surface exchange, as defined in the ALS model
$\delta$	Characteristic distance related to the chemical processes of solid-state diffusion and oxygen surface exchange, as defined in the ALS model
$\epsilon$	The microstructure porosity
$\tau$	The microstructure tortuosity
$\kappa$	Surface exchange coefficient, as defined in the ALS model
$a$	Interfacial surface area per unit cathode volume
$C_{mc}$	The oxygen site concentration in the mixed conductor (mc).
$\kappa^{1D}$	Macrohomogeneous reaction rate constant
$Z^{FLG}$	The FLG impedance
$C_v^s$	Oxygen vacancy concentration at the pore/solid interface
$\Delta C^s$	The concentration oscillation at the pore/solid interface
$\alpha$	The ratio between the interface and the bulk concentration oscillations
$\langle \alpha \rangle$	Volume averaged $\alpha$
$\langle \alpha_0 \rangle$	DC value of $\langle \alpha \rangle$

### 7.3 Numerical implementation of the impedance model

The choice of SBM enabled the use of a standard Cartesian grid and the finite difference method to solve the above pair of equations (Eqs. 7.14 and 7.15). We used the center difference scheme to discretize the domain, which consists of  $352 \times 642 \times 594$  grid points. A uniform grid spacing ( $h = 0.0272$ , nondimensional) was selected to ensure the presence of at least 4 grid points across the pore/solid interface ( $\lambda = 0.0817$ ). The selection of the numerical parameters is discussed in the Section 7.8 (see Figure 7.10, Table 7.3, and the associated text) in detail. The Alternating-Direction Line-Relaxation (ADLR) method<sup>213</sup> was employed to solve the equations. The ADLR method utilizes a tridiagonal matrix solve to obtain the values of the solutions

individually along the x, y, and z directions. To simultaneously solve Eqs. 7.14 and 7.15, an iterative scheme was developed, in which the ADLR method was first used to calculate  $C_R$  for a given RHS of Eq. 7.14, and the resulting values were then used to update the RHS of Eq. 7.15. Subsequently,  $C_I$  was obtained using the Eq. 7.15 with the updated value of  $C_R$ . This procedure was repeated until both  $C_R$  and  $C_I$  numerically converged. The convergence metric was defined as the ratio between the absolute value of the sum of all elements of the change matrix (obtained by taking the difference between the updated concentration and previous concentration) and the sum of all elements of the old concentration matrix. The solution was deemed converged when the metric became less than a specified threshold value. The threshold value was deduced by progressively reducing it and observing the change in the resulting solution. It was found that solution did not change appreciably between the threshold values of  $10^{-10}$  and  $10^{-11}$ . Thus, a value of  $10^{-10}$  was selected as the criterion for the numerical convergence of the solution.

The length scale for the nondimensionalization was chosen as  $l = 0.46 \mu m$ . The reader is referred to a previous work<sup>59</sup> for more details on the selection of  $l$ . Finally, a wide range of values for  $AD_v$  and  $\kappa^{3D}$  are reported in the literature<sup>199</sup> because of the use of different cathode materials and operating temperatures (600-800 °C). Thus, three values of  $\hat{\kappa}^{3D}$  were selected for the study to cover this wide range and simulated the impedance behavior for the frequency values,  $\hat{\omega}$ , between 0 and 2.672. It should be noted that the value of  $\hat{\kappa}^{3D}$  is affected by the values of both  $AD_v$  and  $\kappa^{3D}$ .

#### **7.4 Derivation for impedance expressions and transcendental equation for tortuosity**

Adler, Lane, and Steele proposed a macrohomogeneous model to predict the impedance,  $Z^{3D}$ , of a finitely thick MIEC SOFC cathode, which is commonly known as the ALS model.<sup>28,29</sup> The model gives the impedance response for a symmetric cell with two identical cathodes. Since

only a half cell with a single cathode is considered in this investigation, the ALS impedance expression is divided by 2. Thus,

$$Z^{3D} = \frac{R_{chem}}{\sqrt{(1 + i\omega t_{chem})}} \coth\left(\frac{L}{\delta} \sqrt{(1 + i\omega t_{chem})}\right), \quad (7.16)$$

$$R_{chem} = \frac{RT}{4F^2} \sqrt{\left(\frac{\tau^2}{(1 - \epsilon)C_v^0 D_v a \kappa C_{mc}}\right)}, \quad (7.17)$$

$$t_{chem} = \frac{C_v^0(1 - \epsilon)}{A a \kappa C_{mc}}, \quad (7.18)$$

$$\delta = \sqrt{\left(\frac{C_v^0 D_v (1 - \epsilon)}{a \tau^2 \kappa C_{mc}}\right)}, \quad (7.19)$$

where  $\tau$  is the microstructure tortuosity,  $\epsilon$  is the microstructure porosity,  $\kappa$  is the surface exchange coefficient,  $a$  is interfacial surface area per unit cathode volume,  $C_{mc}$  is the oxygen site concentration (in the unit of mol/m<sup>3</sup>) in the mixed conductor (mc). The ALS model defines the reaction rate as  $A \kappa C_{mc} \Delta C / C_v^0$ , whereas it is defined as  $\kappa^{3D} \Delta C$  (Eq. 7.2) in this chapter. Therefore,  $\kappa$  and  $\kappa^{3D}$  are related as

$$\kappa^{3D} = \frac{A \kappa C_{mc}}{C_v^0}. \quad (7.20)$$

It should be noted that in the original ALS expression,  $\tau$  is used for denoting tortuosity factor, whereas in this chapter,  $\tau$  is used for denoting tortuosity. These two quantities are related; the tortuosity factor is the square of the tortuosity.

The substitution of Eqs. 7.17, 7.18, and 7.19 into 7.16 gives

$$Z^{3D} = \frac{RTL}{4F^2 C_v^0 D_v} \frac{\tau^2}{1 - \epsilon} \frac{\coth\left(\tau L \sqrt{\frac{\alpha \kappa^{3D}}{1 - \epsilon} + i\omega}\right)}{\tau L \sqrt{\frac{\alpha \kappa^{3D}}{1 - \epsilon} + i\omega}}. \quad (7.21)$$

Defining  $\kappa^{1D} = \kappa^{3D} a / (1 - \epsilon)$  as the macrohomogeneous reaction rate constant and using the definition for  $Z_0$  gives

$$Z^{3D} = Z_0 \frac{\tau^2}{1 - \epsilon} \frac{\coth\left(\tau L \sqrt{\frac{\kappa^{1D}}{AD_v} + i\omega}\right)}{\tau L \sqrt{\frac{\kappa^{1D}}{AD_v} + i\omega}}. \quad (7.22)$$

Finally, by following the same methodology as described in the model equation section, Eq. 7.22 can be made nondimensional as

$$\frac{Z^{3D}}{Z_0} = \frac{\tau^2}{1 - \epsilon} \frac{\coth(\tau \hat{L} \sqrt{\hat{\kappa}^{1D} + i\hat{\omega}})}{\tau \hat{L} \sqrt{\hat{\kappa}^{1D} + i\hat{\omega}}}, \quad (7.23)$$

where the nondimensional quantities are defined as  $\hat{L} = L/l$ ,  $\hat{\kappa}^{1D} = \kappa^{1D} l^2 / (AD_v)$ , and  $\hat{\omega} = \omega l^2 / (AD_v)$ . The conversion of Eq. 7.16 into Eq. 7.23 enables a direct comparison of the impedance expression of a complex 3D microstructure with that of the standard expression for 1D Finite Length Gerischer (FLG) impedance. The 1D FLG element represents the impedance of a 1D MIEC domain, where no microstructural effects are present, and the kinetics is co-limited by both surface reaction and bulk diffusion. The FLG impedance,  $Z^{FLG}$ , for a 1D domain with the same macrohomogeneous reaction rate constant,  $\hat{\kappa}^{1D}$ , and thickness,  $\hat{L}$ , as the SOFC cathode under consideration can be written as

$$\frac{Z^{FLG}}{Z_0} = \frac{\coth(\hat{L} \sqrt{\hat{\kappa}^{1D} + i\hat{\omega}})}{\hat{L} \sqrt{\hat{\kappa}^{1D} + i\hat{\omega}}}, \quad (7.24)$$

It is evident from a comparison between Eq. 7.23 and Eq. 7.24 that the microstructure affects the impedance response of a SOFC cathode in two ways. First, the microstructure increases the cathode impedance by a factor of  $\tau^2/(1 - \epsilon)$ . Second, the effective thickness of the cathode is increased by a factor of  $\tau$ . These effects can be exploited in the following way to determine the value of  $\tau$  using the value of  $Z^{3D}$ , which is experimentally known.

A ratio between Eq. 7.23 and Eq. 7.24 gives

$$\frac{Z^{3D}}{Z^{FLG}} = \frac{\tau}{1 - \epsilon} \frac{\coth(\tau \hat{L} \sqrt{\hat{\kappa}^{1D} + i\hat{\omega}})}{\coth(\hat{L} \sqrt{\hat{\kappa}^{1D} + i\hat{\omega}})}. \quad (7.25)$$

By taking the modulus (which is analytically unnecessary but numerically required) and after some rearrangement, Eq. 7.25 can be written as

$$\left| \tau \coth(\tau \hat{L} \sqrt{\hat{\kappa}^{1D} + i\hat{\omega}}) \right| = \left| \frac{Z^{3D}}{Z^{FLG}} \left( (1 - \epsilon) \coth(\hat{L} \sqrt{\hat{\kappa}^{1D} + i\hat{\omega}}) \right) \right|, \quad (7.26)$$

where terms containing  $\tau$  are collected on the left-hand side of the equation, yielding a transcendental equation for  $\tau$ . The nondimensional macrohomogeneous reaction rate constant,  $\hat{\kappa}^{1D} = \kappa^{1D} l^2 / (AD_v) = a l^2 \kappa^{3D} / ((1 - \epsilon) AD_v)$ , is dependent on material properties, namely  $\kappa^{3D}$  and  $AD_v$ , which can be determined from the literature for standard materials, as well as on microstructural characteristics, namely  $a$  and  $\epsilon$ , both of which can be determined experimentally (e.g., using mercury intrusion porosimeter<sup>214</sup>). Therefore, with both  $\hat{\kappa}^{1D}$  and  $Z^{3D}$  known, Eq. 7.26 can be solved to determine the effective tortuosity. However, before implementing this method, the ALS model is needed to be extended, as explained in the next section (Section 7.5).

## 7.5 Extension to the ALS model

The ALS model<sup>28,29</sup> is derived using the volume averaged form of the mass conservation equation (Eq. 7.1 and Eq. 7.2), which can be written as

$$(1 - \epsilon) \frac{\partial C_v}{\partial t} = \frac{AD_v(1 - \epsilon)}{\tau^2} \frac{\partial^2 C_v}{\partial x^2} - a\kappa^{3D}(C_v^s - C_v^0), \quad (7.27)$$

where  $C_v^s$  is the oxygen vacancy concentration at the pore/solid interface. Equation 7.27 can be written in terms of  $\Delta C$  by using the relation described by Eq. 7.4 as

$$(1 - \epsilon) \frac{\partial \Delta C}{\partial t} = \frac{AD_v(1 - \epsilon)}{\tau^2} \frac{\partial^2 \Delta C}{\partial x^2} - a\kappa^{3D}\Delta C^s. \quad (7.28)$$

The ALS model assumes the concentration oscillations at the pore/solid interface,  $\Delta C^s$ , and within the bulk of the solid,  $\Delta C$ , to be equal. However, in a physical system, the amplitude of the concentration oscillation,  $\tilde{C}$ , is smaller at the interface than the amplitude within the bulk because of the surface reaction. This phenomenon is demonstrated by considering a model microstructure with solid cylindrical domain surrounded by the pore phase, as shown in Figure 7.2a. The dimensions of the microstructure are also shown in the figure, and the primary diffusion direction of the model microstructure is along the  $\hat{x}$ -axis. The reaction occurs at the pore/solid interface, i.e., at the surface of the cylinder. Using this model geometry, we determine  $C_R$  and  $C_I$  within the cylinder for  $\hat{\omega} = 0.5$  and for two values of  $\hat{\kappa}^{3D}$  by solving Eqs. 7.8 and 7.9, which are subject to the BBC BC at  $\hat{x} = 1$ . Figure 7.2b and Figure 7.2c show the distribution of  $C_R$  and  $C_I$  along the radial direction of the cylinder at three positions along the  $\hat{x}$ -axis for  $\hat{\kappa}^{3D} = 0.02$  and  $\hat{\kappa}^{3D} = 0.2$ , respectively. The solution values outside the cylinder ( $|\hat{y}| > 1$ ) have no physical meaning as the domain parameter,  $\psi$ , is zero there, and therefore are not included in the plots.

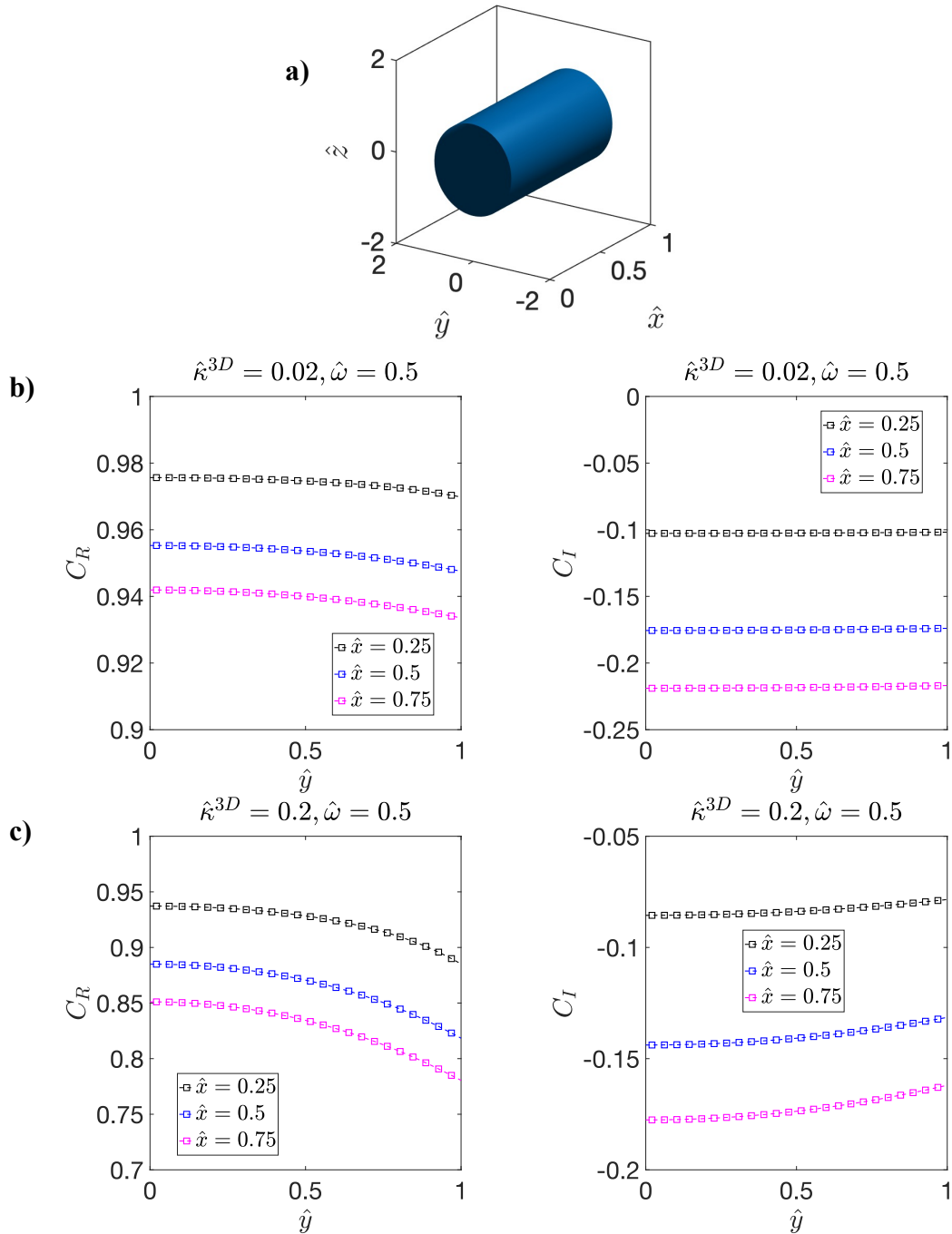


Figure 7.2. Simulated results for the spatial variation in  $C_R$  and  $C_I$  in a model cylindrical microstructure for two values of  $\hat{\kappa}^{3D}$ . The model microstructure, which contains a cylindrical solid domain with unit radius and length surrounded by pore phase. The distribution of  $C_R$  and  $C_I$  along the radial axis of the cylinder at different  $\hat{x}$  positions for  $\hat{\omega} = 0.5$  for (b)  $\hat{\kappa}^{3D} = 0.02$  and (c) 0.2. The solution values outside the cylinder ( $|\hat{y}| > 1$ ) have no physical meaning as the domain parameter,  $\psi$ , is zero there, and therefore are not included in the plots. Due to the radial symmetry of the cylinder, results are only shown for  $\hat{y}$  between zero and one. Reproduced with permission from Ref. 32. Copyright 2021, the authors. Published by Frontiers Media SA.



As can be seen, for a small value of  $\hat{\kappa}^{3D}$ , 0.02, the magnitude of  $C_R$  at  $\hat{y} = 0$  and  $\hat{y} = 1$  are similar (Figure 7.2b), whereas for a larger value of  $\hat{\kappa}^{3D}$ , 0.2, the magnitude of  $C_R$  is significantly smaller at  $\hat{y} = 1$  than at  $\hat{y} = 0$ , as shown in Figure 7.2c. This occurs because for a large  $\kappa^{3D}$ , the reaction consumes the ions at the interface, which is not readily replenished via diffusion, and thus  $C_R$  is smaller in magnitude at the interface than within the bulk. This spatial variation is observed throughout the cylinder, and a similar trend is seen for  $C_I$  as well.

It is evident from the above model case that the difference between the amplitude of the oscillations at the interface and within the bulk cannot be neglected. Thus, we now extend the ALS model. Let  $\alpha$  be the ratio between the interface and the bulk concentration oscillations, i.e.,  $\alpha = \Delta C^s / \Delta C$ . Therefore, Eq. 7.28 becomes

$$(1 - \epsilon) \frac{\partial \Delta C}{\partial t} = \frac{AD_v(1 - \epsilon)}{\tau^2} \frac{\partial^2 \Delta C}{\partial x^2} - \alpha \kappa^{3D} (\alpha \Delta C). \quad (7.29)$$

Eq. 7.29 suggests that the effect of  $\alpha$  can be incorporated into the ALS model by appropriately modifying  $\kappa^{3D}$ . However, this cannot be done as straightforwardly because  $\alpha$  varies in space. Nonetheless, the complexity can be reduced by considering the volume averaged  $\alpha$ , or  $\langle \alpha \rangle$ , to modify the value of  $\kappa^{3D}$ . The quantity  $\langle \alpha \rangle$  is defined as the ratio between average interface and average bulk concentration amplitudes, i.e.,

$$\langle \alpha \rangle = \frac{\int \tilde{C} |\hat{\nabla} \psi| d\hat{V}}{\int |\hat{\nabla} \psi| d\hat{V}} \cdot \left( \frac{\int \tilde{C} \psi d\hat{V}}{\int \psi d\hat{V}} \right)^{-1}, \quad (7.30)$$

where the integral is over the entire volume of the cathode microstructure.

To characterize  $\langle \alpha \rangle$ , we first determined its dependence on  $\hat{\omega}$  for the three values of  $\hat{\kappa}^{3D}$ . The results are summarized in Figure 7.3. Note that examination of the numerical accuracy is presented in Section 7.8 (see Figure 7.10, Table 7.3, and the associated text), and it has been shown that the error in the results is within 2%. As can be seen, for a particular value of  $\hat{\kappa}^{3D}$ ,  $\langle \alpha \rangle$  has

much higher real component than the imaginary component at all  $\hat{\omega}$  values. Moreover, the real component remains constant with increasing  $\hat{\omega}$  before transitioning into a regime where it decreases with increasing  $\hat{\omega}$ . The  $\hat{\omega}$  value where this transition occurs increases with the value of  $\hat{\kappa}^{3D}$ . Furthermore, since  $\langle \alpha \rangle$  remains constant for a wide range of frequency values, we made a further simplifying assumption by approximating  $\langle \alpha \rangle$  by its DC value,  $\langle \alpha_0 \rangle$ . We calculated  $\langle \alpha_0 \rangle$  for 19 values of  $\hat{\kappa}^{3D}$  ranging from  $5 \times 10^{-3}$  to  $6 \times 10^{-1}$  and summarized the results in Figure 7.4. The value of  $\langle \alpha_0 \rangle \approx 1$  for small values of  $\hat{\kappa}^{3D}$ , and it monotonically decreases with increasing  $\hat{\kappa}^{3D}$ . Both characteristics are expected because small values of  $\hat{\kappa}^{3D}$  suggest that the reaction rate is lower than the diffusion rate, and thus there is little difference between the interface and bulk concentration amplitudes. However, for large values of  $\hat{\kappa}^{3D}$ , the reaction rate is much larger than the diffusion rate, which causes the concentration amplitude at the pore/solid interface to be lower than the bulk.

Using  $\langle \alpha_0 \rangle$  as a function of  $\hat{\kappa}^{3D}$  to capture the difference between the surface and bulk concentration amplitudes, we propose a modified macrohomogeneous reaction rate constant,  $\hat{\kappa}^{1D}$ , in the ALS expression as

$$\frac{Z^{3D}}{Z_0} = \frac{\tau^2}{1 - \epsilon} \frac{\coth(\tau \hat{L} \sqrt{\langle \alpha_0 \rangle \hat{\kappa}^{1D} + i \hat{\omega}})}{\tau \hat{L} \sqrt{\langle \alpha_0 \rangle \hat{\kappa}^{1D} + i \hat{\omega}}}. \quad (7.31)$$

Thus, the expression for calculating the effective tortuosity can be modified as

$$\left| \tau \coth(\tau \hat{L} \sqrt{\langle \alpha_0 \rangle \hat{\kappa}^{1D} + i \hat{\omega}}) \right| = \left| \frac{Z^{3D}}{Z_{FLG}} \left( (1 - \epsilon) \coth(\hat{L} \sqrt{\langle \alpha_0 \rangle \hat{\kappa}^{1D} + i \hat{\omega}}) \right) \right|. \quad (7.32)$$

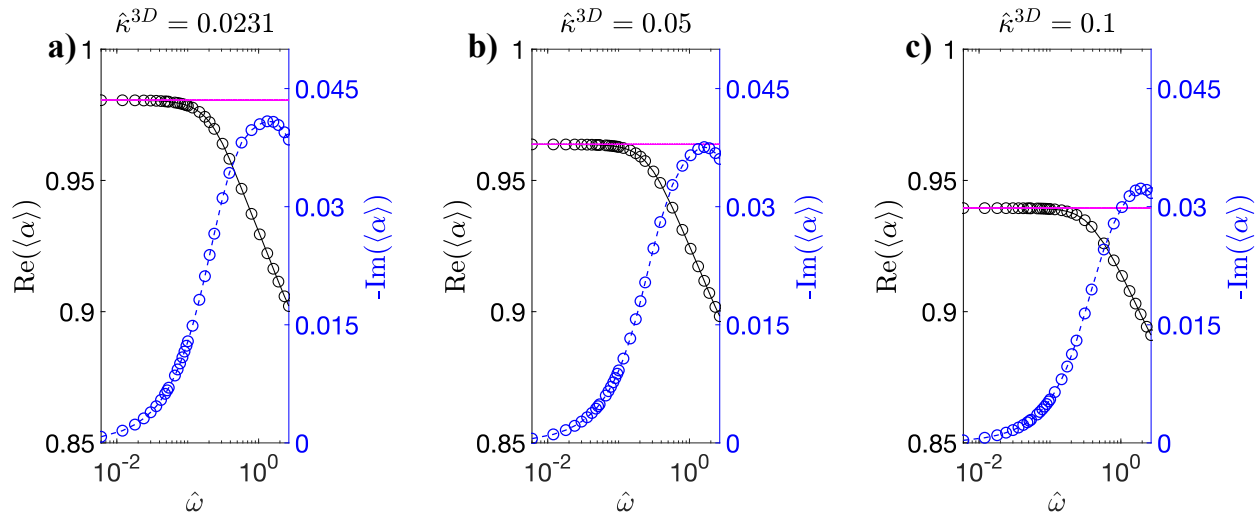


Figure 7.3. Calculated  $\langle \alpha \rangle$  vs.  $\hat{\omega}$  (BCC BC) at (a)  $\hat{\kappa}^{3D} = 0.0231$ , (b) 0.05, and (c) 0.1. The real component (black solid curve) and the imaginary component (blue dashed curve) of  $\langle \alpha \rangle$  are plotted on the left and right y-axes, respectively. The circles indicate the calculated data point. The DC values of  $\langle \alpha \rangle$  are shown with horizontal magenta dotted lines as a reference. Reproduced with permission from Ref. 32. Copyright 2021, the authors. Published by Frontiers Media SA.

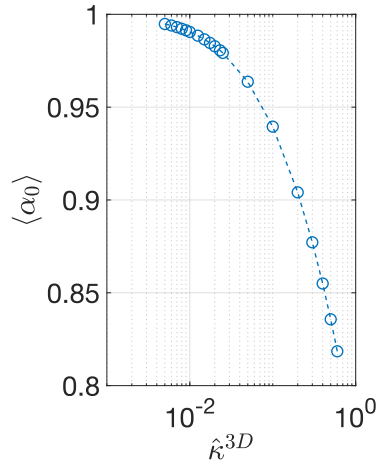


Figure 7.4. DC value of  $\langle \alpha \rangle$ ,  $\langle \alpha_0 \rangle$ , as a function of  $\hat{\kappa}^{3D}$ . Reproduced with permission from Ref. 32. Copyright 2021, the authors. Published by Frontiers Media SA.

## 7.6 Simulated impedance and tortuosity calculation

Figure 7.5 shows the impedance spectra of the experimentally obtained microstructure for three values of  $\hat{\kappa}^{3D}$ , along with the impedance spectra obtained from the analytical expression for the 1D FLG impedance in Eq. 7.24. As expected, the two curves for the same value of  $\hat{\kappa}^{3D}$  deviate significantly, with the FLG curve underestimating the impedance value. To enable a better visualization of the difference a few iso-frequency points, on both the curves, are marked with magenta triangles. We note that the discussion below is for a fixed cathode thickness provided in the numerical implementation section. The effect of cathode thickness on the impedance and tortuosity is discussed qualitatively in Section 7.8.

By solving Eq. 7.32, we calculated  $\tau$  for the three values of  $\hat{\kappa}^{3D}$  over the entire frequency range examined. The results are shown in Figure 7.6. From this comparison, three trends can be observed in the tortuosity data. First, for a given value of  $\hat{\kappa}^{3D}$ ,  $\tau$  remains almost a constant before it begins to decrease with an increase in  $\hat{\omega}$ . The relation between  $\tau$  and  $\log(\hat{\omega})$  at high frequencies can be represented by a linear function with a slope of  $-0.1033$ , as shown by black dashed line in Figure 7.6. Second, the low frequency value of  $\tau$  decreases with an increase in  $\hat{\kappa}^{3D}$ . Finally, the three  $\tau$  vs.  $\hat{\omega}$  curves coincide at high frequencies.

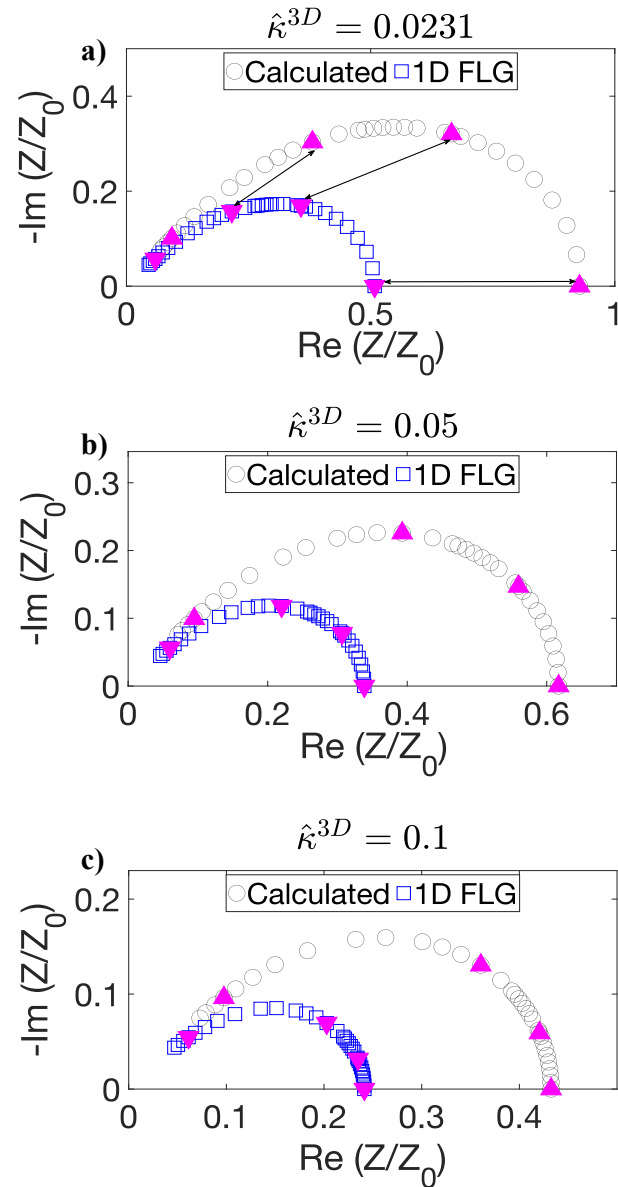


Figure 7.5. Nyquist plots obtained from 3D calculations for the BCC BC (black curve) and 1D FLG model (blue curve) for (a)  $\hat{\kappa}^{3D} = 0.0231$ , (b) 0.05, and (c) 0.1. The iso-frequency points are marked with upright magenta triangles on the black curves and inverted magenta triangles on the blue curves. Three iso-frequency points are noted using arrows in (a). Reproduced with permission from Ref. 32. Copyright 2021, the authors. Published by Frontiers Media SA.

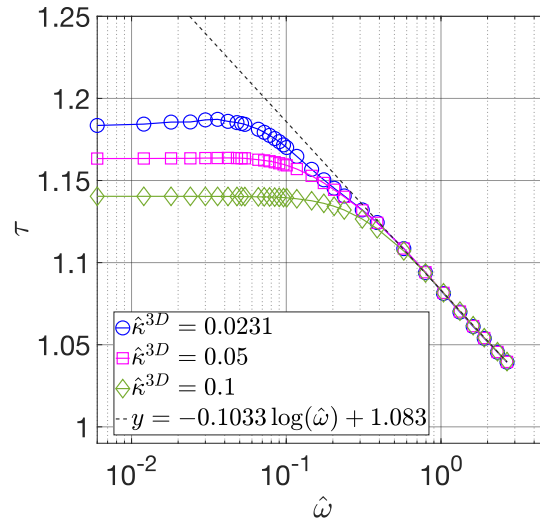


Figure 7.6. Calculated  $\tau$  vs.  $\hat{\omega}$  relations (BCC BC) for  $\hat{\kappa}^{3D} = 0.0231$  (blue circles), 0.05 (magenta squares), and 0.1 (green diamonds). The black dashed line represents the fit with a linear function at high frequencies. Reproduced with permission from Ref. 32. Copyright 2021, the authors. Published by Frontiers Media SA.

To provide further insights, Figure 7.7 shows the distribution of  $C_R$  and  $C_I$  in the complex microstructure at a low value of  $\hat{\omega}$ , 0.018, which is close to the DC case, for three  $\hat{\kappa}^{3D}$  values. For the low value of  $\hat{\kappa}^{3D}$ , 0.0231, the gradient in the concentration amplitude is nonzero in much of the microstructure thickness, as shown in Figure 7.7a. However, with an increase in the value of  $\hat{\kappa}^{3D}$ , the gradient spans lesser and lesser of the microstructure at the same frequency, as qualitatively shown in Figure 7.7b-c. Thus, it is evident that the penetration depth of the diffusing species (oxygen vacancies) at the same frequency of the AC load decreases with an increase in  $\hat{\kappa}^{3D}$ . Furthermore, Figure 7.8 shows the distribution of  $C_R$  and  $C_I$  in the microstructure for three values of  $\hat{\kappa}^{3D}$  at a higher frequency value,  $\hat{\omega} = 1.038$ . As can be seen, the gradient in the concentration amplitude is mostly confined to a small region near the electrolyte/cathode interface for all values of  $\hat{\kappa}^{3D}$  at the high frequency regime. Therefore, the penetration depth for each case at the high frequency value is much smaller than at the low frequency value. Moreover, at  $\hat{\omega} =$

1.038 the penetration depth is similar for all three values of  $\hat{\kappa}^{3D}$ . This shows that the penetration depth is a function of both  $\hat{\kappa}^{3D}$  and  $\hat{\omega}$ . Since the effective tortuosity of a microstructure is directly influenced by the penetration depth,<sup>59</sup> it is evident that the effective tortuosity is also a function of both  $\hat{\kappa}^{3D}$  and  $\hat{\omega}$ . Therefore, it can be inferred that, for a porous medium, where the rate kinetics is co-limited by both the bulk diffusion and surface reaction, the tortuosity is a function not only of the microstructural characteristics but also of  $\hat{\kappa}^{3D}$ , which is a combination of material property. In addition, it also depends on the frequency, as was found in the case for diffusional impedance case.<sup>59</sup> The observed behavior of the effective tortuosity could also be seen from the distribution of reaction-diffusion streamlines,<sup>215</sup> which is a 3D visualization of the flux. As the penetration depth decreases, the streamlines or the trajectories of the oxygen vacancies begin to straighten. The resulting decrease in the deviation from a straight path causes the effective tortuosity to decrease.

We note that there exists an error of up to 9% in the calculated impedance value at high frequencies, as described in Section 7.8 (see Figure 7.10, Table 7.3 and the associated text). The error arises because the accuracy of numerical approximations of the gradients in the concentration amplitudes decreases at high frequencies, as our numerical implementation employs fixed grid resolution throughout the simulation domain. Although this error can be reduced by doubling the grid resolution, such calculations become computationally expensive (as discussed in Section 7.8; see Figure 7.10, Table 7.3 and the associated text) without providing additional insights. In fact, the error does not affect the observed qualitative behavior of the effective tortuosity, which is the one of the two main focuses of this work. Thus, the numerical results presented here are sufficiently accurate for demonstrating the dependence of the effective tortuosity on  $\hat{\kappa}^{3D}$  and  $\hat{\omega}$ . In the future, we plan to implement the model into a finite element framework with adaptive-mesh capability

such as PRISMS-PF framework,<sup>27</sup> in which SBM is already implemented, to increase the computational efficiency of the calculations at high frequencies.

Finally, to further evaluate the accuracy of approximating  $\langle\alpha\rangle$  with  $\langle\alpha_0\rangle$  in the extended ALS model, we compared the tortuosity results with and without this approximation, latter of which include the frequency dependence of  $\langle\alpha\rangle$ . A comparison between the two sets of  $\tau$  value obtained for the three values of  $\hat{\kappa}^{3D}$  is provided in Figure 7.9, which show good agreement. Hence the use of  $\langle\alpha_0\rangle$  as the correction factor is sufficiently accurate for calculating the effective tortuosity of a MIEC SOFC cathode using the EIS data.



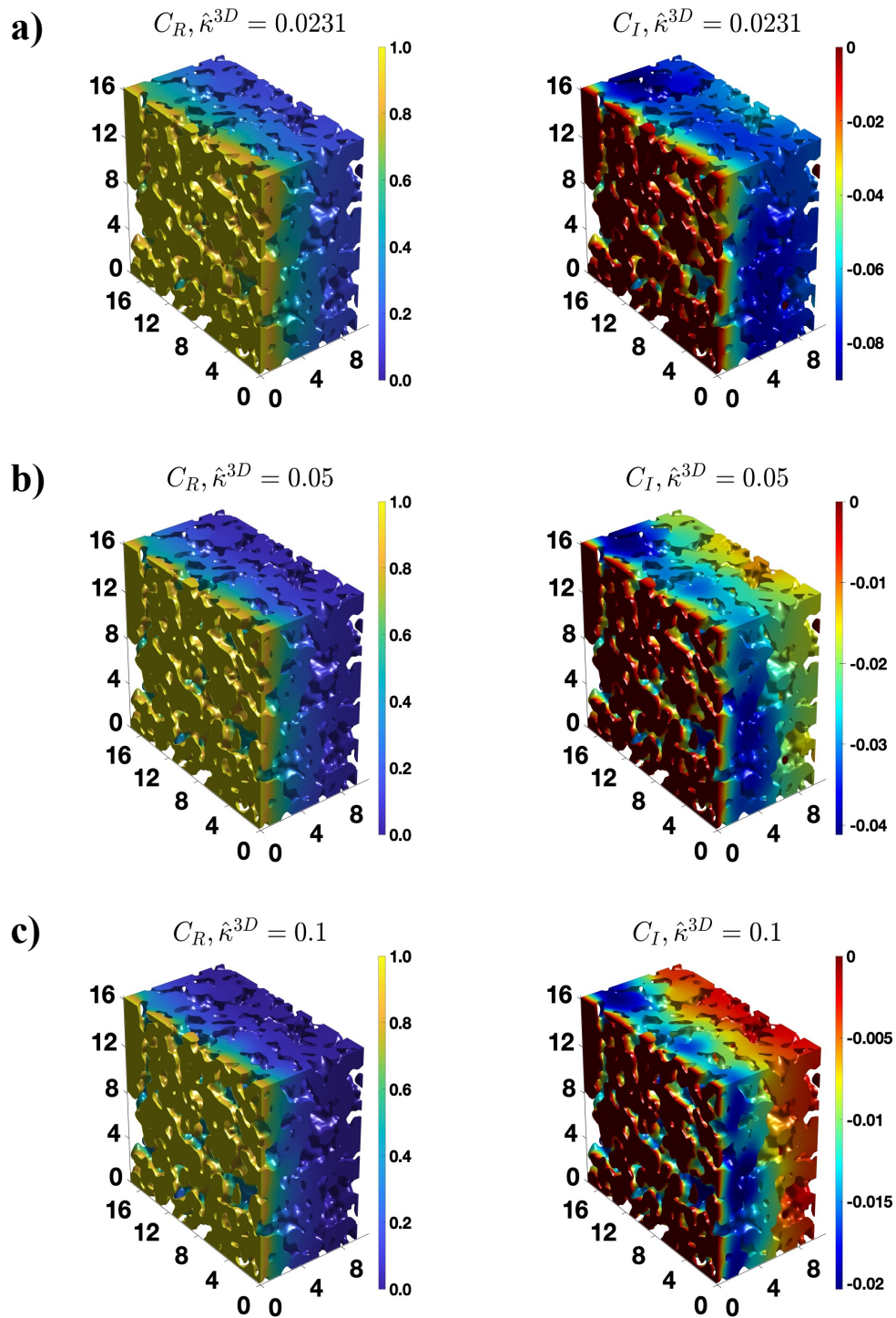


Figure 7.7. The distribution of the real and imaginary components of the concentration amplitude calculated for the BCC BC,  $\hat{\omega} = 0.018$  and (a)  $\hat{\kappa}^{3D} = 0.0231$ , (b) 0.05, and (c) 0.1. Reproduced with permission from Ref. 32. Copyright 2021, the authors. Published by Frontiers Media SA.

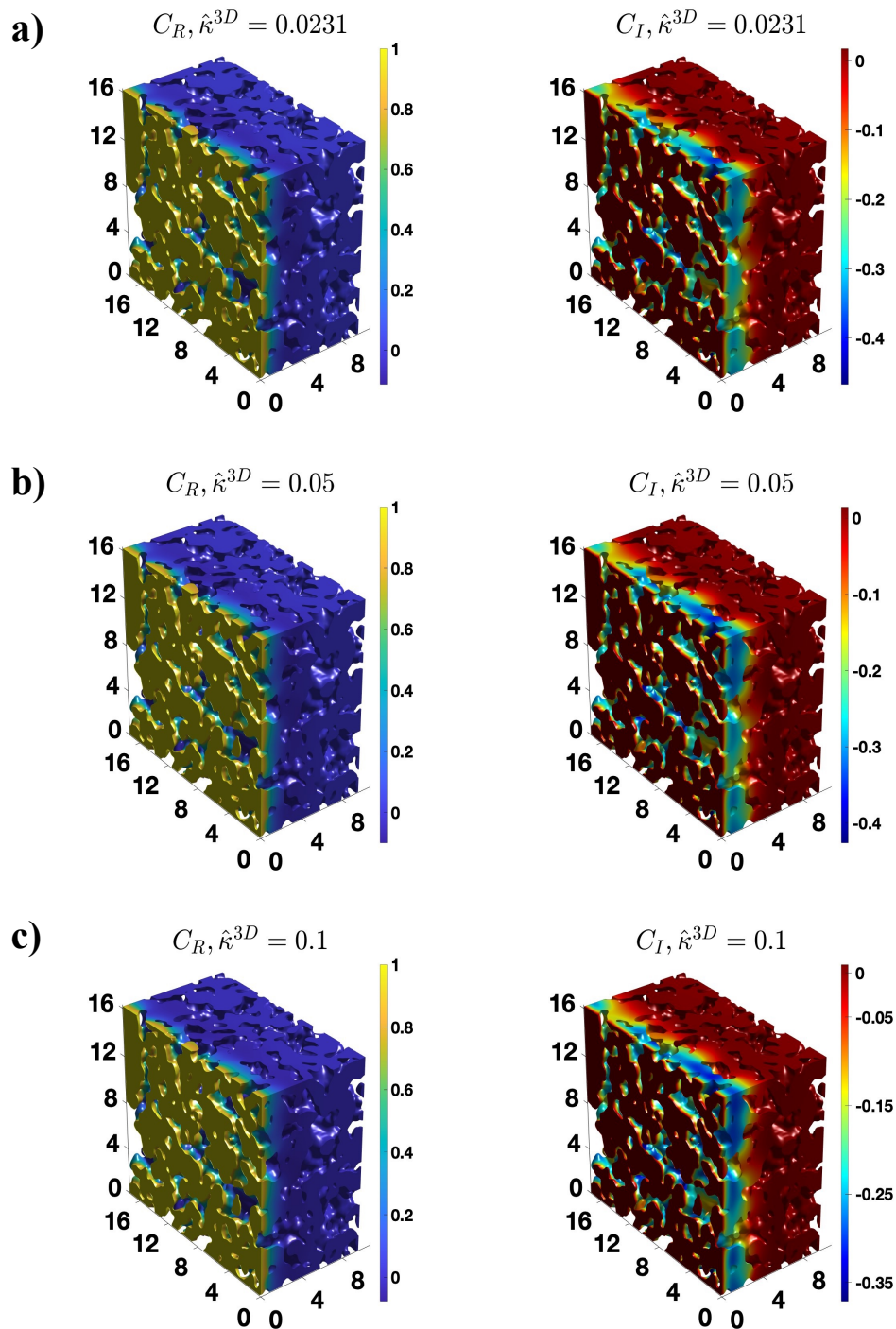


Figure 7.8. The distribution of the real and imaginary components of the concentration amplitude calculated for the BCC BC,  $\hat{\omega} = 1.038$  and (a)  $\hat{\kappa}^{3D} = 0.0231$ , (b) 0.05, and (c) 0.1. Reproduced with permission from Ref. 32. Copyright 2021, the authors. Published by Frontiers Media SA.

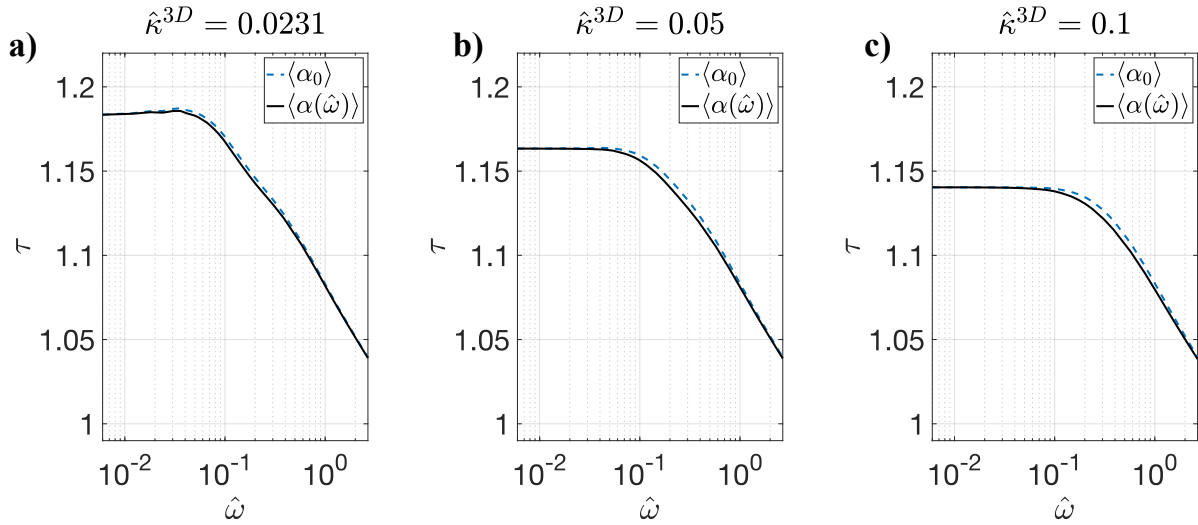


Figure 7.9. Comparisons of the calculated  $\tau$  vs.  $\hat{\omega}$  relations (BCC BC) by using  $\langle \alpha_0 \rangle$  (blue curve) and  $\langle \alpha \rangle$  (black curve) for (a)  $\hat{\kappa}^{3D} = 0.0231$ , (b) 0.05, and (c) 0.1. Reproduced with permission from Ref. 32. Copyright 2021, the authors. Published by Frontiers Media SA.

## 7.7 Chapter 7 Summary

In this chapter, we simulated the impedance behavior of a statistically representative portion of an experimentally determined complex three-dimensional microstructure of an unbiased MIEC SOFC cathode under two different boundary conditions. Our investigation generated two key insights. First, due to the presence of surface reaction, the amplitude of oscillations in the vacancy concentration is lower at the pore/solid interface than within the solid bulk of the cathode. This difference between the interface and bulk amplitude increases with an increase in the ratio between the reaction rate constant and the bulk diffusion coefficient. Therefore, to account for this difference, we extended the ALS model in terms of the ratio of the surface and bulk concentration amplitudes at zero frequency,  $\langle \alpha_0 \rangle$ , and provided numerically evaluated  $\langle \alpha_0 \rangle$  as a function of the reaction rate coefficient,  $\hat{\kappa}^{3D}$ . Second, through the examination of the three-dimensional distribution of the vacancy concentration amplitude, we showed that the penetration depth of the

oxygen vacancies is a function of  $\hat{\kappa}^{3D}$  and the frequency of the applied AC load,  $\hat{\omega}$ . Due to the direct dependence of the effective tortuosity on the penetration depth, the effective tortuosity also becomes a function of  $\hat{\kappa}^{3D}$  and  $\hat{\omega}$  in addition to the microstructure. Furthermore, we developed a method, which utilizes the EIS data, for determining  $\tau$  as a function of  $\hat{\kappa}^{3D}$  and  $\hat{\omega}$  for a cathode with known material properties (such as the reaction rate constant and bulk diffusion constant), pore surface area, and porosity.

## 7.8 Chapter 7 Appendix

### *Numerical accuracy analysis*

We tested the grid spacing used in the three-dimensional calculations by considering a model cylindrical microstructure of a unit (nondimensional) length and radius. These dimensions were selected to ensure that the cylinder has the same surface area to volume ratio as the complex microstructure; such a selection enables us to assume a similar numerical behavior of our calculations involving the experimental microstructure as those involving the model cylindrical microstructure.

Two grid related parameters affect the accuracy of the SBM-based calculations, namely, the grid spacing  $h$  and interfacial thickness  $\lambda$ . We tested three value pairs of the grid parameters. First, keeping the parameter values to be same as the complex microstructure ( $h = 0.0272$ ,  $\lambda = 0.0817$ ), second, decreasing the grid spacing to half and retaining the same interfacial thickness, and third, decreasing both the grid spacing and interfacial thickness to half of the first set of values. It should be noted that among the three configurations, third is the most refined grid while first is the least refined grid. We compare the calculated impedance values for the three configurations at three frequency values  $\hat{\omega} = 1.038$ , 42, and 95, and the results are summarized in Table 7.3, along

with the % difference in the real and imaginary components of the impedance with respect to results for the third configuration.

For the lowest frequency case, which is comparable to  $\hat{\omega} = 0.011$  case in the simulations with the experimental microstructure, the error is small in both the calculated concentration amplitudes and the impedance. In Figure 7.10a,  $C_R$  and  $C_I$  are shown for the test cases for this frequency. The maximum differences in  $C_R$ ,  $C_I$ , and the impedance values between the first and third configuration is  $\sim 0.1\%$ ,  $1\%$ , and  $1\%$  for this frequency. For the intermediate frequency case, which is comparable to  $\hat{\omega} = 0.46$  case in the simulations with the experimental microstructure, the error in  $C_R$  and  $C_I$  is of the same order as that of the previous case, as shown in Figure 7.10b. However, the error in the real component of the impedance value increased to  $5.75\%$  while that in the imaginary component remains less than  $1\%$ , as shown in Table 7.3. A similar trend in errors is observed for the high frequency case, which is comparable to  $\hat{\omega} = 1.038$  case in the simulations with the experimental microstructure. The error in  $C_R$  and  $C_I$  is still comparable to the low and intermediate frequency cases. However, the error in the real component of the impedance value increased to  $8.68\%$  while that in the imaginary component remains less than  $1\%$ , as shown in Table 7.3.

From the above analysis, it can be concluded that the first grid configuration ( $h = 0.0272$ ,  $\lambda = 0.0817$ ) is sufficiently refined to accurately calculate the value of  $C_R$  and  $C_I$  (and therefore  $\langle\alpha\rangle$ ) in the cylindrical microstructure, and consequently, in the experimental microstructure over the entire frequency range studied. However, the numerical accuracy of the first grid configuration for the impedance calculation starts decreasing at intermediate to high frequency values. This decrease in accuracy is expected because with increasing frequency, the gradients in the concentration amplitude becomes larger in magnitude, which becomes harder to resolve with a

fixed grid resolution. Nonetheless, the maximum error observed in the impedance value is  $\sim 9\%$ , which is acceptable because of two reasons. First, this error only occurs at high frequency values and the error leads to an overestimation of the impedance value. Thus, the error does not alter the qualitative behavior of the calculated tortuosity, which is the one of two main focuses of this chapter. Second, the selected resolution offers a good balance between accuracy and computational efficiency. Although the error in the impedance values at high frequencies can be reduced by doubling the grid resolution, a simulation with such a grid would be computationally expensive without yielding additional insights. With the current grid configuration, a typical impedance calculation for the complex microstructure at a given frequency takes  $\sim 12.5$  hrs on 288 CPU cores. Doubling the resolution would result in an eightfold increase in the system size, and thus in the computation time, which makes it costly to run, especially if multiple materials parameters must be examined.

In conclusion, the selected grid parameters ( $h = 0.0272$ ,  $\lambda = 0.0817$ ) offer high accuracy in the calculation of  $C_R$  and  $C_I$  over all frequency values studied here and in the calculation of impedance at low frequency values. For intermediate to high frequency values, this resolution results in up to 9% overestimation in the impedance value; however, the additional accuracy would not lead to new insights for the phenomena considered in this chapter. If quantitative predictions at the high frequency regime are desired, higher resolution, with adaptive mesh, should be considered.

Table 7.3. List of the errors in the real and imaginary components of impedance calculated for three different grids. Reproduced with permission from Ref. 32. Copyright 2021, the authors. Published by Frontiers Media SA.

$\hat{\omega}$	$h$	$\lambda$	$Z^{3D}/Z_0$	% difference in real component	% difference in imaginary component
1.038	0.0272	0.0817	3.31 – 4.52i	0.91%	1.1%
	0.0136	0.0817	3.27 – 4.47i	0.30%	0.04%
	0.0136	0.0408	3.28 – 4.47i	--	--
42	0.0272	0.0817	0.625 – 0.550i	5.75%	0.36%
	0.0136	0.0817	0.591 – 0.552i	0.02%	0.02%
	0.0136	0.0408	0.591 – 0.552i	--	--
95	0.0272	0.0817	0.438 – 0.366i	8.68%	0.60%
	0.0136	0.0817	0.403 – 0.368i	0.02%	0.03%
	0.0136	0.0408	0.403 – 0.368i	--	--

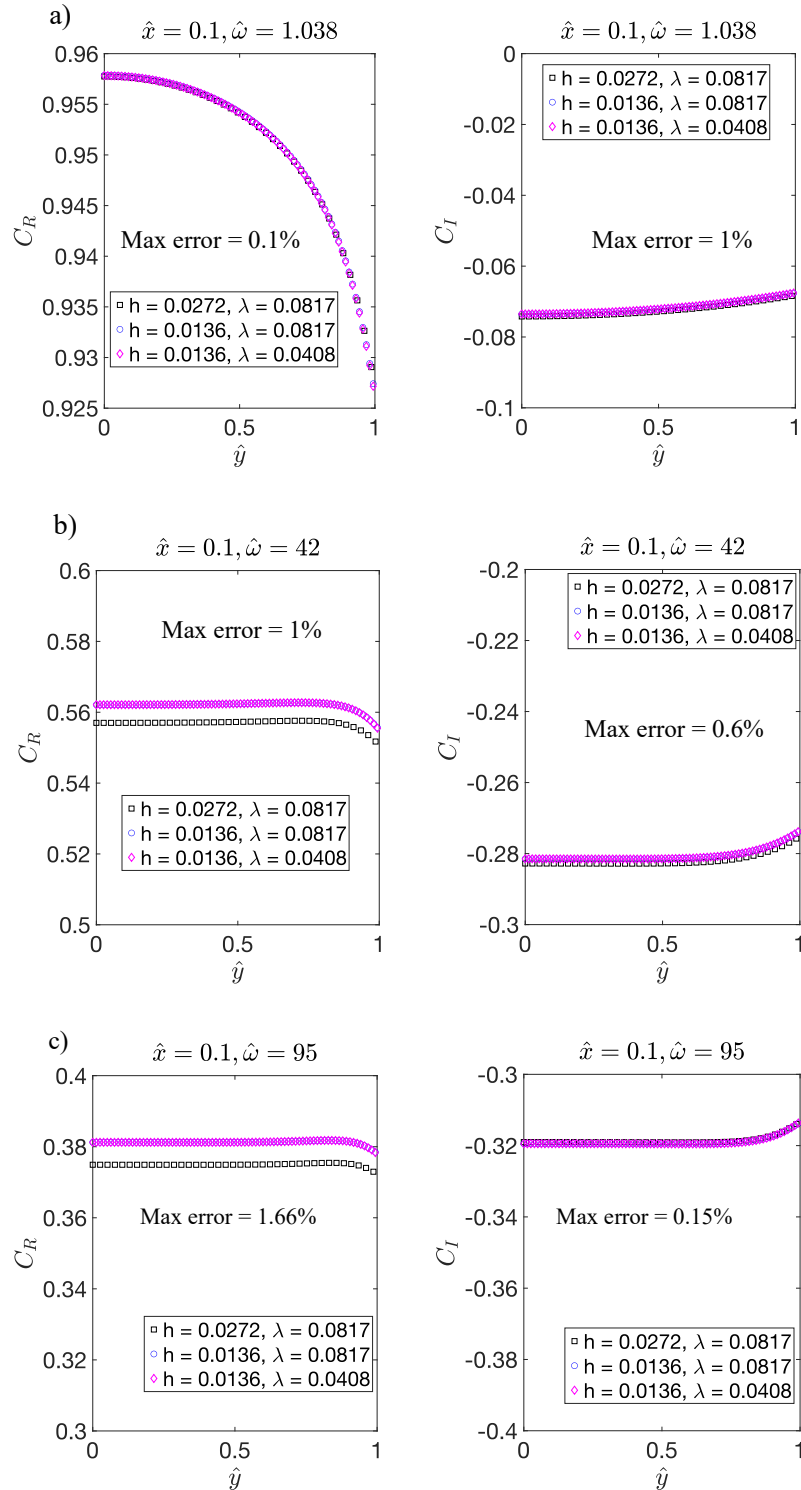


Figure 7.10. Plot of  $C_R$  and  $C_I$  as a function of cylinder radius for the three grid configurations at  $\hat{x} = 0.1$  and (a)  $\hat{\omega} = 1.038$ , (b)  $\hat{\omega} = 42$ , and (c)  $\hat{\omega} = 95$ . Reproduced with permission from Ref. 32. Copyright 2021, the authors. Published by Frontiers Media SA.



### *Effect of cathode thickness on the impedance*

The effect of cathode thickness on the impedance can be predicted by the extended ALS model, Eq. 7.31. By taking  $Z_0$  on the right-hand side, it can be seen that there is the impedance value has an explicit dependence on the cathode thickness in terms of the coth term, and an implicit dependence in terms of tortuosity. To analyze this dependence, we consider cathodes of the same material with three different thicknesses under a DC load. First, we consider a cathode thickness that is much larger than the penetration depth. For such a case, the impedance value does not change with the cathode thickness, assuming there is no gas transport limitation. This is because at a such large cathode thickness, the coth term is almost equal to 1 while tortuosity remains equal to the value corresponding to the penetration depth. Second, we consider a cathode thickness that is smaller than the penetration depth but larger than the average feature size of the microstructure (solid volume/surface area). For such a case, if the cathode thickness is decreased, a decrease in tortuosity will also be observed. However, the coth term will increase much more rapidly because of its decreasing argument. Therefore, the cathode impedance will increase as the cathode thickness is increased. Finally, we consider a cathode thickness that is sufficiently smaller than the average feature size of the microstructure. For this case, tortuosity will be  $\approx 1$  because the microstructural features are truncated by the current-collector/cathode and electrolyte/cathode interfaces and oxygen vacancies can flow directly from one boundary to the other boundary in a straight path. However, the coth term will continue to increase with a reduction in cathode thickness. Therefore, for this case, any further reduction in cathode thickness will lead to an increase in the cathode impedance.

*Results for TCC boundary conditions*

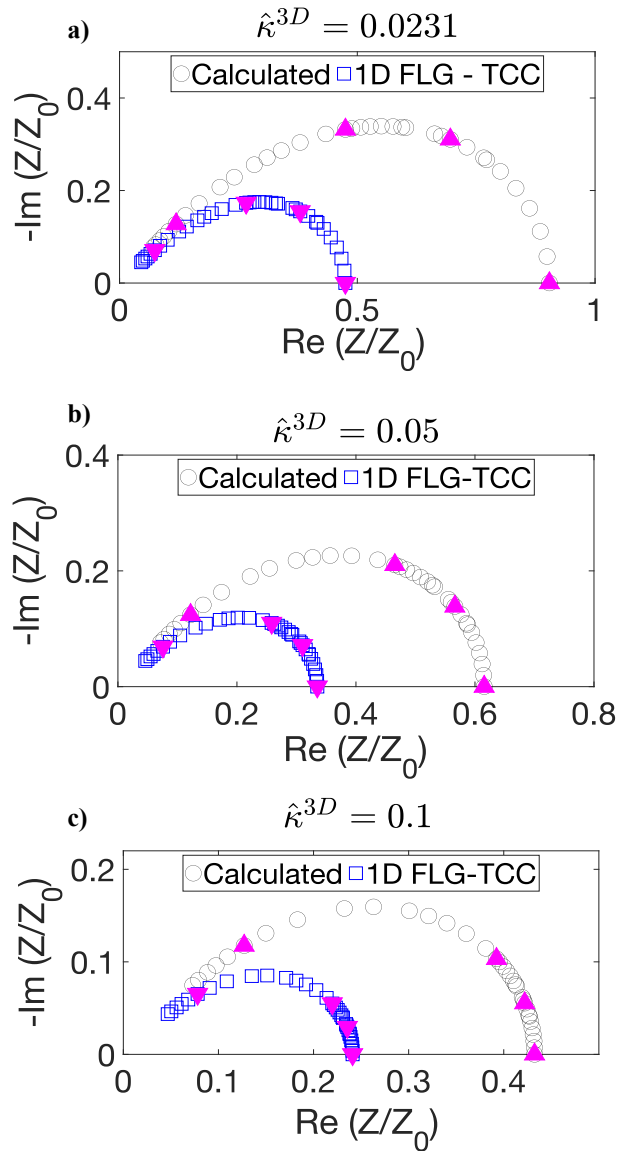


Figure 7.11. Nyquist plots obtained from 3D calculations for the TCC BC (black circles) and 1D FLG-TCC model (blue squares) for (a)  $\hat{\kappa}^{3D} = 0.0231$ , (b) 0.05, and (c) 0.1. The iso-frequency points are marked with upright magenta triangles on the black circles and inverted magenta triangles on the blue curves. Reproduced with permission from Ref. 32. Copyright 2021, the authors. Published by Frontiers Media SA.

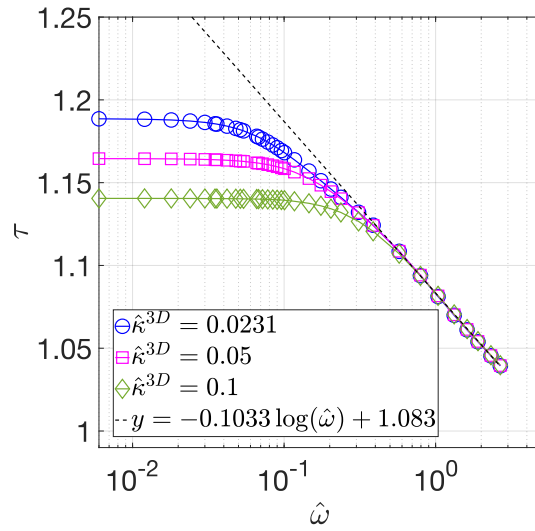


Figure 7.12. Calculated  $\tau$  vs.  $\hat{\omega}$  relations (TCC BC) for  $\hat{\kappa}^{3D} = 0.0231$  (blue circles), 0.05 (magenta squares), and 0.1 (green diamonds). The black dashed line represents the fit with a linear function at high frequencies. Reproduced with permission from Ref. 32. Copyright 2021, the authors. Published by Frontiers Media SA.

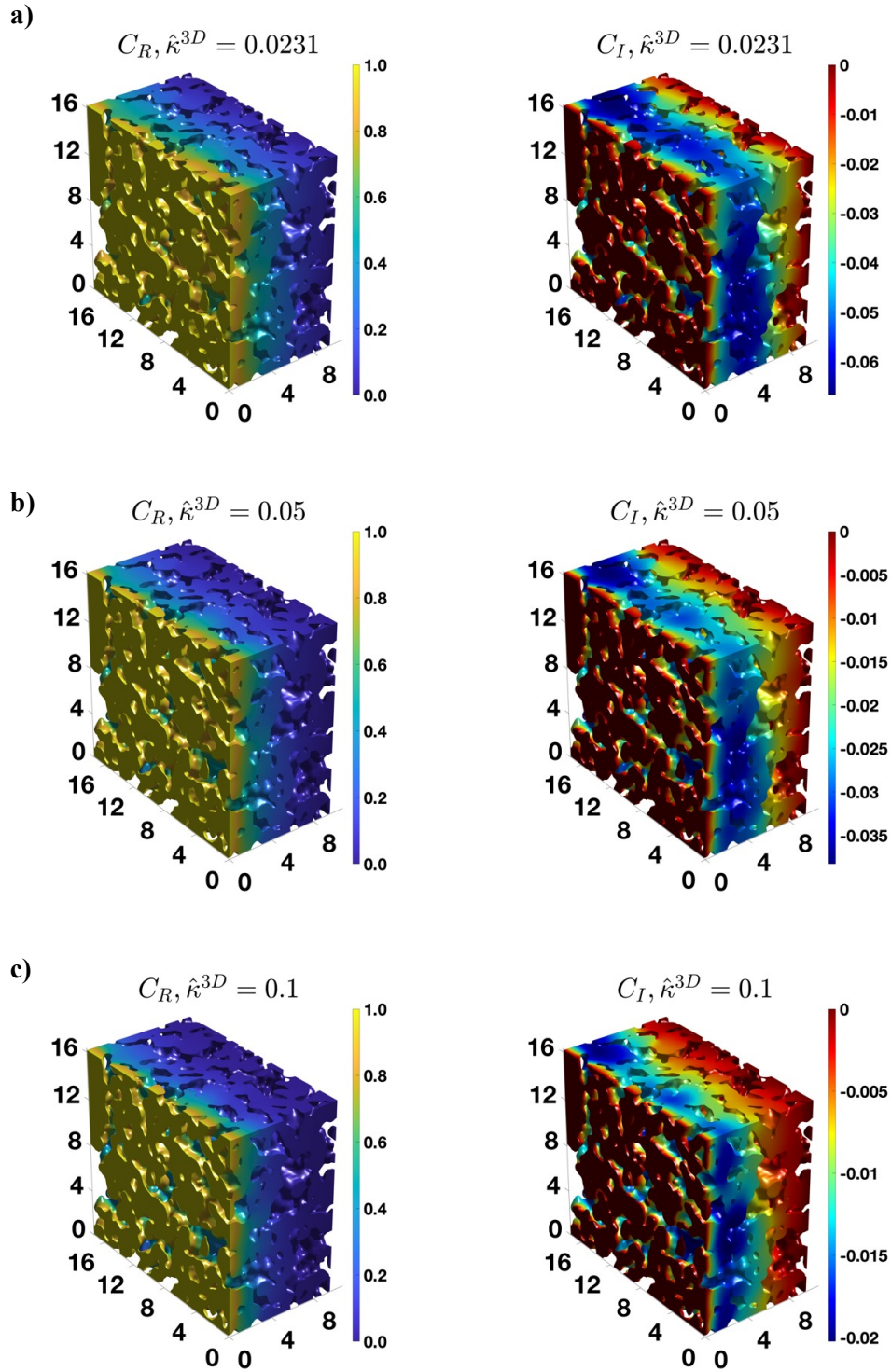


Figure 7.13. The distribution of the real and imaginary components of the concentration amplitude calculated for the TCC BC,  $\hat{\omega} = 0.018$  and (a)  $\hat{\kappa}^{3D} = 0.0231$ , (b) 0.05, and (c) 0.1. Reproduced with permission from Ref. 32. Copyright 2021, the authors. Published by Frontiers Media SA.

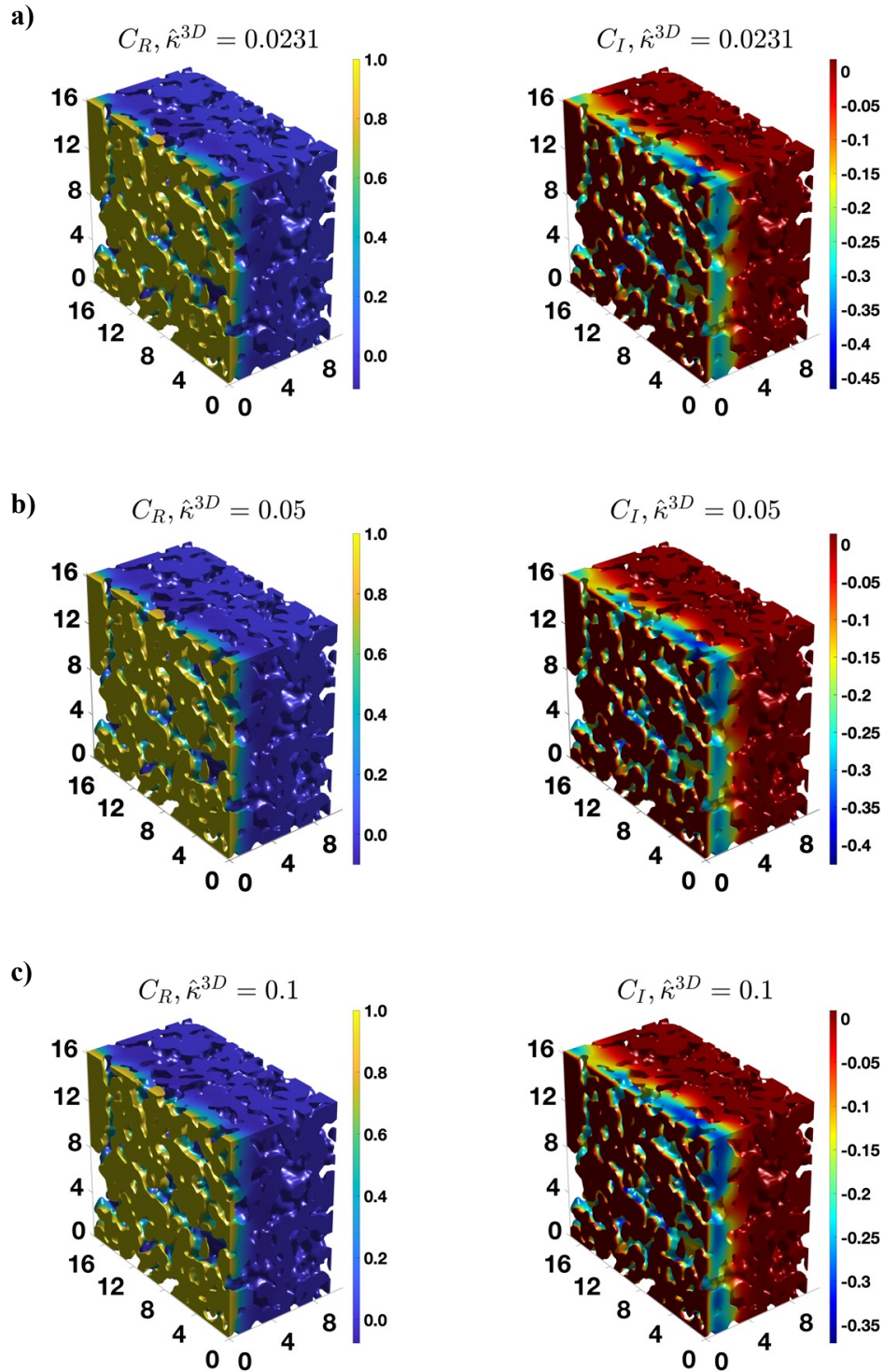


Figure 7.14. The distribution of the real and imaginary components of the concentration amplitude calculated for the TCC BC,  $\hat{\omega} = 1.038$  and (a)  $\hat{\kappa}^{3D} = 0.0231$ , (b) 0.05, and (c) 0.1. Reproduced with permission from Ref. 32. Copyright 2021, the authors. Published by Frontiers Media SA.

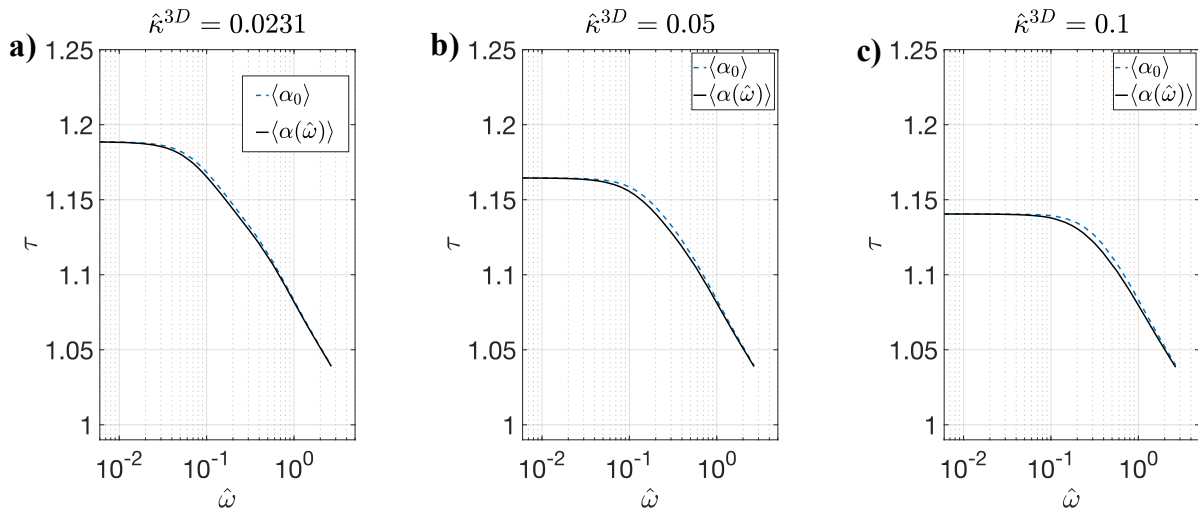


Figure 7.15. Comparison of calculated  $\tau$  vs.  $\hat{\omega}$  relations (TCC BC) by using  $\langle\alpha_0\rangle$  (blue curve) and  $\langle\alpha\rangle$  (black curve) for (a)  $\hat{\kappa}^{3D} = 0.0231$ , (b) 0.05, and (c) 0.1. Reproduced with permission from Ref. 32. Copyright 2021, the authors. Published by Frontiers Media SA.

### ***Data availability***

The shared data for this chapter can be found at the following link:

<https://doi.org/10.13011/m3-ywxf-yw20>.

## **CHAPTER 8**

### **Summary and Future Work**

In this chapter, we provide a summary of the dissertation and discuss the future directions to extend the research conducted in this dissertation.

#### **8.1 Summary**

In this dissertation, we employed a Materials Genome Initiative (MGI)-based approach to investigate the following electrochemical systems: Li-ion batteries (LIBs), Mg alloys undergoing microgalvanic corrosion, and solid oxide fuel cells (SOFCs). We begin by motivating the need to employ such an approach to accelerate the research and development of electrochemical systems in Chapter 1. We also introduce each of the three electrochemical systems studied in this dissertation, along with the challenges associated with each. These challenges include the tradeoff between energy density and fast-charging capabilities of conventional LIB electrodes, degradation of Mg alloys due to microgalvanic corrosion, and difficulty of characterizing SOFC electrodes.

In Chapter 2, we provide the theoretical background on each electrochemical system studied here, including their construction, and mechanism that underlie their functioning. We also describe governing equations for the common physical phenomena observed in electrochemical systems, including the electronic transport in a solid, the ionic transport in a binary electrolyte, the solid-state diffusion of neutral species, the electrochemical reaction at the electrode/electrolyte interface, and the electrochemical impedance.

In Chapter 3, we discuss the three numerical methods, viz. the finite difference method (FDM), finite element method (FEM), and smoothed boundary method (SBM), employed in this dissertation to solve the partial differential equations encountered in the following chapters. For each method, we discuss its fundamentals such as the discretization process, accuracy vs. computational cost tradeoffs and provide an example that illustrates the method's application to solve the 1D diffusion equation. For the FEM and SBM, we also show the derivation process for obtaining the weak form and the SBM form of a partial differential equation, respectively.

In Chapter 4, we detail the modeling work carried out to investigate the effect of the highly order laser-patterned electrode (HOLE) architecture and summarize the associated experimental results provided by our collaborators. We discuss the model equations used to simulate the fast-charging behavior of energy-dense LIB electrodes with and without the HOLE architecture and propose a methodological approach to determine the model parameters. The approach includes an automated parameterization procedure based on the particle swarm optimization (PSO) algorithm.<sup>99,100</sup> Our results show that the HOLE architecture enables fast charging in thick graphite anodes by improving the homogeneity of the electrolyte concentration and reaction current density distribution in the anode volume.

In Chapter 5, we employ the model developed and parameterized in Chapter 4 to determine the optimal HOLE configuration for achieving the best fast-charging performance (measured in terms of accessible capacity) at 4C and 6C. Using 3D simulations, we show that while decreasing the inter-channel spacing improves the fast-charging performance of the HOLE architecture for a constant volume retention, there exists an optimal spacing below which the marginal gain in the performance is not significant. We also establish that the optimal configuration exhibits  $Da_{II} \sim 1$



throughout charging. This fact is further exploited to reduce the computational cost of determining the optimal configuration by developing a semi-analytical framework.

In Chapter 6, we employ phase-field modeling to study the effect of the electrochemical properties of second phases in Mg alloys, the environment, and the spatial distribution of the second phases in the microstructure on the microgalvanic corrosion behavior. Our results show that decreasing either the exchange current density or the corrosion potential of the second phases reduces the corrosion current and promotes more uniform corrosion. Furthermore, we reveal that increasing the electrolyte conductivity improves the corrosion resistance at longer times due to the improved uniformity of corrosion. However, the corrosion current is not as sensitive to the conductivity as it is to the properties of the second phases. Our results also show that the presence of a lamellar region in addition to a bulk  $\alpha$  (the solute-depleted phase) domain in the microstructure proves to be detrimental to the corrosion resistance in both 2D and 3D microstructures.

In Chapter 7, we simulate the impedance behavior of a statistically representative portion of an experimentally determined complex three-dimensional microstructure of an unbiased mixed ion electron conducting (MIEC) SOFC cathode under two different boundary conditions. Our results show that due to the surface reaction, there is a spatial variation in the concentration amplitude. Furthermore, the variation is significant when the ratio between the reaction rate constant and the bulk diffusion coefficient is large, and to account for this variation, we extend the Adler-Lane-Steele (ALS) model. We also show that the effective tortuosity of such cathodes depends not only on the microstructure, but also on the frequency of the applied AC voltage and the material properties like the reaction rate constant and the bulk diffusion coefficient.

## 8.2 Future work

### 8.2.1 *Fast charging of energy-dense Li-ion batteries*

The work conducted in this dissertation to overcome the tradeoff between the energy density and fast-charging capability that exists in conventional LIB electrodes by employing the HOLE architecture can be extended in the following directions:

1. By including Li plating dynamics in the model. This will enable full-cell simulations, which will allow us to achieve the following: optimize charging protocols to achieve faster charging and minimal Li plating; predict the observed energy density at various C rates; and to estimate the capacity degradation caused by Li plating over extended cycling under different operating conditions. One way to implement this modification is to include Li plating as a competing electrochemical reaction in the anode, in addition to the intercalation reaction, as was reported in the literature<sup>216,217</sup> for conventional electrodes.
2. By considering thicker electrodes than this work. Such electrodes when combined with the HOLE architecture could further increase the energy density of batteries, while facilitating fast charging. However, the realization of the optimal configurations for such electrodes might need advances in the laser-patterning processes, as they would need smaller and closer channels than investigated here. Moreover, in such cases, the cathode might also need to be modified with the HOLE architecture, as the cathodic Li-ion transport may become limiting. On the other hand, the thicker anodes might benefit from the combination of the HOLE architecture with the hybrid design, where the graphite is blended with hard carbon to improve the homogeneity of the reaction current density distribution.<sup>23</sup>
3. By accounting for the variation of the electrolyte potential along the thickness of the HOLE anode to improve the accuracy of the semi-analytical framework proposed here to estimate

the time-average value of the second Damköhler number. Such an improvement will further reduce the number of expensive 3D simulations required for validation.

### ***8.2.2 Microgalvanic corrosion in Mg alloys***

The work carried out here to understand the effect of the material properties, the environment, and the microstructure on the dynamics of microgalvanic corrosion can be extended in the following ways:

1. By including diffusion as a transport mechanism in the electrolyte. The model implemented in this work considers the migration of ions as the only transport mechanism in the electrolyte. The proposed extension will enable the application to model systems where large concentration variations are observed in the electrolyte. Note that the *corrosion* application<sup>218</sup> in PRISMS-PF considers the ionic diffusion in the electrolyte, and thus, it should be used as a reference when carrying out this modification.
2. By considering the deposition of corrosion products on the cathode surface. This consideration becomes important in systems where the corrosion products influence the dynamics of the electrochemical reaction at the cathode/electrolyte interface, and thus the overall corrosion behavior. To include this effect, the model can be modified by adding the product phase (which may be porous) that evolves with a prescribed velocity term to the phase evolution equation similar to Eq. 6.6 and appropriately setting the property of the product phase.
3. By considering the effect of different electrochemical properties of the  $\alpha$  phase in the lamellar region and that in the bulk of the microstructure on the corrosion dynamics. Such differences can originate due to the variation of the solute concentration in the two  $\alpha$

phases. One way to carry out such a model extension is to consider two  $\alpha$  phases instead of one and appropriately set the material properties. However, a robust and computationally inexpensive method would be needed to handle the interface between the two  $\alpha$  phases. Alternatively,  $\alpha$  phase may be allowed to have spatially varying properties.

### ***8.2.3 Impedance modeling of SOFC cathodes***

The model developed here to calculate the impedance of a SOFC cathode with experimentally determined microstructure can be extended as follows:

1. By considering electrodes other than MIECs. This will enable the investigation of electrodes, where either surface diffusion is also active, or the surface reaction is limited to the regions where the ionically conducting, the electronically conducting, and the gas phases meet, i.e., the triple phase boundaries. To carry out this modification, one needs to alter the expression of the surface flux (Eq. 7.2).
2. By developing an analytical or semi-analytical framework to determine the ratio of the concentration amplitudes at the pore/solid interface and in the bulk of the solid. Such a framework will reduce the computational cost associated with the determination of tortuosity by using the extended ALS model proposed here. One can begin by considering a simple system such as a model cylindrical microstructure considered in Figure 7.2 and drawing insights from the simulated results to develop the framework.

### 8.3 Conclusion

In conclusion, we employed the three components of the MGI-based approach to varying extents to study three electrochemical systems and overcome specific challenges encountered in each system. Key innovations enabled by this work include the automated parameterization procedure, open-source application with super linear parallel performance to simulate microgalvanic corrosion, and semi-analytical frameworks to reduce the computational cost of simulations. Key scientific insights include the following. For Li-ion batteries, the application of the HOLE architecture enables fast charging of energy-dense graphite electrodes by improving the transport of Li-ions and the homogeneity of the reaction current density distribution. Furthermore, the optimal HOLE configuration has a second Damköhler number  $\sim 1$  throughout charging. For corrosion of Mg alloy, the presence of a lamellar region in addition to a bulk  $\alpha$  domain in the microstructure proves to be detrimental to the corrosion resistance in the microstructures of Mg alloys studied here. Finally, for EIS modeling, the effective tortuosity of SOFC MIEC cathode depends on the material properties (the reaction rate constant and vacancy diffusivity) and the frequency of the applied AC load, in addition to the microstructure.

## References:

1. M. S. Whittingham, *Proc. IEEE*, **100**, 1518–1534 (2012) <http://ieeexplore.ieee.org/document/6184265/>.
2. V. Etacheri, R. Marom, R. Elazari, G. Salitra, and D. Aurbach, *Energy Environ. Sci.*, **4**, 3243 (2011) <http://xlink.rsc.org/?DOI=c1ee01598b>.
3. T. Kim, W. Song, D.-Y. Son, L. K. Ono, and Y. Qi, *J. Mater. Chem. A*, **7**, 2942–2964 (2019) <http://xlink.rsc.org/?DOI=C8TA10513H>.
4. D. Deng, *Energy Sci. Eng.*, **3**, 385–418 (2015) <https://onlinelibrary.wiley.com/doi/10.1002/ese3.95>.
5. N. H. Perry and T. Ishihara, *Materials (Basel)*, **9**, 1–24 (2016).
6. M. B. Mogensen et al., *Clean Energy*, **3**, 175–201 (2019).
7. K. Chen and S. P. Jiang, *J. Electrochem. Soc.*, **163**, F3070–F3083 (2016).
8. J. Hait, R. K. Jana, and S. K. Sanyal, *Miner. Process. Extr. Metall.*, **118**, 240–252 (2009) <http://www.tandfonline.com/doi/full/10.1179/174328509X431463>.
9. C. Boulanger, *J. Electron. Mater.*, **39**, 1818–1827 (2010) <http://link.springer.com/10.1007/s11664-010-1079-6>.
10. A. A. Ojo and I. M. Dharmadasa, *Coatings*, **8**, 262 (2018) <http://www.mdpi.com/2079-6412/8/8/262>.
11. P. Srimuk, X. Su, J. Yoon, D. Aurbach, and V. Presser, *Nat. Rev. Mater.*, **5**, 517–538 (2020) <http://dx.doi.org/10.1038/s41578-020-0193-1>.
12. B. J. Privett, J. H. Shin, and M. H. Schoenfish, *Anal. Chem.*, **82**, 4723–4741 (2010) <https://linkinghub.elsevier.com/retrieve/pii/B9780128138861000048>.
13. G. Koch, in *Trends in Oil and Gas Corrosion Research and Technologies*, p. 3–30, Elsevier (2017) <http://dx.doi.org/10.1016/B978-0-08-101105-8.00001-2>.
14. Y. Zhao et al., *Sustain. Chem.*, **2**, 167–205 (2021) <https://www.mdpi.com/2673-4079/2/1/11>.
15. *Gd. Res.* <https://www.grandviewresearch.com/industry-analysis/fuel-cell-market>.
16. *Yahoo* <https://finance.yahoo.com/news/rechargeable-battery-market-size-share-112200895.html>.
17. W. Cao, J. Zhang, and H. Li, *Energy Storage Mater.*, **26**, 46–55 (2020) <https://doi.org/10.1016/j.ensm.2019.12.024>.
18. *Cleantecnica* <https://cleantecnica.com/2020/02/19/bloombergnef-lithium-ion-battery-cell-densities-have-almost-tripled-since-2010/>.

19. *Ourworldindata* <https://ourworldindata.org/grapher/transistors-per-microprocessor>.
20. J. P. Holdren, *Materials Genome Initiative for Global Competitiveness*, p. 1–18, (2011) [http://www.whitehouse.gov/sites/default/files/microsites/ostp/materials\\_genome\\_initiative-final.pdf](http://www.whitehouse.gov/sites/default/files/microsites/ostp/materials_genome_initiative-final.pdf).
21. H. Liu et al., *ACS Appl. Mater. Interfaces*, **11**, 18386–18394 (2019).
22. K.-H. Chen et al., *J. Power Sources*, **471**, 228475 (2020) <https://doi.org/10.1016/j.jpowsour.2020.228475>.
23. K. Chen et al., *Adv. Energy Mater.*, **11**, 2003336 (2021) <https://onlinelibrary.wiley.com/doi/10.1002/aenm.202003336>.
24. V. Goel, K. Chen, N. P. Dasgupta, and K. Thornton, *Energy Storage Mater.*, **57**, 44–58 (2023) <https://doi.org/10.1016/j.ensm.2023.01.050>.
25. L. K. Aagesen et al., *JOM*, **70**, 2298–2314 (2018) <http://link.springer.com/10.1007/s11837-018-3079-6>.
26. V. Goel, Y. Lyu, S. DeWitt, D. Montiel, and K. Thornton, *MRS Commun.*, **12**, 1050–1059 (2022) <https://doi.org/10.1557/s43579-022-00266-6>.
27. S. DeWitt, S. Rudraraju, D. Montiel, W. B. Andrews, and K. Thornton, *npj Comput. Mater.*, **6**, 29 (2020) <http://dx.doi.org/10.1038/s41524-020-0298-5>.
28. S. B. Adler, J. A. Lane, and B. C. . Steele, *J. Electrochem. Soc.*, **143**, 3554 (1996) <http://jes.ecsdl.org/cgi/doi/10.1149/1.1837252>.
29. S. B. Adler, *Solid State Ionics*, **111**, 125–134 (1998) <https://linkinghub.elsevier.com/retrieve/pii/S0167273898001799>.
30. V. Goel and K. Thornton, *MethodsX*, **8**, 101425 (2021) <https://linkinghub.elsevier.com/retrieve/pii/S2215016121002181>.
31. V. Goel, D. Montiel, and K. Thornton, *Submitt. to J. Electrochem. Soc. (in revision)* (2023).
32. V. Goel, D. Cox, S. A. Barnett, and K. Thornton, *Front. Chem.*, **9** (2021) <https://www.frontiersin.org/articles/10.3389/fchem.2021.627699/full>.
33. J.-M. Tarascon and M. Armand, *Nature*, **414**, 359–367 (2001) <http://www.ncbi.nlm.nih.gov/pubmed/11713543>.
34. Y. Chen, thesis, University of Michigan, Ann Arbor (2022) <https://deepblue.lib.umich.edu/handle/2027.42/174321>.
35. J. Newman and K. E. Thomas-Alyea, *Electrochemical Systems*, 3rd ed., p. 274–275, Wiley, New Jersey, (2004) <https://books.google.com/books?id=eyj4MRa7vLAC>.
36. P. K. Dutta et al., in *Energy, Environment, and Sustainability*, S. Bhattacharya, T. Rajagopalan, A. K. Agarwal, and V. K. Patel, Editors, p. 81–108 (2019)

[http://link.springer.com/10.1007/978-981-13-3269-2\\_4](http://link.springer.com/10.1007/978-981-13-3269-2_4).

37. N. Nitta, F. Wu, J. T. Lee, and G. Yushin, *Mater. Today*, **18**, 252–264 (2015)

<http://dx.doi.org/10.1016/j.mattod.2014.10.040>.

38. K. G. Gallagher et al., *J. Electrochem. Soc.*, **163**, A138–A149 (2016)

<https://iopscience.iop.org/article/10.1149/2.0321602jes>.

39. T. Waldmann, B.-I. Hogg, and M. Wohlfahrt-Mehrens, *J. Power Sources*, **384**, 107–124

(2018) <https://linkinghub.elsevier.com/retrieve/pii/S0378775318301848>.

40. X. G. Zhang, in *Uhlig's Corrosion Handbook*, vol. 51, p. 123, John Wiley & Sons, Inc. Hoboken, NJ, USA (2011).

41. M. Akhoondan and G. E. C. Bell, *Struct. Mag.*, 74–75 (2016).

42. X. Chen, M. Gussev, M. Balonis, M. Bauchy, and G. Sant, *Mater. Des.*, **203**, 109614 (2021)

<https://doi.org/10.1016/j.matdes.2021.109614>.

43. Q. Li et al., *Int. J. Fatigue*, **170**, 107568 (2023)

<https://linkinghub.elsevier.com/retrieve/pii/S0142112323000695>.

44. H. Chen, Z. Lv, L. Lu, Y. Huang, and X. Li, *J. Mater. Res. Technol.*, **15**, 3310–3320 (2021)

<https://doi.org/10.1016/j.jmrt.2021.09.123>.

45. Y. Ji et al., *Trans. Nonferrous Met. Soc. China*, **31**, 3205–3227 (2021)

[http://dx.doi.org/10.1016/S1003-6326\(21\)65727-8](http://dx.doi.org/10.1016/S1003-6326(21)65727-8).

46. M. Esmaily et al., *Prog. Mater. Sci.*, **89**, 92–193 (2017)

<http://dx.doi.org/10.1016/j.pmatsci.2017.04.011>.

47. P.-P. Wu, G.-L. Song, Y.-X. Zhu, Z.-L. Feng, and D.-J. Zheng, *Corros. Sci.*, **184**, 109410

(2021) <https://doi.org/10.1016/j.corsci.2021.109410>.

48. X. Cao et al., *Mater. Chem. Phys.*, **271**, 124928 (2021)

<https://doi.org/10.1016/j.matchemphys.2021.124928>.

49. C. Singh, S. S. Singh, and J. Jain, *Philos. Mag. Lett.*, **102**, 299–306 (2022)

<https://doi.org/10.1080/09500839.2022.2121866>.

50. G. Song, A. Atrens, and M. Dargusch, *Corros. Sci.*, **41**, 249–273 (1998)

<https://linkinghub.elsevier.com/retrieve/pii/S0010938X98001218>.

51. V. Hasannaemi and S. Mukherjee, *J. Electroanal. Chem.*, **848**, 113331 (2019)

<https://doi.org/10.1016/j.jelechem.2019.113331>.

52. L. Wei and W. Qin, *Corros. Sci.*, **206**, 110525 (2022)

<https://doi.org/10.1016/j.corsci.2022.110525>.

53. M.-C. Zhao, M. Liu, G. L. Song, and A. Atrens, *Adv. Eng. Mater.*, **10**, 93–103 (2008)

<https://onlinelibrary.wiley.com/doi/10.1002/adem.200700234>.



54. X. Li, in *Advances in Fuel Cells*, vol. 1, p. 1–46, Elsevier Ltd (2007)  
[http://dx.doi.org/10.1016/S1752-301X\(07\)80006-8](http://dx.doi.org/10.1016/S1752-301X(07)80006-8).
55. Z. Gao, L. V. Mogni, E. C. Miller, J. G. Railsback, and S. A. Barnett, *Energy Environ. Sci.*, **9**, 1602–1644 (2016).
56. J. Nielsen and J. Hjelm, *Electrochim. Acta*, **115**, 31–45 (2014)  
<http://dx.doi.org/10.1016/j.electacta.2013.10.053>.
57. J. Nielsen, T. Jacobsen, and M. Wandel, *Electrochim. Acta*, **56**, 7963–7974 (2011)  
<http://dx.doi.org/10.1016/j.electacta.2011.05.042>.
58. J. P. Diard, B. . Gorrec, and C. Monetella, *Handbook of Electrochemical Impedance Spectroscopy*, (2017) [www.bio-logic.info](http://www.bio-logic.info).
59. H. C. Yu, S. B. Adler, S. A. Barnett, and K. Thornton, *Electrochim. Acta*, **354**, 136534 (2020) <https://doi.org/10.1016/j.electacta.2020.136534>.
60. R. Courant, K. O. Friedrichs, and H. Lewy, *Math Ann*, **100** (1928).
61. V. Thomée, *J. Comput. Appl. Math.*, **128**, 1–54 (2001)  
<https://linkinghub.elsevier.com/retrieve/pii/S0377042700005070>.
62. S. Gerschgorin, *ZAMM - Zeitschrift für Angew. Math. und Mech.*, **10**, 373–382 (1930)  
<https://onlinelibrary.wiley.com/doi/10.1002/zamm.19300100409>.
63. G. G. O'Brien, M. A. Hyman, and S. Kaplan, *J. Math. Phys.*, **29**, 223–251 (1951)  
<https://www.scopus.com/inward/record.uri?eid=2-s2.0-0001162689&partnerID=40&md5=b13e4a5e81bd20d8ec8a8f448ecc39d0>.
64. F. John, *Commun. Pure Appl. Math.*, **5**, 155–211 (1952)  
<https://onlinelibrary.wiley.com/doi/10.1002/cpa.3160050203>.
65. J. Crank and P. Nicolson, *Math. Proc. Cambridge Philos. Soc.*, **43**, 50–67 (1947)  
[https://www.cambridge.org/core/product/identifier/S0305004100023197/type/journal\\_article](https://www.cambridge.org/core/product/identifier/S0305004100023197/type/journal_article).
66. P. D. Lax, *Commun. Pure Appl. Math.*, **14**, 497–520 (1961)  
<https://onlinelibrary.wiley.com/doi/10.1002/cpa.3160140324>.
67. P. D. Lax and B. Wendroff, *Commun. Pure Appl. Math.*, **17**, 381–398 (1964)  
<https://onlinelibrary.wiley.com/doi/10.1002/cpa.3160170311>.
68. B. Bradie, *A friendly introduction to numerical analysis*, Pearson Education India, (2006).
69. T. J. R. Hughes, *The finite element method: linear static and dynamic finite element analysis*, Courier Corporation, (2012).
70. O. C. Zienkiewicz, R. L. Taylor, and J. Z. Zhu, in *The Finite Element Method: its Basis and Fundamentals (Seventh Edition)*, Butterworth-Heinemann, Oxford (2013)  
<https://www.sciencedirect.com/science/article/pii/B9781856176330000198>.

71. J. P. Boyd, *Comput. Math. with Appl.*, **60**, 3108–3122 (2010)  
<http://dx.doi.org/10.1016/j.camwa.2010.10.015>.
72. [https://github.com/prisms-center/phaseField/tree/master/applications/corrosion\\_microgalvanic](https://github.com/prisms-center/phaseField/tree/master/applications/corrosion_microgalvanic).
73. O. C. Zienkiewicz and C. J. Parekh, *Int. J. Numer. Methods Eng.*, **2**, 61–71 (1970)  
<https://onlinelibrary.wiley.com/doi/10.1002/nme.1620020107>.
74. E. L. Wilson and R. E. Nickell, *Nucl. Eng. Des.*, **4**, 276–286 (1966).
75. H.-C. Yu, H.-Y. Chen, and K. Thornton, *Model. Simul. Mater. Sci. Eng.*, **20**, 075008 (2012)  
<https://iopscience.iop.org/article/10.1088/0965-0393/20/7/075008>.
76. Y. Liu, Y. Zhu, and Y. Cui, *Nat. Energy*, **4**, 540–550 (2019)  
<http://dx.doi.org/10.1038/s41560-019-0405-3>.
77. K. G. Gallagher et al., *J. Electrochem. Soc.*, **163**, A138–A149 (2016)  
<https://iopscience.iop.org/article/10.1149/2.0321602jes>.
78. Y. Kim, A. Drews, R. Chandrasekaran, T. Miller, and J. Sakamoto, *Ionics (Kiel)*, **24**, 2935–2943 (2018).
79. L. Li, R. M. Erb, J. Wang, J. Wang, and Y. Chiang, *Adv. Energy Mater.*, **9**, 1802472 (2019).
80. C. Heubner, M. Schneider, and A. Michaelis, *Adv. Energy Mater.*, **10**, 1902523 (2020).
81. D. H. Kim et al., *ACS Energy Lett.*, **4**, 1265–1270 (2019).
82. K.-H. Chen et al., *J. Mater. Chem. A*, **5**, 11671–11681 (2017).
83. X. G. Yang and C. Y. Wang, *J. Power Sources*, **402**, 489–498 (2018).
84. X. G. Yang et al., *Joule*, **3**, 3002–3019 (2019).
85. A. S. Mussa et al., *J. Power Sources*, **422**, 175–184 (2019).
86. J. B. Habedank et al., *J. Electrochem. Soc.*, **165**, A1563–A1573 (2018).
87. N. Dunlap et al., *J. Power Sources*, **537**, 231464 (2022)  
<https://doi.org/10.1016/j.jpowsour.2022.231464>.
88. S. Wu et al., *Chem. Eng. J.*, **430**, 132810 (2022) <https://doi.org/10.1016/j.cej.2021.132810>.
89. W. Mai, F. L. E. Usseglio-Viretta, A. M. Colclasure, and K. Smith, *Electrochim. Acta*, **341**, 136013 (2020) <https://doi.org/10.1016/j.electacta.2020.136013>.
90. F. L. E. Usseglio-Viretta et al., *Electrochim. Acta*, **342**, 136034 (2020)  
<https://doi.org/10.1016/j.electacta.2020.136034>.
91. J. B. Habedank, J. Kriegler, and M. F. Zaeh, *J. Electrochem. Soc.*, **166**, A3940–A3949 (2019) <https://iopscience.iop.org/article/10.1149/2.1241915jes>.

92. L. Kraft, J. B. Habedank, A. Frank, A. Rheinfeld, and A. Jossen, *J. Electrochem. Soc.*, **167**, 013506 (2020) <https://iopscience.iop.org/article/10.1149/2.0062001JES>.
93. L. Hille et al., *Electrochim. Acta*, **392**, 139002 (2021) <https://doi.org/10.1016/j.electacta.2021.139002>.
94. V. De Lauri et al., *ACS Appl. Energy Mater.*, **4**, 13847–13859 (2021).
95. J. Kriegler et al., *Appl. Energy*, **303**, 117693 (2021) <https://doi.org/10.1016/j.apenergy.2021.117693>.
96. L. Schweighofer, B. Eschelmüller, K. Fröhlich, W. Pfleging, and F. Pichler, *Nanomaterials*, **12**, 1574 (2022) <https://www.mdpi.com/2079-4991/12/9/1574>.
97. L. Hille et al., *J. Electrochem. Soc.*, **169**, 060518 (2022).
98. Y. Guo et al., *Energy Storage Mater.*, **51**, 476–485 (2022) <https://doi.org/10.1016/j.ensm.2022.07.007>.
99. M. Clerc and J. Kennedy, *IEEE Trans. Evol. Comput.*, **6**, 58–73 (2002) <http://ieeexplore.ieee.org/document/985692/>.
100. J. Kennedy and R. Eberhart, in *Proceedings of ICNN'95 - International Conference on Neural Networks*, vol. 4, p. 1942–1948, IEEE (1995) <http://ieeexplore.ieee.org/document/488968/>.
101. J. S. Newman and C. W. Tobias, *J. Electrochem. Soc.*, **109**, 1183–1191 (1962) <http://jes.ecsdl.org/cgi/doi/10.1149/1.2425269>.
102. J. Newman and W. Tiedemann, *AIChE J.*, **21**, 25–41 (1975) <https://aiche.onlinelibrary.wiley.com/doi/abs/10.1002/aic.690210103>.
103. M. Doyle, J. Newman, A. S. Gozdz, C. N. Schmutz, and J. M. Tarascon, *J. Electrochem. Soc.*, **143**, 1890 (1996).
104. M. Doyle and J. Newman, *J. Power Sources*, **54**, 46–51 (1995).
105. M. Doyle, T. F. Fuller, and J. Newman, *Electrochim. Acta*, **39**, 2073–2081 (1994).
106. T. F. Fuller, M. Doyle, and J. Newman, *J. Electrochem. Soc.*, **141**, 1–10 (1994) <https://iopscience.iop.org/article/10.1149/1.2054684>.
107. N. Epstein, *Chem. Eng. Sci.*, **44**, 777–779 (1989) <https://linkinghub.elsevier.com/retrieve/pii/0009250989850535>.
108. K. Zaghbi, G. Nadeau, and K. Kinoshita, *J. Electrochem. Soc.*, **147**, 2110 (2000) <https://iopscience.iop.org/article/10.1149/1.1393493>.
109. T. V. S. L. Satyavani, B. Ramya Kiran, V. Rajesh Kumar, A. Srinivas Kumar, and S. V. Naidu, *Eng. Sci. Technol. an Int. J.*, **19**, 40–44 (2016) <http://dx.doi.org/10.1016/j.jestch.2015.05.011>.

110. T. Aida, T. Toma, and S. Kanada, *J. Solid State Electrochem.*, **24**, 1415–1425 (2020) <https://link.springer.com/10.1007/s10008-020-04640-z>.
111. M. Winter, P. Novák, and A. Monnier, *J. Electrochem. Soc.*, **145**, 428–436 (1998) <https://iopscience.iop.org/article/10.1149/1.1838281>.
112. F. Pouraghajan et al., *J. Electrochem. Soc.*, **165**, A2644–A2653 (2018).
113. S. Malifarge, B. Delobel, and C. Delacourt, *J. Electrochem. Soc.*, **164**, E3329–E3334 (2017).
114. F. L. E. Usseglio-Viretta et al., *J. Electrochem. Soc.*, **165**, A3403–A3426 (2018).
115. J. Landesfeind, M. Ebner, A. Eldiven, V. Wood, and H. A. Gasteiger, *J. Electrochem. Soc.*, **165**, A469–A476 (2018).
116. W. Wang, D. Juarez-Robles, and P. P. Mukherjee, *J. Electrochem. Soc.*, **167**, 080510 (2020) <https://iopscience.iop.org/article/10.1149/1945-7111/ab8975>.
117. J. Landesfeind, J. Hattendorff, A. Ehrl, W. A. Wall, and H. A. Gasteiger, *J. Electrochem. Soc.*, **163**, A1373–A1387 (2016) <https://iopscience.iop.org/article/10.1149/2.1141607jes>.
118. Y. C. K. Chen-Wiegart et al., *J. Power Sources*, **249**, 349–356 (2014) <http://dx.doi.org/10.1016/j.jpowsour.2013.10.026>.
119. J. Fu, H. R. Thomas, and C. Li, *Earth-Science Rev.*, **212**, 103439 (2021) <https://doi.org/10.1016/j.earscirev.2020.103439>.
120. M. Ebner, D.-W. Chung, R. E. García, and V. Wood, *Adv. Energy Mater.*, **4**, 1301278 (2014) <https://onlinelibrary.wiley.com/doi/10.1002/aenm.201301278>.
121. N. O. Shanti et al., *Acta Mater.*, **71**, 126–135 (2014) <http://dx.doi.org/10.1016/j.actamat.2014.03.003>.
122. D. W. Chung, M. Ebner, D. R. Ely, V. Wood, and R. Edwin García, *Model. Simul. Mater. Sci. Eng.*, **21** (2013).
123. S. J. Cooper, A. Bertei, P. R. Shearing, J. A. Kilner, and N. P. Brandon, *SoftwareX*, **5**, 203–210 (2016) <http://dx.doi.org/10.1016/j.softx.2016.09.002>.
124. B. Tjaden, D. J. L. Brett, and P. R. Shearing, *Int. Mater. Rev.*, **63**, 47–67 (2018) <https://doi.org/10.1080/09506608.2016.1249995>.
125. M. Ebner and V. Wood, *J. Electrochem. Soc.*, **162**, A3064–A3070 (2015) <https://iopscience.iop.org/article/10.1149/2.0111502jes>.
126. A. Nickol et al., *J. Electrochem. Soc.*, **167**, 090546 (2020) <https://iopscience.iop.org/article/10.1149/1945-7111/ab9404>.
127. Y. Bai et al., *Electrochim. Acta*, **109**, 355–364 (2013) <http://dx.doi.org/10.1016/j.electacta.2013.06.134>.

128. K. Tang, X. Yu, J. Sun, H. Li, and X. Huang, *Electrochim. Acta*, **56**, 4869–4875 (2011) <http://dx.doi.org/10.1016/j.electacta.2011.02.119>.
129. M. Ender, *J. Power Sources*, **282**, 572–580 (2015) <http://dx.doi.org/10.1016/j.jpowsour.2015.02.098>.
130. M. D. Levi and D. Aurbach, *J. Phys. Chem. B*, **101**, 4641–4647 (1997).
131. A. Nyman, M. Behm, and G. Lindbergh, *Electrochim. Acta*, **53**, 6356–6365 (2008) <https://linkinghub.elsevier.com/retrieve/pii/S0013468608005045>.
132. F. Wang and M. Tang, *J. Electrochem. Soc.*, **167**, 120543 (2020).
133. Z. Chen, D. L. Danilov, R.-A. Eichel, and P. H. L. Notten, *Energy Storage Mater.*, **48**, 475–486 (2022) <https://doi.org/10.1016/j.ensm.2022.03.037>.
134. K. A. Smith, C. D. Rahn, and C. Y. Wang, *Energy Convers. Manag.*, **48**, 2565–2578 (2007).
135. K. Smith and C.-Y. Wang, *J. Power Sources*, **160**, 662–673 (2006) <https://linkinghub.elsevier.com/retrieve/pii/S0378775306001017>.
136. M. Ecker, S. Käbitz, I. Laresgoiti, and D. U. Sauer, *J. Electrochem. Soc.*, **162**, A1849–A1857 (2015).
137. J. Schmalstieg, C. Rahe, M. Ecker, and D. U. Sauer, *J. Electrochem. Soc.*, **165**, A3799–A3810 (2018).
138. S. S. Zhang, *J. Power Sources*, **164**, 351–364 (2007).
139. D. E. Goldberg, *Genetic Algorithms in Search, Optimization and Machine Learning*, 1st ed., Addison-Wesley Longman Publishing Co., Inc., USA, (1989).
140. J. C. Forman, S. J. Moura, J. L. Stein, and H. K. Fathy, *Proc. Am. Control Conf.*, 362–369 (2011).
141. J. C. Forman, S. J. Moura, J. L. Stein, and H. K. Fathy, *J. Power Sources*, **210**, 263–275 (2012) <http://dx.doi.org/10.1016/j.jpowsour.2012.03.009>.
142. G. Huang et al., *Comput. Mater. Sci.*, **194**, 110459 (2021) <https://linkinghub.elsevier.com/retrieve/pii/S0927025621001841>.
143. H. Arunachalam and S. Onori, *J. Electrochem. Soc.*, **166**, A1380–A1392 (2019) <https://iopscience.iop.org/article/10.1149/2.0051908jes>.
144. D. Sauerteig et al., *J. Power Sources*, **378**, 235–247 (2018) <https://doi.org/10.1016/j.jpowsour.2017.12.044>.
145. M. Ecker et al., *J. Electrochem. Soc.*, **162**, A1836–A1848 (2015).
146. M. Tang, P. Albertus, and J. Newman, *J. Electrochem. Soc.*, **156**, A390–A399 (2009).

147. Z. Du, D. L. Wood, C. Daniel, S. Kalnaus, and J. Li, *J. Appl. Electrochem.*, **47**, 405–415 (2017).
148. S. Cui et al., *Adv. Energy Mater.*, **6**, 1–9 (2016).
149. S. J. An, J. Li, C. Daniel, S. Kalnaus, and D. L. Wood, *J. Electrochem. Soc.*, **164**, A1755–A1764 (2017).
150. R. Amin and Y. M. Chiang, *J. Electrochem. Soc.*, **163**, A1512–A1517 (2016).
151. A. Nyman, M. Behm, and G. Lindbergh, *Electrochim. Acta*, **53**, 6356–6365 (2008).
152. S. Kazemiabnavi, thesis, University of Michigan, Ann Arbor (2019) <https://hdl.handle.net/2027.42/155293>.
153. H. Arunachalam, S. Onori, and I. Battiato, *J. Electrochem. Soc.*, **162**, A1940–A1951 (2015) <https://iopscience.iop.org/article/10.1149/2.0771509jes>.
154. N. Kotak, P. Barai, A. Verma, A. Mistry, and P. P. Mukherjee, *J. Electrochem. Soc.*, **165**, A1064–A1083 (2018).
155. H. Arunachalam, S. Onori, and I. Battiato, in *2015 American Control Conference (ACC)*, vol. 2015-July, p. 305–310, IEEE (2015) <http://ieeexplore.ieee.org/document/7170753/>.
156. R. A. Enrique, S. DeWitt, and K. Thornton, *MRS Commun.*, **7**, 658–663 (2017).
157. A. M. Colclasure et al., *J. Electrochem. Soc.*, **166**, A1412–A1424 (2019).
158. Y. Yamada, M. Yaegashi, T. Abe, and A. Yamada, *Chem. Commun.*, **49**, 11194 (2013) <http://xlink.rsc.org/?DOI=c3cc46665e>.
159. A. L. Davis et al., *ACS Energy Lett.*, **6**, 2993–3003 (2021) <https://pubs.acs.org/doi/10.1021/acseenergylett.1c01063>.
160. S. Malifarge, B. Delobel, and C. Delacourt, *J. Electrochem. Soc.*, **164**, E3329–E3334 (2017) <https://iopscience.iop.org/article/10.1149/2.0331711jes>.
161. M. M. Avedesian and H. Baker, *ASM specialty handbook: magnesium and magnesium alloys*, ASM international, (1999).
162. J. Xie et al., *J. Magnes. Alloy.*, **9**, 41–56 (2021) <https://doi.org/10.1016/j.jma.2020.08.016>.
163. N. Birbilis, M. A. Easton, A. D. Sudholz, S. M. Zhu, and M. A. Gibson, *Corros. Sci.*, **51**, 683–689 (2009) <http://dx.doi.org/10.1016/j.corsci.2008.12.012>.
164. G. Song, A. Atrens, D. Stjohn, J. Nairn, and Y. Li, *Corros. Sci.*, **39**, 855–875 (1997) <https://linkinghub.elsevier.com/retrieve/pii/S0010938X96001722>.
165. S. Thomas, N. V. Medhekar, G. S. Frankel, and N. Birbilis, *Curr. Opin. Solid State Mater. Sci.*, **19**, 85–94 (2015) <http://dx.doi.org/10.1016/j.cossms.2014.09.005>.
166. L. J. Liu and M. Schlesinger, *Corros. Sci.*, **51**, 1733–1737 (2009)

<http://dx.doi.org/10.1016/j.corsci.2009.04.025>.

167. R. K. Singh Raman, *Metall. Mater. Trans. A*, **35**, 2525–2531 (2004)  
<http://link.springer.com/10.1007/s11661-006-0233-5>.

168. G. S. Frankel and N. Sridhar, *Mater. Today*, **11**, 38–44 (2008)  
[http://dx.doi.org/10.1016/S1369-7021\(08\)70206-2](http://dx.doi.org/10.1016/S1369-7021(08)70206-2).

169. J. X. Jia, G. Song, and A. Atrens, *Corros. Sci.*, **48**, 2133–2153 (2006)  
<https://linkinghub.elsevier.com/retrieve/pii/S0010938X05002659>.

170. G. Ben-Hamu, D. Eliezer, K. S. Shin, and S. Cohen, *J. Alloys Compd.*, **431**, 269–276 (2007).

171. M.-C. Zhao, M. Liu, G. Song, and A. Atrens, *Corros. Sci.*, **50**, 1939–1953 (2008)  
<https://linkinghub.elsevier.com/retrieve/pii/S0010938X08001340>.

172. M. C. Zhao et al., *Mater. Sci. Forum*, **618–619**, 473–478 (2009)  
<https://www.scientific.net/MSF.618-619.473>.

173. A. E. Coy, F. Viejo, P. Skeldon, and G. E. Thompson, *Corros. Sci.*, **52**, 3896–3906 (2010)  
<http://dx.doi.org/10.1016/j.corsci.2010.08.006>.

174. W. Liu, F. Cao, L. Chang, Z. Zhang, and J. Zhang, *Corros. Sci.*, **51**, 1334–1343 (2009)  
<http://dx.doi.org/10.1016/j.corsci.2009.03.018>.

175. C. Ubeda et al., *Corros. Sci.*, **165**, 108384 (2020)  
<https://doi.org/10.1016/j.corsci.2019.108384>.

176. V. K. Beura, P. Garg, V. V. Joshi, and K. N. Solanki, in *Minerals, Metals and Materials Series*, p. 217–223, Springer International Publishing (2020) [http://dx.doi.org/10.1007/978-3-030-36647-6\\_34](http://dx.doi.org/10.1007/978-3-030-36647-6_34).

177. K. B. Deshpande, *Electrochim. Acta*, **56**, 1737–1745 (2011)  
<http://dx.doi.org/10.1016/j.electacta.2010.09.044>.

178. N. Moelans, B. Blanpain, and P. Wollants, *Phys. Rev. B*, **78**, 024113 (2008)  
<https://link.aps.org/doi/10.1103/PhysRevB.78.024113>.

179. T. Uehara and R. F. Sekerka, *J. Cryst. Growth*, **254**, 251–261 (2003)  
<https://linkinghub.elsevier.com/retrieve/pii/S0022024803011205>.

180. J. W. Cahn and J. E. Hilliard, *J. Chem. Phys.*, **28**, 258–267 (1958)  
<http://aip.scitation.org/doi/10.1063/1.1730145>.

181. A. F. Chadwick, J. A. Stewart, R. A. Enrique, S. Du, and K. Thornton, *J. Electrochem. Soc.*, **165**, C633–C646 (2018) <https://iopscience.iop.org/article/10.1149/2.0701810jes>.

182. A. J. Bard and L. R. Faulkner, *Electrochemical Methods: Fundamentals and Applications*, 2nd ed., p. 661, Wiley, New York, NY, (2002).

183. A. D. Südholz, N. T. Kirkland, R. G. Buchheit, and N. Birbilis, *Electrochem. Solid-State Lett.*, **14**, C5 (2011) <https://iopscience.iop.org/article/10.1149/1.3523229>.
184. N. R. G. Walton, *Desalination*, **72**, 275–292 (1989) <https://linkinghub.elsevier.com/retrieve/pii/0011916489800128>.
185. C. Wagner, *J. Electrochem. Soc.*, **98**, 116 (1951) <https://iopscience.iop.org/article/10.1149/1.2778113>.
186. G. L. Song, Ed., *Corrosion Prevention of Magnesium Alloys*, p. 232–282, Elsevier Science, (2013) <https://books.google.com/books?id=OgxaAgAAQBAJ>.
187. S. C. Hayden et al., *Nano Lett.*, **22**, 7087–7093 (2022) <https://pubs.acs.org/doi/10.1021/acs.nanolett.2c02122>.
188. M. A. R. Niania, A. K. Rossall, J. A. Van den Berg, and J. A. Kilner, *J. Mater. Chem. A*, **8**, 19414–19424 (2020).
189. H. J. Hwang, J. W. Moon, S. Lee, and E. A. Lee, *J. Power Sources*, **145**, 243–248 (2005).
190. M. Liu, Z. Liu, M. Liu, and L. Nie, *Int. J. Hydrogen Energy*, **38**, 1082–1087 (2013) <http://dx.doi.org/10.1016/j.ijhydene.2012.10.048>.
191. C. Y. Yoo and H. J. M. Bouwmeester, *Phys. Chem. Chem. Phys.*, **14**, 11759–11765 (2012).
192. N. H. Perry, J. J. Kim, S. R. Bishop, and H. L. Tuller, *J. Mater. Chem. A*, **3**, 3602–3611 (2015).
193. A. Nenning et al., *J. Electrochem. Soc.*, **164**, F364–F371 (2017).
194. D. A. G. Bruggeman, *Ann. Phys.*, **416**, 636–664 (1935) <http://doi.wiley.com/10.1002/andp.19354160705>.
195. A. Çeçen et al., *J. Electrochem. Soc.*, **159**, B299–B307 (2012).
196. J. R. Wilson et al., *Nat. Mater.*, **5**, 541–544 (2006).
197. B. Tjaden, D. J. L. Brett, and P. R. Shearing, *Int. Mater. Rev.*, **63**, 47–67 (2018) <https://www.tandfonline.com/doi/full/10.1080/09506608.2016.1249995>.
198. J. Scott Cronin et al., *J. Electrochem. Soc.*, **159**, B385–B393 (2012) <https://iopscience.iop.org/article/10.1149/2.053204jes>.
199. S. L. Zhang et al., *Energy Environ. Sci.*, **11**, 1870–1879 (2018).
200. S. L. Zhang et al., *J. Mater. Chem. A*, **7**, 21447–21458 (2019).
201. A. Haffelin, J. Joos, M. Ender, A. Weber, and E. Ivers-Tiffée, *J. Electrochem. Soc.*, **160**, F867–F876 (2013) <http://jes.ecsdl.org/cgi/doi/10.1149/2.093308jes>.
202. J. M. C. Pereira, J. E. P. Navalho, A. C. G. Amador, and J. C. F. Pereira, *Chem. Eng. Sci.*, **117**, 364–375 (2014) <http://dx.doi.org/10.1016/j.ces.2014.06.028>.



203. B. Rüger, A. Weber, and E. Ivers-Tiffée, *ECS Trans.*, **7**, 2065–2074 (2007).
204. M. E. Lynch et al., *Nano Energy*, **2**, 105–115 (2013)  
<http://dx.doi.org/10.1016/j.nanoen.2012.08.002>.
205. C. Kreller et al., *ECS Trans.*, **35**, 815–822 (2011)  
<https://iopscience.iop.org/article/10.1149/1.3570062>.
206. C. R. Kreller, thesis, University of Washington (2011)  
<https://proxy.lib.umich.edu/login?url=https://www.proquest.com/dissertations-theses/measurement-modeling-material-microstructural/docview/865807958/se-2?accountid=14667>.
207. W. C. Jung and H. L. Tuller, *Solid State Ionics*, **180**, 843–847 (2009).
208. J. Mizusaki, I. Yasuda, J. Shimoyama, S. Yamauchi, and K. Fueki, *J. Electrochem. Soc.*, **140**, 467–471 (1993).
209. T. Jacobsen and K. West, *Electrochim. Acta*, **40**, 255–262 (1995).
210. B.A. Boukamp, H.J.M. Bouwmeester, B. A. Boukamp, and H. J. M. Bouwmeester, *Solid State Ionics*, **157**, 29–33 (2003).
211. B. A. Boukamp, M. Verbraeken, D. H. A. Blank, and P. Holtappels, **177**, 2539–2541 (2006).
212. P. Holtappels, M. Verbraeken, U. Vogt, D. H. A. Blank, and B. A. Boukamp, *Solid State Ionics*, **177**, 2029–2032 (2006).
213. J. Hofhaus and E. F. Van de Velde, *SIAM J. Sci. Comput.*, **17**, 454–478 (1996)  
<http://epubs.siam.org/doi/10.1137/S1064827593253872>.
214. H. M. Rootare and C. F. Prenzlöw, *J. Phys. Chem.*, **71**, 2733–2736 (1967)  
<https://pubs.acs.org/doi/abs/10.1021/j100867a057>.
215. Y. Zhang et al., *J. Mater. Chem. A*, **7**, 10256–10263 (2019)  
<http://xlink.rsc.org/?DOI=C9TA01784D>.
216. X.-G. Yang, Y. Leng, G. Zhang, S. Ge, and C.-Y. Wang, *J. Power Sources*, **360**, 28–40 (2017) <http://dx.doi.org/10.1016/j.jpowsour.2017.05.110>.
217. W. Mei, L. Jiang, C. Liang, J. Sun, and Q. Wang, *Energy Storage Mater.*, **41**, 209–221 (2021) <https://doi.org/10.1016/j.ensm.2021.06.013>.
218. <https://github.com/prisms-center/phaseField/tree/master/applications/corrosion>.